A tale of two oviducts: anatomical and cellular heterogeneity in the mouse oviduct epithelium across adulthood and aging

Keerthana Harwalkar

Department of Human Genetics
McGill University, Montréal

August 2024

A thesis submitted to McGill University in partial fulfillment of the requirements of the degree of Doctor of Philosophy

Abstract

The oviduct/fallopian tube is a structure that extends from the uterus to the ovary. It provides an optimal environment for fertilization and preimplantation development. However, our knowledge of its regional and cellular heterogeneity is still limited. We demonstrated that the basic coiling pattern in the oviduct serves as reliable landmarks for all 5 regions that have distinct mucosal fold morphologies: distal infundibulum (INF), ampulla (AMP), ampulla-isthmus junction (AIJ), isthmus (ISM), and proximal uterotubal junction (UTJ). Lining the mucosal folds are two types of epithelial cells: multi-ciliated (MCC) and secretory cells (SC). We showed distinct transcription factor (TFs) expression and proportions/distribution patterns of MCCs in each region. Taken together, each of these regions were lined with distinct pairs of MCCs and SCs – totaling 7 epithelial subtypes.

Upon performing SmartSeq analysis from 30 cells of each epithelial subtype, we found that each subtype expresses numerous differentially expressed genes and geneset enrichment indicating distinct identity and functional diversity. Additionally, we found a minor population in the INF/AMP that represents a SC-to-MCC transitory state.

In aging, we found a unique phenotype restricted to INF/AMP MCCs, including progressive cytoplasmic vacuolation and nuclear anomaly that begins in 7-month-old (7mo) mice. The timeline of this cytoplasmic vacuolation was unaffected by lack of ovulation or estrous cycling, suggesting that this phenotype may result from an altered INF/AMP microenvironment. In agreement with this, single-Cell RNASeq analysis of all INF/AMP cells from 18mo mice showed upregulation of cellular stress & ROS-associated genesets, relative to 3mo. Interestingly, *in vitro* organotypic slice cultures exposed to hypoxia or hydroxyurea developed similar cytoplasmic vacuoles. However, unlike the *in vivo* phenotype, MCC-specific vacuoles were noted in slice cultures from all oviduct regions. Interestingly, we found that the

ovarian artery fed directly into the ovary and INF/AMP, while the uterine artery supplied the proximal oviduct. In aging, absence of blood vessel labeling in the ovary suggests a decline in oxygenation of the ovary and INF/AMP, which could be resulting in the altered microenvironment. This is important in the context of high-grade serous ovarian carcinomas (HGSCs), which originate specifically from the distal fallopian tube. We speculate that a distinct INF/AMP cellular identity and an altered microenvironment in aging could contribute to HGSC initiation or progression. Collectively, our results revealed anatomical and cellular heterogeneity in each oviduct region, while implying functional diversity.

Résumé

L'oviducte/la trompe de Fallope est une structure qui s'étend de l'utérus à l'ovaire. Il fournit un environnement optimal pour la fécondation et le développement préimplantatoire. Cependant, notre connaissance de son hétérogénéité régionale et cellulaire est encore limitée. Nous avons démontré que le schéma d'enroulement de base de l'oviducte sert de repère fiable pour les cinq régions qui présentent des morphologies de plis muqueux distinctes: l'infundibulum distal (INF), l'ampoule (AMP), la jonction ampoule-isthme (AIJ), l'isthme (ISM) et la jonction utéro-tubaire proximale (UTJ). Les plis muqueux sont tapissés par deux types de cellules épithéliales: les cellules multiciliées (MCC) et les cellules sécrétrices (SC). Nous avons montré que l'expression de facteurs de transcription (TF) et les proportions/la distribution des MCC étaient distinctes dans chaque région. Chacune de ces régions était tapissée de paires distinctes de MCC et de SC, soit un total de 7 sous-types épithéliaux.

En effectuant une analyse SmartSeq à partir de 30 cellules de chaque sous-type épithélial, nous avons constaté que chaque sous-type exprime de nombreux gènes différentiellement exprimés et un enrichissement d'ensemble de gènes indiquant une identité distincte et une diversité fonctionnelle. En outre, nous avons trouvé une petite population dans l'INF/AMP qui représente un état transitoire de SC à MCC.

Au cours du vieillissement, nous avons découvert un phénotype unique limité aux MCC de l'INF/AMP, comprenant une vacuolisation cytoplasmique progressive et une anomalie nucléaire qui commence chez les souris âgées de 7 mois (7mo). La chronologie de cette vacuolisation cytoplasmique n'est pas affectée par l'absence d'ovulation ou de cycle œstral, ce qui suggère que ce phénotype peut résulter d'une altération du microenvironnement de l'INF/AMP. En accord avec cela, une analyse RNASeq de toutes les cellules INF/AMP de souris 18mo a montré une augmentation de la régulation d'ensembles de gènes associés au stress cellulaire et aux ROS, par rapport à 3mo. De plus, des cultures *in vitro* de tranches

organotypiques exposées à l'hypoxie ou à l'hydroxyurée ont développé des vacuoles cytoplasmiques similaires. Cependant, contrairement au phénotype *in vivo*, des vacuoles spécifiques aux MCC ont été observées dans des cultures de tranches de toutes les régions de l'oviducte. Il est intéressant de noter que nous avons identifié que l'artère ovarienne alimente directement l'ovaire et l'INF/AMP, tandis que l'artère utérine alimente l'oviducte proximal. Dans le vieillissement, l'absence de marquage des vaisseaux sanguins dans l'ovaire suggère une diminution de l'oxygénation de l'ovaire et de l'INF/AMP, qui pourrait être à l'origine de l'altération du microenvironnement. Cet aspect est important dans le contexte des carcinomes séreux de haut grade de l'ovaire (HGSC), qui proviennent spécifiquement de la region distale de la trompe de Fallope. Nous supposons qu'une identité cellulaire INF/AMP distincte et un microenvironnement altéré au cours du vieillissement pourraient contribuer à l'initiation ou à la progression des HGSC. Dans l'ensemble, nos résultats ont révélé une hétérogénéité anatomique et cellulaire dans chaque région de l'oviducte, qui implique une diversitée fonctionelle.

Table of Contents

List of Abbreviations

13mo	13-month-old
18mo	18-month-old
2D	2-dimensional
2-DG	2-deoxyglucose
3D	3-dimensional
5mo	5-month-old
6-AN	6-Aminonicotinamide
7mo	7-month-old
Acta2	Actin Alpha 2, Smooth Muscle
Actg2	Actin Gamma 2, Smooth Muscle
Adam3	A disintegrin and metalloprotease 3
Adarb1	Adenosine Deaminase RNA Specific B1
Adgrd1	Adhesion G Protein-Coupled Receptor D1
AIJ	Ampulla-isthmus junction
Amhr2	Anti-Mullerian hormone receptor 2
AMP	Ampulla
APCs	Antigen presenting cells
AT	Acetylated tubulin
ATP	Adenosine triphosphate
ATP1A1	ATPase Na+/K+ Transporting Subunit Alpha 1
BRCA1/2	BRCA1/2 DNA Repair Associated
C3	Complement C3
CBF	Ciliary beat frequency
Cd3e	CD3 Epsilon Subunit Of T-Cell Receptor Complex
Cd52	CD52 Molecule
Celsr1	Cadherin EGF LAG Seven-Pass G-Type Receptor 1
CHO	Chinese hamster ovary cells
CHX	Cycloheximide
Cnr1	Cannabinoid receptor 1
Cre	Cre recombinase
Cre-ER	Tamoxifen-inducible Cre recombinase fused to the estrogen receptor

CRISPR	Clustered regularly interspaced palindromic repeats
Dcn	Decorin
DCPPs	Demilune cell and parotid proteins
DEGs	Differentially expresses genes
Dmd	Dystrophin
DMSO	Dimethyl sulfoxide
DNA	Deoxyribeonucleic acid
dNTP	deoxynucleotide triphosphate
dpc	Days post copulation
E13.5	Embryonic day 13.5
E2	Estradiol
ECAD	Epithelial cadherin
ECM	Extracellular matrix
EIF2A	Eukaryotic Translation Initiation Factor 2A
Emx2	Empty Spiracles Homeobox 2
Epcam	Epithelial Cell Adhesion Molecule
ER	Endoplasmic reticulum
Erg	ETS Transcription Factor ERG
Esr1	Estrogen receptor 1
EVs	Extracellular vesicles
FGFs	Fibroblast Growth Factors
fl/fl	Flox/flox
Fltp / Cfap126	Flattop / Cilia and Flagella Associated Protein 126
Fltp-h2b-Venus	Fltp-driven H2B-Venus reporter
Foxa2	Forkhead Box A2
Foxa2-Venus	Foxa2-venus fusion reporter
Foxj1	Forkhead Box J1
FRT	Female reproductive tract
FSH	Follicle stimulating hormone
FTs	Fallopian tubes
Gata3	GATA Binding Protein 3
Gata6	GATA Binding Protein 6
GFP	Green fluorescent protein

GnRH	Gonadotropin-releasing hormone
GSEA	Gene Set enrichment analysis
H&E	Haematoxylin & Eosin
H2-Aa	Histocompatibility 2, class II antigen A, alpha
H2AX	H2A.X Variant Histone
Hbb-bs	Hemoglobin, beta adult s chain
HcG	Human chorionic gonadotropin
HGSCs	High Grade Serous Ovarian Carcinomas
Hif1a	Hypoxia Inducible Factor 1 Subunit Alpha
Hoxa10/d10/a11/d11	Homeobox A10/D10/A11/D11
Hoxa13/d13	Homeobox A13/D13
Hoxa9/d9	Homeobox A9/D9
HU	Hydroxyurea
Igf1	Insulin Like Growth Factor 1
Igfbp6	Insulin Like Growth Factor Binding Protein 6
IGFR	Insulin Like Growth Factor 1 Receptor
INF	Infundibulum
ISM	Isthmus
Krt5	Keratin 5
LH	Luteinizing hormone
Lim1	LIM Homeobox 1
Ly6a	Lymphocyte antigen 6A-2/6E-1
MADM	Mosaic analysis with double markers
MCCs	Multi-ciliated cells
MD	Müllerian duct / paramesonephric ducts
MDCK	Madin-Darby canine kidney cells
miR-dKO	miR-34b/c and miR-449 miRNA cluster double knockout
MRKH	Mayer-Rokitansky-Küster-Hauser Syndrome
Msln	Mesothelin
mTmG	Cell membrane-targeted, two-color fluorescent Cre-reporter allele (cell membrane-localized tdTomato (mT) is replaced by cell membrane-localized EGFP (mG) after Cre recombination).
NK	Natural killer cells

NPPC	Natriuretic peptide type C
NPR2	Natriuretic peptide receptor 2
Nr2f1	Nuclear Receptor Subfamily 2 Group F Member 1
O2	Oxygen
OC	Ovarian cancer
OCC	Oocyte cumulus complex
OCT	Optical coherence tomography
Ovgp1	Oviductal Glycoprotein 1
OVX	Ovariectomy
P4	Progesterone
PAS-AB	Periodic acid-Schiff/Alcian blue
Pax2	Paired Box 2
Pax2-GFP Bac	GFP expression driven by the *Pax2* regulatory sequences of the BAC gene
Pax8	Paired Box 8
PCD	Primary ciliary dyskinesia
PCP	Planar cell polarity
Pdgfra	Platelet Derived Growth Factor Receptor Alpha
Pecam1	Platelet And Endothelial Cell Adhesion Molecule 1
PGI2	Prostacyclin
Pgr	Progesterone receptor
Prom1	Prominin 1
Prox1	Prospero Homeobox 1
PVC	Persistent vaginal cornification
RBCs	Red blood cells
RER	Rough endoplasmic reticulum
Rfx3	Regulatory Factor X3
Rgs5	Regulator Of G Protein Signaling 5
RNASeq	Ribonucleic acid sequencing
RNR	Ribonucleotide reductase
RNS	Reactive nitrogen species
ROS	Reactive oxygen species
SCENIC	Single-Cell rEgulatory Network Inference and Clustering

SCOUTs	Secretory Cell OUTgrowths
scRNASeq	Single cell ribonucleic acid sequencing
SCs	Secretory cells
SEE-FIM	Sectioning and Extensively Examining the FIMbria
SEM	Scanning electron microscopy
Slc1a3	Solute Carrier Family 1 Member 3
Sox13	SRY-Box Transcription Factor 13
Sox17	SRY-Box Transcription Factor 17
Sox17-mCherry	Sox17-mCherry fusion reporter
Sox3	SRY-Box Transcription Factor 3
Sox7	SRY-Box Transcription Factor 7
Srebf2 / SREBP2	Sterol Regulatory Element Binding Transcription Factor 2 / Sterol Regulatory Element-Binding Protein 2
STICs	Serous tubal intraepithelial carcinomas
tdT / tdTomato	Tandem Tomato
TEM	Transmission electron microscope
Tex101	Testis Expressed 101
TFs	Transcription factors
Tgfbr2	Transforming Growth Factor Beta Receptor 2
TP53 / P53 / Trp53	Tumor Protein P53
Trp73	Tumor Protein P73
UMAP	Uniform Manifold Approximation and Projection
UPR	Unfolded protein response
UTJ	Uterotubal junction
VCD	4-vinylcyclohexene diepoxide
WD	Wolffian duct / mesonephric duct / Leydig's duct / nephric duct
Wnt	Wingless-related integration site
Wnt4	Wnt Family Member 4
Wnt7a	Wnt Family Member 7A
Wt1	Wilms Tumor 1
YFP	Yellow fluorescent protein
Zfp866	Zinc finger protein 866

List of Figures

Chapter 1

Chapter 2

Chapter 3

Chapter 4

Chapter 5

List of Tables

Acknowledgements

I would like to thank the Rosalind and Morris Goodman Cancer Research Institute (GCI), McGill's Faculty of Medicine and Health Sciences (FMHS), McGill's Department of Human Genetics, McGill's Centre for Research in Reproduction and Development (CRRD), Fonds de recherche du Québec - Santé (FRQS), and International Society for Key Women Educators/Delta Kappa Gamma (DKG) for funding me during my PhD; and acknowledge the receipt of the Charlotte and Leo Karassik Foundation Oncology Studentship, FRQS doctoral training grant, DKG World Fellowship 2021, 2021 Donner Foundation Fellowship, Hugh E. Burke PhD Fellowship, Rolande and Marcel Gosselin Graduate Studentship, CRRD Winter 2019 trainee fellowship, Alexander McFee Fellowship, and CRRD Fall 2016 fellowship.

I would like to express my sincere gratitude and appreciation to my supervisor Dr. Yojiro Yamanaka for accepting me into his lab and providing me with opportunities to learn. He has asserted that he is not a teacher many times, but along the way, I can undeniably state that I have learnt a lot from him and his unsatiable curiosity of the world. I would also like to thank my committee members Dr. Aimee Ryan and Dr. Daniel Dufort for their invaluable feedback and constructive criticism throughout the years - I have grown so much as a person, both personally and as a scientist, under their tutelage.

I would like to thank the PIs and very long list of McBouYaCo current/past members (McCaffrey, Bouchard, Yamanaka and Cockburn labs) for providing constructive feedback and always being open to discussions. A big thank you to all the people in the Department of Human Genetics and the fourth floor of the GCI for providing an amazing, collaborative research environment. I would also like to thank the staff belonging to the Advanced BioImaging Facility (ABIF), the Flow Cytometry Core Facility (FCCF), Histology Innovation Platform, McGill Genome Centre, and the Canadian Centre for Computational Genomics (C3G), Genome Quebec Innovation Centre for their technical expertise and timely help. I thank Dr. Alain S Pacis for performing the bioinformatic analyses in Chapters 3 & 4.

I express my gratitude toward Nobuko Yamanaka, Dr. Matthew J Ford, Katie Teng, Hengameh Kazemdarvish, YuQi Li, Abiramy Jeyagaran, Dr. Aaron Kwong, Warwick Pitman, Dr. Emily Tang, and Dr. Dardan Konjusha, for help with experiments, training/mentoring, invaluable feedback, and/or constructive criticism. A big thank you to all the students who have helped with experiments over the years, including Stephanya Zimakas, Alex Frances Thornton, Selina Zhao, Brenna Yang, Mitaali Taskar, Vera Lynn, Jenny Li, and Matthew L Chang. I also thank Dr. Matthew J Ford for constructive feedback on my Introduction chapter, and Dr. Sophie Viala for the French translation of my thesis abstract.

I am grateful to Mio, Bananas, Leo, Elyse, Philo, Bean and their owners – all of whom have helped keep me sane via general catitude, biscuit-making, and adorable pictures. Thank you to Richa Saynak, who has been a steadfast presence and a great help over these years, especially during my first couple of years in Montréal. Additionally, I would like to thank fellow site coordinators, volunteers and staff with Let's Talk Science at McGill University and the national office, particularly Maxana Weiss, who has been with me through thick and thin – here's hoping we both get out of this with our sanity intact!

As well, I am grateful to my lifelong friends Dr. Jayashree Raghavan, Shriya Kota, and Monisha S.V, for their constant encouragement. Most of all, I would like to extend my utmost gratitude to my parents, Kavitha and Sudheendra Harwalkar, and sister, Shalini Harwalkar, for their steadfast support, guidance and encouragement throughout my PhD.

Contribution to original knowledge

In this work,

1. I discovered anatomical and cellular heterogeneity along the mouse oviduct epithelium and showed that each morphologically distinct region had a distinct MCC proportion and distribution pattern, a unique pair of MCCs and SCs, TF expression, and potential functions, totaling 7 subtypes of epithelial cells.

2. I sequenced these 7 populations and found numerous differentially expressed genes, region-specific TFs, and enrichment of distinct biological processes, suggesting distinct cellular identities and functions. I also found a SC-to-MCC transitory population in the INF/AMP.

3. I discovered an INF/AMP MCC-specific aging phenotype that reflects a mild, but chronically stressed microenvironment within the aged INF/AMP. This altered microenvironment, alongside a distinct INF/AMP cellular identity, could contribute to HGSC initiation and/or progression.

Format of the thesis

This manuscript-based thesis follows guidelines specified by the Department of Human Genetics, McGill University.

Contribution of authors

All the work presented in this thesis is original research, designed, performed, and analyzed by me, supervised by Dr. Yojiro Yamanaka.

Chapter 2

- Dr. Matthew J Ford, Katie Teng, Nobuko Yamanaka, and Brenna Yang performed some sectioning, immunofluorescence, and/or animal work.
- Figure 1F was provided by Katie Teng.
- Dr. Ingo Burtscher and Dr. Heiko Likert generated mouse lines used and shared unpublished information.
- Dr. Matthew J Ford, Katie Teng, and Nobuko Yamanaka edited the manuscript.

Chapter 3

- RNASeq analyses was performed in collaboration with Dr. Alain S Pacis.
- Immunofluorescence staining for Fig. 3.3E-P was performed in concert with Alex Frances Thornton.

Chapter 4

- Ovariectomized mice for Figure 4.4 and 13mo dam/breeder mice for Figure 4.7 were provided by Nobuko Yamanaka.
- RNASeq analyses was performed in collaboration with Dr. Alain S Pacis.
- Some sectioning and/or staining was performed in concert with Selina Zhao, Alex Frances Thornton, Vera Lynn, and Mitaali Taskar.
- Figure 4.2 H, I was provided by Katie Teng.
- Sections for Supplementary Figure S4.6 I, J were provided by Dr. Matthew J. Ford.
- Cardiac perfusion and imaging for Figure 4.7A-O was performed by Dr. Yojiro Yamanaka and Warwick Pitman.

1. General introduction

1.1. The female reproductive tract (FRT)

The mammalian FRT is composed of various internal and external organs involved in copulation, gamete release/entry/movement, fertilization, pre-implantation embryonic movement/development, post-implantation/fetal embryonic development, and birth. From anterior to posterior, the internal organs are the ovaries, Fallopian/uterine tubes, uteri, cervix, and the vagina, while the external organs are the genitalia or vulva. In the process of reproduction, immature oocytes contained in the ovaries undergo maturation through a process called folliculogenesis. Mature oocytes released by the ovary are then picked up by the FTs, where female and male gametes meet, and fertilization occurs. Following successful fertilization, preimplantation embryos travel along the FTs to reach the uterus where post-implantation development occurs. Birth of a newborn is facilitated by uterine contractions and cervical dilation that move the developed fetus through the vagina after a species-specific gestational period within the uterus [1].

1.2. Anatomy of the Fallopian tube/oviduct

In humans and non-human primates, the uterine tubes, eponymically called Fallopian tubes (FTs), extend from a single/fused uterus as uncoiled, bowed tubes. These tubes are divided into 4 distinct, but contiguous regions based on mucosal fold morphology and thickness of the smooth muscle layer: 1) the uterotubal junction (UTJ) located within and most proximal to the uterine wall, 2) the isthmus, 3) the ampulla, and 4) the distal-most infundibulum that extends into finger-like projections called fimbria that encompass the ovary. Mucosal folds are lined with multi-ciliated and secretory epithelial cells. The end distal-most to the uterus, the fimbriae, has the highest proportion of multi-ciliated cells (MCCs), while the UTJ has the lowest. Secretory cells (SCs) also form a gradient, albeit with the highest proportion being in the UTJ, and lowest in the fimbriae [2, 3]. The terms distal and proximal used in this thesis are used to reference location in relation to the uterus.

1.2.1. Anatomy of the mouse oviduct

FTs in mice, commonly known as oviducts, are highly coiled tubes that extend from the uterus to the ovary. Similar to primate FTs, sections of the coiled mouse oviduct show an outermost mesothelial layer that is contiguous with connective tissue called the mesosalpinx, followed by smooth muscle, stroma, and lumen-facing monolayer epithelium that lines morphologically distinct mucosal folds. The mesosalpinx along the tube and in between the oviduct coils gathers dorsally, maintaining a seemingly consistent coiling pattern with some variation during ovulation and pregnancy. Although anatomically dissimilar from the primate FTs, mouse oviducts are also divided into 4 regions based on distinct mucosal fold morphologies and smooth muscle thickness: 1) the UTJ located within and most proximal to the uterus, 2) isthmus (ISM), 3) ampulla (AMP), and 4) the region distal-most to the uterus - the infundibulum (INF). Finally, between the ampulla and isthmus is a transition region called ampulla-isthmus junction (AIJ) [4]. The AIJ has not been reported as a morphologically distinct region in primate FTs.

1.2.1.1. Mucosal fold morphologies along the mouse oviduct

The end of the UTJ, called the intramural UTJ, is located within the uterus and is continuous with the uterine luminal epithelium. Mucosal folds in the UTJ are longitudinal. These folds transition to transverse mucosal folds in the ISM, and then into short longitudinal folds in the AIJ, followed by longitudinal mucosal folds in the AMP. Finally, these lumen-facing longitudinal mucosal folds continue into the INF, where they form an overhang that faces the oviduct exterior. This funnel-shaped end is located directly adjacent to the ovary and within connective tissue that encompasses the ovary, called the ovarian bursa [4]. The ovarian bursa is not reported in the primate FRT, where the ovary and fimbriae/infundibulum are directly exposed to the peritoneum.

Not much is known about mucosal fold development in oviducts. Mice with mesenchyme-specific constitutively activated Notch1 (*Amhr2-cre; Rosa*^{Notch1}) present with uncoiled oviducts wrapped over the ovaries, with generally preserved mucosal fold morphologies [5], suggesting that mucosal fold formation is in part independent from oviduct coiling. Instead, mucosal fold morphologies likely result from a combination of planar cell polarity (PCP) signaling/localization at the cellular level, mechanical properties of each layer including stiffness and rigidity, length and thickness of each layer, smooth muscle contraction, and mechanical buckling of the proliferating epithelial layer during development [6]. In agreement with this, the INF and AMP region of *Celsr1-/-* mice have disorganized mucosal folds with ectopic branches, lined with epithelium that are rounder/less elongated than wild-type epithelium. Interestingly, in chimeras created using wild-type and *Celsr1-/-* mouse embryonic stem cells, small *Celsr1-/-* epithelial clones present with abnormal cell shape, while larger clones present with both abnormal cell shape and ectopic mucosal fold branching, suggesting that PCP acts in a cell autonomous manner by regulating epithelial cell shape. Consequently, this affects INF/AMP mucosal fold morphology at the tissue/mucosal fold level [7]. It is unknown if the mucosal fold morphologies in the AIJ, ISM, and UTJ are also affected in *Celsr1-/-* mice, but the mechanisms of fold formation are likely similar. Finally, it is unclear whether disorganized mucosal folds and a predicted reduction in luminal space of *Celsr1-/-* oviducts [7, 8] contributes to its infertility, however, one of the reasons for infertility in *Amhr2-cre; Rosa*^{Notch1} mice is blockages or mucosal fold outgrowths/overgrowths in the oviduct that prevent gamete movement [5], underscoring the importance of proper mucosal fold formation for reproduction. The function of these mucosal folds alone is unclear, but similar longitudinal folds are noted in birds and frogs [8], suggesting that folding patterns and their functions could be evolutionarily conserved.

1.3. Development of the FRT

Knowledge of FRT development comes from descriptions and targeted mutagenesis studies in mouse and chicken models. At mouse embryonic day E11.5, the coelomic epithelium adjacent to the mesonephric ducts, eponymically called the Wolffian ducts (WDs), thickens into a multi-layer *Emx2+/Lim1+/Wnt4+/Pax2+* placode initially made of 'mesoepithelial' precursor cells that show some mesenchymal-like (Vimentin expression, mesenchymal morphology) and epithelial-like (arranged on a basement membrane) characteristics. At E12.5, the placode invaginates caudally, encountering and crossing over the WD. At E13.5, it elongates to merge with the urogenital sinus. This three-step thickening, invagination and elongation process leads to the formation of the epithelium-lined paramesonephric ducts, eponymically called the Müllerian ducts (MDs), on the lateral sides of each genital ridge. Between E14.5-16.5, in XX mammals, the MD begins differentiating into the FT/oviduct, uteri, cervix, and the rostral one-third of the vagina, while the WDs regress due to absence of anti-Müllerian hormone and testosterone. Hox gene expression in the mesenchyme controls FRT segmentation, with spatially restricted expression of *Hoxa9/d9* in oviducts, *Hoxa10/d10/a11/d11* in uterine horns, and *Hoxa13/d13* in the cervix and vagina [9, 10].

Multiple genes required for FRT development have been identified through knockout studies. Loss of *Emx2* or *Lim1* is embryonic lethal and results in death at E10-E11 [11, 12]. In a low number of inbred/outbred *Lim1-/-* escapers/survivors, no MD derivatives are noted in newborn mice, and it is shown that Lim1 requirement in MD invagination and elongation is cell autonomous [12]. *Wnt4-/-* mice lack MD derivatives due to an arrest in invagination [13]. In *Pax2-/-* mice, thickening and invagination occurs, but elongation does not. Absence of the WD in *Pax2-/-* mice [14] is thought to be the cause for this arrested MD elongation. In line with this, lack of *Wnt9b*- or *Gata3*-mediated paracrine interactions with the WD also results in arrested MD elongation [15]. Thus, successful MD elongation is dependent on its interactions with the WD, while coelomic thickening and invagination are not. Correspondingly, in humans, deletions encompassing *LIM1* on chromosome 17, mutations in *WNT4*, *PAX2* polymorphism/mutations, and *WNT9B* polymorphism/mutations have been identified in patients with Müllerian agenesis, also called Mayer-Rokitansky-Küster-Hauser Syndrome (MRKH syndrome), or Müllerian abnormalities having varying phenotypes [9], suggesting evolutionarily conserved mechanisms during early MD formation. On the other hand, MD elongation and segmental differentiation into the distinct FRT organs involve distinct gene regulatory networks in different vertebrate species, likely reflecting their functional divergence [16].

As early as E13.5, the rostral MD expresses WT1, while PAX2 is restricted to the caudal MD. This rostral-caudal specificity in WT1 and PAX2 expression is also observed in the adult mouse oviduct, where WT1 is expressed in the INF/AMP epithelium, with the proportion of WT1-expressing cells decreasing across the AIJ and ISM. Conversely, PAX2 is expressed in the ISM and UTJ epithelium. Taken together, this suggests that the adult mouse oviduct regions that are located distal and proximal to the uterus are developmentally distinct [17], and it is interesting to hypothesize that these populations may develop from the rostral invaginated MD and part of the caudal elongated MD, respectively.

While the oviduct regions distal and proximal to the uterus are developmentally distinct, mechanisms/genes involved in oviduct differentiation/segmentation into morphologically distinct regions are unknown. Known markers of oviduct epithelium include PAX2, PAX8 and OVGP1, which are thought to be SC-specific, while acetylated tubulin and FOXJ1 are MCC-specific. However, it is now known that WT1 is expressed in the distal oviduct, while PAX2 is restricted to the proximal oviduct and is expressed in both SCs and MCCs [17]. Accordingly, a re-examination of these known markers and discovery of region-specific markers is required to better define the epithelial subtypes in the oviduct which will aid future investigations into their function and homeostasis.

1.4. The Fallopian tube/oviduct in reproduction

In humans, a single ovum released by the ovary is picked up by the fimbriae and transported to the ampulla, while sperm enters the FT via the uterotubal junction and isthmus. Fertilization occurs in the ampulla, and the preimplantation embryo travels along the FTs for 3-4 days to reach the uterus for post-implantation development. The functional importance of mucosal epithelial cells remains controversial. Interestingly, primary ciliary dyskinesia (PCD), a genetic condition affecting the structure and function of motile cilia, is often reported to cause infertility, subfertility, and/or ectopic pregnancy [18], suggesting that MCCs of the fimbriae/infundibulum could be actively involved in ovum pickup and/or preimplantation embryo transport. However, since fertility prognoses for PCD patients with a FRT is difficult due to the lack of simple, non-invasive techniques to evaluate MCC motility, studies tend to evaluate fertility based on pregnancy failure after ≥12 months of unprotected intercourse, which is likely a cause for some inconsistency in these findings.

Despite its crucial role as the site of fertilization and a conduit during early embryogenesis, not much is known about the FT, likely because advances in *in vitro* fertilization techniques allows for the bypass of the FT. However, ~30% of diagnosed infertility/subfertility cases worldwide are attributed to FT-associated pathologies. Reported causes of this tubal infertility include congenital absence/malformation, diverticula, occlusion/hydrosalpinx, infections (Chlamydia trachomatis, Gonorrhea, genital tuberculosis), endometriosis, infections after insertion of intrauterine contraceptive devices, and complications following abdominal surgery [19]. Due to the lack of knowledge on etiology or disease pathology, as well as the asymptomatic nature of tubal infertility, these cases are difficult to study or diagnose until individuals self-disclose during medical examinations.

1.4.1. Function of the mouse oviduct

Knowledge of FT/oviduct function comes from extensive studies in mouse and various other animals like rats, hamsters, guinea pigs, pigs, and cows.

1.4.1.1. OCC pickup and transport along the mouse oviduct

Similar to primate FTs, the proportion of MCCs along the tube is thought to form a gradient of high to low from distal to proximal, relative to the uterus. Conversely, SC proportion along the tube forms a gradient of low to high [20] (Figure 1.1). MCCs in the distal-most INF aid the movement of the ovulated oocyte-cumulus complex (OCC) into the AMP, where fertilization occurs. In hamsters, force generated by cilia beating is insufficient for OCC pickup, instead, OCCs adhere to the MCCs of the INF and are transferred into the oviduct [21]. In line with this, one of the issues that *miR-34b/c* and *miR-449* miRNA cluster double knockout (miR-dKO) mice present with, is infertility due to defects in multi-ciliogenesis. Due to the absence of MCCs, OCCs remain within the ovarian bursa and are not transported into the oviduct, leading to female infertility regardless of a functional ovary [22]. Thus, MCCs are required for OCC entry into the distal oviduct, but it is unknown whether OCCs adhere to MCCs or are swept in by MCC-generated flow in mice. MCCs in live open-book preparations of the INF/AMP region are shown to transport particles or ova unidirectionally, toward the AMP [23]. Further, INF/AMP MCCs in *Celsr1-/-* mice present with abnormal ciliary polarity and misoriented basal feet, which affects the direction of cilia beating and randomizes the movement of fluorescent beads placed on open-book preparations [7], likely contributing to *Celsr1-/-* mouse female infertility. Thus, INF/AMP MCCs play a crucial role in OCC pickup and transport along the distal oviduct.

While it is unknown whether MCCs and SCs have other functions, transmission electron microscopy (TEM) studies in sheep, goat, rat, golden hamster, and mouse [24-28] show both high and moderately electron dense secretory granules in the INF and AMP, suggesting a proteinaceous/serous secretion. In line with this, the AMP region swells up with oviductal fluid, follicular fluid, and OCCs following ovulation. After oviduct entry, *in vivo* studies using optical coherence tomography (OCT) through implanted optical windows show quick, circular OCC movement while within the AMP [29], likely due to flow created by MCC beating. Spermatozoa entering via the proximal UTJ migrate to and fertilize OCCs in the AMP.

Studies in various species suggest that extracellular vesicles (EVs), including exosomes and microvesicles, in oviductal fluid decreases zona pellucida binding to prevent fertilization by multiple spermatozoa, while also supporting oocyte maturation [30]. Bovine oocytes that are matured and/or fertilized *in vivo* show higher blastocyst yield, when compared to *in vitro* maturation and/or fertilization yields [31]. Further, cultured porcine oocytes treated with oviductal fluid are more likely to develop into blastocysts following *in vitro* fertilization [32].

1.4.1.2. Spermatozoa movement along the mouse oviduct

In the opposing direction, spermatozoa that enter the mouse FRT quickly move to the uterus [33], with only a small fraction entering the UTJ [34]. *Adam3,* a spermatozoa specific peptidase, has been shown to be essential for sperm entry into the UTJ. *Adam3-/-* spermatozoa, with defective zona pellucida binding ability but no reported motility or morphology defect, can enter the uterus but not the UTJ [35]. Loss of multiple factors/genes involved in ADAM3 maturation have also been reported to cause defects in zona pellucida binding and UTJ entry [36]. It is proposed that disruption of *Adam3*, a pseudogene in humans and macaques [37], leads to impaired binding of spermatozoa to intramural UTJ epithelium, a process thought to precede UTJ entry [38], however there is no evidence for sperm binding to SCs. Instead, wild-type spermatozoa form unidirectional, oriented clusters within the uterus and around the UTJ, termed sperm cooperation, that beat synchronously and contribute to the generation of strong forces for successful UTJ entry. Along these lines, *Tex101-/-* spermatozoa, also with no reported motility or morphology defect, form misoriented/disordered, small sperm clusters that can enter the uterus but not the UTJ, even in the presence of wild-type sperm clusters that successfully enter the UTJ [39].

By ligating the proximal oviduct at multiple locations, fluid production is shown to be the highest in the ISM. This fluid flow is in the adovarian direction [40], i.e., toward the ovary and opposing the direction of OCC/zygote movement, likely supporting spermatozoa movement into the ISM. In line with this, drug-based suppression of muscle contractions inhibits/reduces shuttling fluid flow between the UTJ and ISM, leading to a loosening of sperm assemblage and decrease in the fraction of spermatozoa moving into the distal ISM, in a dose-dependent manner [41]. Sperm migration from the ISM is also directionally guided by OCC-induced elevation of natriuretic peptide type C (NPPC) in the AMP. Most spermatozoa with loss of function mutations in natriuretic peptide receptor 2 (*Npr2*) did not migrate to the AMP [42] and loss of NPPC expression in FRT epithelium-specific *Tgfbr2-/-* (*Wnt7a*^{Cre}*; Tgfbr2*$^{f/f}$) mice leads to significantly reduced the number of sperm entering the AMP [43], in both cases resulting in a drastic reduction in the number of fertilized embryos. Thus, spermatozoa movement into and along the proximal oviduct is aided by adovarian fluid flow, muscle contractions, and AMP-specific guidance cues like NPPC expression following ovulation. Although the role of MCCs in the proximal oviduct is unclear, lack of MCCs in miR-dKO oviducts leads to a significant reduction in the proportion of spermatozoa entering the oviduct. Since OCCs also do not enter miR-dKO oviducts due to lack of MCCs [22], a possible cause for this reduction could be a lack of guiding cues/chemoattractants.

Spermatozoa entering the mouse oviduct slow down considerably [33], possibly due to the presence of viscoelastic fluid/mucus [44], which could be a mechanism to prevent further movement of spermatozoa having motility defects. Additionally, many spermatozoa in the isthmus are found with their heads adhered to the ISM epithelium [45] at the bottom of the mucosal folds, still actively beating their tails. Others were found swimming in the lumen [33]. Since the number of spermatozoa ascending from proximal to distal progressively decreases [34], this could imply that sperm attachment to oviduct epithelium is a way of reducing the number of spermatozoa reaching the AMP. However, detachment of sperm that is adhered to oviduct epithelium involves a high amplitude, erratic beating of the sperm flagella, termed hyperactivation, that allows them to penetrate viscoelastic medium more efficiently than fresh sperm [46]. It is currently unclear whether freely swimming spermatozoa or sperm attached to the mucosal epithelium go on to fertilize OCCs in the AMP. Taken together, the proximal oviduct acts as a gateway to prevent entry of defective spermatozoa and fertilization of individual ova by multiple spermatozoa, also called polyspermy, by progressively reducing the number of spermatozoa entering the oviduct. Finally, fluid flow in the AIJ is gentle and spermatozoa are thought to switch to a combination of sperm cooperation, spermatozoa tail beating/swimming, rheotaxis [41, 47], and response to guiding cues like AMP-specific NPPC expression [42, 43] to reach the AMP for fertilization.

Isthmic mucus accumulation during estrus stage is seen in macaques, rabbits, and humans [48]. TEM studies in various animals show predominantly low electron dense secretory granules that take up most of the cytoplasm in SCs of the isthmus [24-27], suggesting mucus-containing secretory granules, although this has not been confirmed in mice. Further, spermatozoa attachment to oviduct mucosal epithelium is also observed in various species. In addition to mice, studies in cattle, hamsters, pigs, sheep, horses, and birds [45, 49-54] allude to the presence of sperm attachment/storage sites, typically called sperm reservoirs. Scanning electron microscopy (SEM) studies of bull spermatozoa show attachment of uncapacitated sperm to oviduct MCCs [49], likely by carbohydrate recognition [55]. Finally, studies in various animals also suggest that EVs produced by the oviduct bind to sperm and provide proteins that are thought to aid sperm function, survival, motility, and interaction with OCCs [30].

1.4.1.3. Oviduct contribution to preimplantation embryo survival and transport

Following fertilization in the AMP, zygotes (or unfertilized OCCs) move into the proximal AMP and begin short, pulsatile oscillations, with progressive loss of cumulus cells as they move into the ISM. Longer bidirectional, pulsatile oscillations are noted in the ISM, attributed to peristaltic smooth muscle contractions [29]. In rats, inhibition of smooth muscle contractions suppresses these bidirectional oscillations but does not influence the speed of ova/embryo unidirectional transport along the oviduct, likely because MCC beating is unaffected [56]; however, the resultant live birth rate following this inhibition is unknown. Another critical factor to consider is the modulation of adovarian fluid production/flow. In *Adgrd1-/-* mice, unattenuated fluid production results in preimplantation embryos or similarly sized glass beads being retained in the AIJ, and not transported along the oviduct [57]. This combination of smooth muscle/luminal constriction [29], flow in the uterine direction caused by MCC beating, and adovarian fluid flow results in a valve-like mechanism, referred to as the tubal lock, that retains embryos in the distal region. Additionally, the lack of MCCs in miR-dKO mice also leads to a decrease in percentage of live births following surgical transfer of 2-cell stage embryos into the oviduct, but no significant change when blastocysts are surgically transferred into the uteri [22]. Thus, although OCC transport into the oviduct requires MCCs, embryo transport to the uterus does not exclusively depend on oviduct MCCs, likely because smooth muscle contractions are unaffected in miR-dKO oviducts; however, the efficiency of this transport is compromised. Along these lines, aberrant smooth muscle contraction and relaxation in *Cnr1-/-* mice affects preimplantation embryo transport from the ISM to uterus, often resulting in pregnancy failure [58]. Thus, preimplantation embryo transport in the AMP-

AIJ depends on MCCs and timely attenuation of fluid production in the ISM/adovarian fluid flow, while transport from the ISM to uterus depends on MCCs and smooth muscle contractions. While it is clear that the oviduct aids in embryo transport, the exact location of embryos in the oviduct between 1.0-3.0 dpc is unknown.

The mouse oviduct is also thought to support preimplantation embryo development by producing EVs and embryotrophic factors like *C3*, *Igf1*, FGFs, DCPPs, etc. Interestingly, progesterone receptor-mediated ablation of *Igf1* (Pgr^{Cre}; $Igf1^{f/f}$) in mice resulted in a higher proportion of embryos with developmental defects being retained within the oviduct, despite no discernible oviduct defect. Since Igf1 is expressed in the stromal and muscle compartment [59], embryo retention could be due to defective muscle contraction, but the cause for developmental defects is unknown. Addition of EVs collected from the ISM improved the survival rate of cultured bovine blastocysts following vitrification, however EVs collected from the AMP did not do the same [60], suggesting region-specific, functional differences in EVs. In mice, although unclear if it is region-specific, elevation of prostacyclin (PGI_2) is noted in oviducts at 2-3 dpc [61], and exposure of a PGI_2 analogue to embryos at 4-cell to morula stage results in higher rates of hatching, implantation, and birth following embryo transfer [62-64]. Further, interaction of spermatozoa with the oviduct epithelium results in higher concentrations of oviductal EVs and proteins, as compared to lower concentrations in fluid collected from oviducts where females are mated with vasectomized male mice. Embryo culture upon supplementation with EVs collected from oviducts following spermatozoa interaction results in improved birth rate, indicating that sperm-oviduct interaction and presence of gonadotropins induced by superovulation could contribute to the timed elevation of EV production [65]. However, pseudopregnancy can be induced with cervical stimulation without the need for male mice, allowing for embryo implantation and development following embryo transfer [66]. Although unknown if EV production elevation occurs in the absence of male mice, this suggests that seminal fluid/spermatozoa-FRT interaction is not the only factor influencing receptivity. Nonetheless, oviductal fluid may play a role in embryo survival, but the proteins/molecular cargo responsible, timing, and cell types/region-specificity of production are mostly unknown [30]; this is likely due to the difficulty in isolating sufficient volumes of oviductal fluid from animals with inaccessible, deep-seated, and/or small oviducts.

Although the mucosal epithelium along the oviduct is directly exposed to gametes/embryos and aids in their successful survival/transport, it is thought that there are only two types of epithelial cells that line the mucosal folds: MCCs and SCs. Apart from proportional differences, it is unclear if there is any transcriptional or functional diversification of these MCCs and SCs in each region along the oviduct. Uniform Manifold Approximation and Projection (UMAP) clustering, following single cell RNA-Seq (scRNASeq) of epithelial cells from an entire adult oviduct, shows that SCs and MCCs of distal and proximal regions cluster separately, enabling the identification of a few distal and proximal-specific markers like *Wt1* and *Ly6a* that are unaffected by estrous cycling. However, epithelial cells of the AIJ and UTJ could not be identified, due to low sequencing depth and lack of known markers [17].

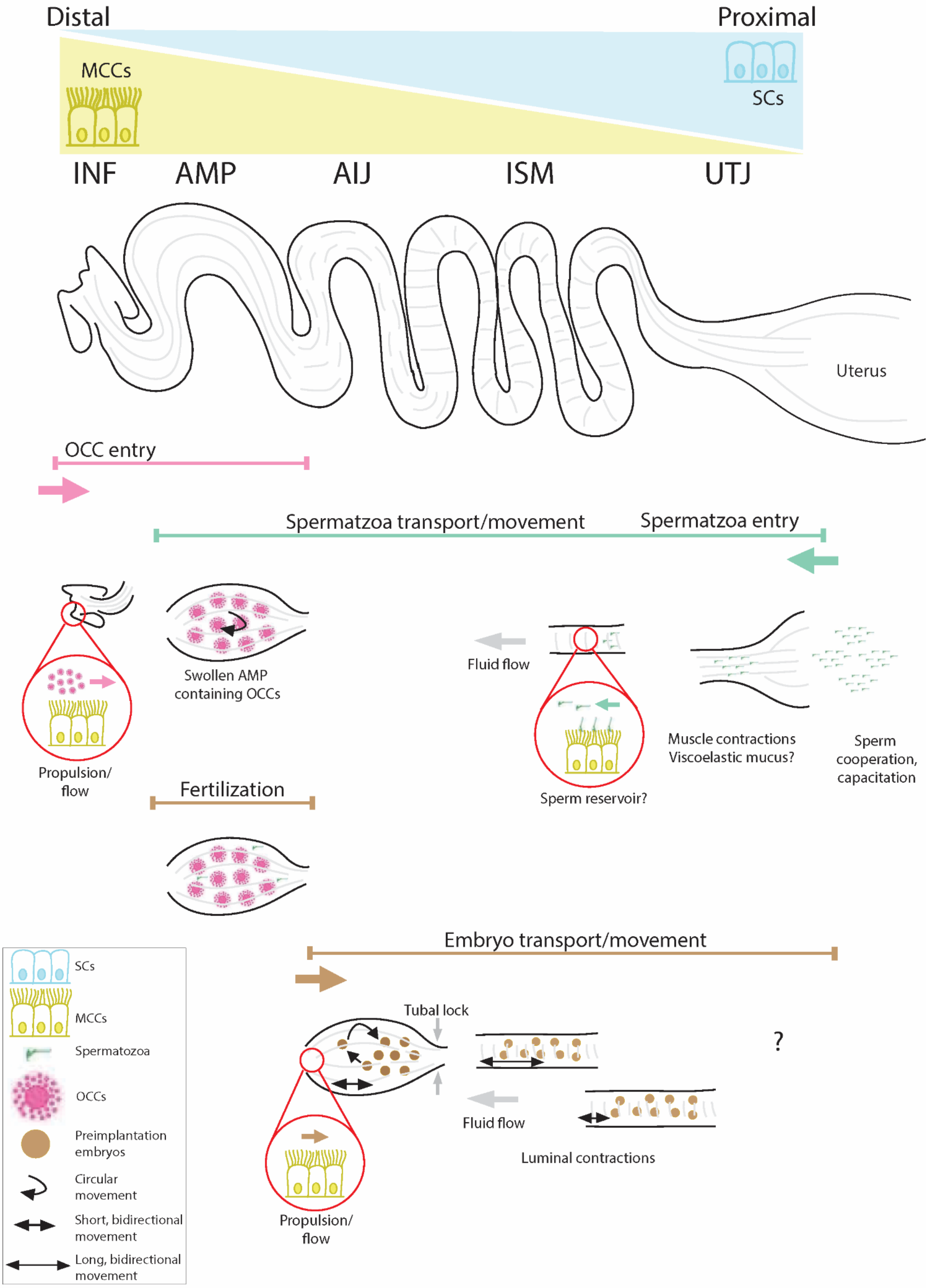
Distal
Proximal
MCCs
SCs
INF
AMP
AIJ
ISM
UTJ
Uterus
OCC entry
Spermatozoa transport/movement
Spermatozoa entry
Propulsion/ flow
Swollen AMP containing OCCs
Fluid flow
Sperm reservoir?
Muscle contractions Viscoelastic mucus?
Sperm cooperation, capacitation
Fertilization
Embryo transport/movement
Tubal lock
Fluid flow
Luminal contractions
?
Propulsion/ flow
SCs
MCCs
Spermatozoa
OCCs
Preimplantation embryos
Circular movement
Short, bidirectional movement
Long, bidirectional movement

Figure 1. 1: Gamete and preimplantation embryo transport along the mouse oviduct. Proportions of MCCs and SCs are thought to form a simple gradient along the mouse oviduct. OCCs are transported into the oviduct by MCCs, and move to the AMP, where they move in a circular manner. Spermatozoa enter in unidirectionally oriented clusters called sperm cooperation, and their transport to the AMP is aided by muscle contractions and adovarian fluid flow. As they enter the proximal oviduct, spermatozoa slow down, likely due to viscoelastic mucus, and are found either freely swimming or attached to MCCs. Fertilization occurs in the AMP, following which preimplantation embryo transport in the AMP-AIJ is aided by MCC beating and attenuation of adovarian fluid flow/production. Embryo transport from the ISM to uterus depends on MCCs and smooth muscle contractions.

1.5. Hormonal regulation of the FRT

During adulthood, the FRT undergoes structural and morphological changes in response to hormonal regulation in a cyclic manner, called the menstrual cycle in animals that undergo menses/menstruation or estrous cycle in non-menstruating animals. Hormonal regulation and subsequent FRT changes are species-specific.

1.5.1. Human menstrual cycling during adulthood

The menstrual cycle in humans is 25-30 days long and divided into two phases: 1) menstruation and follicular/proliferative phase, and 2) ovulation and the luteal/secretory phase. The follicular phase begins with menstruation/menses that lasts 5-7 days, during which the thickened endometrial wall sloughs off and germ cells mature into a fertilizable oocyte. Day 7-14 of the follicular phase is characterized by gradually increasing levels of serum estradiol (E2). Release of mature oocyte by the ovary, termed ovulation, occurs on day 14, and is controlled by gonadotropin-releasing hormone (GnRH) production by the hypothalamus. Pulsatile GnRH release causes luteinizing hormone (LH) and follicle-stimulating hormone (FSH) to be released by the anterior pituitary. E2 levels peak towards the end of the follicular phase, resulting in LH and FSH surge that lasts 24-36 hours and culminates in ovulation. This released oocyte enters the uterine tube where fertilization and preimplantation development/travel occurs. Remnants of the released oocyte transforms into the corpus luteum that continue to grow and produce high levels of progesterone (and to a lesser extent, E2) during the luteal phase (day 14-28). High progesterone (P4) levels suppress FSH and LH production and involves thickening of the endometrial lining for embryo implantation. The fertilized oocyte/preimplantation embryo reaches the uterus and implants in the thickened endometrium, resulting in production of human chorionic gonadotropin (hCG) by the implanted embryo and maintenance of the P4-producing corpus luteum for 8-12 weeks, after which the placenta begins producing P4. If fertilization does not occur, the corpus luteum will atrophy in 10-12 days due to lack of LH/hCG, leading to a decrease in P4, E2, and consequently, a release n the negative feedback on LH and FSH, resulting in menses. In addition to changes in the endometrium and ovary, cyclic changes in cervical mucous and morphology of exfoliated vaginal epithelial cells also correlate with changing steroid hormone levels [67-70].

1.5.2. Murine estrous cycling during adulthood

The mouse estrous cycle lasts for 4-6 days and is divided into 4 phases/stages: 1) Proestrus, 2) Estrus, 3) Metestrus, and 4) Diestrus. Proestrus stage is characterized by elevated E2 levels produced by the ovarian granulosa cells, that result in a bolus of GnRH release from the hypothalamus, which further induces a LH and FSH surge by the anterior pituitary. High levels of FSH induces the antral follicles grow exponentially, and ovulation occurs at around 12-14 hours after the LH peak, during estrus stage. Following ovulation, P4 production by the corpus luteum increases, inhibiting LH secretion and further ovulation. This high P4 and low/gradually increasing E2 levels indicate metestrus and diestrus stage. If mating does not occur during estrus stage, the corpus luteum regresses and progesterone levels decrease, allowing for the next cycle of ovulation. In cases of successful mating, P4 levels remain high, accompanied by a prolactin surge produced by the pituitary [71, 72]. Additionally, a nidatory peak in E2 is essential for blastocyst adhesion and uterine receptivity in mice and rats [73]. Cyclic changes in the internal and external FRT organs accompany estrous cycling, including stage-specific swelling of the vulva, openness of the vagina, changes in vaginal cytology, anatomical changes in the uterine horns, thickening of the endometrium/uterine stromal compartment, changes in folding of the uterine epithelium and lumen shape/size [71].

1.5.3. Finely tuned coordination of oviduct function controlled by estrous cycling

Coordination of gamete transport, fertilization, and embryo transport is associated with hormonally regulated estrous cycling, controlled by the hypothalamic-pituitary-ovary axis.

Oviducts show a mixture of anti- and pro-inflammatory signalling during estrous cycling, with fibroblasts showing a peak in inflammatory pathways at metestrus, as compared to the rest of the estrous stages. Although proportions of immune cells in the stromal compartment remains consistent between estrous stages, M1 macrophages are abundant at estrus while at metestrus, M2 macrophages are abundant. Oviducts and uteri also show the highest structural remodeling and extracellular matrix/ECM-associated signaling [74], which could be associated with morphological changes during gamete and embryo entry/transport. However, since cells for scRNASeq are isolated from entire oviducts in this study, it is unknown whether there are any region-specific transcriptional or immune cell subtype variation during the estrous cycle.

TEM studies show dynamic changes in SC organelle structures during the estrus cycle. Well-developed rough endoplasmic reticulum (RER) and Golgi complex, and numerous, apically located secretory granules are seen during estrus stage. However, during diestrus stage, decrease in the size of RER, Golgi complex, as well as the number of secretory granules is noted. SCs are also narrower during diestrus stage; they protrude from the epithelial monolayer, with cytoplasm and plasma membrane-surrounded nuclei sometimes projecting into the lumen. MCCs, on the other hand, show lower electron density and no secretory granules in their cytoplasm. RER and Golgi complex are relatively less developed, but these cells contain numerous mitochondria. Estrous cycle-associated changes are not easily recognizable in MCCs, but cytoplasmic lipid droplets are reported to increase in number during diestrus stage [28]. Interestingly, ciliary beat frequency (CBF) of MCCs in the isolated INF/AMP regions during estrus stage is lower than in diestrus stage [23], suggesting estrous cycling also regulates

CBF. In line with this, a high dose of E2 is shown to decrease CBF, while low doses are shown to increase CBF in fimbriae of guinea pigs. Additionally, P4 can reduce CBF in guinea pigs [75] and mice [76]. These observations agree with *in vivo* preovulatory E2 and P4 elevation during estrus stage [71], which could result in the reported INF/AMP CBF decrease. Finally, regardless of CBF differences in INF/AMP samples isolated from estrus or diestrus stage mice, OCCs are transported unidirectionally on open-book preparations [23]. These studies focus on the INF/AMP region likely because landmarks, morphological features, and MCC location/proportions for the AIJ, ISM, and UTJ regions are not clearly defined.

FRT epithelium-specific ablation of estrogen receptor 1 (*Wnt7a*^{Cre}*; Esr1*$^{f/f}$) affects cumulus cells surrounding ovulated oocytes, spermatozoa UTJ entry due to formation of unusual uterine plugs, both *in vivo* and *in vitro* fertilization, and preimplantation embryo survival beyond 0.5 dpc. Removal of cumulus cells or isolation of OCCs prior to ovulation/oviduct entry resulted in successful *in vitro* fertilization and embryo development, suggesting that OCC exposure to an abnormal oviduct microenvironment could be the cause. *Esr1-/-* oviduct epithelium does not respond to preovulatory E2 elevation due to loss of receptor, resulting in unmodulated/elevated protease activity that affects both the 0.5 dpc zona pellucida and zygote plasma membrane integrity, leading to embryo death [77]. Additionally, these mice show impaired embryo transport following 0.5 dpc embryo transfer, alongside an increase in INF cilia length and decrease in CBF [78]. However, despite E2 being associated with hormone signalling pathway regulation in MCCs [59], MCC-specific ablation of *Esr1* does not affect embryo transport or fertility [79]. In *Pgr*^{Cre}*; Esr1*$^{f/f}$ mice, loss of *Esr1* is reported in the ISM, UTJ, uterus and pituitary gland, resulting in retention of embryos in the oviduct, lower embryo viability, and lower circulating P4 levels [80]. Taken together, this suggests that FRT epithelium-specific *Esr1* signaling is required for downregulation of protease activity after ovulation, as well as embryo survival and transport, while ISM/UTJ-specific *Esr1* signaling and elevation of circulating P4 levels are required for embryo transport in the oviduct. INF/AMP MCC contribution to embryo transport in Pgr^{Cre}; $Esr1^{f/f}$ mice is unaffected, and since proximal ISM and UTJ regions have low proportions of MCCs, it is likely that embryo transport is instead affected by dysregulation of smooth muscle contraction/relaxation in these models. Although it is unclear whether Esr1 signaling regulates muscle contraction for embryo transport, it is known that PGR is involved in timely embryo transport [81]. In line with this, expression of genes associated with smooth muscle contraction, cilia beating, cell adhesion, cell migration, invasion are predicted to be negatively regulated in whole oviducts isolated from *Pgr-/-* mice, as compared to *Pgr+/-* oviducts [82]. Similar to E2 and P4 differentially regulating ESR/PGR receptor expression in mouse uterine stroma and epithelium [83], embryo transport in the oviduct could be directly regulated by E2, or indirectly by E2-mediated regulation of P4/PGR signaling. These studies highlight the importance of timed E2 and P4 regulation/signaling for coordination of gamete/embryo survival and transport in the oviduct. Additionally, despite direct exposure of gametes/embryos to the oviduct epithelium, epithelial function or response during estrous cycling or gamete/embryo travel is unclear.

1.6. Epithelial turnover/maintenance mechanisms in the adult oviduct

Epithelial cell turnover in the oviduct is thought to be directed by bipotent PAX8 SC. Lineage tracing using the $Pax8\text{-}rtTA;tetO\text{-}Cre;Yfp^{fl/fl}$ mouse line, which marks all PAX8-expressing cells with yellow fluorescent protein (YFP) following doxycycline induction at postnatal day 4 or between E13.5-P4, demonstrates that PAX8-expressing SCs can divide into both PAX8-expressing SCs and PAX8-negative MCCs [84]. Additionally, lineage tracing of stromal and epithelial cells shows that the adult oviduct epithelium is maintained by PAX8-expressing epithelial cells, with no evidence for stromal transdifferentiation [85]. Interestingly, in the $Pax8^{Cre/+}$; $Rosa26^{tdT/tdT}$ mouse line, which presents with mosaic tdTomato labeling in some tissues/cells due to low PAX8 expression, labeling was mostly restricted to the distal oviduct epithelium by postnatal day 3, and this pattern is maintained in adult oviducts as old as 13-months, suggesting that distal and proximal oviduct epithelial cells are maintained independently [17]. In tamoxifen-inducible *Prom1*$^{tm1(cre/ERT2)Gilb}$*; Rosa26*$^{tdT/tdT}$ mice, PROM1/CD133 expression and/or tdTomato labeling is noted in some SCs/MCCs in the INF/AMP, predominantly in MCCs of the AIJ and ISM, and not expressed in the UTJ. Labelled SCs in the INF/AMP differentiate into MCCs within 1-month following induction, resulting in almost exclusive MCC labeling throughout the tube. Interestingly, over the course of 5 months following induction, the proportion of tdTomato-positive cells in the INF/AMP did not change significantly, but these labelled cells progressively drifted from the base to the tip of the mucosal folds. Conversely, while the location of tdTomato-positive cells at the bottom of the folds in the ISM did not change, a slight decrease in the proportion of these cells is noted, suggesting distinct turnover dynamics in the distal and proximal oviduct. Additionally, the proportion of proliferating cells in the distal oviduct changes during the estrus cycle, but this no changes are noted in the proximal oviduct, further suggesting that the two regions respond differently during the estrous cycle [86]. In another study, lineage tracing in inducible *Foxj1*$^{CreER/+}$*; Rosa26*$^{mTmG/+}$ mice calculates the half-life of MCCs in the INF/AMP region to be ~6 months [87]. Finally, a recent study found a *Slc1a3*, *Pax8*, *Trp53*-expressing progenitor population that, when lineage traced using *Slc1a3-CreERT; Rosa26*$^{tdT/tdT}$ mice, give rise to both SCs and MCCs in the distal oviduct, with no significant contribution to the proximal. Labelled cells form clusters 30 days after induction and persist for over a year [88]. Taken together, the developmentally distinct distal and proximal oviduct epithelial populations are maintained independently and likely have different turnover mechanisms/rates, but overall, the oviduct epithelium has a low turnover rate.

In vitro culture of epithelial cells from the distal and proximal adult oviduct in Wnt-high media and surrounded by ECM results in self-organization into 3-dimensional (3D), hollow spheres made of monolayer epithelium, called organoids [89], that can recapitulate *in vivo* organ structure and/or function. Organoids derived from the oviduct epithelium initially comprise of PAX8-expressing, non-ciliated cells but can undergo ciliogenesis. Interestingly, organoids derived from the distal oviduct epithelium are larger and more in number as compared to those derived from the proximal oviduct epithelium, likely due to paracrine signaling and cell identity-specific or cell-intrinsic homeostatic differences [89, 90]. Further, similar to *in vivo* distal-proximal restricted WT1 and PAX2 expression, *in vitro* organoids derived from the distal oviduct express WT1, while those derived from the proximal oviduct express PAX2; indicating that the adult distal and proximal epithelial cell identity is maintained in the absence of the underlying stromal compartment [17]. Due to a lack of region-specific markers and landmarks along the oviduct, it is unclear whether the AIJ and UTJ are distinct regions or considered a part of the distal and/or proximal regions in some of the above-mentioned studies.

1.7. The FRT in aging

Aging results in a gradual, irreversible decline in organ function and on female fertility. Fertility rates decrease with increasing age due to a decline in number and quality of oocytes; this is accompanied by increased risk of pregnancy loss, incidence of disorders/diseases that affect fertility, and rates of aneuploidy [91].

1.7.1. Age-associated decline in menstrual/estrous cyclicity

1.7.1.1. Age-associated decline in human menstrual cyclicity

Irregular or shortened menstrual cycles, termed menopause transition or perimenopause, occurs in individuals around 46-55 years of age and lasts for 7-14 years. Lack of menstrual cycling that persists for 12 months is an indicator of menopause. The cause for this decline in cyclicity is thought to be a combination of oocyte depletion [92] and age-related changes in the central nervous system/GnRH secretion. Lack of folliculogenesis leads to decrease in E2 and P4, resulting in increased serum LH and FSH levels. Serum E2 and P4 levels are also markedly decreased. Perimenopause is associated with vaginal epithelium atrophy, increased vaginal/urinary infections, bone loss, increased incidence of cardiovascular disease, and other psychosocial effects including fatigue and depression [93, 94].

1.7.1.2. Age-associated decline in murine estrous cyclicity

Peak estrous cyclicity is noted at around 5-months of age in single housed, unmated, inbred C57BL/6J mice, and a decline in this cyclicity occurs by ~9 months. The initial phase of decline that occurs at 10-12-months of age is characterized by a progressive lengthening of estrous cycles [95] and is correlated with a delay, followed by impairment in preovulatory E2 elevation. Preovulatory P4 elevation and circulating E2 levels also decrease with age [96, 97]. Transplantation of ovaries from young 2-month-old mice to aged 12-month-old mice restores preovulatory E2 and P4 elevation; however, mean E2 levels across the estrous cycle did not increase after transplantation. Conversely, transplantation of ovaries from 12-month-old mice to 2-month-old mice prevented preovulatory E2 and P4 elevation but maintained mean E2 levels [98], demonstrating that the preovulatory E2 surge is controlled by the ovary but maintenance of basal E2 levels is likely controlled by extra-ovarian, likely neuroendocrine, factors. During the cessation of estrous cycling that occurs between 11 to 16-months of age, mice often present with constant proestrus/estrus/early metestrus-type smears called persistent vaginal cornification (PVC), polyfollicular ovaries, and absence of corpus lutea [96], or rarely present with either 1) repeated pseudopregnancy-like episodes characterized by elevated E2, uterine response to deciduogenic stimuli, and ovulations separated by 10–14-day intervals during which vaginal smears show mainly white blood cells, or 2) anestrus/persistent diestrus [97, 99]. The duration of these post-cyclic stages varies between mice, but they eventually all enter persistent diestrus, which is characterized by low circulating E2 and P4, and an atrophic ovary [100]. Levels of intercellular collagen marked by Picosirius red staining are highest in the uterus, oviduct, and vagina, with no increase in the ovary and cervix of aged mice, indicating that fibrosis in the FRT accumulates gradually during aging [74]. Further, 8-month-old pregnant mice show a reduction in litter size, longer mean gestation and labour duration due to delayed P4 withdrawal and impaired myometrial contraction. Increase in cervical distensibility is also noted [101].

Although inter-cohort variation in studies pertaining to estrous cycling in young/aged inbred C57BL6 mice is high, it is unlikely that this is caused by genetic variation. Reports suggest that this variation could be due to colony population density, multiple housing, male/female pheromones, parity, environmental modulations, or intrauterine proximity of male and female fetuses during embryonic development [95, 100].

		Human	Mouse
FRT anatomy	Differences	- Ovary exposed to peritoneum. - Bowed, uncoiled FTs. - Simplex uterus.	- Ovary encompassed by the ovarian bursa. - Coiled oviducts. - Bipartite uterus.
	Similarities	- Single cervix.	- Single cervix.
FT/oviduct anatomy	Differences	- No AIJ is reported. - Fimbriae are finger-like projections at the distal end that encompasses the ovary. Fimbrial epithelium is exposed to the peritoneum.	- Transition region called the ampulla-isthmus junction (AIJ) is reported. - INF is a funnel-shaped region at the distal end, located adjacent to ovary. INF is encompassed by the ovarian bursa, and not exposed to the peritoneum.
	Similarities	- 4 regions from distal to proximal: fimbriae/INF, AMP, ISM, UTJ. - Two types of epithelial cells: MCCs and SCs. - Proportion of MCCs forms a gradient. High in the fimbriae and low in the UTJ.	- 4 regions from distal to proximal: INF, AMP, ISM, UTJ. - Two types of epithelial cells: MCCs and SCs. - Proportion of MCCs forms a gradient. High in the INF and low in the UTJ.
Hormonal cycle	Differences	- Called menstrual cycle. - Cycle length = 25-30 days. - Begins with menses/shedding of the endometrium.	- Called estrous cycle. - Cycle length = 4-5 days. - Begins with proestrus, no menses/shedding.

		- 2 phases: menstruation & follicular/proliferative phase, ovulation & luteal/secretory phase.	- 4 stages: proestrus, estrus, metestrus, and diestrus.
	Similarities	- Spontaneous ovulation controlled by hormonal cycle.	- Spontaneous ovulation controlled by hormonal cycle.
FRT response to hormonal cycling	Differences	- Endometrium sheds during menstruation. - Folliculogenesis and thickening of endometrium during follicular phase. - Ovulation/oocyte release from the ovary on day 14. - Thickening of the endometrium and oocyte/embryo transport along the FT during luteal phase. - Unknown if changes in organ/lumen shape occur.	- No shedding/menses. - Follicular growth and maturation during proestrus. - Ovulation occurs at around 12-14 hours after LH peak, during estrus stage. - Metestrus and diestrus are analogous to luteal phase, involving uterine elongation and changes in vaginal epithelium. - Cyclic changes in cervical shape, uterine thickness, uterine lumen shape, uterine cell composition/morphology, vaginal appearance are reported.
	Similarities	- Cyclic, hormonally regulated changes in FRT organs. - Cyclic changes in cervical mucous and morphology of	- Cyclic, hormonally regulated changes in FRT organs. - Cyclic changes in cervical cell

		exfoliated vaginal epithelial cells are reported.	composition/morphology and morphology of exfoliated vaginal epithelial cells are reported.
Menopause/ anestrus	Differences	- Menopause transition/perimenopause, involving irregular or shortened cycles, occurs in individuals around 46-55 years of age and lasts for 7-14 years. - Menopause is characterised by lack of menstrual cycling that persists for 12 months, and its timing varies between individuals.	- Decline in estrous cyclicity occurs by ~9 months of age. Cessation of estrous cycling occurs between 11 to 16-months of age. - Duration of post-cyclic stages varies between mice, but eventually all enter persistent diestrus or anestrus.
	Similarities	- Gradual decline in menstrual cyclicity, followed by lack of cycling.	- Gradual decline in estrous cyclicity, followed by lack of cycling.

Table 1. 1: Summary of similarities and differences between human and mouse FRTs and hormonal cycles.

1.7.2. Mouse oviductal response to aging

Oviduct structural and ECM remodeling occur during each estrous cycle in mice. This repetitive remodeling results in increased Picosirius red-positive intercellular collagen or fibrosis in the stromal compartment of aged 12 to 24-month-old mice. Interestingly, termination of estrous cycling by triggering premature ovarian insufficiency using 4-vinylcyclohexene diepoxide (VCD) treatment reduces fibrosis in the oviduct, but not significantly, suggesting that both aging and repetitive estrous cycling contribute to fibrosis in the oviduct. FRT aging is also accompanied by an increase in the fraction of immune cells within the stromal compartment; in particular, the aged oviduct shows an increase in numbers of natural killer (NK), B, and dendritic cells [74]. However, since this study was performed on whole oviducts, it is unclear if distinct regions of the oviduct respond differently to aging.

TEM studies of the AMP epithelium in 22- to 24-month-old mice show that MCCs contain large vacuoles containing heterogeneously dense materials, while SCs have dilated rough endoplasmic reticulum, smaller Golgi complex, fewer mitochondria, and no secretory granules. These age-associated changes are noted in mice as early as 7 months of age [28], however, the cause, chronology, and regional specificity of these changes are unknown. Since ovary function in aged mice is also significantly reduced [96], it is unclear whether these changes contribute to subfertility or infertility in aged mice. Although unclear if this is region-specific, increased P4 levels during diestrus is proposed to eliminate defective cells in p53-null mice [102], bringing up the possibility of aging-associated lengthening/loss of estrous cycling preventing removal of damaged cells. Another possible cause for the observed cytoplasmic vacuolation is repetitive ovulation and low epithelial cell turnover, resulting in repetitive cellular stress and/or DNA damage.

1.8. The Fallopian tube/oviduct in cancer

Ovarian cancer (OC) is the seventh most common cancer among women in the world. OCs can be classified as epithelial, stromal cell, germ cell OCs, with epithelial OCs making up 85-95% of cases. Epithelial OCs are further classified into multiple subtypes, among which High Grade Serous Ovarian Carcinomas (HGSCs) are the most common subtype, accounting for up to 70% of all OCs. Individuals with serous OCs are typically diagnosed at advanced stages when the survival rate is relatively low [103, 104]. This is likely due to its asymptomatic nature, deep-seated location of the ovary, and lack of knowledge on its etiology and cell of origin. Although called an OC, a majority of HGSCs originate from the uterine/Fallopian tubes [105]. Using the SEE-FIM (Sectioning and Extensively Examining the FIMbria) protocol, serous tubal intraepithelial carcinomas (STICs) were observed predominantly in the distal fimbrial region of uterine tubes from *BRCA*+ individuals undergoing bilateral salpingo-oophorectomies [106], as well as in cases not selected for *BRCA* status but classified as serous ovarian carcinomas [107].

It is hypothesized that repetitive/incessant ovulation over an individual's reproductive lifespan could result in the accumulation of DNA damage and Mullerian metaplasia/neoplastic transformation [108]. Ovulation is accompanied by release of inflammatory cytokines, reactive oxygen species (ROS), and follicular rupture resulting in irreversible damage/apoptosis of the ovarian surface epithelium (OSE) [109]. In the context of precursor lesions discovered in the fimbriae of individuals undergoing salpingo-oophorectomies/HGSC patients, factors released during this "incessant ovulation" could also affect the directly adjacent distal uterine tube epithelium, resulting in progressive DNA damage, accumulation of mutations, Secretory Cell OUTgrowths (SCOUTs), and STICs that translocate onto the ovary to form tumors that present as HGSCs [110]. Serous OCs and their precursors typically contain TP53 mutations and stable p53 protein expression, called the *P53* signature [111]. In support of this "incessant ovulation" hypothesis, *P53* signature is significantly associated with lower parity, suggesting that repetitive ovulation is a risk factor for *P53* signature development in the fimbriae [112] and could be a risk factor for serous OCs. In addition, longer duration oral contraceptive use is directly proportional to reduced OC risk [113, 114].

Another major risk factor for most cancers is aging, and individuals with OC are typically over 65 years of age [115], which is typically correlated with “incessant ovulation” over the reproductive lifespan and/or accumulation of mutations with age. However, age-associated changes in hormonal regulation and reproductive organs of menopausal/postmenopausal individuals are also factors to consider.

1.8.1. Mouse models of oviduct-derived HGSC

Pax8-rtTA;tetO-Cre and *Ovgp1-iCreERT2* inducible mouse lines have been used to successfully induce HGSC from the oviduct, however, Pax8 and Ovgp1 are expressed throughout the oviduct and also in other tissues [116, 117], leading to tumorigenesis in organs other than oviduct. *Pax8-rtTA;tetO-Cre* mouse line crossed with Mosaic Analysis with Double Markers(*MADM)*-mutants presents with sporadic, low frequency/single-cell labelling and knockouts/mutations in a combination of tumor suppressors, enabling clonal tracing of mutant cells. In this study, clonal expansion was followed only till 5 months post induction, after which mice present with invasive uterine tumors without ovarian tumor formation. Both large and small clones are observed throughout the oviduct epithelium, but large clones are predominantly located in the distal INF/AMP region [118], indicating differences in distal-proximal response to loss of tumor suppressors and subsequent clonal progression. Additionally, since HGSC precursor lesions in patients are predominantly found in the distal fimbriae, cancer modeling using non-specific inducible mouse lines may not accurately recapitulate tumorigenesis. Using a combination of CRISPR-cas9, Cre excision, *in vivo* injection into the oviduct lumen and electroporation to control the targeted area for inducing mutations/Cre excision, it is shown that cells in the distal oviduct can progressively develop SCOUTs, STICs, ovarian tumors, metastases, and ascites in immunocompetent mice over 11-16 months post surgery, depending on the mutation combination used [119]. Thus, the distal oviduct epithelium may be uniquely susceptible to malignant transformation. Interestingly, a recent study implicates a *Krt5*, *Prom1*, *Trp73*-expressing preciliated population within the distal oviduct that undergoes malignant transformation upon conditional deletion of *Trp53* and *Rb1*, using *Krt5-CreERT; Trp53*$^{loxP/loxP}$ *Rb1*$^{loxP/loxP}$*; Rosa26*$^{tdT/tdT}$ mice [88]. Finally, since most HGSCs are diagnosed in the latter part of the reproductive lifespan or after the reproductive lifespan has passed, it is interesting to speculate that oviduct aging results in an altered microenvironment that is conducive to tumorigenesis and progression.

1.9. General hypothesis and objectives

Despite evidence for distinct oviductal response to gametes/embryos, the oviduct is considered a simple tube that acts as a conduit. This is likely due to advances in *in vitro* fertilization techniques, permitting bypass of the FT. However, studies have shown that the cell-of-origin of HGSCs, a subtype of epithelial OCs, is located within the distal FT epithelium, bringing this organ into the limelight. This distal FT susceptibility to malignant transformation led me to hypothesize that the distal FT epithelium is distinct from the rest of the tube. However, not much is known about the FT/oviduct. The mouse oviduct is considered a simple tube with 4 distinct regions based on mucosal fold morphology: INF, AMP, ISM and UTJ, lined with two subtypes of cells: MCCs and SCs that form a gradient along the tube.

I have three objectives:

- **Characterization of anatomical and cellular heterogeneity along the tube to aid reliable comparison between distinct oviduct regions**: In Chapter 2, using a combination of modern imaging techniques, 3D imaging of wholemount tubes, and mouse fluorescence reporter lines, I demarcate 4 morphologically distinct regions with distinct MCC proportion/distribution patterns, TF expression, and potential functions.

- **Identification of region-specific genes/TFs to confirm distinct MCC/SC populations along the tube and infer functional diversity**: In Chapter 3, using the description of the oviduct epithelium from Chapter 2, I optimize a low input, pooled SmartSeq approach for all regionally restricted epithelial subtypes, thus confirming distinct MCC/SC subtypes, potential functions, and suggesting distinct cellular identities along the tube.

- **Exploring distal oviduct susceptibility through the lens of aging**: The distal oviduct is thought to be exposed to ROS and inflammatory cytokines during each cycle of ovulation, resulting in accumulation of DNA damage and HGSC due to repetitive DNA/cellular damage throughout the reproductive lifespan. In line with this, HGSCs are typically diagnosed later in life, beyond 65 years of age. Thus, I hypothesized that the distinct INF/AMP cellular identity shown in Chapter 3, coupled with a permissive/optimal microenvironment in aging, contributes to distal oviduct susceptibility. In Chapter 4, I report an INF/AMP-specific aging phenotype that reflects a mild, but chronically stressed distal microenvironment.

2. Anatomical and cellular heterogeneity in the mouse oviduct—its potential roles in reproduction and preimplantation development

Keerthana Harwalkar[1,2], Matthew J Ford[1], Katie Teng[1,2], Nobuko Yamanaka[1], Brenna Yang[1], Ingo Burtscher[3,4], Heiko Lickert[3-6], Yojiro Yamanaka[1,2,*]

[1]Rosalind and Morris Goodman Cancer Research Centre, Montréal, Québec, Canada

[2]Department of Human Genetics, McGill University, Montréal, Québec, Canada

[3]Institute of Diabetes and Regeneration Research, Helmholtz Diabetes Center, Helmholtz Center Munich, Munich, Germany

[4]Institute of Stem Cell Research, Helmholtz Center, Munich, Germany

[5]German Centre for Diabetes Research (DZD), Munich, Germany

[6]Department of Medicine, Technical University of Munich, Munich, Germany

*Correspondence: 1160 Pine Avenue West, rm419, Montreal, Quebec H3A 1A3, Canada.

Tel.: 514-398-8776; E-mail: yojiro.yamanaka@mcgill.ca

Published: 09 March 2021

Biology of Reproduction, Volume 104, Issue 6, June 2021, Pages 1249–1261, https://doi.org/10.1093/biolre/ioab043

2.1. Abstract

The oviduct/fallopian tube is a tube-like structure that extends from the uterus to the ovary. It is an essential reproductive organ that provides an environment for internal fertilization and preimplantation development. However, our knowledge of its regional and cellular heterogeneity is still limited. Here, we examined the anatomical complexity of mouse oviducts using modern imaging techniques and fluorescence reporter lines. We found that there are consistent coiling patterns and turning points in the coiled mouse oviduct that serve as reliable landmarks for luminal morphological regionalities. We also found previously unrecognized anatomical structures in the isthmus and uterotubal junction, which likely play roles in reproduction. Furthermore, we demarcated the ampulla–isthmus junction as a distinct region. Taken together, the oviduct mucosal epithelium has highly diverse structures with distinct epithelial cell populations, reflecting its complex functions in reproduction.

2.2. Introduction

Mouse oviducts, called fallopian tubes (FTs) in humans, are a part of the female reproductive tract; they are tube-like structures that extend from the uterus to the ovary. This organ is essential for mammalian reproduction, including internal fertilization and preimplantation development. Sperm and oocytes enter from opposite ends of the oviduct to meet at a transiently distended region of the oviductal ampulla (AMP) for fertilization. After fertilization, preimplantation embryos travel down the oviduct lumen toward the uterus [1, 2]. They remain in the oviduct for relatively consistent period of time without direct physical contact between the embryos and oviductal mucosal epithelium due to the remaining presence of the oocyte zona pellucida, a proteinaceous shell that surrounds each embryo during its time in the oviduct [3]. The oviduct luminal environment is transiently modulated by the oviductal mucosal epithelium to accommodate sperm migration, fertilization, and preimplantation development [4–6]. Without this regulation, the oviduct luminal environment is too harsh for reproduction because it is primarily adjusted against bacterial infections [6]. On the other hand, if a preimplantation embryo does not properly traverse the tube, for example, due to an obstruction or constriction in the luminal space, this leads to ectopic pregnancy in humans [7]. This indicates that a proper spatiotemporal coordination between the oviduct and gamete/embryo movement is essential for successful pregnancy.

Although the oviduct is essential for reproduction, with a portion of human infertility cases being due to deficiencies in the oviduct [8], the complexity of mucosal fold patterns and cellular heterogeneity of the oviduct mucosal epithelium have not been fully explored. The pioneering work on the mouse oviduct [9] described intensive oviduct coiling and complex luminal morphology. Four regionalities are recognized in the mouse oviduct, from distal to proximal with point of reference as the uterus: the infundibulum (INF), AMP, isthmus (ISM), and uterotubal junction (UTJ). It has been generally thought that the oviductal mucosal epithelium consists of two cell types: multiciliated cells (MCCs) and nonciliated secretory cells (SCs), with the proportion of MCCs forming a descending gradient from the distal to proximal [10, 11]. However, in our parallel study, we identified that distal and proximal luminal epithelial cells are two distinct lineages from as early as E12.5 in the Mullerian duct, presenting with unique gene expression [12].

In this study, we revisit the oviduct using modern imaging techniques and mouse fluorescence reporter lines. Due to its intensive coiling, traditional 2D tissue sectioning methods have limitations in the analysis of 3D complexity. Through our careful 3D analysis, we recognized consistent coiling patterns between mice, with corresponding changes in luminal regional morphology. In addition, we identified previously unrecognized anatomical structures in the ISM and UTJ, likely playing roles in successful pregnancy. The AMP–ISM junction (AIJ) was a unique region different from the AMP and ISM in its MCC distribution pattern, mucosal fold morphology, transcription factor expression, and acidic mucin secretion. Our results revealed anatomical and cellular heterogeneity in the mouse oviduct mucosal epithelium, suggesting functional diversity in each morphologically distinct region.

2.3. Results

2.3.1. Consistent coiling patterns in mouse oviducts maintained by its attachment to the mesosalpinx

The mouse oviduct is a highly coiled tube that extends from the uterus to the ovary. This coiling makes precise regional comparison difficult in standard 2D tissue sectioning methods. The mesosalpinx, which connects the oviduct to the body wall, gathers inferior to the coils and stabilizes them. It is also connected to the ovarian bursa as well as the uterine mesometrium, which is further attached to the dorsal mesentery [9]. We carefully compared several female reproductive tracts (n = 10 oviducts) to examine if they have consistent coiling patterns (Figure 1A, Supplementary Figure S1). Although occasional contractions of the AMP and ISM myosalpinx [13] created variation, their coiling pattern appeared consistent. The coiling pattern of the left and right oviducts was mirror images of each other. When the left oviduct was placed with the ovary on top and the uterus at bottom, the AMP was always positioned to the left side and the ISM was positioned to the right side (Figure 1A).

Based on the reproducible coiling patterns, we numbered each turn from the distal end (Figure 1C and D). Turns 1–4 were highly consistent. Turn 4 was often positioned inferior to Turns 2 and 3. Turns 5–7 presented with more variation, likely due to ISM contractions, with Turn 5 frequently curled toward the deep position. This created additional Turns 4.5 and 5.5 (Figure 1D and E, Supplementary Figure S1). Turns 9–11 were again relatively consistent. Turn 11 was often located at the deep position of the coiled oviduct and connected to the uterus (Figure 1B–D, Supplementary Figure S1). When the oviduct was straightened, each turn was still recognizable and the mucosal fold patterns along the oviduct were visible under a dark field illumination of a dissecting microscope (Figure 1F). The turning positions were reliable landmarks for mucosal fold patterns along the mouse oviduct.

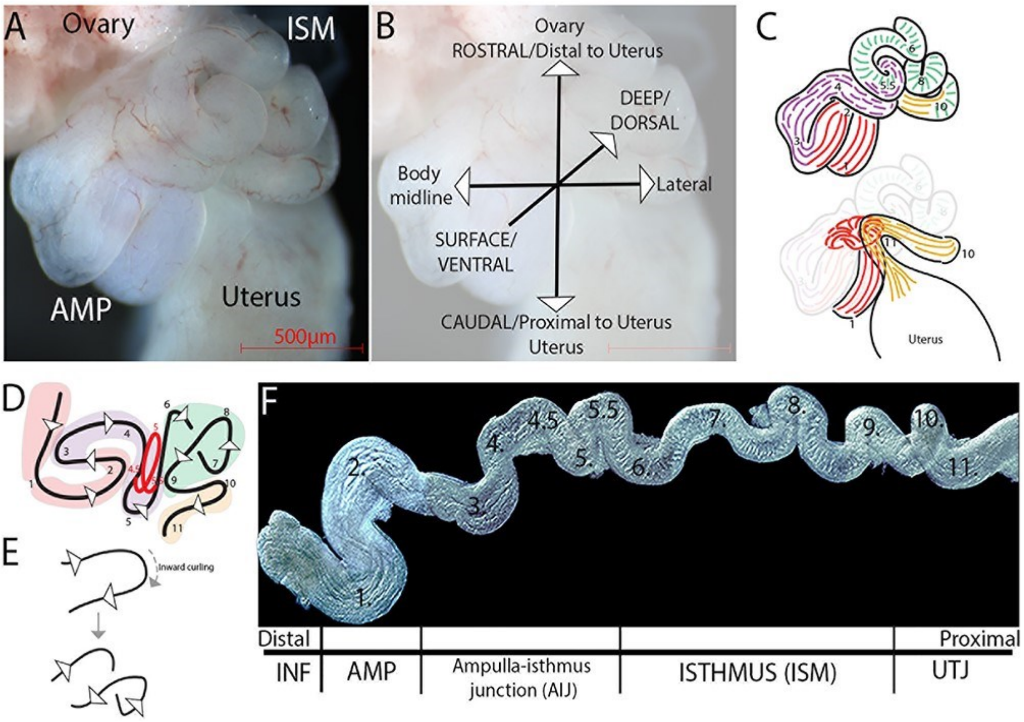

Figure 1: Consistent coiling pattern and turning points in the mouse oviduct.

(A) Ventral view of the left mouse oviduct when the ovary–uterus axis is rostral–caudal, with AMP on the left and ISM on right-hand side of the image. (B) Axes representing the orientation of the coiled left oviduct. The surface/dorsal view to deep/ventral view is represented by a line directed into the paper. (C) Diagrams of the oviduct shown in A. Surface view (top) showing the body of the oviduct. Deep view (bottom) showing the INF and UTJ. The colors represent distinct mucosal fold morphologies: INF/AMP in red, AIJ in purple, ISM in green, and UTJ in yellow. (D) A simple illustration of the consistent coiling pattern and regionalities; 11 turns were reproducibly identified. Turn 5 was often curled toward the deep position (solid red line), creating Turns 4.5 and 5.5. The coiling pattern from Turn 5 to Turn 7 showed variation due to ISM contractile movement. Turns 1–3 and Turns 8–11 had consistent coiling pattern. (E) Coiling pattern in the ISM. The complex coiling pattern is created by a combination of turning and curling. (F) A stretched oviduct with mesosalpinx removed. Tiled images of the stretched oviduct were manually aligned. A plain black background was added; N = 10 oviducts.

2.3.2. 3D imaging reveals transition of epithelial fold patterns along the mouse oviduct

In order to investigate mucosal fold patterns and their transition along the oviduct, we undertook high-resolution 3D confocal imaging analysis after tissue clearing. The INF is a funnel-like structure located at the distal end of the oviduct, adjacent to the ovary [9]. The mucosal epithelium of the INF was everted at its opening, called the ostium (Figure 2A, D, and G), where the lumen of the oviduct communicates with that of the ovarian bursa, exposing mucosal epithelium to the inner space of the ovarian bursa (Supplementary Figure S2). At the ostium, almost every two exterior longitudinal folds merged into one mucosal fold and continued into the AMP (Figure 2E). The distal end of the INF was not blunt, but often beveled to fit the ostium along the ovarian surface (Supplementary Figure S2). In contrast to the circular smooth muscle layer noted in a transverse section, the exterior mucosal folds were not radially symmetric (Figure 2B and D, Supplementary Figure S3A), with one side forming an overhang (Figure 2D and F, Video 1). Exterior folds on the contralateral side of the overhang were shorter and laid flat against the smooth muscle layer (Figure 2B and F, Video 1). The mucosal epithelium lining these exterior folds was continuous with the epithelium-lined ligament that connected to the ovarian bursa and ovary (Figure 2F, Supplementary Figure S2 and S3A). The INF mucosal folds consisted of 12–18 longitudinal folds (Supplementary Figure S3A, Figure 2B; n = 8 oviducts). Every other mucosal fold was tall (80–184 μm), reaching the center area of the lumen, with a short fold roughly half the height (16–80 μm) between two tall ones (Figure 2B, Supplementary Figure S3A). Each fold has a thin layer of stromal cells underneath the epithelium, without smooth muscle cells. The smooth muscle layer is only at the circumference, framing the tube-like shape at the INF [9].

The longitudinal mucosal folds of the INF and AMP were continuous (Figure 2A). The AMP had 15–20 inner mucosal folds (Figure 2C, Supplementary Figure S3B; n = 8 oviducts). The number of folds reduced between Turn 3 and 4 (5–12 mucosal folds; Figure 2H–K, Supplementary Figure S3C and D; n = 8 oviducts). Between Turns 4 and 5.5, the longitudinal folds were not continuous but showed slit-like breaking points (Figure 2L, Supplementary Figure S4B–D). Toward the proximal end, the AIJ longitudinal folds were often bent and had frequent breakpoints, with multiple convolutions (Figure 2M, Supplementary Figure S4A–F). Around Turn 6, transverse mucosal folds of the ISM were observed (Figure 2N, Supplementary Figure S3E and F), creating furrows extending along the circumference, comparable with a bellows shape (Figure 2P). Around Turn 6–8, the distal ISM, its transverse mucosal folds were not perfectly aligned/parallel but often fused (Figure 2N). On the other hand, around Turn 8–9, the transverse mucosal folds of the proximal ISM were aligned and parallel (Figure 2O).

The transition from transverse mucosal folds of the ISM to the longitudinal mucosal folds of the UTJ was observed around Turn 10 (Figure 2Q, Supplementary Figure S3G). In this transition area, the isthmic transverse folds were on the anti-mesosalpinx side, whereas 1–2 longitudinal UTJ folds were located on the opposing mesosalpinx side (Figure 2Q and R). UTJ longitudinal folds were inserted into the uterine stroma, forming the intramural UTJ (Figure 2S–U, Supplementary Figure S2). Interestingly, we found small luminal compartments within the intramural UTJ formed by breakpoints in the UTJ longitudinal folds (Supplementary Figure S4G–K, Figure 2T, Video 2). The intramural UTJ lumen communicated with the uterine lumen through the colliculus tubarius (Figure 2S, Video 2, Supplementary Figure S4G), as described previously [9, 14].

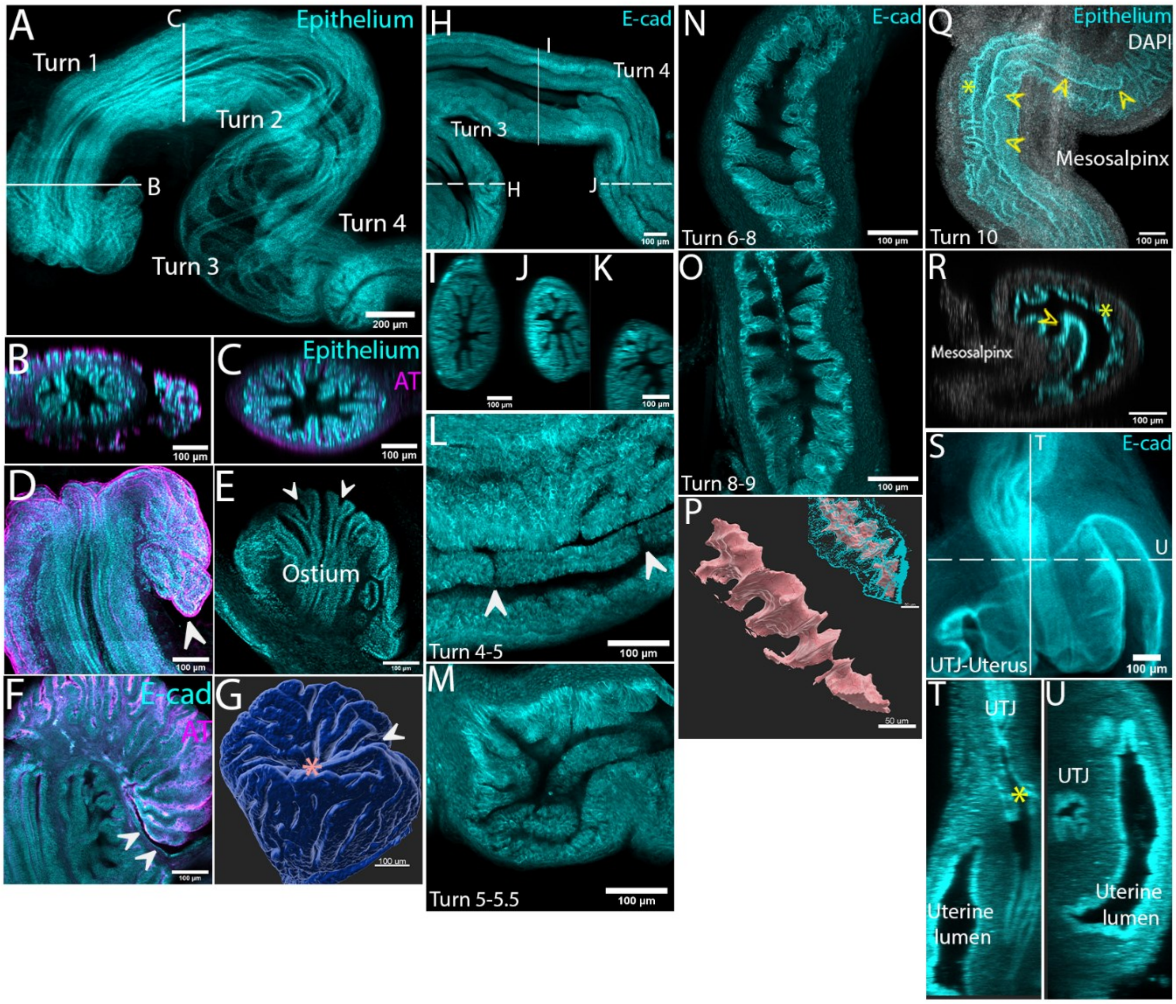

Figure 2: Distinct 3D luminal morphologies along the mouse oviduct.

(A) The distal end of the oviduct from Turns 1–4, including the INF, AMP, and AIJ. Continuous, longitudinal folds extended from the INF into Turns 3–4. Sum slices projection of 90 optical sections. White lines indicate location of orthogonal views in (B) and (C). (B) XZ orthogonal view of the INF. (C) YZ orthogonal view of the AMP. Tall and short mucosal folds alternate along the circumference. (D) Exterior folds of the INF were continuous with the mucosal folds. The marginal edge of the exterior folds formed an overhang (white arrowhead). Maximum projection of 23 optical sections. (E) Two exterior folds merged into a single mucosal fold at the ostium (white arrowheads). (F) Intersection of overhanging and flattened exterior mucosal folds. Mucosal epithelium of exterior folds was connected to an epithelium-lined connective tissue (white arrowheads). (G) Surface rendered image of the INF. The exterior folds created a relatively wide flat surface leading to the ostium (pink asterisk). A slit opening towards the ovary (white arrow). (H) Continuous longitudinal folds from Turns 3 to 4 of the AIJ. White lines indicate the location of orthogonal views in I–K. (I) The area between Turns 2 and 3, (J) Turns 3 and 4, (K) Turns 4 and 5. A decrease of the number of longitudinal folds was noted. (L) The distal AIJ at Turns 4–5. Breakpoints in the longitudinal folds (white arrows). (M) The proximal AIJ at Turns 5–6. Short and bent longitudinal folds and luminal convolutions. (N) The distal ISM at Turns 6–8. Transverse mucosal folds were angled. (O) The proximal ISM at Turns 8–9. Aligned, parallel transverse mucosal folds. (P) Surface rendering of the bellows-shaped isthmic lumen. A merged image of the epithelial cell surface rendering and luminal surface rendering (inset). Scale bar = 50 μm. (Q) The transition between the ISM and UTJ around Turn 10. One longitudinal fold (yellow arrowheads) on the mesosalpinx side extended into the UTJ, with isthmic transverse folds on the anti-mesosalpinx side (yellow asterisk). (R) XZ orthogonal view in (Q). (S) The UTJ–uterus connection. The UTJ lumen, located within the uterine stroma, connected into the uterine lumen. Average projection of 115 optical sections. (T) Longitudinal orthogonal view in (S). Breakpoints in the longitudinal folds formed small compartments (white arrow). (U) Transverse view in (S). Intramural UTJ was at the mesosalpinx side of the uterine lumen. Epithelium: a combined signal of PAX8 and FLTP-H2B-Venus (used in A–E, Q, R; see Methods and Materials section); AT: acetylated tubulin; E-cad: E-cadherin; N = 4 mice. Scale bar = 100 μm, unless mentioned above.

2.3.3. MCCs in the ISM are clustered at the trenches of transverse mucosal folds

It is thought that the proportion of MCCs forms a descending gradient from the distal end adjacent to the ovary [10, 11]. Since the mouse oviduct has complex mucosal folds and a highly coiled structure, it is important to perform 3D image analysis to capture the whole view of their distribution pattern. Using a FLTP-H2B-Venus (Flattop-driven H2B-Venus reporter) transgenic mouse line [15] for visualization of MCCs, we found that the distribution of FLTP-H2B-Venus+ve cells did not show a simple gradient, but a sharp reduction between Turns 2 and 3 (Figure 3A and B). A high proportion of FLTP-H2B-Venus+ve cells in the INF and AMP was observed (57.9 ± 3.57 and 55.4 ± 9.6%, respectively, mean ± SD; Figure 3G, Supplementary Figure S3A and B), with a relatively low proportion in the AIJ and ISM (ranging from 18 to 25%; Figure 3G, Supplementary Figure S3C–F). No FLTP-H2B-Venus+ve cells were found in the UTJ (Figure 3G, Supplementary Figure S3G).

In the INF and AMP, MCCs were uniformly distributed on the mucosal folds (Figure 3C and D, Supplementary Figure S3A and B). In the distal AIJ around Turn 3, MCCs were sparsely distributed (Figure 3E, Supplementary Figure S3C and S4A–D). Some MCCs in the proximal AIJ were located in the trenches of transverse mucosal folds (Figure 3F, Supplementary Figure S3D and S4E and F), similar to the ISM (Figure 3H–S), whereas others were sparsely distributed on the folds (Figure 3F, Supplementary Figure S3D and S4E and F). Although the location of MCCs changed progressively, there was no significant difference in the proportion of MCCs within the AIJ (17.99 ± 0.42% in distal compared with 21.67 ± 5.71% in proximal, Figure 3G).

In the ISM, interestingly, MCCs clustered in the trenches of the transverse folds (Figure 3H, Supplementary Figure S3E and F). Rosette arrangement of MCC clusters (Figure 3N and O) generated MCC grooves (Figure 3J and K) and pits (Figure 3L and M). All cilia were projected into one focal point within the clusters (Figure 3J–M), creating the stripe patterns of multicilia in the ISM (Figure 3I). The noted stripe patterns were very similar to the sperm distribution pattern shown in previous studies [14, 16, 17]. Although the trench localization of MCCs in both distal and proximal ISM did not change (Figure 3P–S), there was a significant decrease in the proportion of MCCs in the proximal ISM (distal 25.26 ± 4.45% and proximal 14.91 ± 5.02%; Figure 3G). The density of MCCs was lower in the proximal ISM (Figure 3P and Q) because the number of MCCs forming each cluster was smaller (Figure 3R and S).

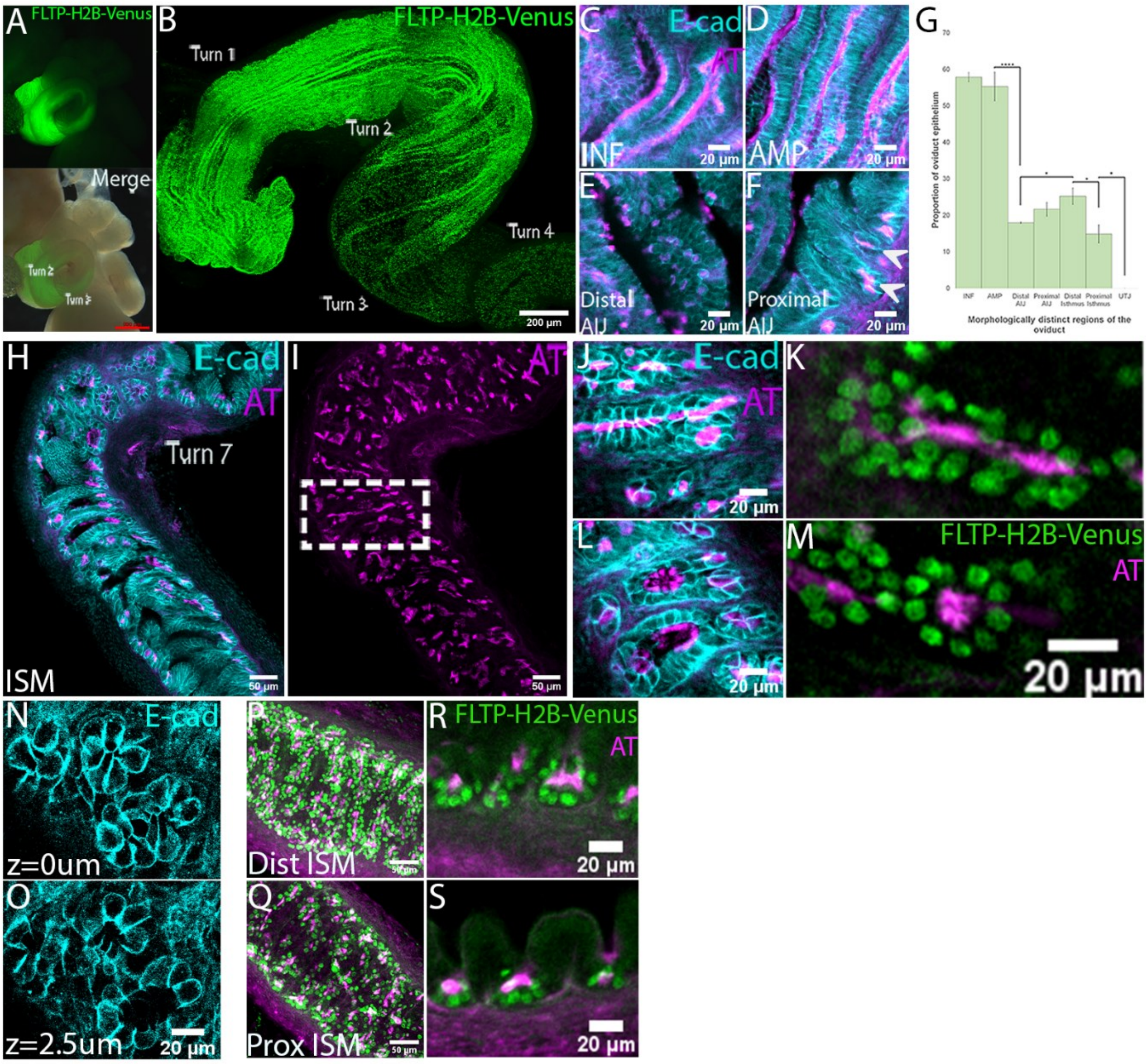

Figure 3: Distribution of multiciliated cells in the oviduct and unique multiciliated cell clusters in the ISM.

(A) Unfixed oviduct of an FLTP-H2B-Venus female. Strong GFP signal in the INF and AMP. Scale bar = 500 µm. (B) Distribution of FLTP-H2B-Venus cells in the INF, AMP, and AIJ. A sharp reduction of H2B-Venus+ve cells between Turns 2 and 3. The same image series as Figure 2A. Maximum projection of 90 optical sections. Scale bar = 200 µm. (C–F) Distribution patterns of MCCs in the INF, AMP, and AIJ. (C, D) Uniform distribution of MCCs in the INF (C) and AMP (D). Cilia are evenly distributed on the apical surface. (E) MCCs are sparsely distributed in the epithelium of the distal AIJ. Cilia localization is not uniform but often limited at the periphery or center of the apical surface of MCCs. (F) MCCs in the proximal AIJ. They are located in the trenches (white arrowheads), similar to the ISM, but some are sparsely distributed on the folds. (G) Proportions of FLTP-H2B-Venus+ve MCCs along the oviduct. Regions of high (around 60% in INF/AMP), low (around 20% in AIJ/ISM), and absent (0% in UTJ) were recognized. ****$P < 0.0001$, *$P < 0.05$. Error bars indicate standard deviation. Quantification was performed on transverse sections like those in Supplementary Figure S2A–G; $N = 8$ oviducts. (H–S) MCCs in the ISM. (H) A single optical section of the distal ISM. All MCCs are clustered in the trenches of the epithelial folds. (I) Maximum projection of acetylated tubulin staining from 41 optical sections. A groove pattern of the multicilia distribution, resembling the sperm distribution pattern [14, 16]. (J, K) A groove of MCC clusters. (L, M) Multiciliated cell pits. Cilia project to one focal point. (N, O) Live open-book preparations of the ISM isolated from E-cadherin–mCFP mice showing a rosette arrangement of cell clusters at the trenches, bottom of pits (N), close to mucosal surface (O). (P, Q) Difference in density of MCCs along the ISM. Maximum projections of FLTP-H2B-Venus and AT staining of the distal (P) and proximal (Q). Higher density of MCCs in the distal ISM than in the proximal ISM. (R, S) Longitudinal orthogonal views of distal (R) and proximal (S) isthmic transverse folds. More MCCs contribute to form single pits/grooves in the distal ISM. AT: acetylated tubulin; E-cad: E-cadherin. Scale bars = 20 µm/50 µm.

2.3.4. Distinct subtypes of SCs and MCCs in distal and proximal regions in mice and marmosets

In a parallel study, we demonstrated that distal and proximal oviduct mucosal epithelial populations are two developmentally distinct lineages as early as the E12.5 Mullerian duct. Based on single-cell transcriptome analysis, we identified that WT1 and PAX2 are specific markers for the distal and proximal regions, respectively. Interestingly, PAX8 is a marker for SCs only in the distal region, but is expressed in both SCs and MCCs of the proximal oviduct epithelium [12] (Figure 4A–F, Supplementary Figure S5A and D).

We searched for other transcription factors differentially expressed in the two regions and identified SOX17 and FOXA2. SOX17 and FOXA2 are both expressed in the uterine glandular epithelium but not in the uterine luminal epithelium [18, 19]. In contrast to their co-expression pattern in the uterine gland, their expression patterns in the oviduct were different. The expression of SOX17 in the oviduct was similar to PAX8 (Figure 4G–L, Supplementary Figure S5B and E). SOX17 was expressed in most PAX8+ve SCs of the INF and AMP (81.6 ± 15.12 and 72.2 ± 15.26% of PAX8+ve SCs, respectively, mean ± SD). Some double negative SCs (PAX8−ve; SOX17−ve) were also present (9.44 ± 3.16% in INF and 11.3 ± 4.76% in AMP) in the distal oviduct. On the other hand, SOX17 was expressed in both MCCs and SCs of the proximal regions (Figure 4H–L, Supplementary Figure S5B and E). Interestingly, FOXA2 was predominantly expressed in MCCs of the INF and AMP, but absent in the ISM–UTJ epithelium (Figure 4M–R, Supplementary Figure S5C and F).

We wondered whether these distal/proximal regionalities were evolutionarily conserved in other mammalian species, particularly in primates. The marmoset (Callithrix jacchus) is a nonhuman primate that has recently acquired a lot of attention because of its potential to be used as a genetic model for human diseases [20]. The adult marmoset female reproductive tract is anatomically similar to that of the human— uncoiled, bowed FTs extending from a single fused uterus [21]. At the distal end, finger-like projections called fimbriae, encompass the ovary (Supplementary Figure S6A and B, N = 3 marmosets). As expected, the proportion of MCCs was higher in the distal fimbriae and AMP (23.1 ± 5.99%) relative to the proximal ISM (6.67 ± 3.39%) (Figure 4S–V), whereas no MCCs were observed in the FT–uterus junction (0 ± 0%) (Figure 4W). In the mucosal epithelium of the fimbriae and AMP, PAX8 and SOX17 were expressed in SCs but not in MCCs (Figure 4X–Z, c–e), whereas in the ISM, both PAX8 and SOX17 were expressed in SCs and MCCs, similar to mice (Figure 4a and f). All epithelial cells in the FT–uterus junction expressed PAX8 and SOX17 (Figure 4b and g). These results indicate that distinct epithelial populations in the distal/proximal regions of the FT epithelium were evolutionarily conserved between mice and primates.

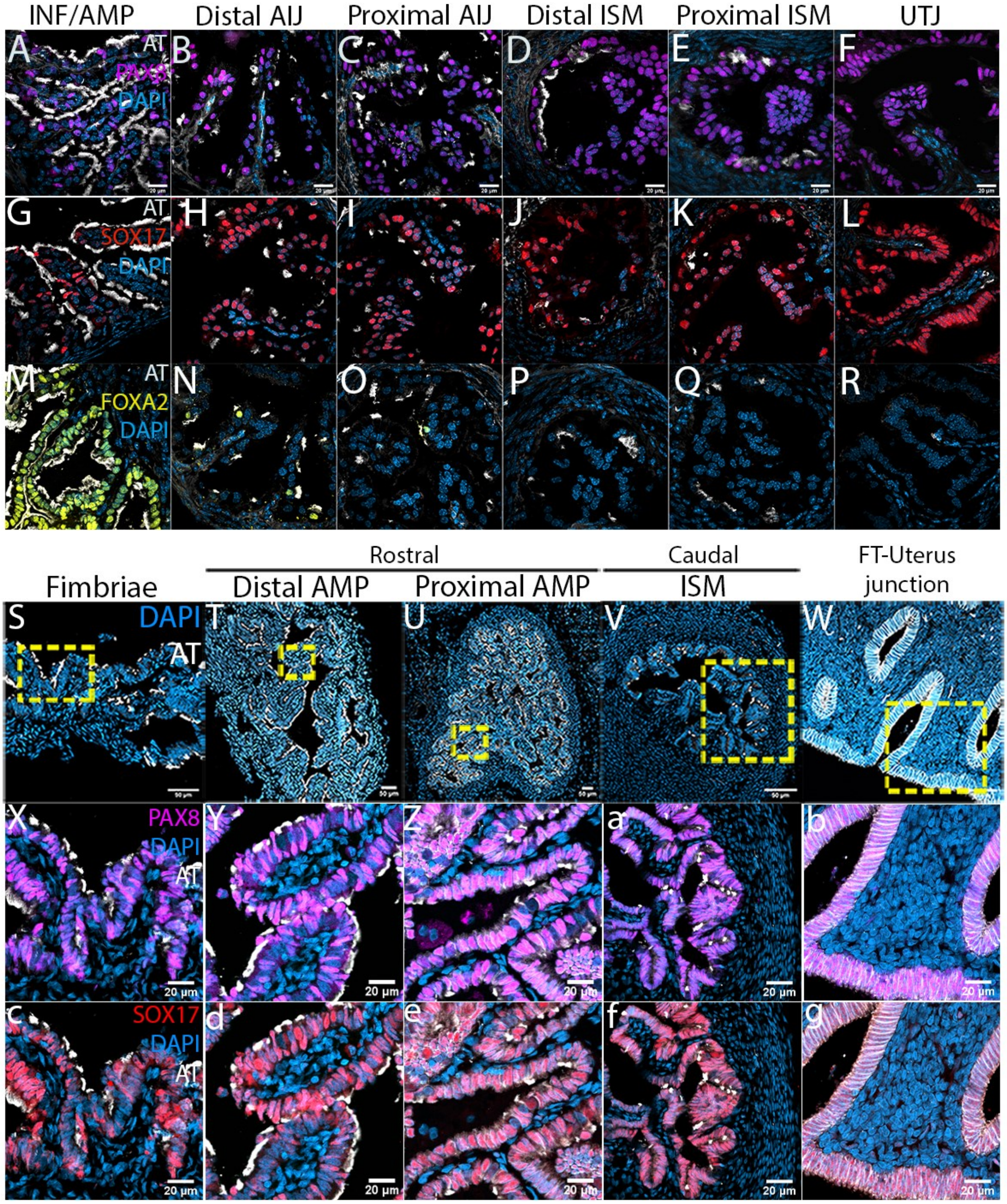

Figure 4: Distinct expression patterns of transcription factors in distal and proximal luminal epithelium in mice and marmosets.

Expression patterns of PAX8 (A–F), SOX17 (G–L), and FOXA2 (M–R) in the mouse oviduct. (A, G, M) INF/AMP. (B, H, N) Distal AIJ. (C, I, O) Proximal AIJ. (D, J, P) Distal ISM. (E, K,

Q) Proximal ISM. (F, L, R) UTJ. (A, G) PAX8 and SOX17 were expressed in nonciliated SCs in the INF and AMP. (B–F, H–L) PAX8 and SOX17 were expressed in all epithelial cells, both MCCs and nonciliated SCs. (M) FOXA2 was expressed in MCCs in the INF and AMP. (N–O) A very few MCCs in the AIJ expressed FOXA2. (P–R) No FOXA2-expressing cells in the ISM and UTJ; N = 8 oviducts. (S–W) Luminal morphology and MCC distribution in the marmoset fallopian tube. (S–U) The fimbriae and AMP showed complex luminal epithelial folds. (U) Dispersed AT+ve MCCs in the proximal AMP. (V) In the ISM, the lumen size is smaller, with thicker stromal and muscularis layer. Less complex folds. (W) The fallopian tube–uterus junction. The lumen size is larger. Smooth luminal surface lined with epithelium. Gland-like structures were noted, with no MCCs. (X–g) PAX8 and SOX17 expression pattern along the marmoset fallopian tube. (X–Z, c-e) PAX8 and SOX17 were expressed in nonciliated SCs in the INF and AMP. In the proximal AMP, the proportion of AT+ve MCCs were low, but they were PAX8−ve (Z) and SOX17−ve (e). (a, f) In the ISM, all epithelial cells were PAX8+ve (a) and SOX17+ve (f). (b, g) In the tube–uterine junction, all epithelial cells were PAX8+ve (b) and SOX17+ve (g), including gland-like structures. AT: acetylated tubulin; N = 3 marmosets. Scale bar = 20 μm.

2.3.5. A sharp boundary of distal and proximal cell populations between Turns 2 and 3

A sharp reduction in the proportion of MCCs was observed between Turns 2 and 3 (Figure 3A and B). We found that the change in distribution pattern of PAX8+ve cells was complementary to the change in distribution pattern of FLTP-H2B-Venus+ve MCCs (Figure 5A–H). The distal epithelium with high proportion of FLTP-H2B-Venus+ve MCCs showed low proportion of PAX8+ve SCs, whereas the proximal epithelium with low proportion of FLTP-H2B-Venus+ve MCCs showed uniform PAX8+ve cells (both MCCs and SCs) with a straight boundary (Figure 5B–D). In a transverse section, the folds with dispersed PAX8+ve cells showed high proportion of FLTP-H2B-Venus+ve cells, with their expression being mutually exclusive. On the other hand, the folds with uniform PAX8+ve cells showed dispersed FLTP-H2B-Venus+ve cells where they were co-expressed (Figure 5E–H). The distribution pattern of SOX17 was identical to that of PAX8+ve cells (Figure 5I and J). This boundary was always beveled, with the proximal population extending distally on the mesosalpinx side, located on the inner side of Turns 2–3 (Figure 5A, K, and L).

In our parallel study, we demonstrated that PAX2 expression is restricted to the proximal oviduct mucosal epithelial cells [12]. Using BAC paired box 2 gene (Pax2)-green fluorescent protein (GFP) mice [22], the boundary of the proximal Pax2-GFP+ve and distal Pax2-GFP−ve cells was visualized between Turns 2 and 3, coinciding with the other boundaries above (Figure 5M and N). In a transverse section of the boundary, we observed localization of distal Pax2-GFP−ve cells on the anti-mesosalpinx side, and proximal Pax2-GFP+ve cells on the mesosalpinx side (Figure 5O). A couple of folds at this boundary showed Pax2-GFP+ve cells on one side and Pax2-GFP−ve cells on the other side, opposed at the ridge of the same fold. The boundary of the distinct distribution patterns of FOXA2+ve cells (Figure 5P and Q) and SOX17+ve cells (Figure 5R and S) also coincided. Therefore, all boundaries of the distinct distal/proximal expression patterns of PAX8, FOXA2, SOX17, and PAX2 coincided with the distinct distal/proximal distribution pattern of MCCs between Turns 2 and 3. This supports the conclusion of our parallel study that the distal/proximal epithelial cells are separately maintained distinct lineages [12].

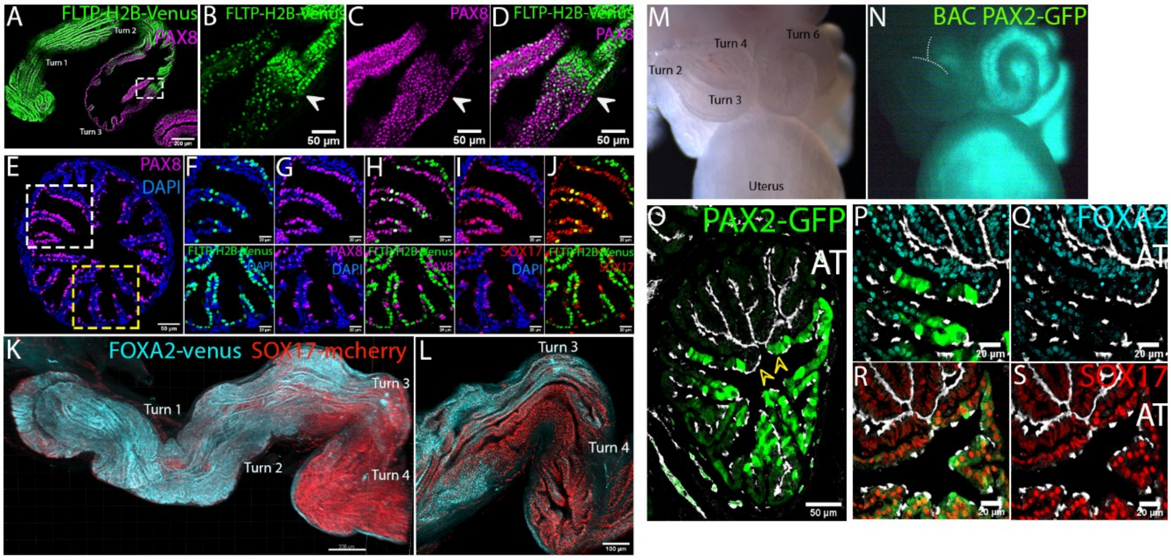

Figure 5: Sharp boundary of distal and proximal epithelial populations in the AIJ.

(A–D) The sudden reduction of FLTP-H2B-Venus+ve cells coincides with the expression of PAX8 in both MCCs and SCs. Scale bar = 200 µm. (B) A boundary of the high proportion of FLTP-H2B-Venus+ve cells in the distal epithelium with the low proportion of FLTP-H2B-Venus+ve cells in the proximal epithelium. (C) A boundary of the distal epithelium where PAX8 was predominantly expressed in SCs with the proximal epithelium comprising MCCs and SCs that both express PAX8. (D) These two boundaries coincide (white arrowheads). Scale bars = 50 µm. (E) A transverse section of the boundary area. The folds with uniform PAX8+ve cells (white dotted box) and the folds with dispersed PAX8+ve cells (yellow dotted box). Scale bar = 50 µm. (F–H) (top panels) The folds with uniform PAX8+ve cells showed dispersed FLTP-H2B-Venus+ve cells. PAX8 and FLTP-H2B-Venus are co-expressed. (Bottom panels)

The folds with dispersed PAX8+ve cells have high proportion of FLTP-H2B-Venus+ve cells. PAX8 and FLTP-H2B-Venus are mutually exclusive. Scale bar = 20 µm. (I, J) SOX17 expression is identical to PAX8. (K) 3D distribution pattern of FOXA2-venus and SOX17-mcherry cells. Their boundary of distinct distal/proximal distribution patterns between Turns 2 and 3. Maximum projection. Scale bar = 200 µm. (L) Single optical section. The proximal epithelium with uniform SOX17+ve cells extended distally on the mesosalpinx side, the inner side of Turn 3, forming a beveled boundary; N = 4 mice. Scale bar = 100 µm. (M, N) Proximally restricted Pax2-GFP expression. GFP expression boundary around Turns 2–3. (O) Transverse section showing the separate distribution of Pax2-GFP+ve and GFP−ve cells. A couple of folds show GFP+ve cells on one side and GFP−ve cells in the other side of the fold (yellow arrowheads). The GFP+ve and GFP−ve epithelia opposed at the ridge of the fold. The GFP+ve epithelium had fewer MCCs. Scale bar = 50 µm. (P, Q) Low proportion of FOXA2+ve cells in the Pax2-GFP+ve epithelium. (R, S) Uniform expression of SOX17 in Pax2-GFP+ve epithelium. AT: acetylated tubulin; N = 4 mice. Scale bar = 20 µm.

2.3.6. Proximally extended WT1 expression generates a distinct population in the distal PAX2+ve cells of the AIJ

WT1 is uniquely expressed in the distal luminal epithelial cells [12] (Figure 6A–F). Interestingly, however, the boundary of WT1+ve and WT1−ve cells was different from the sharp boundary mentioned above between Turns 2 and 3, it was shifted proximally to around Turn 6 (Figure 6G and J). WT1 was not restricted in the Pax2-GFP−ve distal cell population, but was also expressed in the Pax2-GFP+ve cell population of the AIJ (Figure 6B, C, and G–I). The proportion of WT1+ve cells gradually decreased within the AIJ (Figure 6M, Supplementary Figure S7; 89.5 ± 15.12 and 52.5 ± 9.8% in distal and proximal AIJ, respectively). Interestingly, in the proximal AIJ between Turns 5 and 5.5, WT1+ve cells were predominantly nonciliated SCs, lining the short/broken longitudinal folds located on the anti-mesosalpinx side (Figure 3F, 6K and M). On the mesosalpinx side, where ISM-like transverse folds were observed, WT1+ve cells were absent from transverse folds (Figure 6C and K). Similar to the other two boundaries of AMP–AIJ and ISM–UTJ, the AIJ–ISM boundary was also beveled; the proximal WT1−ve isthmic transverse folds extended distally on the mesosalpinx side to the area of WT1+ve short/broken longitudinal folds. No WT1+ve cells were found in the proximal ISM and UTJ (6.97 ± 2.6 and 0 ± 0% in distal to proximal ISM, respectively; Figure 6D–F and M); however, we observed three to four patches of WT1+ve cells beyond the AIJ–ISM boundary in the distal ISM (Figure 6J and L).

Periodic acid–Schiff–Alcian blue (PAS–AB) staining is a common staining method to visualize neutral–acid mucin secretion from mucosal epithelia. When we stained the oviduct with PAS–AB staining, dense AB staining, indicating acid mucus secretion, was observed only in the AIJ epithelium at metestrus/diestrus, whereas no staining was noted in the AMP and ISM (Figure 6N; N = 3 mice). At estrus, no AB staining was observed in the oviduct, whereas some

PAS staining, indicating neutral mucus secretion, was detected in the uterine glands (Supplementary Figure S8).

Taken together, our results indicated that the AIJ is different from the AMP and ISM in mucosal fold morphology (i.e., longitudinal with breakpoints), MCC distribution (i.e., sparse/dispersed), WT1 expression in the PAX2+ve population, and secretion regulation.

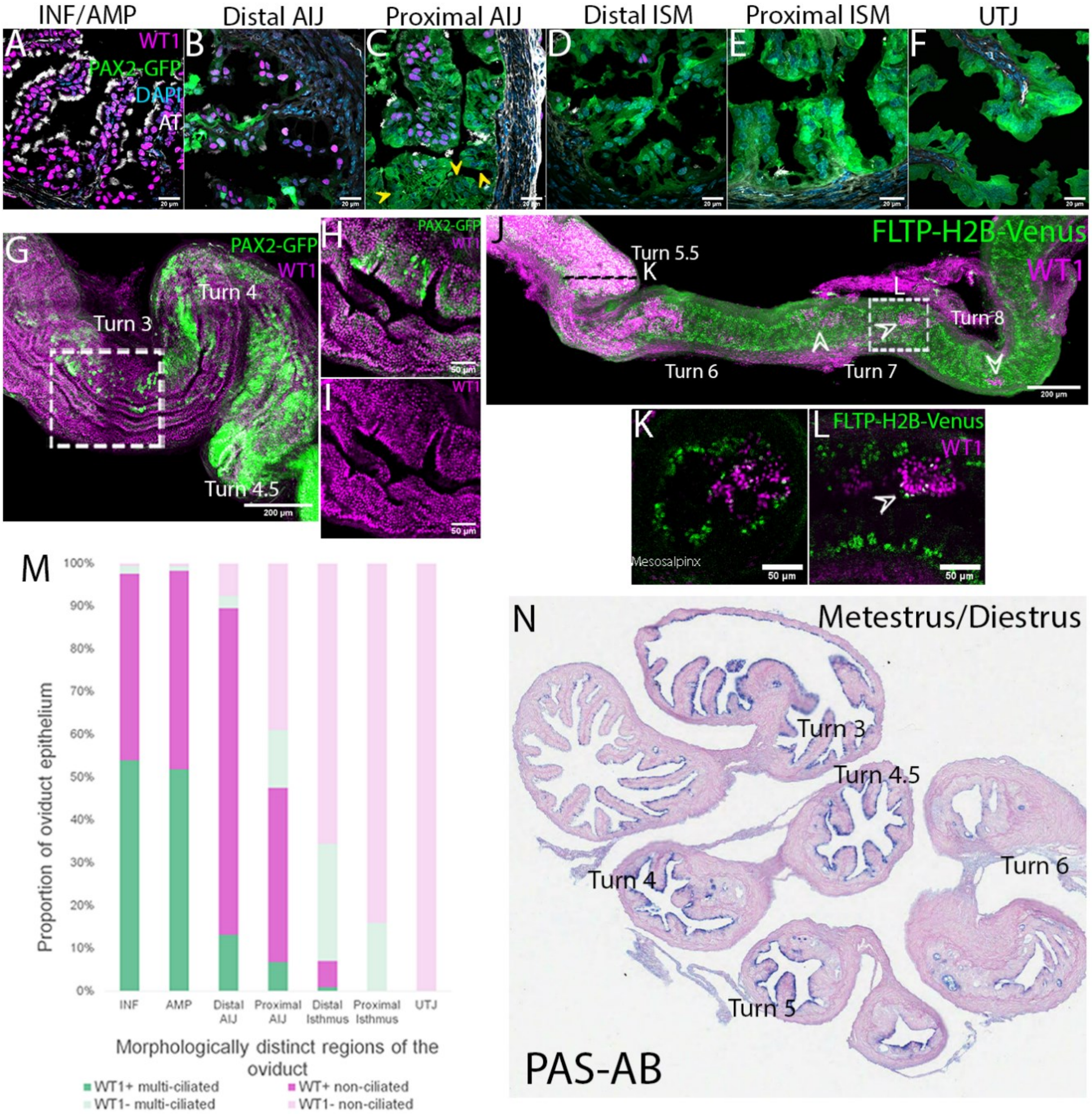

Figure 6: Boundary of WT1 expression extends into the proximal AIJ.

(A–F) Distribution of WT1+ve and Pax2-GFP+ve cells in the oviduct epithelium. (A) INF/AMP. Uniform WT1+ve cells with no Pax2-GFP expression in the epithelium. (B, C) Distal and proximal AIJ. Co-expression of WT1 and Pax2-GFP. Some Pax2-GFP+ve cells are WT1−ve in the proximal AIJ (yellow arrowheads). (D) Distal ISM. (E) Proximal ISM. (F) UTJ. Scale bar = 20 μm. (G) WT1 expression extended into the proximal Pax2-GFP+ve population. Scale bar = 200 μm. (H, I) WT1 and PAX2 were co-expressed, but the level of WT1 was lower in the Pax2-GFP+ve cells; N = 4 oviducts. Scale bar = 50 μm. (J) WT1 expression boundary was located around Turn 6 with a few patches of WT1+ve cells in the distal ISM (white arrows). Scale bar = 200 μm. (K) Orthogonal view marked as the black dotted line in (J). WT1+ve cells were distributed on the folds on the anti-mesosalpinx side. The opposing mesosalpinx side had FLTP-H2B-Venus+ve cells in the trenches of transverse folds. They were not co-expressed. (L) Single optical section of the area indicated by a white dotted box in (J). Patches of coherent WT1+ve cells on the folds. WT1+ve cells were FLTP-H2B-Venus−ve. Scale bar = 50 μm. (M) Proportions of WT1+ve cells along the oviduct epithelium. Quantification was performed on transverse sections like A–F. (N) PAS–AB staining of the mouse oviduct during metestrus/diestrus. Dark Alcian blue staining was noted in only the AIJ epithelium. AT: acetylated tubulin.

2.3.7. Oocytes and preimplantation embryos travel along the oviduct during fertilization and preimplantation development

It is known that fertilization takes place in the AMP [17, 23]. However, it is still unknown how the oocyte and sperm entering from the opposite ends of the oviduct can meet consistently at the AMP. Following ovulation, the AMP was swollen and filled with a clear serous fluid (Figure 7A and B). The oocyte–cumulus complexes were located around Turn 2, within the AMP (Figure 7B and C), encompassing the boundary of the two distal and proximal epithelial populations, as visualized by the sudden decrease in MCC proportion (Figure 7D). Interestingly, the swollen AMP maintained its shape even after the oviduct was detached from the uterus and the ovary, suggesting that both ends of the AMP were closed with no fluid leakage (Figure 7B). We found that both ends of the swollen AMP appeared physically constricted to close the lumen (Figure 7E). Indeed, when we injected trypan blue solution into the swollen AMP using a micropipette, the solution easily diffused into the AMP lumen, but entered neither the AIJ nor the ovarian bursa (Figure 7F and G; N = 3 mice). In contrast, when we tried to inject into the ISM of an estrus stage oviduct, a very small amount of the dye solution could be injected, the solution did not distribute in either direction within the ISM luminal space (Figure 7F and H, Supplementary Figure S9A and B). This suggests that the proximal region of the oviduct was sealed, possibly due to physical constriction, blocking any fluid flow and oocyte movement into the ISM.

Although the oviduct is known to be the place where preimplantation development occurs [1, 2], it is unknown whether the embryos are free floating in the oviduct lumen or they are located in a specific region of the oviduct. By 0.75 dpc, zygotes moved into the AIJ (Figure 7I and J). At 1.5 dpc, two-cell stage embryos were found in the ISM (Figure 7K and L), appearing floating in the lumen (Supplementary Figure S9C and D) with occasional ISM contractions. Interestingly, at 2.5 dpc, we found morula embryos in the UTJ (Figure 7M–O). The embryos formed a queue within the compartments found at the oviduct–uterus junction (Figure 2N and O).

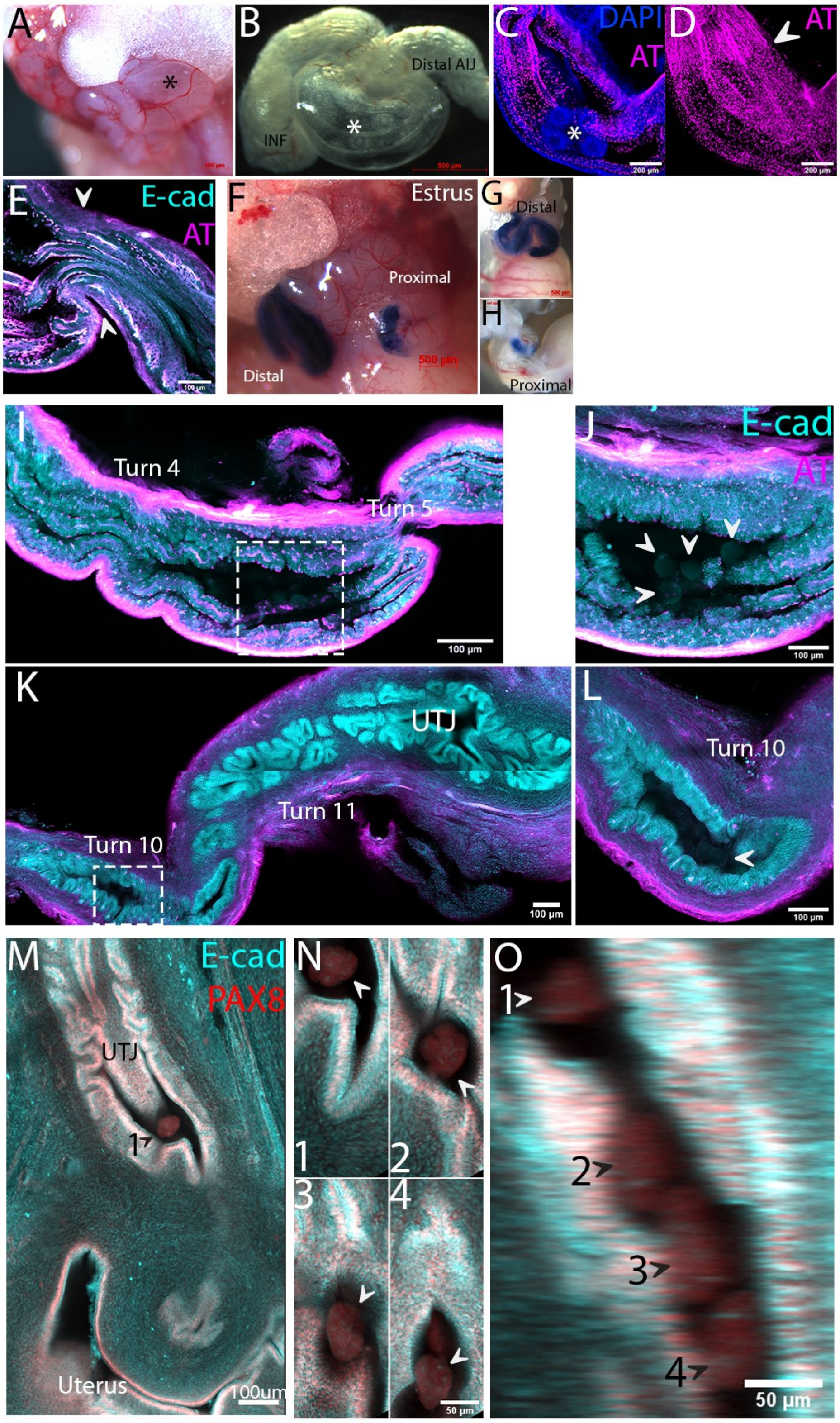

Figure 7: Preimplantation embryo travel in oviduct luminal space.

(A) Prominent swollen AMP after ovulation (black asterisk). (B) A swollen AMP after dissection. Several oocyte–cumulus complexes are visible (white asterisk). Scale bar = 500 µm. (C) A swollen AMP containing 0.5 dpc embryos (white asterisk). Single optical section. (D) Maximum projection of AT staining of (C). The boundary of the distal/proximal populations (white arrow). Scale bar = 200 µm. (E) Single optical section showing the AIJ side of a swollen AMP. The lumen was closed by lumen constriction (white arrows). Scale bar = 100 µm. (F–H) Injection of trypan blue solution. (G) In the AMP and INF, trypan blue solution spread evenly, but did not into the AIJ or the ovarian bursa. (H) In the ISM, only a small amount of trypan blue solution could be injected. The blue dye did not spread but stayed at the injection site. (I) 0.75 dpc one-cell stage embryos in the AIJ around Turn 5. Characteristic broken longitudinal folds are observed, with sparsely distributed MCCs. Four zygotes are in the area marked with a dotted box. (J) Higher magnification of the area marked in (I). Floating zygotes (white arrowheads). This suggests that the AIJ was no longer sealed in this area by this time point. (K) 1.5 dpc. A two-cell stage embryo in the proximal ISM around Turn 10. A two-cell embryo is in the area marked in a dotted box. (L) Higher magnification of the area marked in (K). A two-cell embryo (white arrowhead). Scale bar = 100 µm. (M–O) 2.5 dpc. (M) Compartments were located at the junction of the oviduct and uterus. The first embryo and uterine lumen are shown (black arrow, numbered 1). Scale bar = 100 µm. (N) Four embryos (white arrows) located at different z-positions along the UTJ. (P) YZ orthogonal view. Four morula embryos formed a queue (white/black arrows, numbered 1–4). AT: acetylated tubulin; E-cad: E-cadherin; N = 3 mice. Scale bar = 50 µm.

2.4. Discussion

The oviduct is an essential organ for reproduction in mammals; however, its anatomical complexity and cellular heterogeneity have not been fully appreciated. Using modern imaging techniques and mouse fluorescence reporter lines, we made four major findings as follows (Figure 8): (1) AIJ is a distinct region from AMP and ISM. Thus, the oviduct consists of five regions: INF, AMP, AIJ, ISM, and UTJ; (2) INF/AMP, AIJ, and ISM have a unique pair of SCs and MCCs; (3) MCC clusters in the ISM form unique pits/groove structures at the trenches of transverse mucosal folds; and (4) E2.5 morula embryos are located in small compartments within the UTJ. In addition, we showed that consistent turning points in the mouse oviduct were associated with distinct luminal morphologies and epithelial populations. Many previous studies incorrectly compare different regions of the oviduct in traditional 2D sections due to lack of landmarks for the coiled oviduct. Our study described these turning points as reliable landmarks for precise description and comparison.

In the distal region, the primary role of MCCs is to support movement of the cumulus oocyte complex [24]. On the other hand, the role of MCCs in the ISM is unknown. Since multicilia of clustered MCCs in the ISM project to the inside of pit/groove structures at the trenches of transverse mucosal folds, it is not clear if they can create a fluid flow in the luminal space to support preimplantation embryo movement. Interestingly, the stripe pattern of multicilia in the ISM is reminiscent of the immobilized sperm localization pattern [14, 16]. Furthermore, scanning electron microscopic studies of bull sperm indicate attachment of uncapacitated sperm to MCCs of the oviduct [25]. Studies in various species including mice allude to the presence of sperm attachment sites in the ISM, usually called sperm reservoirs [17, 26–30]. In addition, the gene expression pattern of ISM MCCs is different from that of INF/AMP MCCs [12], suggesting functional differences of MCCs in each region. The MCC clusters we identified in the ISM could function as sperm reservoirs, playing important roles in sperm viability, hyperactivation, and capacitation [26, 30].

Classic transmission electron microscopic studies in various mammalian species suggest that the distal and proximal oviduct epithelial cells have distinct secretary functions [31–35]. High to moderate electron-dense secretory granules in the INF and AMP suggest proteinaceous, serous secretion. Predominantly low electron-dense secretory granules suggest mucus-containing secretory granules in the ISM [31, 32, 35]. Our results were consistent with these classic observations. In the distal region, a clear serous fluid was observed in the swollen, estrus stage AMP. Interestingly, acid mucus secretion was observed in the AIJ predominantly at metestrus. It is recognized that various secretion molecules like anti-bacterial and fungal peptides are also secreted from the oviductal mucosal epithelial cells [4–6, 36]. How these secretions are regulated during the estrous cycle will be very important to understand gynecological diseases and infertility.

We identified that a sharp boundary of the distal PAX2−ve and proximal PAX2+ve populations was located between Turns 2 and 3. Interestingly, the boundary of WT1 expression did not coincide with this boundary, but was shifted proximally. This created a unique cell population of the AIJ that expressed WT1 in the proximal PAX2+ve population (Figure 8A). The unique AIJ mucosal fold morphology is briefly reported [4, 9, 37]. In addition to WT1/PAX2 expression, we found three other unique characteristics of the AIJ different from the AMP and ISM. First, multiple breakpoints and convolutions of AIJ longitudinal folds, in contrast to continuous longitudinal folds in the AMP and transverse folds in the ISM. Second, sparse distribution of PAX8+ve MCCs on the AIJ folds, in contrast to the uniform distribution of PAX8−ve MCCs on the AMP folds and the MCC pits/grooves in the ISM. Third, AIJ-specific acid mucin secretion indicated by Alcian blue staining at metestrus/diestrus, in contrast to no staining in the AMP and ISM. Taken together, we propose that the AIJ is a unique region different from the AMP and ISM, with distinct functions and unique gene expression.

Mouse preimplantation embryos stay in the oviduct for 3 days before implanting into the uterine lining [1, 2]; however, the location of embryos was unknown. We found that by E2.5 around the eight-cell stage, the embryos moved into previously unrecognized compartments of the UTJ, where the oviduct inserts into the uterus. In contrast to earlier stages where the embryos appeared to be floating in the ISM, E2.5 embryos formed a queue in the UTJ. It will be very interesting to determine what controls the timing of embryo entry into the uterus.

The intimate relationship between the oviduct epithelial cells and gametes/preimplantation embryos is essential for successful pregnancy. Our work provides a foundation to understand the oviduct luminal environment and homeostasis in reproduction.

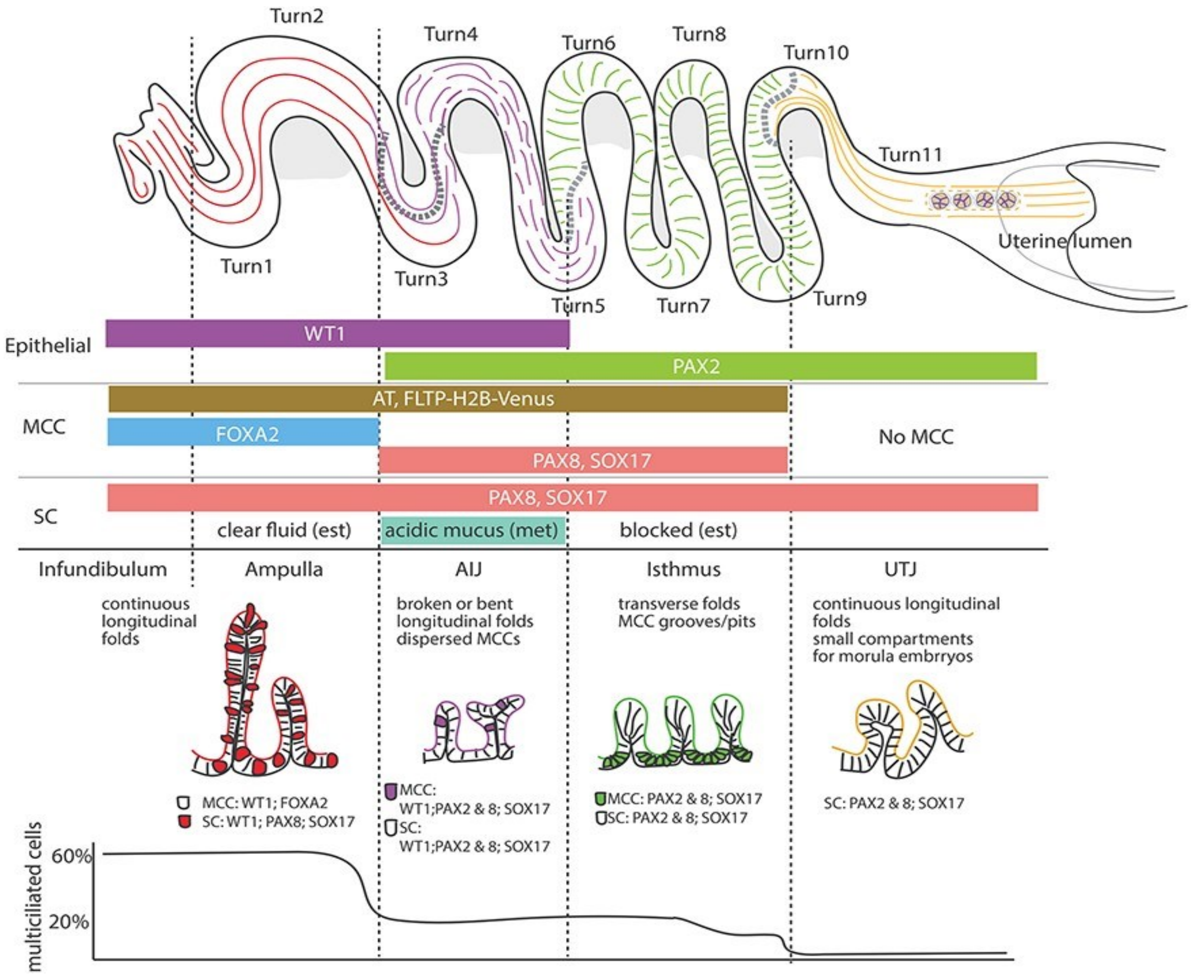

Figure 8: Model of anatomical and cellular heterogeneity of the oviductal luminal epithelium.

Anatomical and cellular heterogeneity of the oviductal luminal epithelium. Turning points are linked with luminal morphological transitions. Five distinct regionalities, INF, AMP, AIJ, ISM, and UTJ, can be defined by luminal epithelial fold morphology, MCC distribution pattern, transcriptional factor expression pattern, and secretion. The INF/AMP, AIJ, and UTJ mucosal fold representations are that of transverse sections; however, the ISM mucosal fold representation is that of a longitudinal section. The distribution of MCCs did not form a gradient, but had three distinct proportions: high (INF/AMP), low (AIJ/ISM), and none (UTJ). Small compartments for morula embryos in the UTJ are also shown.

2.5. Methods and materials

2.5.1. Animals

All animal work was performed in accordance with institutional guidelines and was approved by the Faculty of Medicine Animal Care Committee (AUP #7843); it was undertaken at the Goodman Cancer Research Centre animal facility. *Pax2-GFP Bac* [22] mice were kindly provided by Dr. Maxime Bouchard (McGill). *Fltp-H2B-Venus* [15], *FoxA2-venus* [38], *Sox17-mCherry* mice [39] mice were generated by Dr. Heiko Lickert and Dr. Ingo Burtscher (IDR Munich, Germany). *E-cadherin-mCFP* mice (monomeric cyan fluorescent protein fused to endogenous cadherin 1 protein ; B6.129P2(Cg)-$Cdh1^{tm1Cle}$/J) were obtained from JAX. Adult mice used in this study were 2–4 months of age; oviducts were collected at random estrous stages. Where required, estrous stages were analyzed using vaginal smears stained with crystal violet [40]. Necropsy specimens of adult female marmoset reproductive tracts were kindly provided by Dr. Jim Gourdon (CMARC, McGill) and Dr. Keith Murai (McGill).

2.5.2. Whole-mount immunostaining, tissue clearing, and 3D confocal imaging

After euthanasia, mouse female reproductive tracts were collected and straightened by removing the mesosalpinx. The straightened oviduct was fixed with DMSO (Dimethyl sulfoxide, Sigma Aldrich D8418): methanol in the ratio 1:4 and cut into three to four pieces prior to placing at −20°C overnight. The antibody staining protocol was as described in [41]. Blocking was done overnight in solution containing 1% Triton X-100 (Sigma-Aldrich, T8787), 2% powdered milk, and 1× phosphate-buffered saline (PBS, BioShop Canada Inc., PBS405), henceforth referred to as PBSMT. Primary and secondary antibody staining was performed in PBSMT for 5 and 2 days, respectively, at 4° on a shaker. After six 30 min long PBSMT washes, the oviduct pieces were transferred successively to methanol:PBT (1:1, PBT: 1× PBS and 1% Triton X-100), 100% methanol (BioShop Canada Inc., MET302.1), 3% H2O2 (BioShop

Canada Inc., HYP001.1), and 100% methanol prior to benzyl alcohol/benzyl benzoate (BABB) clearing. BABB-cleared samples were placed on a #1.5 coverslip (Fisher Scientific, 12-545F) with 10–15 µl BABB prior to imaging using the 10× objective (numerical aperture 0.30) on LSM 800 or 710 (Zeiss). Section interval for 3D confocal imaging was 4.32 µm. Usually, 40–110 optical sections were taken.

The fixation and clearing methods used for 3D confocal imaging are known to cause dehydration and tissue shrinkage [42]; thus, we confirmed our findings using 4% paraformaldehyde-fixed open-book preparations, 80% TDE-cleared (2,2'-Thiodiethanol, Sigma-Aldrich, 88559) oviducts, and 2D cryo/paraffin sections. When possible, we imaged live oviducts and open-book preparations dissected from various transgenic mice.

2.5.3. Antibodies

Primary antibodies (1/250 dilution): anti-PAX8 (Proteintech, 10336-1-AP), anti-GFP (Abcam, ab13970), anti-mCherry (Abcam, ab213511), anti-WT1 (Abcam, ab89901), anti-acetylated tubulin (labeled as AT, Sigma, T7451), anti-Sox17 (R&D, AF1924), anti-FoxA2 (Cell Signaling, 3143), and anti-E-cadherin (Invitrogen, 13-1900). Secondary antibodies (1/450 dilution): Alexa Fluor (AF) anti-rabbit 555 (Invitrogen, A31572), AF anti-rabbit 649 (Invitrogen, A21245), AF anti-rabbit 488 (Invitrogen, A21206), AF anti-mouse 649 (Invitrogen, A32787), AF anti-mouse 488 (Invitrogen, A21202), AF anti-goat 568 (Invitrogen, A11057), AF anti-rat 488 (Invitrogen, A21208), anti-chicken 488 (Sigma, SAB4600031), DAPI (4, 6-diamidino-2-phenylindole, Thermo Fisher, 62248)/Hoescht 33342 (Thermo Fisher, 62249), AF 488 phalloidin (Lifetech, A12379), and AF 635 phalloidin (Lifetech, A34054).

2.5.4. *Trypan blue injection into the mouse oviduct*

Estrus stage and pseudo-pregnant females were anesthetized. The female reproductive tract was exposed either dorsally or ventrally. Under a dissection microscope, filtered trypan blue solution (STEMCELL Technologies, #07050) was injected into the swollen AMP or the ISM using a glass needle. Mice were euthanized; the reproductive tracts were dissected out and straightened slightly.

2.5.5. *Image analysis, cell counts, and statistics*

3D confocal images were stitched using ImarisStitcher and visualized using FIJI and Imaris. 3D rendering was performed using surfaces function and distance transformation (outside a surface object) MATLAB XTension, followed by manual background removal on Imaris. For optical projections, Maximum/Average/Sum Slices projection in FIJI was used. In some images of Figure 2, PAX8 immunostaining and FLTP-H2B-Venus were overlaid with a single color (cyan) to visualize the epithelial layer in the oviduct, indicated as Epithelium.

2D sections were visualized using FIJI and Zen. Measurements and epithelial cell counting for straightened mouse oviducts were performed manually on FIJI using only transverse 2D sections. Unpaired, two-tailed t-test was performed to gauge significance only between successive distal and proximal regions (INF versus AMP, AMP versus distal AIJ, distal AIJ versus proximal AIJ, proximal AIJ versus distal ISM, distal ISM versus proximal ISM, and proximal ISM versus UTJ). For marmoset FT 2D sections, cell counting was performed manually on either transverse or longitudinal sections, with AT and DAPI staining.

2.6. Acknowledgements

The authors thank the Rosalind and Morris Goodman Cancer Research Centre Histology, the McGill Advanced Bioimaging Facility, and the McGill Integrated Core of Animal

Modeling for technical support. The authors thank Dr. Maxime Bouchard for the Pax2-GFP mouse line. The authors also thank Drs. Keith Murai and Jim Gourdon for marmoset necropsy specimens.

2.7. References

[1] Kölle S, Hughes B, Steele H. Early embryo-maternal communication in the oviduct: A review. Mol Reprod Dev 2020; 87:650–662.

[2] Moore EL, Wang S, Larina IV. Staging mouse preimplantation development *in vivo* using optical coherence microscopy. J Biophotonics 2019; 12:167–182.

[3] Prasad SV, Skinner SM, Carino C, Wang N, Cartwright J, Dunbar BS, Williams Z. Structure and function of the proteins of the mammalian zona pellucida. Cells Tissues Organs 1999; 285:251–258.

[4] Barton BE, Herrera GG, Anamthathmakula P, Rock JK, Willie AM, Harris EA, Takemaru K, Winuthayanon W. Roles of steroid hormones in oviductal function. Reproduction 2020; 159:R125–R137.

[5] Li S, Winuthayanon W. Oviduct: Roles in fertilization and early embryo development. J Endocrinol 2017; 232:R1–R26.

[6] Winuthayanon W, Bernhardt ML, Padilla-Banks E, Myers PH, Edin ML, Lih FB, Hewitt SC, Korach KS, Williams CJ. Oviductal estrogen receptor α signaling prevents protease-mediated embryo death. Elife 2015; 4:1–28.

[7] Marion LL, Meeks GR. Ectopic pregnancy: History, incidence, epidemiology, and risk factors. Clin Obstet Gynecol 2012; 55:376–386.

[8] Briceag I, Costache A, Purcarea VL, Cergan R, Dumitru M, Briceag I, Sajin M, Ispas AT. Fallopian tubes--literature review of anatomy and etiology in female infertility. J Med Life 2015; 8:129–131.

[9] Agduhr E. Studies on the structure and development of the bursa ovarica and the tuba uterina in the mouse. Acta Zool 1927; 8:1–133.

[10] Dirksen ER, Satir P. Ciliary activity in the mouse oviduct. Tissue Cell 1972; 4:389–403.

[11] Stewart CA, Behringer RR. Mouse oviduct development. In: Kubiak J. (eds) Mouse Development. Results and Problems in Cell Differentiation. Berlin, Heidelberg: Springer, 2012; 55:247–262.

[12] Ford MJ, Harwalkar K, Pacis AS, Maunsell H, Wang YC, Badescu D, Teng K, Yamanaka N, Bouchard M, Yamanaka Y. Oviduct epithelial cells constitute two developmentally distinct lineages that are spatially separated along the distal-proximal axis. bioRxiv Preprint 2020.

[13] Dixon RE, Hwang SJ, Hennig GW, Ramsey KH, Schripsema JH, Sanders KM, Ward SM. Chlamydia infection causes loss of pacemaker cells and inhibits oocyte transport in the mouse oviduct 1. Biol Reprod 2009; 80:665–673.

[14] Muro Y, Hasuwa H, Isotani A, Miyata H, Yamagata K, Ikawa M, Yanagimachi R, Okabe M. Behavior of mouse spermatozoa in the female reproductive tract from soon after mating to the beginning of fertilization. Biol Reprod 2016; 94:1–7.

[15] Gegg M, Bottcher A, Burtscher I, Hasenoeder S, Campenhout CV, Aichler M, Walch A, Grant SGN, Lickert H. Flattop regulates basal body docking and positioning in mono- and multiciliated cells. Elife 2014; 3:1–24.

[16] La Spina FA, Molina LCP, Romarowski A, Vitale AM, Falzone TL, Krapf D, Hirohashi N, Buffone MG. Mouse sperm begin to undergo acrosomal exocytosis in the upper isthmus of the oviduct. Dev Biol 2016; 411:172–182.

[17] Suarez SS. Sperm Transport and Motility in the Mouse Oviduct: Observations in situ. Biol Reprod 1987; 36:203–210.

[18] Hirate Y, Suzuki H, Kawasumi M, Takase HM, Igarashi H, Kanai Y, Kanai-Azuma M. Mouse Sox 17 haploinsufficiency leads to female subfertility due to impaired implantation. Sci Rep 2016; 6:2–10.

[19] Spencer TE, Pru CA, Kelleher AM, DeMayo FJ, Peng W, Pru JK. Forkhead box a2 (FOXA2) is essential for uterine function and fertility. Proc Natl Acad Sci 2017; 114:E1018–E1026.

[20] Okano H, Hikishima K, Iriki A, Sasaki E. The common marmoset as a novel animal model system for biomedical and neuroscience research applications. Semin Fetal Neonatal Med 2012; 17:336–340.

[21] Cui KH, Matthews CD. Anatomy of adult female common marmoset (Callithrix jacchus) reproductive system. J Anat 1994; 185:481–486.

[22] Pfeffer PL, Payer B, Reim G, di Magliano MP, Busslinger M. The activation and maintenance of Pax2 expression at the mid-hindbrain boundary is controlled by separate enhancers. Development 2002; 129:307–318.

[23] Avilés M, Coy P, Rizos D. The oviduct: A key organ for the success of early reproductive events. Anim Front 2015; 5:25–31.

[24] Talbot P, Geiske C, Knoll M. Oocyte pickup by the mammalian oviduct. Mol Biol Cell 1999; 10:5–8.

[25] Lefebvre R, Chenoweth PJ, Drost M, LeClear CT, Mac Cubbin M, Dutton JT, Suarez SS. Characterization of the oviductal sperm reservoir in cattle. Biol Reprod 1995; 53:1066–1074.

[26] Maillo V, Sanchez-Calabuig MJ, Lopera-Vasquez R, Hamdi M, Gutierrez-Adan A, Lonergan P, Rizos D. Oviductal response to gametes and early embryos in mammals. Reproduction 2016; 152:R127–R141.

[27] Sasanami T, Matsuzaki M, Mizushima S, Hiyama G. Sperm storage in the female reproductive tract in birds. J Reprod Dev 2013; 59:334–338.

[28] Suarez SS. Formation of a reservoir of sperm in the oviduct. Reprod Domest Anim 2002; 37:140–143.

[29] Suarez SS. Carbohydrate-mediated formation of the oviductal sperm reservoir in mammals. Cells Tissues Organs 2001; 168:105–112.

[30] Suarez SS. Interactions of gametes with the female reproductive tract. Cell Tissue Res 2016; 363:185–194.

[31] Abe H. The mammalian oviductal epithelium: Regional variations in cytological and functional aspects of the oviductal secretory cells. Histol Histopathol 1996; 11:743–768.

[32] Abe H, Oikawa T. Regional differences in the ultrastructural features of secretory cells in the golden hamster (Mesocricetus auratus) oviductal epithelium. J Anat 1991; 175:147–158.

[33] Lauschová I. Influence of estrogen and progesterone on ultrastructural indices of oviductal epithelium in sexually immature mice. Acta Vet 1999; 68:13–21.

[34] Lauschová I. Secretory cells and morphological manifestation of secretion in the mouse oviduct. Scripta Medica 2003; 76:203–214.

[35] Murray MK. Morphological features of epithelial cells in the sheep isthmus oviduct during early pregnancy. Anat Rec 1997; 247:368–378.

[36] Ghersevich S, Massa E, Zumoffen C. Oviductal secretion and gamete interaction. Reproduction 2015; 149:R1–R14.

[37] Burton JC, Wang S, Stewart CA, Behringer RR, Larina IV. High-resolution three-dimensional *in vivo* imaging of mouse oviduct using optical coherence tomography. Biomed Opt Express 2015; 6:2713.

[38] Burtscher I, Barkey W, Lickert H. Foxa 2-venus fusion reporter mouse line allows live-cell analysis of endoderm-derived organ formation. Genesis 2013; 51:596–604.

[39] Burtscher I, Barkey W, Schwarzfischer M, Theis FJ, Lickert H. The Sox17-mCherry fusion mouse line allows visualization of endoderm and vascular endothelial development. Genesis 2012; 50:496–505.

[40] McLean AC, Valenzuela N, Fai S, Bennett SAL. Performing vaginal lavage, crystal violet staining, and vaginal cytological evaluation for mouse estrous cycle staging identification. J Vis Exp 2012; 67:4–9.

[41] Arora R, Fries A, Oelerich K, Marchuk K, Sabeur K, Giudice LC, Laird DJ. Insights from imaging the implanting embryo and the uterine environment in three dimensions. Development 2016; 143:4749–4754.

[42] Azaripour A, Lagerweij T, Scharfbillig C, Jadczak AE, Willershausen B, Van Noorden CJF. A survey of clearing techniques for 3D imaging of tissues with special reference to connective tissue. Prog Histochem Cytochem 2016; 51:9–23.

2.8. Supplementary Figures

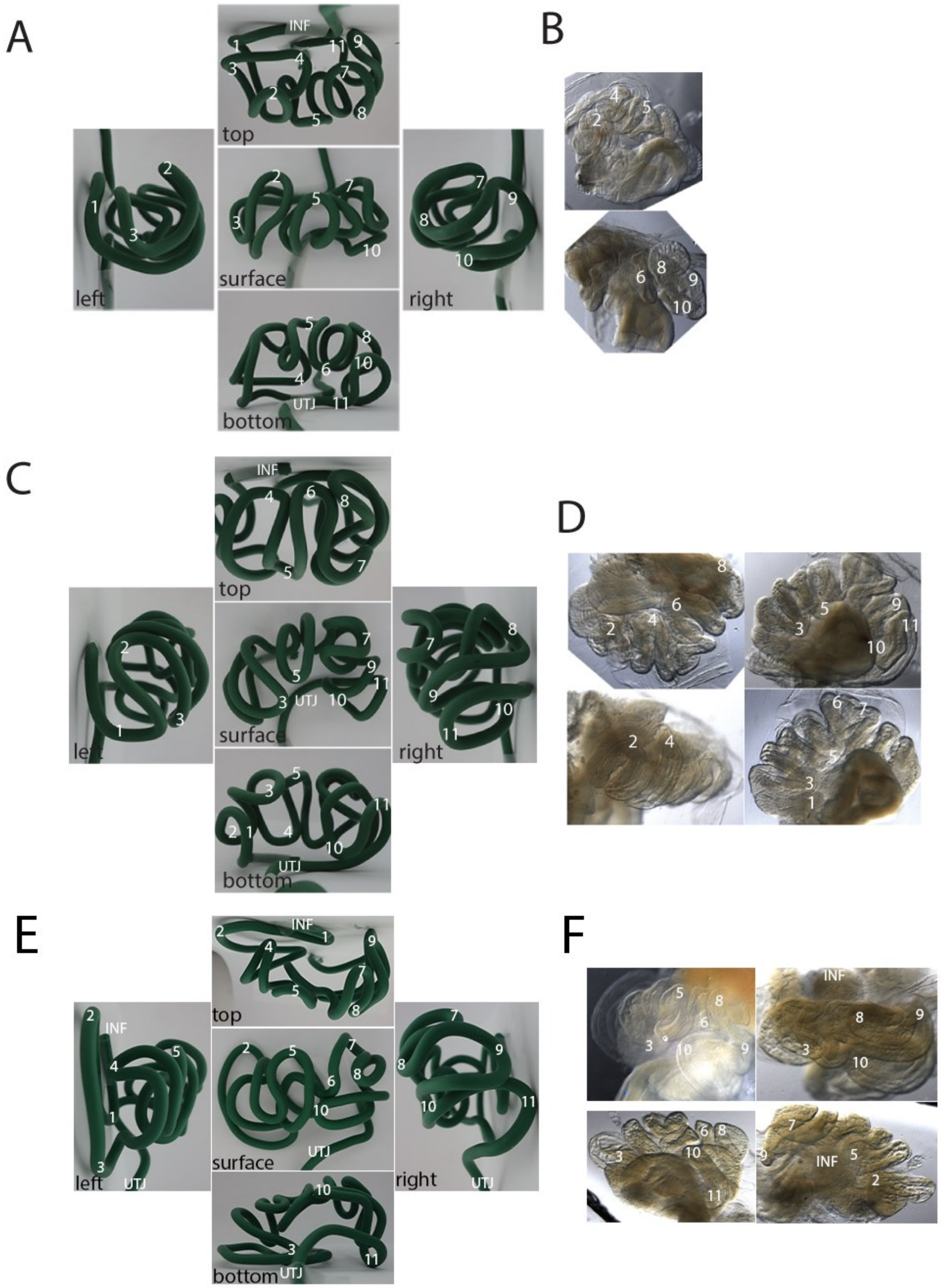

Supplementary Figure S 1:*Wire models of oviduct coiling patterns.*

(A) A wire model of a right oviduct. (B) The TDE cleared oviduct modeled in (A). (C) A wire model of another right oviduct. (D) The TDE cleared oviduct modeled in (C). (E) A wire model of a third right oviduct. (F) The TDE cleared oviduct modeled in (E).

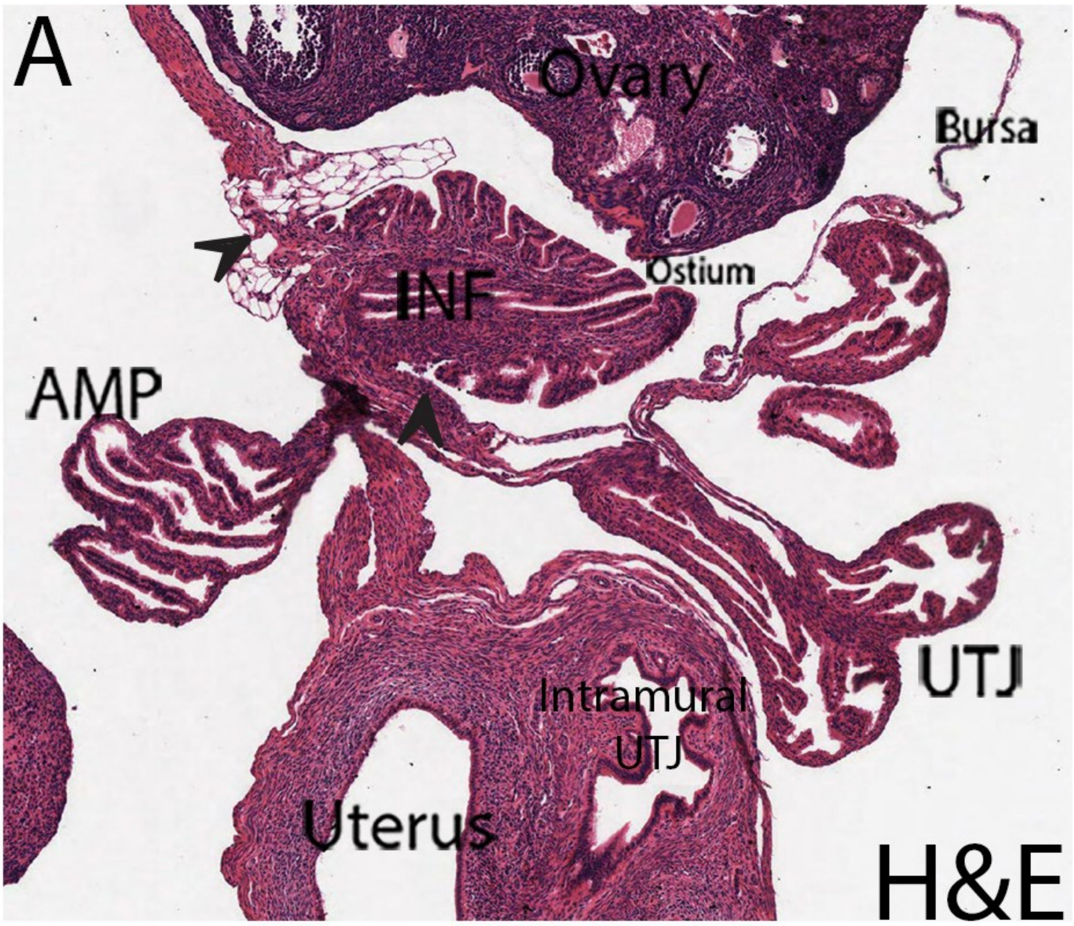

Supplementary Figure S 2: *Relative position of the ovary, INF and uterus in a 2D tissue section.*

H&E staining of a mouse female reproductive tract with the ovary. The INF is located inside of the ovarian bursa adjacent to the ovary. The exterior folds on the ovarian side are taller and complex than the opposite side. The mucosal epithelium of exterior folds was continuous with the epithelium lining the ovarian bursa and ovarian hilum (black arrows).

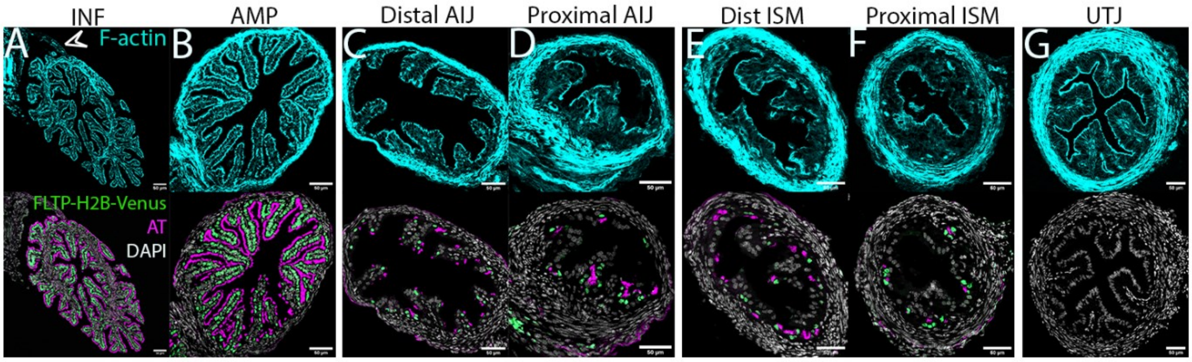

Supplementary Figure S 3: *Transverse sections of distinct luminal fold patterns and multi-ciliated cell distribution***.**

(A-G) Transverse sections of different areas of the oviduct. Top panels are F-actin staining. Bottom panels are FLTP-H2B-Venus and acetylated tubulin (AT) staining, both marking multi-ciliated cells. (A) INF, white arrowhead shows flattened exterior folds continuous with connective ligament. (B) AMP. (C) Distal AIJ. (D) Proximal AIJ. (E) Distal ISM. (F) Proximal ISM. (G) UTJ. The quantification of the proportions of FLTPH2B-GFP+ve cells was performed and presented in Figure 3G. N=4 mice.

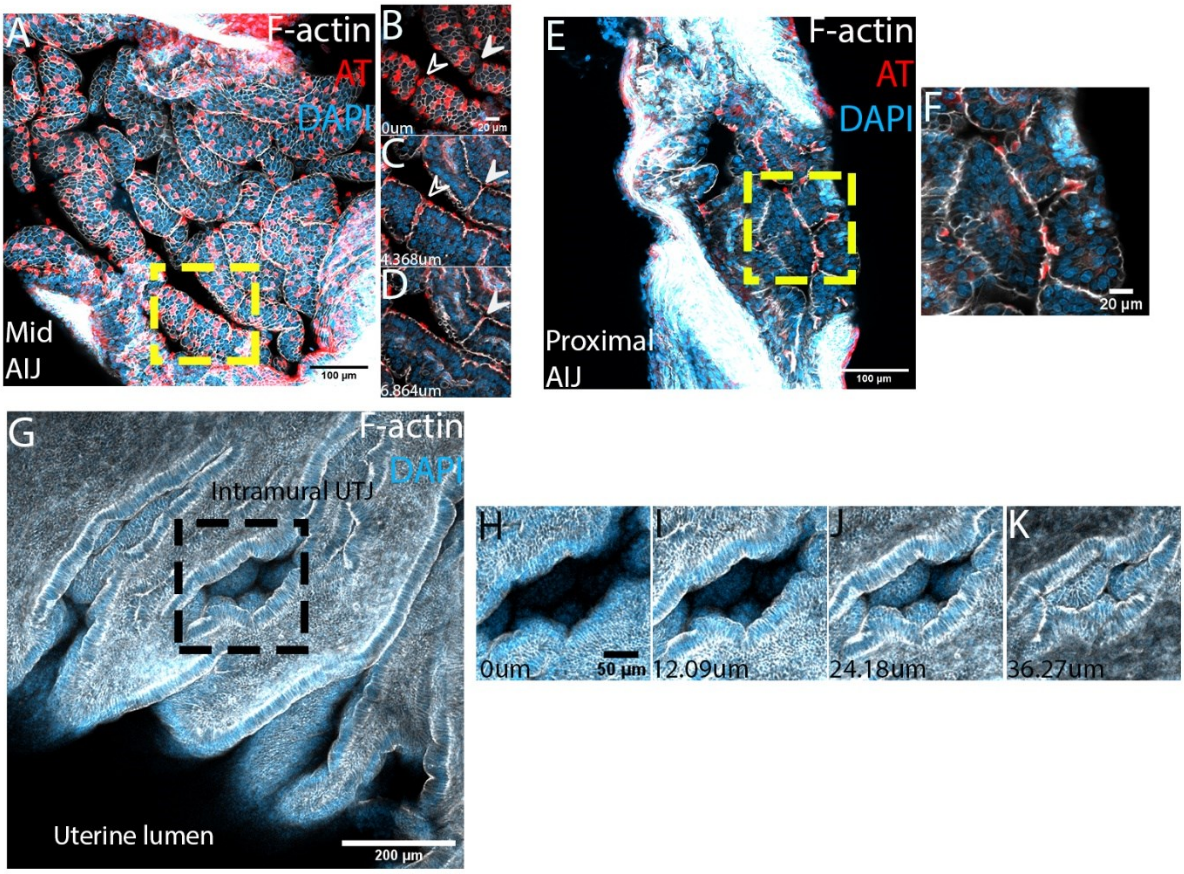

Supplementary Figure S 4: *Comparison of AIJ and UTJ breakpoints using open-book preparations***.**

(A-F) Fixed open-book preparations of the AIJ. (A) Surface view of mid AIJ discontinuous folds, presenting with convolutions and sparse MCC distribution. (B-D) AIJ mucosal folds had slit-like breakpoints (white arrows and arrowheads). Multiple z-stacks of region represented by yellow box in (A). (E, F) Surface view of proximal AIJ discontinuous folds, presenting with frequent breakpoints and MCC distribution in trenches. (F) Z-stack of region represented by yellow box in (E). (G-K) Surface view of a compartment in the intramural UTJ. (H-K) Longitudinal folds of the UTJ had breakpoints that formed compartments in the intramural UTJ. Multiple z-stacks of region represented by black box in (G).

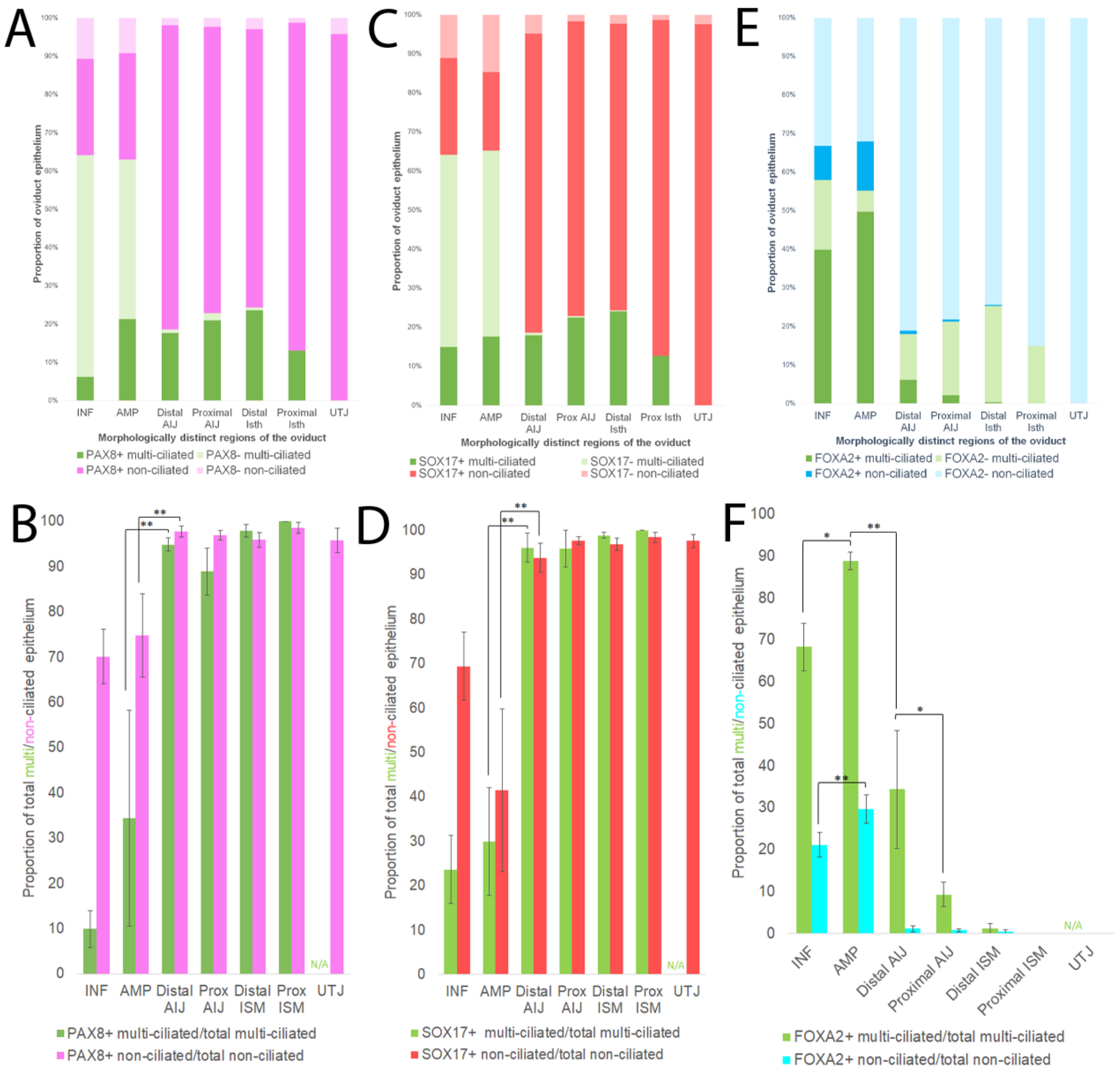

Supplementary Figure S 5: *Changes in proportions of PAX8+ve, SOX17+ve and FOXA2+ve cells in multi-ciliated and non-ciliated secretory cells along the mouse oviduct***.**

(A) Proportion of PAX8+ve cells in MCCs and SCs of total epithelial cells. (B) Proportion of PAX8+ve cells in respective cell types. (C) Proportion of SOX17+ve cells in MCCs and SCs of total epithelial cells. (D) Proportion of SOX17+ve cells in respective cell types. (E) Proportion of FOXA2+ve cells in MCCs and SCs of total epithelial cells. (F) Proportion of FOXA2+ve cells in respective cell types. N=8 oviducts. Oviducts were collected at random estrous stages and quantification was performed on transverse tissue sections like Fig.4. ***<0.001, **<0.01, *<0.05. Error bars indicate standard deviation.

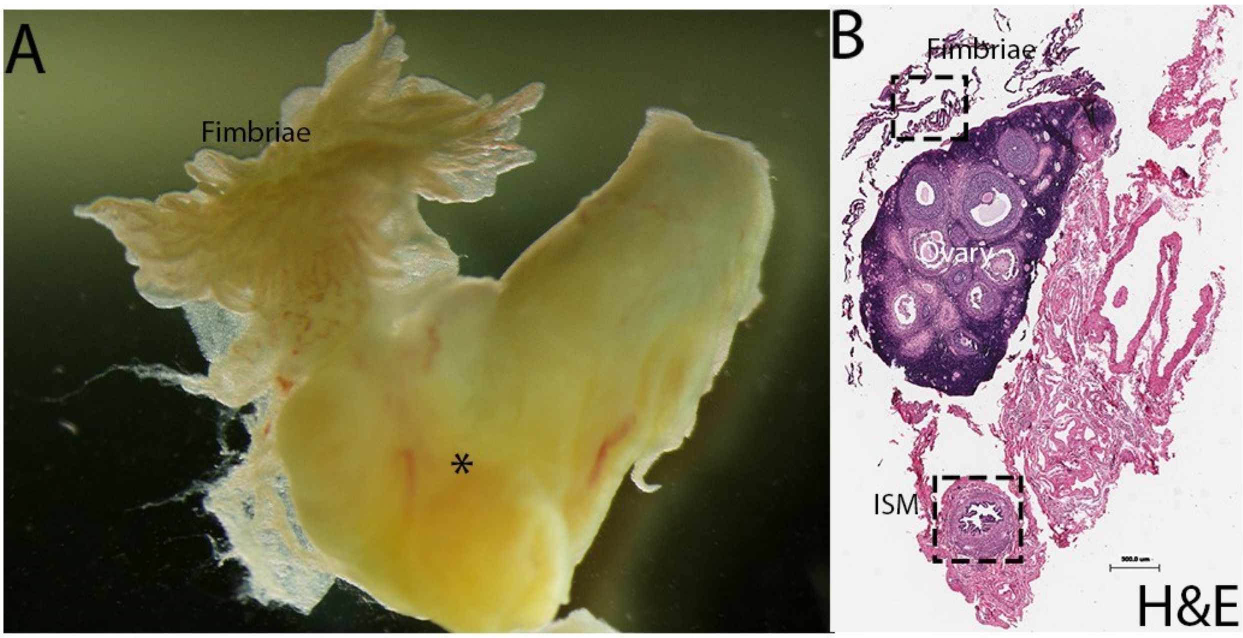

Supplementary Figure S 6: *Marmoset fallopian tube***.**

(A) Marmoset fallopian tube. Prominent fimbriae, finger-like projections, are visible at the rostal end (arrow). No coiling. One bend (black asterisk) (B) H&E staining of fimbriae located adjacent to the ovary and ISM after the bend.

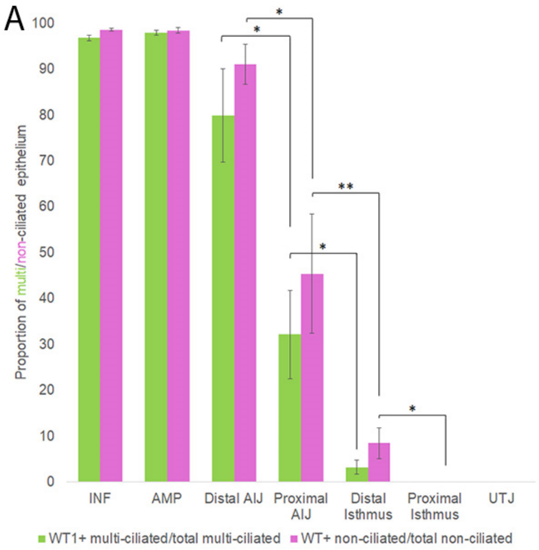

Supplementary Figure S 7: *Proportion of WT1+ve cells in multi-ciliated and secretory cells***.**

Proportion of WT1+ve cells in respective cell types. Oviducts were collected at random estrous stages and quantification was performed on transverse tissue sections like Figure 6A-F. N=8 oviducts. **<0.01, *<0.05. Error bars indicate standard deviation.

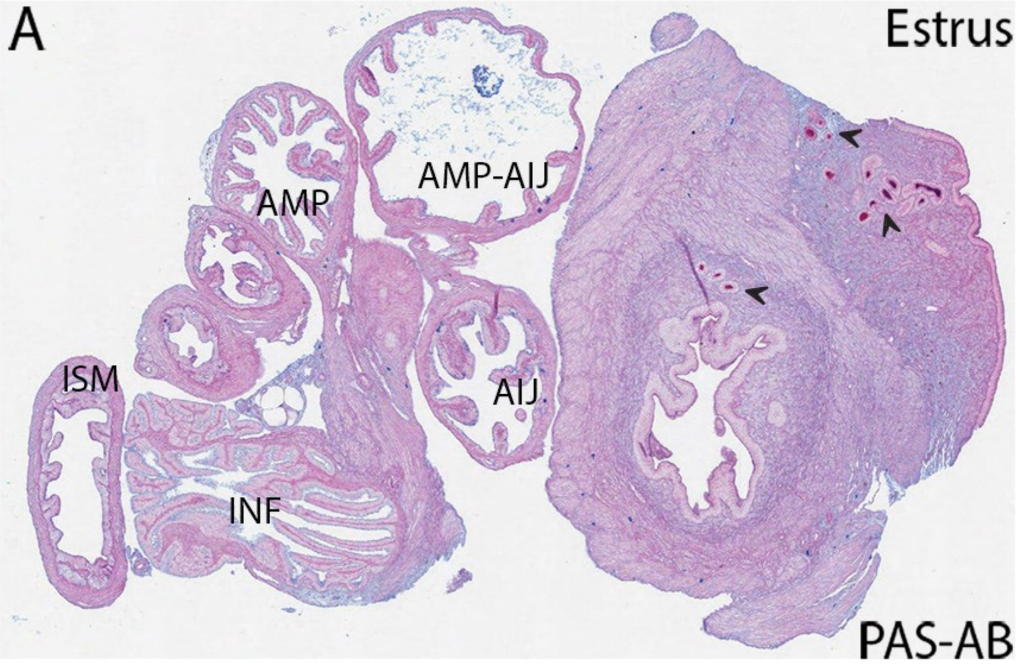

Supplementary Figure S 8: *PAS-AB staining in estrus stage***.**

PAS-AB staining in the estrus stage. No alcian blue staining in the estrus stage mouse oviduct. Red PAS staining in uterine glands (black arrows).

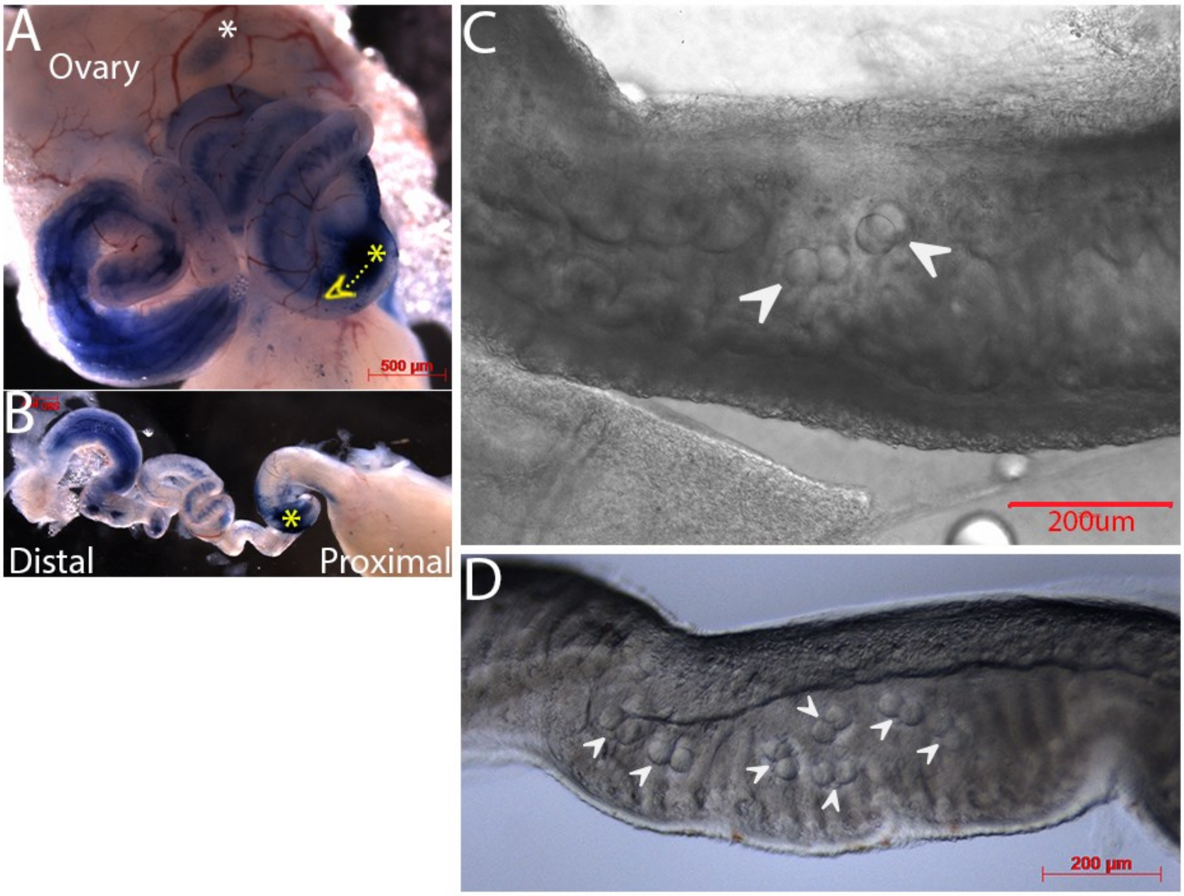

Supplementary Figure S 9: *Trypan blue injection in non-ovulated mice, and location of floating 2-cell stage embryos.*

(A) Trypan blue injection into the ISM (yellow asterisk) of mouse oviduct not containing oocytes. Yellow dotted line and arrowhead indicate location and direction of injection, respectively. Trypan blue solution spread into the distal oviduct and the ovary (white asterisk). (B) Stretched oviduct with trypan blue injected in the ISM (yellow asterisk). (C) 2-cell stage embryos observed floating in ISM of live oviduct (white arrows). (D) 2-cell stage embryos noted in ISM of fixed, TDE-cleared oviduct (white arrows).

2.9. Conceptual link between Chapter 2 and 3

In chapter 2, I demonstrated that the basic coiling pattern in the oviduct serves as reliable landmarks for all 5 regions that have distinct mucosal fold morphologies: INF, AMP, AIJ, ISM, and UTJ. While it was previously thought that the oviduct mucosa was lined with only two types of epithelial cells: multi-ciliated (MCC) and secretory cells (SC) that formed a simple gradient along the tube, I showed that each of these regions were lined with distinct pairs of MCCs and SCs – totaling 7 epithelial subtypes, that expressed distinct combinations of TFs. MCC distribution was not a simple gradient, instead, each region had its own proportion and distribution pattern. Additionally, I demarcated the AIJ, which is typically considered a simple AMP to ISM transition region, as a distinct region due to its distinct mucosal fold morphology, MCC proportion, TF expression, and acidic mucus secretion implying potential function. However, while distinct TF expression patterns were noted these epithelial subtypes, expression often overlapped between regions and/or cell types.

Thus, in chapter 3, I optimized the SmartSeq platform to sequence all 7 epithelial subtypes, identify region-specific TFs and cell-subtype specific differentially expressed genes (DEGs) and confirm that these 7 populations are distinct cell subtypes/identities.

3. Distinct cellular identities and potential functional diversity in mucosal epithelial populations along the mouse oviduct

Keerthana Harwalkar[1,2], Alain S Pacis[4], Alex Frances Thornton[2], Yojiro Yamanaka[1,2,3,*]

[1]Department of Human Genetics, McGill University, Montréal, Québec, Canada

[2]Rosalind and Morris Cancer Research Institute, McGill University, Montréal, Québec H3A 1A3, Canada

[3]McGill's Integrated Core of Animal Modeling (MICAM), McGill University, Montréal, Québec H3A 1A3, Canada

[4]Canadian Centre for Computational Genomics (C3G), Genome Quebec Innovation Centre, McGill University, Montréal, Québec H3A 1A4, Canada

*Corresponding author

3.1. Abstract

The mouse oviduct is a coiled tube that is demarcated into four morphologically distinct regions: INF/AMP, AIJ, ISM, and UTJ from distal to proximal, relative to the uterus. Epithelial cells that line the mucosal folds set a timely, region-specific luminal environment for gamete and preimplantation embryo transport. We previously demonstrated that each morphologically distinct region is lined with a unique pair of MCCs and SCs, totalling 3 subtypes of multi-ciliated (MCCs) and 4 subtypes of secretory (SCs) cells. However, little is known about the degree of differences between these regionally restricted epithelial cell subtypes.

In this study, we FACS-sorted these 7 subtypes of cells to perform low input, pooled RNASeq from a single mouse by using a double transgenic *Fltp-h2b-Venus* and *Sox17-mCherry* reporter mouse line that marks MCCs and SCs. In the INF/AMP epithelium, we sorted an additional minor population that had unique characteristics. Using SmartSeq SS4, we found that each subtype of MCC or SC expressed numerous differentially expressed genes (DEGs) and enrichment of distinct sets of biological processes, reflecting their distinct functions. Since transcription factors (TFs) is the central players in gene regulation, we investigated TF expression along the tube and found that regionally restricted MCCs and SCs expressed distinct combinations of TFs. Our data further demonstrates distinct cellular identities in the morphologically distinct regions.

3.2. Introduction

The mouse oviduct is a coiled tube that connects the uterus to the ovary and provides a conduit for gamete and preimplantation embryo transport. Based on mucosal fold morphology, proportion of multi-ciliated cells (MCCs) and transcription factor (TF) expression, this tube is demarcated into 4 regions from distal to proximal of the uterus: the infundibulum (INF), ampulla (AMP), ampulla-isthmus junction (AIJ), isthmus (ISM), and uterotubal junction (UTJ) [1].

The INF/AMP epithelium, located directly adjacent to the ovary, captures the ovulated oocyte-cumulus complex (OCC) via active beating of INF/AMP MCCs and provides a luminal environment suitable for fertilization [2]. On the other hand, the UTJ acts like a gate, permitting only a small fraction of spermatozoa into the oviduct [3-5]. Viscoelastic fluid/mucus in the proximal oviduct considerably slows down spermatozoa [3, 6]. Additionally, the ISM is considered a sperm reservoir, with many spermatozoa found with their heads adhered to the bottom of the ISM mucosal folds [7], where MCCs are located [1]. Following fertilization, distal oviduct MCC beating and decreased fluid production in the ISM allows preimplantation embryo transport along the AIJ [8], while transport from the ISM to uterus depends on MCCs [2] and smooth muscle contractions [9, 10]. During travel along the oviduct, gametes and preimplantation embryos are exposed to the luminal environment in different regions of the oviduct.

The luminal environment is created by the mucosal epithelial cells, which is composed of only two cell types, MCCs and SCs. It is unknown if there is any diversification in gene expression and functions among MCCs and SCs in each region. 10x genomics droplet single-cell RNA-Seq (scRNASeq) of luminal epithelial cells from an entire adult oviduct shows that SCs and MCCs of distal and proximal clusters were moderately separated, enabling the identification of a few distal and proximal-specific markers like WT1 and LY6A that are independent of estrous cycling. Due to high commonality in abundant genes and relatively low capture rates of low abundant genes like transcription factors (TFs), clustering analyses could not distinguish all the proximal populations, namely AIJ, ISM and UTJ, as distinct populations [11], despite apparent anatomical differences and distinct MCC distribution patterns/frequency [1]. To overcome the low capture rates of low abundance genes in 10x genomics strategy, we chose the SmartSeq SS4 platform and pooled MCCs or SCs (~30 cells each) from each region in this study. We manually dissected out each region of the oviduct based on anatomical landmarks [1] from a single female that carried fluorescence reporters allowing segregation of MCCs and SCs using fluorescence-assisted cell sorting (FACS). Deeper sequencing of regionally restricted SCs and MCCs allowed the identification of region-specific TFs, numerous differentially expressed genes (DEGs), and cell subtype-specific biological processes during estrus stage. Our data demonstrated that each morphologically distinct region consists of a unique pair of SCs and MCCs distinct in TF expression, gene expression patterns, and potential unique functions, alongside many commonly expressed genes.

3.3. Results

3.3.1. Isolation of MCCs and SCs from each region of the mouse oviduct for SmartSeq

In our previous study, we demonstrated that the adult mouse oviduct consists of four anatomically distinct regions in terms of mucosal fold morphology, proportion and distribution patterns of MCCs and SCs that line the mucosal folds, and gene expression patterns. The INF/AMP has the highest proportion of MCCs (~60%), followed by low proportions in the AIJ and ISM (~20%), and no MCCs in the UTJ [1]. The *Fltp-h2b-Venus* mouse line [12] marked all MCCs in the oviduct (Figure 3.1A-D), identical to the known MCC master TF, FOXJ1 (Figure 3.1E-I). SOX17 uniquely marked SCs in the INF/AMP epithelium while in the AIJ, ISM and UTJ epithelium, SOX17 marked all mucosal epithelial cells, including SCs and MCCs (Figure 3.1J-M) [1]. The *Sox17-mCherry* fusion mouse line [13] faithfully reports SOX17 expression in the mouse oviduct (Figure 3.1N).

In the INF/AMP epithelium, all epithelial cells were labelled with nuclear Venus and/or mCherry (Figure 3.1A-D). Venus+ cells in the INF/AMP were MCCs marked by apical acetylated tubulin (AT) (Figure 3.1A). Interestingly, using transverse cryosections, we also found a population of double positive cells (Venus+ and mCh+) that made up 13.93±7.58% of the epithelium, apart from 39.4±10.67% Venus+ MCCs and 33.45±10.10% mCh+ SCs in the INF/AMP epithelium (Figure 3.1O). In the AIJ and ISM, all epithelial cells were mCh+ (Figure 3.1B, C, N). Therefore, AT+ve MCCs were double positive while SCs were only mCh+ (Figure 3.1B, C). The AIJ epithelium comprised of 74.98±4.39% mCh+ SCs and 24.13±4.5% Venus+mCh+ MCCs, while the ISM contained 82.53±5.12% mCh+ SCs and 17.47±5.12% Venus+mCh+ MCCs (Figure 3.1O). No MCCs were found in the UTJ (Figure 3.1D, H), with all cells being mCh+ SCs (Figure 3.1D, O). Taken together, we found 8 epithelial cell populations from four regions of the oviduct: a pair each of MCCs and SCs in the INF/AMP, AIJ and ISM, SCs in the UTJ, and a minor double positive population in the INF/AMP.

Since the oviduct is a hormonally regulated organ, variation in individual females is inevitable even if we track the hormonal cycle. To avoid this, we sorted 30 cells each of the 8 populations from a single female at estrus-stage for RNASeq analysis (N=2), permitting direct comparison of the distinct regions. Principal component analysis (PCA) revealed a moderate separation between MCC (I1, I3, A1, IS1) and SC (I2, A2, IS2, U) populations (Figure 3.1P). We found some variation between the two females. Interestingly, SC population IS2 clustered away from the other SC populations but closely with MCC population IS1, particularly #104. This suggests that regional commonality is higher than the MCC/SC difference. The minor double population in the INF/AMP is the only population clustered together from two different females/replicates, while other regional subpopulations were not clustered together. MCC populations I1 and A1 in each female were clustered. Interestingly, #101 MCC IS1 was clustered closely with #104 MCC I1 and A1. This might suggest progressive responses to ovarian hormones along the oviduct.

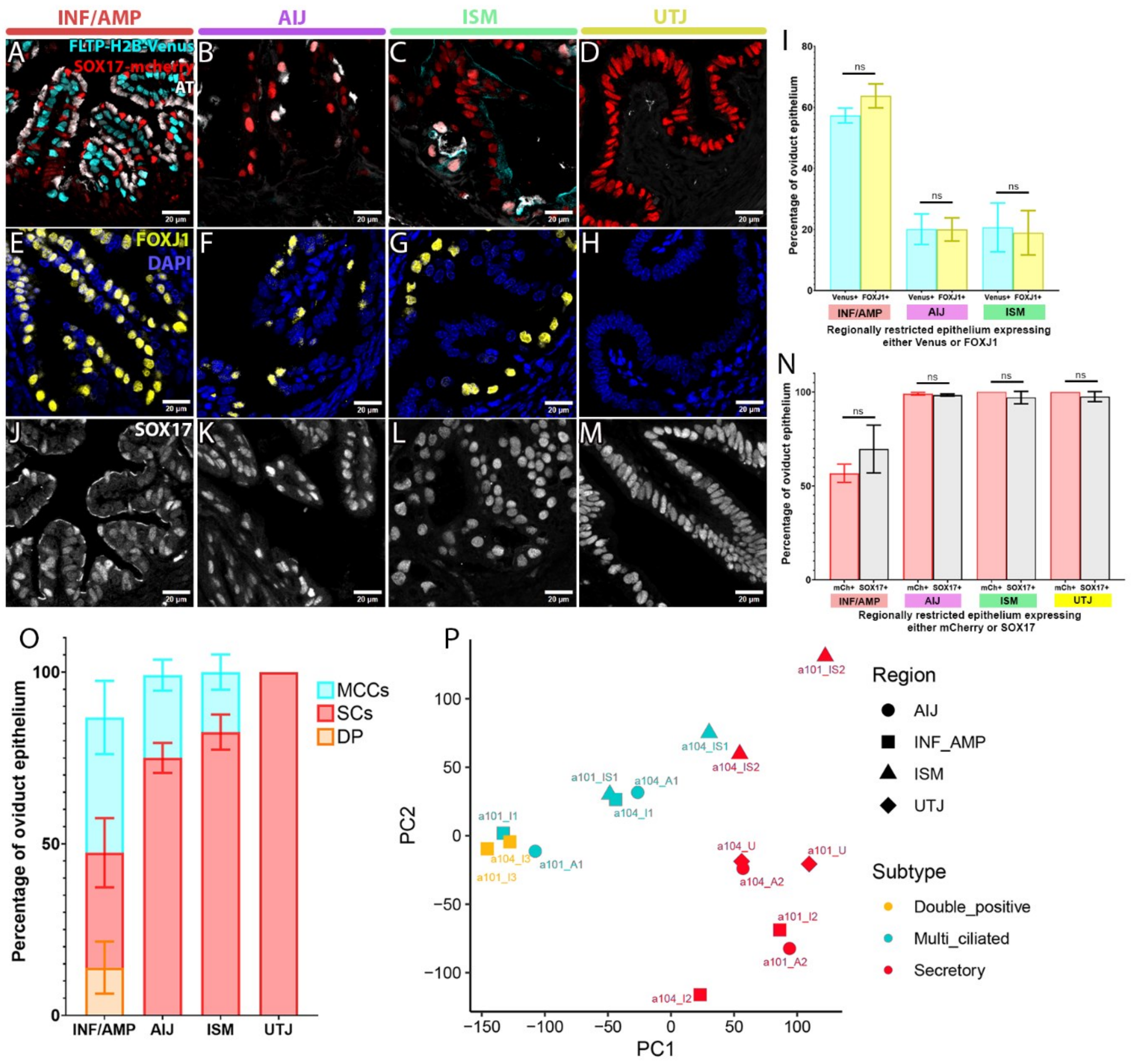

Figure 3. 1: FLTP-H2B-Venus and SOX17-mCherry double transgenic mouse line marks MCCs and SCs along the mouse oviduct.

(A-D) Venus and mCherry expression in the INF/AMP (A), AIJ (B), ISM (C), and UTJ (D). Venus+ cells showed apical acetylated tubulin (AT)+ve multi-cilia (A-C), while mCh+ cells do not (A-D). MCCs in the AIJ and ISM are Venus+ and mCh+ (B, C). (E-H) FOXJ1 expression along the oviduct. The INF/AMP region had the highest proportion of FOXJ1+ve MCCs (E), followed by the AIJ and ISM (F, G), and no MCCs in the UTJ (H). (I) Percentage of Venus+ or FOXJ1+ve epithelium along the tube. Venus and FOXJ1 were largely co-expressed. (J-M) SOX17 expression in the INF/AMP (J), AIJ (K), ISM (L), and UTJ (M). All epithelial cells in the AIJ, ISM, and UTJ were SOX17+ve (K-M). (N) Percentage of mCh+ or SOX17+ve epithelium along the tube. mCh and SOX17 were largely co-expressed. (O) Percentage of MCCs, SCs, and double positive (DP) epithelium along the tube, as counted on transverse tissue sections, classified based on Venus and mCh expression. Three epithelial populations were found in the INF/AMP region: Venus+ MCCs, mCh+ SCs, and Venus+mCh+ DP. Two populations each were found in the AIJ and ISM: Venus+mCh+ MCCs and mCh+ SCs, and one population of mCh+ SCs found in the UTJ. (P) PCA plot of two estrus stage SmartSeq replicates (a101 and a104), with 8 samples each, that correspond to the 8 identified populations. I1, I2 and I3 were Venus+, mCh+, double positive populations from the INF/AMP, respectively. A1 and IS1 were Venus+mCh+ populations from the AIJ and ISM respectively, while A2 and IS2 were mCh+ alone. U represents mCh+ cells from the UTJ. ns = $p \geq 0.05$. Scale bar length = 20μm.

3.3.2. *Heterogeneity in MCC and SC transcriptome and biological processes along the mouse oviduct.*

From the INF/AMP region, we isolated Venus+ MCCs (I1), mCh+ SCs (I2), and the minor double positive (I3) population. Numerous differentially expressed genes (DEGs) were detected in I2 (2639 DEGs), as compared to I1 (28 DEGs) or I3 (789 DEGs; Supplementary Figure S3.1A). Among the top 10 DEGs detected in I1 was *Prox1* (Supplementary Figure S3.1B), a homeobox transcription factor (TF) that is the key transcriptional factor for the lymphatic system [14]. It also plays essential roles in the development of the heart, eye lens, liver, pancreas and neurogenesis [15]. In agreement with the SmartSeq, we confirmed that PROX1 was expressed in MCCs of the INF/AMP (Supplementary Figure S3.1C, D). Further, I2 SCs did not share DEGs with either I1 or I3 (Supplementary Figure S3.1A), and showed upregulation of genesets associated with inflammatory response, wound healing, cytokine production, chemotaxis, and response to bacteria/stimuli, relative to I1 and I3 (Supplementary Figure S3.1F).

I3 is a unique, minor double-positive population. I1 and I3 shared 2282 DEGs (Supplementary Figure S3.1A). Many of the top 10 DEGs shared by the I1 and I3 were involved in ciliogenesis or expressed in ciliated cells (Supplementary Figure S3.1D). Additionally, based on expression of known TFs like *Foxj1* and *Trp73* (Supplementary Figure S3.1E), we concluded that I3 was a population of MCCs. In agreement with this, double positive cells in histology sections were FOXJ1+ve (96.28±1.27%). It is shown that *Pax8*+ve SCs give rise to *Pax8*+ve SC and *Pax8*-ve MCCs in a lineage tracing study of the mouse oviduct [16]. Indeed, *Pax8* was enriched only in I2, but not in I1 and I3 (Supplementary Figure S3.1E). Interestingly, I3 showed enrichment of genesets associated with ciliogenesis such as cilium, microtubule and axoneme organization/assembly, relative to even I1 (Supplementary Figure S3.1F), suggesting that I3 was a transitory population from SC to MCC. However, the I3 gene expression pattern was not a simple intermediate of SCs I2 and MCC I1. A recent study identified a potential transitional pre-ciliated cell type in the INF/AMP that expressed *Krt5*, *Trp73*, and *Prom1* but not *Trp53* in single cell RNA seq analysis [17]. While we did not detect *Krt5* in our SmartSeq, *Trp73* and *Prom1* were enriched in I3 (Supplementary Figure S3.1E).

All three MCC subtypes (I1, A1 and IS1) commonly express *Foxj1* and *Trp73* (Supplementary Figure S3.1E). Each subtype of regionally restricted MCCs located in the INF/AMP (I1), AIJ (A1) and ISM (IS1) expressed numerous DEGs – 169, 328 and 1288 respectively (Figure 3.2A; Supplementary Figure S3.1G). Using Geneset Enrichment Analysis (GSEA), we found enrichment of genesets associated with cilia organization, function and motility in I1 MCCs (Figure 3.2C), which has been shown to be actively involved in OCC transport into the oviduct [2]. In contrast, A1 MCCs showed unique upregulation of uronic acid, flavonoid, and xenobiotic glucuronidation/metabolism associated genesets (Figure 3.2C). The IS1 MCCs showed enrichment in genesets associated with immune response, vasculature development, and biological adhesion (Figure 3.2C). IS1 MCCs are located in the trenches of the transverse mucosal folds, forming rosette-like structures with apically focal multi-cilia [1]. Interactions with spermatozoa are suspected [7] where the MCCs are located [1].

Non-ciliated cells in the oviduct are typically considered SCs that regulate the oviduct luminal environment. Each subtype of regionally restricted SCs located in the INF/AMP (I2), AIJ (A2), ISM (IS2), and UTJ (U) also expressed numerous DEGs – 511, 156, 1702, and 610 respectively (Figure 3.2B; Supplementary Figure S3.1H). I2 SCs showed upregulation of genesets linked to protein synthesis, ribosome biogenesis/function energy production/regulation, redox regulation and RNA turnover/localization (Figure 3.2D), likely reflecting secretory function and response to follicular fluid. Geneset associated with ROS response was enriched in the A2 SCs (Figure 3.2D), similar to A1 MCCs (Figure 3.2C). Distinct gene expression pattern and biological processes between INF/AMP and AIJ confirmed the distinct properties of the AIJ epithelium. IS2 SCs, similar to IS1 MCCs, showed enrichment in immune response activation and regulation, and downregulation in energy production (Figure 3.2D). In U SCs, genesets related to anti-viral, anti-bacterial response and embryonic placenta morphogenesis were upregulated while genesets associated with immune response activation and regulation are relatively downregulated (Figure 3.2E). Taken together, this suggests that MCCs and SCs in each region were transcriptionally and functionally distinct.

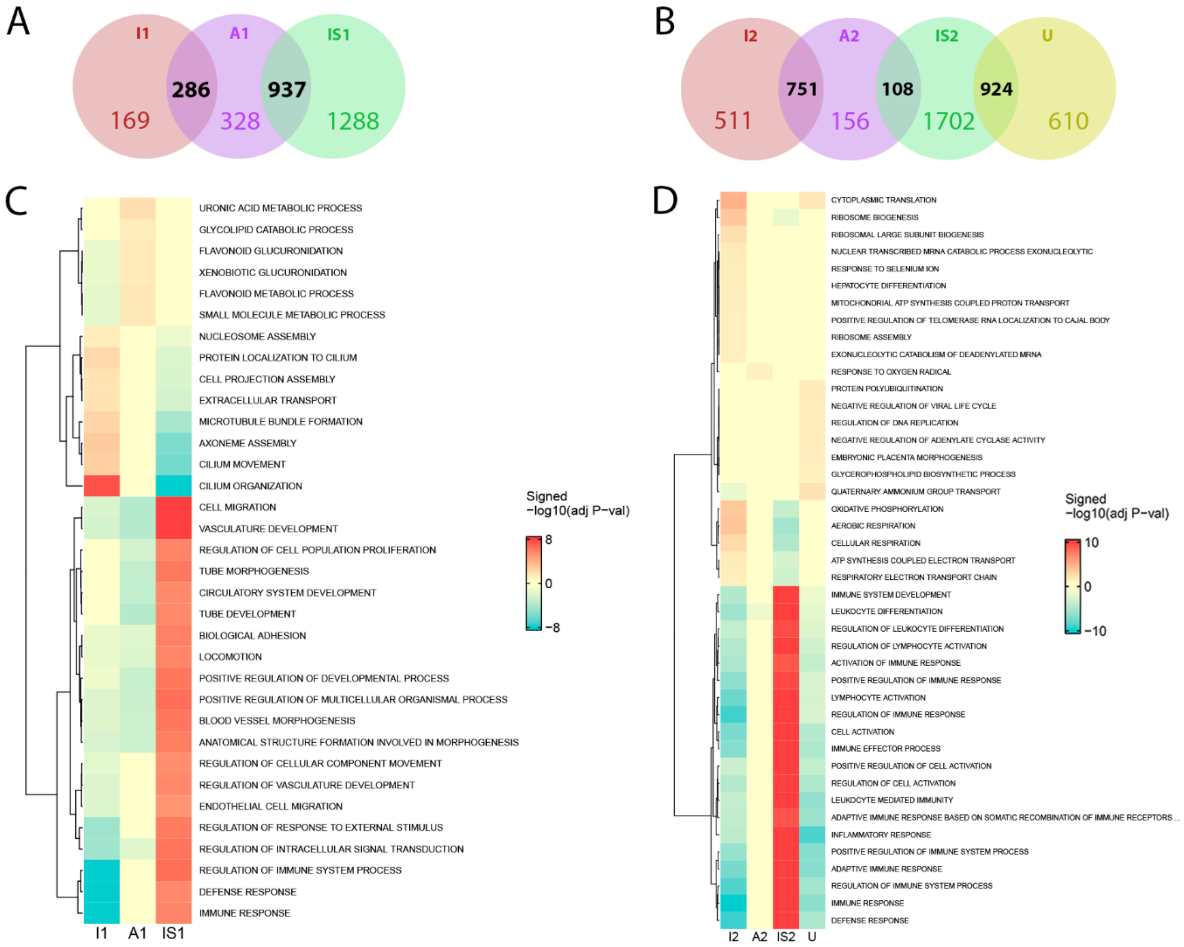

Figure 3. 2: Distinct gene expression and biological process in regionally restricted MCCs and SCs along the oviduct.

(A, B) Number of DEGs in MCCs (B) and SCs (C) along the tube. (C, D) Geneset Enrichment Analysis showing top 10 upregulated genesets in MCC (C) and SC (D) populations along the tube.

3.3.3. Unique expression patterns of transcription factors suggesting distinct cellular identity.

Regulation of gene expression is controlled by an interplay between transcription factors (TFs), co-factors, and regulatory elements, thus dictating the function and identity of a cell [18]. In our previous 10x single cell transcriptome analysis, we were unable to identify regional differences within the oviduct epithelium. We suspected that this is due to low capture rates of low abundance genes in 10x scRNAseq v2 and common genes being abundantly expressed. Capturing TFs is difficult due to their relatively low expression, but their differential expression is important for cellular identity and functions. To determine if the cell populations we identified along the mouse oviduct are distinct cell identities, we compared differential TF expression in our dataset among each subtype of MCCs or SCs (Supplementary Figure S3.2A-C) and along the tube. All regions had unique TFs not expressed in other regions, except the AIJ populations which did not have unique TFs (Figure 3.3A, B). In our previous study, we found that the AIJ population co-expresses the distal TF WT1 and proximal-specific PAX2 [1, 11]. Therefore, we explored TFs that were differentially expressed in the INF/AMP and AIJ but not the rest of the tube (Figure 3.3C) and those differentially expressed in the AIJ and ISM but not the INF/AMP (Figure 3.3D). As expected, we identified *Wt1* and *Pax2* as differentially expressed in the distal and proximal oviduct epithelium (Figure 3.3C, D), respectively.

The INF/AMP epithelium showed enrichment of *Gata6* (Figure 3.3B), and this was confirmed by immunofluorescence staining. GATA6 was expressed in both SCs and MCCs of the INF/AMP (Figure 3.3E), showed low to no expression in the AIJ and ISM epithelium (Figure 3.3F, G), and was not expressed in the UTJ (Figure 3.3H). GATA6 expression levels in INF/AMP SCs, marked by SOX17, was higher than in MCCs (Figure 3.3E). The INF/AMP and AIJ epithelium showed enrichment of *Sox3* (Figure 3.3C), and we found that SOX3 was expressed in MCCs and SCs of the INF/AMP (Figure 3.3I), SCs and some MCCs of the AIJ (Figure 3.3J), only SCs of the ISM (Figure 3.3K) and showed low to no expression in the UTJ (Figure 3.3L). The proximal oviduct epithelium showed differential *Sox7* expression (Figure 3.3D). SOX7 was expressed in SCs of the INF/AMP (Figure 3.3M), both MCCs and most SCs of the AIJ and ISM (Figure 3.3N, O), and all epithelial cells of the UTJ (Figure 3.3P). MCCs in the AIJ and ISM, marked by FOXJ1, showed higher SOX7 intensity than SCs (Figure 3.3N, O).

The INF/AMP and AIJ epithelium showed differential enrichment of *Nr2f1*, as compared to the rest of the tube (Figure 3.3B, C). However, NR2F1 protein expression was noted in a few INF/AMP epithelial cells, predominantly at the tips of some of the mucosal folds (Supplementary Figure S3.2D). While only INF/AMP epithelium showed *Sox13* enrichment (Figure 3.3B), all epithelial cells along the tube showed SOX13 protein expression (Supplementary Figure S3.2E-H). ISM populations showed *Erg* enrichment (Figure 3.3B), but ERG protein expression was noted throughout the tube. INF/AMP epithelial cells showed cytoplasmic ERG expression that was typically located around the nucleus (Supplementary Figure S3.2I), while some proximal epithelial cells showed cytoplasmic and/or nuclear ERG (Supplementary Figure S3.2J-L). INF/AMP and AIJ epithelial cells showed enrichment of *Srebf2* (Figure 3.3C). However, the INF/AMP MCCs, marked by FOXJ1, often showed cytoplasmic and apical SREBP2 protein localization, with some nuclear localization (Supplementary Figure S3.2M, Q). AIJ and ISM MCCs showed cytoplasmic and nuclear localization, while some SCs showed nuclear localization (Supplementary Figure S3.2N, O, R, S). UTJ epithelium showed cytoplasmic, apical localization of SREBP2 (Supplementary Figure S3.2P). It is interesting to speculate that these differences in mRNA and protein expression corresponds with regulation of distinct functions in other estrous stages.

While there were many differentially expressed TFs among each subtype of MCCs or SCs (Supplementary Figure S3.2A-C), it is unknown whether these populations also express gene regulatory networks or co-factors associated with the differentially expressed TFs. Thus, we performed single-cell regulatory network inference and clustering (SCENIC) analysis [19] to infer transcriptional regulators modulating cell type-specific gene regulatory networks in each MCC and SC subtype. I1 and I3 showed higher *Foxa2*, *Zfp866* and *Adarb1* regulon activity, relative to A1 and IS1 (Supplementary Figure S3.3A), suggesting that INF/AMP MCC identity/function is regulated by distinct gene regulatory networks. Additionally, FOXA2 is expressed in INF/AMP MCCs but not the rest of the tube [1]. I3 showed high *Foxj1*, *Trp73*, *Rfx3*, and *Sox13* regulon activity, relative to all other MCC populations (Supplementary Figure S3.3A), suggesting that I3 is a distinct cell state. Interestingly, *Foxj1*, *Trp73* and *Rfx3* are associated with ciliogenesis, with *Rfx3* being a transcriptional co-activator to *Foxj1* [20]. I2, A2, IS2, and U SC populations showed high activities of distinct regulon/TF combinations (Supplementary Figure S3.3B). Finally, IS2 alone showed high activities in a combination of regulons relative to other SC populations (Supplementary Figure S3.3B), suggesting distinct cellular state/identity.

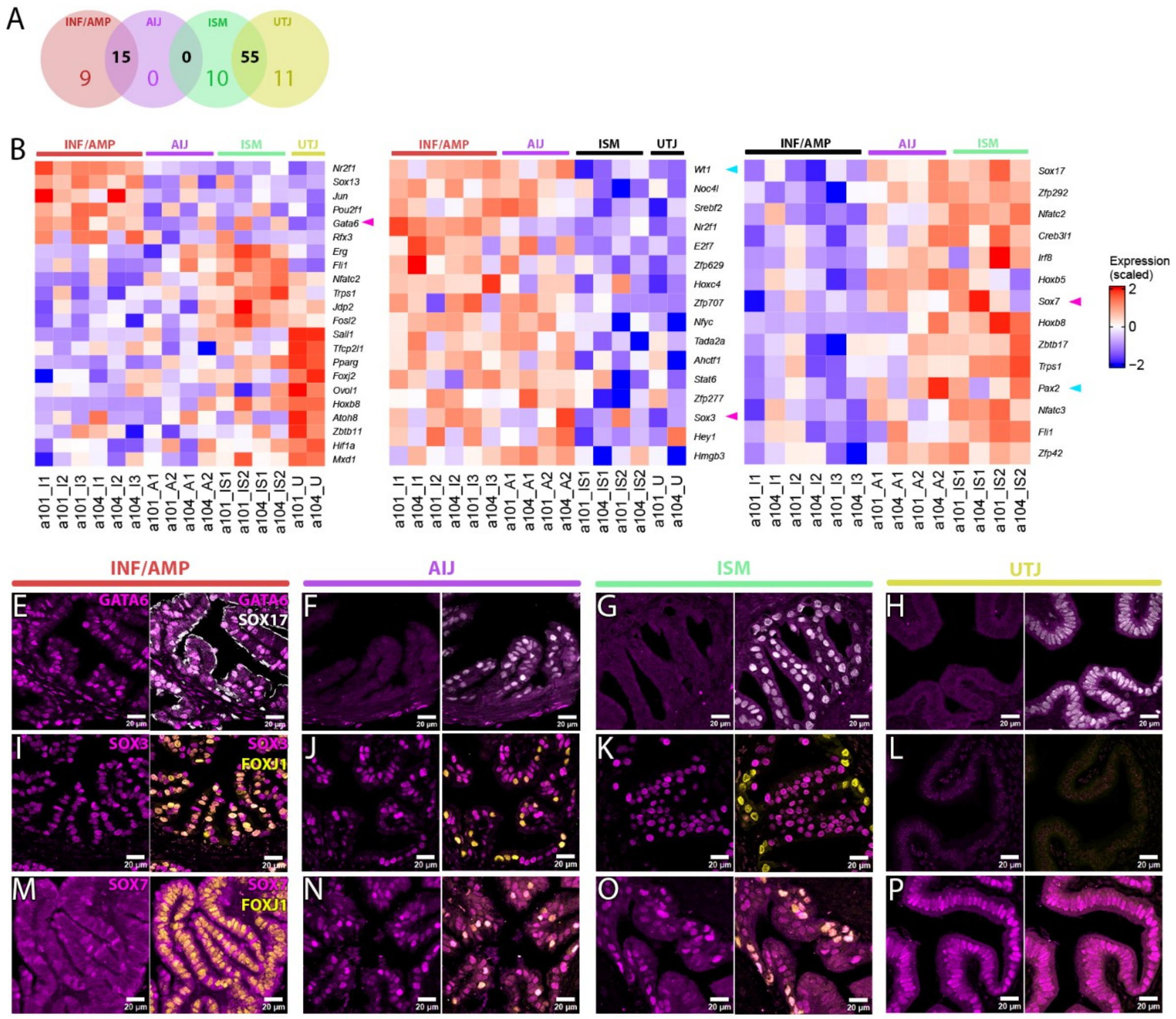

Figure 3. 3: Epithelial populations in each region expressed distinct combinations of TFs.

(A) Number of differentially expressed TFs in regionally restricted epithelial populations. (B) Heatmap of differentially expressed TFs in regionally restricted epithelial populations. Expression of genes marked with black arrows was assessed by immunofluorescence in Supplementary Figure 2. Expression of gene marked with magenta arrow was confirmed in Fig. 3E-H. (C) Heatmap of TFs differentially expressed in INF/AMP and AIJ populations, but not ISM and UTJ. Expression of *Wt1*, marked with cyan arrow, is previously confirmed by immunostaining [1]. Expression of genes marked with black arrows was assessed by immunostaining in Supplementary Figure 2. Expression of gene marked with magenta arrow was confirmed with immunofluorescence in Fig. 3I-L. (D) Heatmap of TFs differentially expressed in AIJ and ISM, but not INF/AMP populations. Expression of gene marked with magenta arrow was confirmed in Fig. 3M-P. Expression of *Pax2*, marked with cyan arrow, is previously confirmed by immunofluorescence [11]. (E-H) Expression pattern of GATA6 along the oviduct. GATA6 was expressed in MCCs and SCs of the INF/AMP (E), with low to no expression in the AIJ/ISM epithelium (F, G) and no expression in the UTJ (H). (I-L) Expression pattern of SOX3 along the tube. SOX3 is expressed in MCCs and SCs of the INF/AMP (I), predominantly SCs in the AIJ/ISM (J, K), with low expression in the UTJ (L). (M-P) Expression pattern of SOX7 along the tube. SOX7 is expressed in SCs of the INF/AMP (M), SCs and MCCs in the AIJ/ISM (N, O), and all SCs in the UTJ (P). Scale bar length = 20µm.

3.4. Discussion

The mouse oviduct luminal epithelium is thought to be composed of only two subtypes of cells: MCCs and SCs. In our previous studies, we demonstrated the oviduct luminal epithelium consists of four distinct regions with distinct mucosal fold morphology, MCC proportion, distributions, and transcription factor (TF) expression. Each region has a unique pair of MCCs and SCs. Although we identified TF expression differences with immunostaining, 10X single cell RNAseq analysis did not reveal a clear separation of distinct cell populations, likely due to high similarity in abundant genes and low coverage of low abundant genes like TFs [1, 11]. In this study, we isolate MCCs and SCs from each morphologically distinct region of the mouse oviduct using the *Fltp-h2b-Venus*; *Sox17-mCherry* double transgenic mouse line to perform SmartSeq RNA sequencing on ~30 pooled cells each from the 8 subtypes of epithelial cells, from a single mouse. *Fltp*/*Fltp-h2b-Venus* is involved in basal body positioning during late ciliogenesis and marks all MCCs [12], while *Sox17-mCherry* [13] marked SCs in the INF/AMP and all epithelial cells in the rest of oviduct. We identified differences in TF and gene expression, confirming that the oviduct epithelium consists of four distinct regions comprising a unique pair of MCCs and SCs, while avoiding any effect of estrous cycling as each replicate is from a single mouse. This reflects distinct regulation and reproductive functions within each region of the oviduct.

Each subtype of epithelial cell isolated from the four regions expressed numerous DEGs, suggesting distinct functions. INF/AMP MCCs (I1) showed enrichment of genes associated with cilia organization and function compared to the AIJ and ISM MCCs. This is consistent with their primary role of transporting OCCs into the oviduct [2]. INF/AMP SCs, on the other hand, showed upregulation in protein synthesis, RNA recycling, energy production/regulation, redox regulation, wound healing, and chemotaxis. After ovulation, the AMP region gets swollen with OCCs, follicular fluid and oviductal fluid. Additionally, the presence of proteinaceous/serous secretory granules in the INF/AMP SCs is documented using TEM [21], suggesting active secretions from the INF/AMP SCs. It is known that the process of ovulation results in the release of reactive oxygen species (ROS) and inflammatory cytokines [22]. Thus, these enriched genesets could correspond with secretion and response to ovulation/follicular fluid.

Functional differences in each region have been suspected but not fully understood. We previously characterized the AIJ as a distinct region that showed acidic mucus secretion during metestrus/diestrus stage [1]. OCCs and follicular fluid, which contains steroid hormones, carbohydrates, and metabolites [23], are transported along the AMP and AIJ. Since both MCCs and SCs in The AIJ region showed enrichment of genesets associated with detoxification of steroid hormones/metabolites and ROS response, it is interesting to speculate that the enrichment of these biological processes during estrus stage reflects detoxification or breakdown of follicular fluid components.

ISM MCCs and SCs showed enrichment in vasculature development, immune response, inflammatory response, and biological adhesion. Changes in tone of vasculature is thought to aid sphincteric mechanisms of the oviduct; for example, the tubal lock mechanism at the AIJ-ISM that retains embryos in the distal rabbit oviduct [24]. Further, it is interesting to speculate that enrichment of these biological processes may be in preparation for spermatozoa entry and adhesion to the base of the mucosal folds, where MCCs are located. Spermatozoa entering the mouse oviduct slow down considerably [3], likely due to the presence of viscoelastic fluid/mucus [6]. Further, spermatozoa attachment to epithelium at the bottom of ISM mucosal folds is observed in mice, with active tail beating [7]. Detachment of attached sperm involves a high amplitude, erratic beating of the sperm flagella, termed hyperactivation, that allows them to penetrate viscoelastic medium more efficiently than fresh sperm [25].

The UTJ is the junction separating the oviduct from uterine lumen. The UTJ epithelium, which is comprised of SCs, showed upregulation of genesets associated with anti-viral, anti-bacterial response and embryonic placenta morphogenesis, likely reflecting response to spermatozoa entry and/or preimplantation embryos. In our previous study, we showed that 8-cell stage embryos form a queue within compartments at 2.5 days post copulation [1], and it is interesting to speculate that the UTJ provides an optimal microenvironment for these embryos. Taken together, this suggests that MCCs and SCs along the mouse oviduct have distinct functions; however, genesets associated with various biological processes are often shared by MCCs and SCs within each region, reflecting distinct luminal microenvironments in each region.

In this study, we identified a minor population of double-positive epithelial cells (I3) in the INF/AMP epithelium that was distinct from either I1 or I2 and not a simple intermediate of the two. This I3 population showed high *Foxj1*, *Rfx3*, *Trp73*, and *Sox13* regulon activity in SCENIC analyses, suggesting that it was a distinct cell state. Additionally, we also showed *Prom1*, *Trp73* and *Foxj1* expression, while *Trp53* and *Pax8* were not detected in I3. Based on expression patterns of these genes, I3 may be similar to a population of transitional preciliated cells that is identified by a separate study as a cell state susceptible to malignant transformation [17]. Interestingly, tamoxifen-induced labelling of Prom1-expressing cells in Prom1$^{\mathrm{tm1(cre/ERT2)Gilb}}$; Rosa26$^{\mathrm{tdT/tdT}}$ mice labels some SCs and MCCs in the INF/AMP, however, almost exclusive MCC labeling is observed at 1-month post induction, suggesting that labelled SCs differentiate into MCCs [26]. In line with this, I3 showed enrichment of genesets associated with ciliogenesis and cilia organization, even when compared to the I1 population. Taken together, the *Prom1*-expressing I3 population may represent a late SC-to-MCC transitory state.

3.5. Methods and materials

3.5.1. Animals

All animal work was performed in accordance with institutional guidelines and was approved by the Faculty of Medicine Animal Care Committee (AUP #7843); it was undertaken at the Goodman Cancer Research Institute animal facility. *Fltp-h2b-Venus* [12] and *Sox17-mCherry* [13] mouse lines were a kind gift from Dr. Heiko Lickert. Adult mice used in this study were 2–4 months of age; where required, estrous stages were analyzed using vaginal smears stained with crystal violet [27].

Genotyping for *Fltp-h2b-Venus* mice was performed with touchdown PCR, using following three primers: 5′-AGCCATACCACATTTGTAGAGG-3′, 5′-CAGCATGGCATAGATCTGGAC-3′, and 5′-GAGGCTGACTGGGAACAATC-3′. Homozygotes showed a 387 bp band, while heterozygotes showed two bands sized 317 bp and 387 bp. *Fltp-h2b-Venus* mice were maintained as homozygotes. The *Sox17-mCherry* mouse line was maintained as heterozygotes, and genotyping was performed with touchdown PCR using the three primers: 5’-GTGTATAAGCCCGAGATGG-3’, 5’-CTCAACTGTTCAAGTGGCAG-3’, and 5’-GACTACACCATCGTGGAACAG-3’, resulting in two bands that were 288 bp and 340 bp.

3.5.2. Isolation of epithelial cells

Mice homozygous for *Fltp-h2b-Venus* and heterozygous for *Sox17-mCherry* were used for SmartSeq. Oviducts from a single 3mo double transgenic mouse in estrus were straightened out in 1X PBS (Bio Basic, PD8117). The four regions were manually separated and moved into a 4-well dish with 500µl of media containing 1X PBS, 100 IU/ml of Penicillin, 100ug/ml of Streptomycin (Gibco, 15140122), and 10% fetal bovine serum (FBS, Wisent Bioproducts, 090-150). Region by region, they were transferred onto the lid of the 4-well plate with a drop of media containing 5mg/ml collagenase B (Sigma-Aldrich, COLLB-RO) and 5U/100ul DNase I (Thermo Scientific, EN0521). This solution with small tissue pieces was transferred to a 1.5ml tube containing 100µl of the above-mentioned dissociation solution and incubated for 35-40 minutes at 37°C. They were spun down at 1,500rpm for 5 minutes, resuspended in 500µl 1X PBS, and spun down again. Samples were resuspended in 50µl of warmed 0.25% Trypsin-EDTA (Gibco, 25200056) followed by a 7-minute incubation at 37°C. Trypsinization was halted with media, and mechanical dissociation was performed by passing through a 27 ½ gauge insulin needle (BD, 324704). The resulting single cell suspension was passed through a 40µm cell strainer (Corning, 352340), centrifuged at 1,500rpm for 7 minutes and resuspended in 200µl 1X PBS. Cell suspensions were spiked with 0.2µl 5mg/µl DAPI (Thermofisher) just prior to sorting to identify dead or dying cells.

3.5.3. SmartSeq SS4 RNA library preparation and sequencing

~30 Venus+, mCh+, and/or double positive cells were sorted directly into 3µl lysis mix on the FACSAria Fusion (BD Biosciences) using FACSDIVA (Version 8). Lysis mix contained 1/32000 diluted ERCC molecules, 5000U RNAse inhibitor, 12µM Nextera-PolyT30-15N primers, 0.4% (v/v) Triton X-100, water, and 10mM each of dNTP mix. Positive control contained 1µl 1/4000 ERCC added to 3µl lysis mix, while negative control contained only lysis mix. Lysis mix with sorted cells were centrifuged at 1500rpm for 3min, and run in a thermocycler (Mastercycler EP gradient S, Eppendorf) with the program: 72°C for 3min, 4°C for 10min, 25°C for 1min, hold at 4°C. Samples were placed at -80°C and transported to the McGill Genome Centre on dry ice for further processing.

4µl of RT mix, containing 5X SS4 first-strand buffer, 100mM DTT, 12µM Nextera-TSO-15N, 40U/µl RNAse inhibitor, 200U/µl SS4 reverse transcriptase, water, 5M Betaine, and 100mM MgCl2, was added to each sample and briefly spun down. Samples were placed in a thermocycler and the following program was run: 50°C, 30min for 1 cycle; 55°C & 50°C, 30s each for 10 cycles; 60°C & 55°C, 30s each for 5 cycles; 50°C, 30s for 1 cycle; 65°C & 60°C, 30s each for 5 cycles; 50°C, 30s for 1 cycle; 70°C & 65°C, 30s each for 5 cycles; 50°C, 30s for 1 cycle; 75°C & 70°C, 30s each for 5 cycles; 50°C, 1min for 1 cycle; 80°C, 10min for 1 cycle; hold at 4°C. 0.5µl of ExoI was added to each sample, followed by vortexing and spin down. Samples were run in the thermocycler with the following program: 37°C, 30min for 1 cycle; 85°C, 15min for 1 cycle; hold at 4°C. The entire 7.5µl of each sample was added into fresh PCR tubes containing 17.5µl of PCR mix: PCR-grade water, 10X Advantage 2 PCR buffer, 50X dNTP mix, 12µM Nextera-cDNA-PCR primer (in-house), and 50X Advantage 2 Polymerase Mix (Advantage 2 PCR Kit). Samples were run on a thermocycler with the following program: 95°C, 1min for 1 cycle; 95°C, 20s & 58°C, 4min & 68°C, 6min for 5 cycles; 95°C, 20s & 64°C, 30s & 68°C, 6min for 9 cycles; 95°C, 30s & 64°C, 30s & 68°C, 7min for 4 cycles; 72°C, 10min for 1 cycle; hold at 4°C. The final PCR product (or sequence ready library) was diluted 6-fold and loaded onto a Caliper HS DNA Chip (Agilent) for quality control. Libraries were sequenced on a PE150 lane using NovaSeq SP to obtain ~50 million reads per sample.

3.5.4. Sequencing analyses

The primary reads were aligned to the GRCm38 mouse genome and transcriptome from Gencode, using Hisat2, in stranded and paired-end mode [28, 29]. Reads from the 5' exons were demultiplexed and UMIs counted, using regular expressions according to the 5' end sequencing patterns on an Apache Spark cluster [30]. For all downstream analyses, we excluded low expressed genes with a read count lower than 5 in all samples. Raw counts were normalized using *edgeR*'s TMM algorithm [31] and were then transformed to log2-counts per million (log2CPM) using the *voom* function implemented in the *limma* R package [32]. To assess differences in expression between cell-types (i.e., compare each cell-type against all others), we fitted a linear model using the *lmfit* function. Nominal p-values were corrected for multiple testing using the Benjamini-Hochberg method. Marker genes and TFs were identified using adjusted P-value < 0.2. Gene set enrichment analysis based on pre-ranked gene list by fold-change (log2) was performed using the R package *fgsea* (http://bioconductor.org/packages/fgsea/). Gene regulatory network analysis was performed using SCENIC [19].

3.5.5. Immunofluorescence

Uncoiled or coiled oviducts/reproductive tracts were fixed with 4% paraformaldehyde (PFA, Polysciences) for 30 minutes, followed by three washes with 1X PBS. Fixed samples were calibrated in 15% and 30% sucrose either at 4 degrees overnight or 3-4 hours at room temperature prior to OCT (Fisher HealthCare, 23-730-571) embedding and sectioning at 4-6- or 10-micron thickness. For immunofluorescence (IF), sections were brought to room temperature, incubated with 1X PBS, 0.1% Triton X-100 (Sigma-Aldrich, T8787), and 0.5% Triton X-100, followed by 1-3 hour-long permeabilization and blocking using 0.1% Triton X-100 and 1% FBS in 1X PBS at room temperature. Primary antibody staining was performed overnight at 4°C, in permeabilization and blocking solution. Primary antibodies were washed off with multiple washes of 1X PBS and 0.1% Tween (Sigma Aldrich, P9416), followed by secondary antibody staining overnight at 4°C, in 1X PBS. After the secondary antibodies were washed off, 1-2 drops of homemade mounting media, prepared with 20% w/v n-propyl gallate (Sigma Aldrich, P3130) made in DMSO (Dimethyl sulfoxide, Sigma Aldrich, D8418) and 90% glycerol (BioShop, GLY001) in 1X PBS, were pipetted onto the sections and #1.5 coverslips (VWR, 48393-251) were placed over the stained sections. #1.5 coverslips were sealed to the slides using nail polish. IF sections were imaged with 20x (N.A 0.80) or 63x (N.A 1.4) objectives, on LSM710 or LSM800 confocal microscopes (Zeiss).

3.5.6. Antibodies

Primary antibodies (1/250 dilution, unless specified): anti-SOX17 (R&D Systems, AF1924), anti-FOXJ1 (Abcam, ab235445), anti-mcherry (Abcam, ab213511/Invitrogen, #M11217), anti-GFP (Abcam, ab13970), anti-acetylated tubulin (Sigma, T7451), anti-GATA6 (Cell Signaling, 5851T), anti-SOX3 (R&D Systems, AF2569), anti-SOX7 (R&D Systems, AF2766), anti-NR2F1 (1/500, Proteintech, 24573-1-AP), anti-ERG (Abcam, ab92513), anti-SREBP2 (Abcam, ab30682).

Secondary antibodies (1/450 dilution): Alexa Fluor (AF) anti-rabbit 555 (Invitrogen, A31572), AF anti-rabbit 649 (Invitrogen, A21245), AF anti-rabbit 488 (Invitrogen, A21206), AF anti-mouse 649 (Invitrogen, A32787), AF anti-mouse 488 (Invitrogen, A21202), AF anti-goat 568 (Invitrogen, A11057), AF anti-rat 488 (Invitrogen, A21208), anti-chicken 488 (Sigma, SAB4600031), DAPI (4′ ,6-diamidino-2-phenylindole, Thermo Fisher, 62248), Hoescht 33342 (Thermo Fisher, 62249), AF 488 phalloidin (Lifetech, A12379), and AF 635 phalloidin (Lifetech, A34054).

3.5.7. Cell counts and statistics

2D sections were visualized using FIJI and Zen. Epithelial cell counting for straightened mouse oviducts were performed manually on FIJI using transverse tissue sections. 2x2 pixel-sized circles were placed within the nucleus to measure integrated density across 4 channels. Thresholds to define positive and negative cells were set manually for cell counts. Prism Graphpad was used to plot graphs and perform unpaired, two-tailed *t*-test to gauge significance.

3.6. Acknowledgements

The authors would like to thank Ms. Camille Stegan and Mr. Julien Leconte (McGill's Flow Cytometry Core Facility) for help with troubleshooting FACS. We would also like to thank Drs. Yu Chang Wang, Dunarel Badescu, Spyridon Oikonomopoulos, Jiannis Ragoussis (McGill Genome Centre), and Dr. Matthew J Ford (GCI, McGill University) for help and discussions with SmartSeq experiments. As well, we thank the McGill Advanced Bioimaging Facility (ABIF) and the McGill Integrated Core of Animal Modeling (MICAM) for technical support.

3.7. References

[1] Harwalkar, K., Ford, M.J., Teng, K., Yamanaka, N., Yang, B., Burtscher, I., Lickert, H., and Yamanaka, Y. (2021). Anatomical and cellular heterogeneity in the mouse oviduct—its potential roles in reproduction and preimplantation development†. Biology of Reproduction *104*, 1249-1261. 10.1093/biolre/ioab043.

[2] Yuan, S., Wang, Z., Peng, H., Ward, S.M., Hennig, G.W., Zheng, H., and Yan, W. (2021). Oviductal motile cilia are essential for oocyte pickup but dispensable for sperm and embryo transport. Proc Natl Acad Sci U S A *118*. 10.1073/pnas.2102940118.

[3] Muro, Y., Hasuwa, H., Isotani, A., Miyata, H., Yamagata, K., Ikawa, M., Yanagimachi, R., and Okabe, M. (2016). Behavior of Mouse Spermatozoa in the Female Reproductive Tract from Soon after Mating to the Beginning of Fertilization. Biol Reprod *94*, 80. 10.1095/biolreprod.115.135368.

[4] Yamaguchi, R., Muro, Y., Isotani, A., Tokuhiro, K., Takumi, K., Adham, I., Ikawa, M., and Okabe, M. (2009). Disruption of ADAM3 impairs the migration of sperm into oviduct in mouse. Biol Reprod *81*, 142-146. 10.1095/biolreprod.108.074021.

[5] La Spina, F.A., Puga Molina, L.C., Romarowski, A., Vitale, A.M., Falzone, T.L., Krapf, D., Hirohashi, N., and Buffone, M.G. (2016). Mouse sperm begin to undergo acrosomal

exocytosis in the upper isthmus of the oviduct. Dev Biol *411*, 172-182. 10.1016/j.ydbio.2016.02.006.

[6] Suarez, S.S., and Pacey, A.A. (2006). Sperm transport in the female reproductive tract. Hum Reprod Update *12*, 23-37. 10.1093/humupd/dmi047.

[7] Suarez, S.S. (1987). Sperm transport and motility in the mouse oviduct: observations in situ. Biol Reprod *36*, 203-210. 10.1095/biolreprod36.1.203.

[8] Bianchi, E., Sun, Y., Almansa-Ordonez, A., Woods, M., Goulding, D., Martinez-Martin, N., and Wright, G.J. (2021). Control of oviductal fluid flow by the G-protein coupled receptor Adgrd1 is essential for murine embryo transit. Nat Commun *12*, 1251. 10.1038/s41467-021-21512-w.

[9] Wang, H., Guo, Y., Wang, D., Kingsley, P.J., Marnett, L.J., Das, S.K., DuBois, R.N., and Dey, S.K. (2004). Aberrant cannabinoid signaling impairs oviductal transport of embryos. Nat Med *10*, 1074-1080. 10.1038/nm1104.

[10] Wang, S., and Larina, I.V. (2021). *In vivo* dynamic 3D imaging of oocytes and embryos in the mouse oviduct. Cell Rep *36*, 109382. 10.1016/j.celrep.2021.109382.

[11] Ford, M.J., Harwalkar, K., Pacis, A.S., Maunsell, H., Wang, Y.C., Badescu, D., Teng, K., Yamanaka, N., Bouchard, M., Ragoussis, J., and Yamanaka, Y. (2021). Oviduct epithelial cells constitute two developmentally distinct lineages that are spatially separated along the distal-proximal axis. Cell Rep *36*, 109677. 10.1016/j.celrep.2021.109677.

[12] Gegg, M., Böttcher, A., Burtscher, I., Hasenoeder, S., Van Campenhout, C., Aichler, M., Walch, A., Grant, S.G., and Lickert, H. (2014). Flattop regulates basal body docking and positioning in mono- and multiciliated cells. Elife *3*. 10.7554/eLife.03842.

[13] Burtscher, I., Barkey, W., Schwarzfischer, M., Theis, F.J., and Lickert, H. (2012). The Sox17-mCherry fusion mouse line allows visualization of endoderm and vascular endothelial development. Genesis *50*, 496-505. 10.1002/dvg.20829.

[14] Wigle, J.T., and Oliver, G. (1999). Prox1 function is required for the development of the murine lymphatic system. Cell *98*, 769-778. 10.1016/s0092-8674(00)81511-1.

[15] Elsir, T., Smits, A., Lindström, M.S., and Nistér, M. (2012). Transcription factor PROX1: its role in development and cancer. Cancer Metastasis Rev *31*, 793-805. 10.1007/s10555-012-9390-8.

[16] Ghosh, A., Syed, S.M., and Tanwar, P.S. (2017). *In vivo* genetic cell lineage tracing reveals that oviductal secretory cells self-renew and give rise to ciliated cells. Development *144*, 3031-3041. 10.1242/dev.149989.

[17] Flesken-Nikitin, A., Ralston, C.Q., Fu, D.-J., De Micheli, A.J., Phuong, D.J., Harlan, B.A., Armstrong, A.P., McKellar, D., Ghuwalewala, S., Schimenti, J.C., et al. (2024). Pre-ciliated tubal epithelial cells are prone to initiation of high-grade serous ovarian carcinoma. Nat Commun 15, 8641 (2024). https://doi.org/10.1038/s41467-024-52984-1.

[18] Larcombe, M.R., Hsu, S., Polo, J.M., and Knaupp, A.S. (2022). Indirect Mechanisms of Transcription Factor-Mediated Gene Regulation during Cell Fate Changes. Advanced Genetics *3*, 2200015. https://doi.org/10.1002/ggn2.202200015.

[19] Aibar, S., González-Blas, C.B., Moerman, T., Huynh-Thu, V.A., Imrichova, H., Hulselmans, G., Rambow, F., Marine, J.C., Geurts, P., Aerts, J., et al. (2017). SCENIC: single-cell regulatory network inference and clustering. Nat Methods *14*, 1083-1086. 10.1038/nmeth.4463.

[20] Didon, L., Zwick, R.K., Chao, I.W., Walters, M.S., Wang, R., Hackett, N.R., and Crystal, R.G. (2013). RFX3 modulation of FOXJ1 regulation of cilia genes in the human airway epithelium. Respir Res *14*, 70. 10.1186/1465-9921-14-70.

[21] Komatsu, M., and Fujita, H. (1978). Electron-microscopic studies on the development and aging of the oviduct epithelium of mice. Anat Embryol (Berl) *152*, 243-259. 10.1007/bf00350523.

[22] Murdoch, W.J., and Martinchick, J.F. (2004). Oxidative damage to DNA of ovarian surface epithelial cells affected by ovulation: carcinogenic implication and chemoprevention. Exp Biol Med (Maywood) *229*, 546-552. 10.1177/153537020422900613.

[23] Mariani, G., and Bellver, J. (2018). Chapter 9 - Proteomics and Metabolomics Studies and Clinical Outcomes. In Reproductomics, J.A. Horcajadas, and J. Gosálvez, eds. (Academic Press), pp. 147-170. https://doi.org/10.1016/B978-0-12-812571-7.00010-1.

[24] Verco, C.J., Gannon, B.J., and Jones, W.R. (1984). Variations in rabbit oviduct microvascular architecture after ovulation induced by hCG. J Reprod Fertil *72*, 15-19. 10.1530/jrf.0.0720015.

[25] Suarez, S.S., and Dai, X. (1992). Hyperactivation enhances mouse sperm capacity for penetrating viscoelastic media. Biol Reprod *46*, 686-691. 10.1095/biolreprod46.4.686.

[26] Ford, M.J., Harwalkar, K., Kazemdarvish, H., Yamanaka, N., and Yamanaka, Y. (2023). CD133/Prom1 marks proximal mouse oviduct epithelial progenitors and adult epithelial cells with a low generative capacity. Biol Open *12*. 10.1242/bio.059963.

[27] McLean, A.C., Valenzuela, N., Fai, S., and Bennett, S.A. (2012). Performing vaginal lavage, crystal violet staining, and vaginal cytological evaluation for mouse estrous cycle staging identification. J Vis Exp, e4389. 10.3791/4389.

[28] Leek, J.T., and Storey, J.D. (2007). Capturing Heterogeneity in Gene Expression Studies by Surrogate Variable Analysis. PLOS Genetics *3*, e161. 10.1371/journal.pgen.0030161.

[29] Kim, D., Paggi, J.M., Park, C., Bennett, C., and Salzberg, S.L. (2019). Graph-based genome alignment and genotyping with HISAT2 and HISAT-genotype. Nature Biotechnology *37*, 907-915. 10.1038/s41587-019-0201-4.

[30] Zaharia, M., Xin, R.S., Wendell, P., Das, T., Armbrust, M., Dave, A., Meng, X., Rosen, J., Venkataraman, S., Franklin, M.J., et al. (2016). Apache Spark: a unified engine for big data processing. Commun. ACM *59*, 56–65. 10.1145/2934664.

[31] Robinson, M.D., and Oshlack, A. (2010). A scaling normalization method for differential expression analysis of RNA-seq data. Genome Biology *11*, R25. 10.1186/gb-2010-11-3-r25.

[32] Ritchie, M.E., Phipson, B., Wu, D., Hu, Y., Law, C.W., Shi, W., and Smyth, G.K. (2015). limma powers differential expression analyses for RNA-sequencing and microarray studies. Nucleic Acids Res *43*, e47. 10.1093/nar/gkv007.

3.8. Supplementary figures

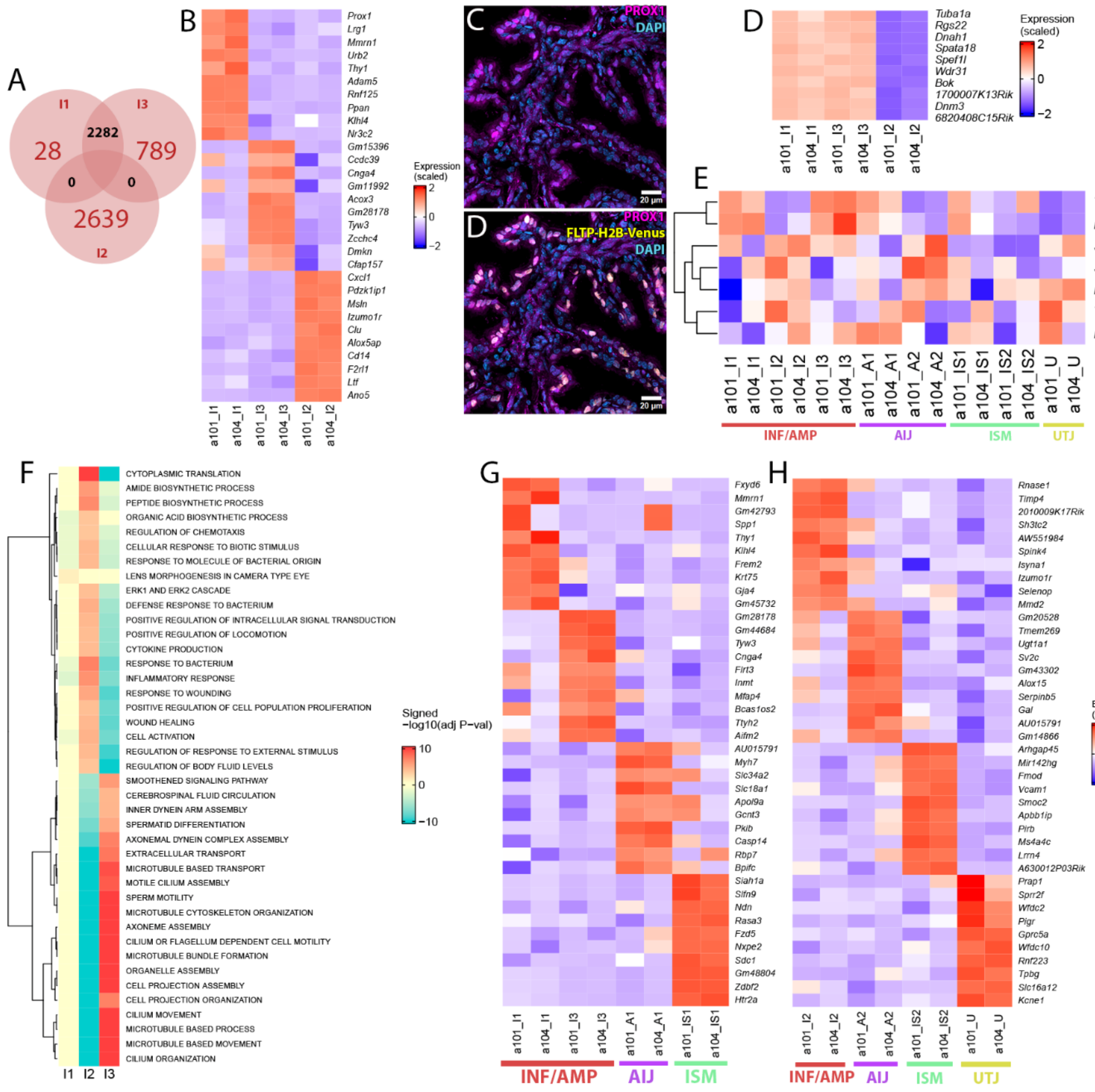

Supplementary Figure S3. 1: *Minor double positive population may represent a SC-to-MCC transitory population.*

(A) Number of DEGs in the three INF/AMP populations (I1, I2, I3). (B) Top 10 DEGs in I1, I3, and I2 populations. (C, D) PROX1 expression in the INF/AMP. PROX1 and Venus were co-expressed (D), suggesting that PROX1 was MCC-specific. (E) Top 10 DEGs shared by I1 and I3, but not detected in I2. (F) Expression of known genes in all 8 populations. (G) Top 10 upregulated genesets in I1, I2, and I3 INF/AMP populations. (H) Top 10 DEGs in 4 MCC populations along the oviduct. (I) Top 10 DEGs in 4 SC populations along the oviduct. Scale bar length = 20µm.

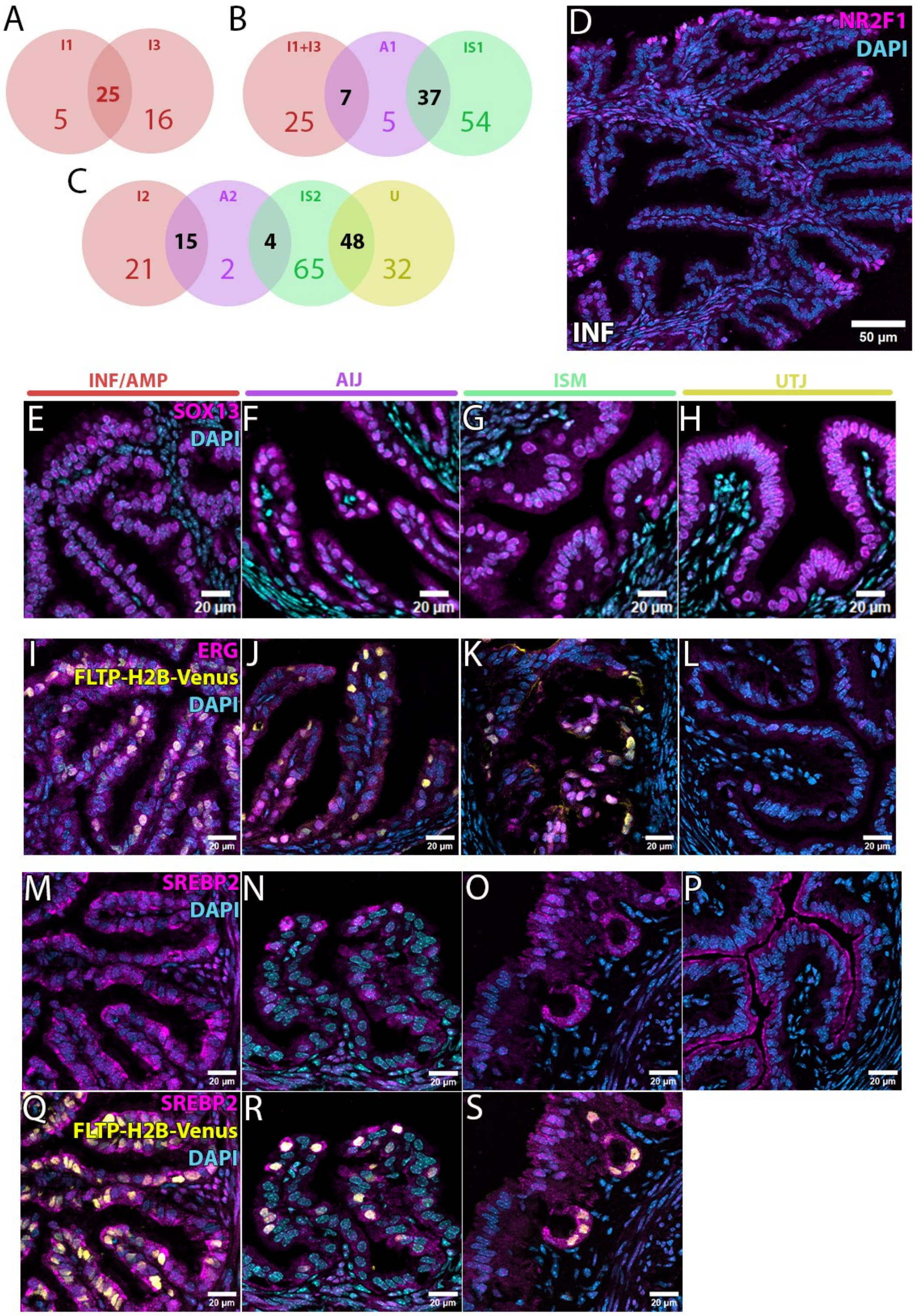

Supplementary Figure S3. 2: *mRNA-protein expression differences in some TFs.*

(A) Number of differentially expressed TFs in I1 and I3 populations, as compared to the rest of the tube. (B, C) Number of differentially expressed TFs in MCCs (B) and SCs (C) along the tube. (D) NR2F1 expression in the INF/AMP. Few epithelial cells at the tip of some INF folds expressed NR1F1. (E-H) SOX13 expression along the mouse oviduct. All epithelial cells of the INF/AMP (E), AIJ (F), ISM (G), UTJ (H) expressed SOX13. (I-L) ERG expression along the tube. ERG was expressed in the cytoplasm, surrounding the nucleus of INF/AMP epithelium (I). Some AIJ and ISM cells showed nuclear ERG (J, K). Few UTJ epithelial cells showed nuclear ERG localization. (M-S) SREBP2 expression along the oviduct. Apical SREBP2 expression was noted in MCCs of the INF/AMP (M, Q), with apical and nuclear expression in AIJ MCCs (N, R) and some ISM epithelial cells (O, S). Cytoplasmic, apical ERG localization was noted in the UTJ epithelium (S). Scale bar length = 20µm.

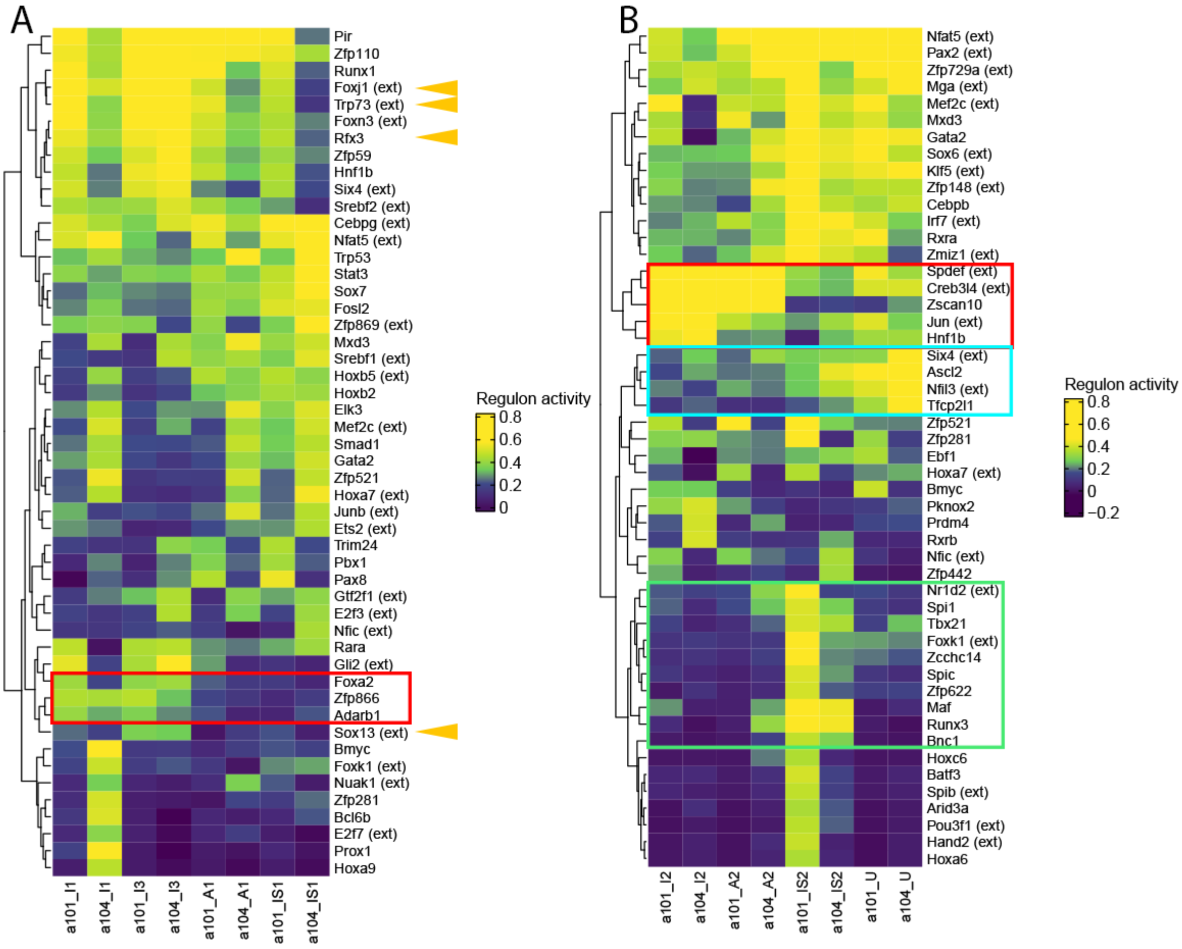

Supplementary Figure S3. 3: *Distinct regulon activities in MCCs and SCs along the tube, suggesting distinct cell states.*

(A, B) SCENIC analysis of MCC (A) and SC (B) populations predicting distinct gene regulatory networks. Orange arrows show high regulon activity in I3. Red boxes show distinct regulon activity in distal populations, while the cyan box shows distinct regulon activity in the proximal SCs. Green box shows distinct regulon activities in ISM SCs.

3.9. Conceptual link between Chapter 3 and 4

In chapters 2 & 3, I showed that each morphologically distinct region consists of a unique pair of SCs and MCCs, with distinct gene expression and potential functions. This is particularly interesting in the context of HGSCs, which present with precursor lesions in the distal FT epithelium but not the proximal. A distinct INF/AMP cellular identity could contribute to its susceptibility to malignant transformation.

Additionally, HGSCs typically occur/are diagnosed later in life, suggesting that aging-associated changes in the organ could also contribute to its distinct susceptibility. Along these lines, I found an MCC-specific aging phenotype, with large cytoplasmic vacuoles and deformed nucleus, restricted to the distal INF/AMP region and not noted in the proximal regions. Thus, in Chapter 4, I investigated the chronology and cause of this distal-specific aging-associated phenotype.

4. Aging-associated vacuolation of multi-ciliated cells in the distal mouse oviduct reflects unique cell identity and luminal microenvironment

Keerthana Harwalkar[1,2], Nobuko Yamanaka[2,3], Alain S Pacis[4], Selina Zhao[2], Katie Teng[1,2], Warwick Pitman[1,2], Mitaali Taskar[2], Vera Lynn[2], Alex Frances Thornton[2], Matthew J Ford[2], Yojiro Yamanaka[1,2,3,*]

[1]Department of Human Genetics, McGill University, Montréal, Québec, Canada

[2]Rosalind and Morris Cancer Research Institute, McGill University, Montréal, Québec H3A 1A3, Canada

[3]McGill's Integrated Core of Animal Modeling (MICAM), McGill University, Montréal, Québec H3A 1A3, Canada

[4]Canadian Centre for Computational Genomics (C3G), Genome Quebec Innovation Centre, McGill University, Montréal, Québec H3A 1A4, Canada

*Corresponding author

4.1. Abstract

The female reproductive organs present the earliest aging characteristics, such as a decline in fertility and estrous cyclicity, due to oocyte depletion and ovarian atrophy. While age-related changes in the ovary are well-documented, it is unclear if any age-associated changes occur in the other female reproductive organs, such as the oviduct/Fallopian tube. The recent recognition of the distal end of the Fallopian tube as the tissue of origin of high-grade serous tubal ovarian carcinomas (HGSCs), and that its patient demographic is strongly biased to postmenopausal women, urged us to investigate age-associated changes in this organ.

At the distal end of aged oviducts in mice, we found vacuolated multi-ciliated cells (MCCs) with a severely apically displaced and deformed nucleus. This phenotype was unique in the distal oviduct epithelium, called the infundibulum (INF) and ampulla (AMP). Ovariectomy did not affect the timeline of MCC vacuolation, suggesting little involvement of ovulation and hormonal regulation. MCC vacuolation was induced in hypoxia or hydroxyurea treatments in *in vitro* organotypic culture of all oviduct regions, not limited to the INF/AMP epithelium. This suggests high oxygen demand in MCCs, compared to other cell types, and a uniquely stressed INF/AMP epithelial microenvironment *in vivo*. We found that the blood circulation of INF/AMP depended on the ovarian artery, different from the rest of the oviduct epithelium and its circulation declined along with ovarian activities. We conclude that a decline in local blood circulation and distinct cellular identity of the INF/AMP epithelium caused age-associated MCC vacuolation, reflecting its mild, chronically stressed microenvironment.

4.2. Introduction

The oviduct is a tube that extends from the uterus to the ovary, with 4 regions demarcated by their mucosal fold morphologies, epithelial cell transcription factor expression, and proportion/distribution of multi-ciliated cells (MCCs). These regions are the infundibulum/ampulla (INF/AMP), ampulla-isthmus junction (AIJ), isthmus (ISM), and uterotubal junction (UTJ) from distal to proximal, relative to the uterus [1, 2]. Gamete and preimplantation embryo movement occurs in the oviduct, aided by the mucosal epithelium [3, 4] and smooth muscle contractions [5]. These functions are controlled by hormonal regulation, via the hypothalamic-pituitary-ovary axis, in a cyclic manner over the course of 4-5 days, called the estrous cycle in mice. Peak estrous cyclicity is noted at around 5-months of age in single housed, unmated, inbred C57BL/6J mice, and a decline in this cyclicity occurs from ~9 months. The initial phase of decline that occurs at 10-12-months of age is characterized by a progressive lengthening of estrous cycles [6]. Alongside this loss of estrous cyclicity, a decline in oocyte quality, impaired decidualization, uterine fibrosis [7, 8], prolongation of gestation/labour, and decreased litter size [9] are noted.

Although classified as a type of ovarian cancer, High Grade Serous Ovarian Carcinomas (HGSCs) originate from the distal fimbrial region of the Fallopian tubes [10, 11]. The frequency of ovulation across the reproductive lifespan is considered as a risk factor because of repetitive exposures to inflammatory cytokines and reactive oxygen species (ROS), that can induce mutations in the adjacent fimbrial epithelium [12]. On the other hand, the distal INF/AMP epithelium is developmentally and transcriptionally distinct from the rest of the oviduct epithelia [1, 13]. Therefore, this raises a possibility that the INF/AMP epithelial cells are uniquely susceptible to malignant transformation, a concept known as cellular pliancy [14]. HGSCs are diagnosed later in life, in individuals typically over 65 years of age [15], suggesting that aging may provide a unique permissive environment for HGSC initiation and/or progression.

In this study, we found MCC-specific vacuolation in the INF/AMP epithelium of mice at around 7 months of age. Size and frequency of these MCC vacuoles increased with age. Ovariectomy did not change the timeline of vacuolation, suggesting no association with repetitive ovulation or hormonal regulation. Hypoxia and hydroxyurea (HU) treatments in *in vitro* organotypic cultures induced vacuolation in MCCs of all oviduct regions, not limited to the INF/AMP epithelium. This confirms the general high energy demand of MCCs but simultaneously suggests a unique INF/AMP microenvironment *in vivo*. We realized that the INF/AMP blood circulation was coupled to that of the ovary via the ovarian artery and demonstrated that blood circulation into the ovary and INF/AMP was reduced in aged females. Thus, we conclude that MCC vacuolation in the INF/AMP epithelium of aged females is primarily due to constant high-energy demand of MCCs compared to other cell types. MCC vacuolation unique to the INF/AMP epithelium was caused by its distinct cellular property and a mild, chronically stressed INF/AMP microenvironment, due to unique circulation patterns. We propose that this could contribute to age-associated vulnerability to HGSC.

4.3. Results

4.3.1. Epithelium-lined diverticula along the aged mouse oviduct

To investigate any age-related structural changes in the mouse oviduct, we examined whole-mount and 3D confocal images of oviducts isolated from 7-month-old (7mo), 13-month-old (13mo), and 18-month-old (18mo) females. 7mo oviducts did not present with any obvious structural changes (Figure 4.1A, B). Outpouching of the continuous smooth muscle layer was noted in 13mo oviducts, predominantly in the proximal AIJ and ISM regions (Figure 4.1C, E), but not evident in the distal INF/AMP (Figure 4.1D). In oviducts isolated from 18mo mice, the distal INF/AMP region presented with outpouching of the smooth muscle (Figure 4.1G), similar to those noted in the proximal oviducts of 13mo mice (Figure 4.1E). Large outpouched cysts were restricted to the proximal oviduct (Figure 4.1F, H). Interestingly, these cysts observed throughout the tube in 18mo mice were lined with E-CAD+ve epithelium that connected into the oviduct lumen (Figure 4.1I-K), indicating that these structures were diverticula. Indeed, the outpouched epithelium that faced the lumen was SOX17+ve (Figure 4.1I-K), confirming that it originated from the oviduct epithelium [1]. It is likely caused by tears in the smooth muscle layer, potentially due to the stiffened tube structure [16] and luminal pressure. Age associated fibrosis, muscle layer thickness, and continued peristaltic movements of the oviduct could contribute to the formation of diverticula; in particular, the large diverticula observed in the ISM and UTJ.

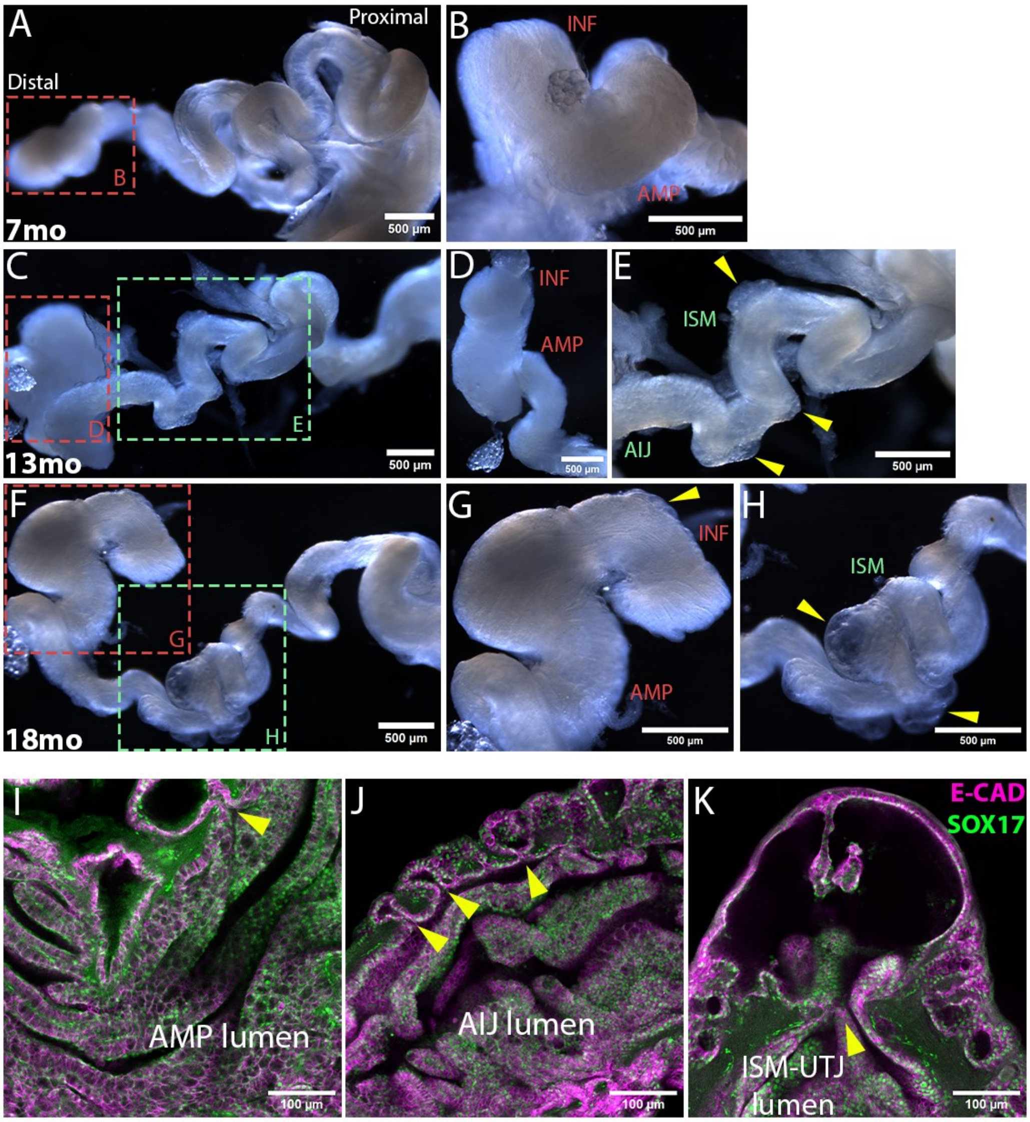

Figure 4. 1: Epithelial outpouching along the aged mouse oviduct.

(A-H) Whole-mount images of an uncoiled oviduct dissected from a 7mo (A, B), 13mo (C-E) and 18mo (F-H) mouse showing outpouching (yellow arrows in E, G, H). Aged 13mo and 18mo oviducts were less translucent and stiff, relative to 7mo oviducts. Red and green dotted squares indicate location of magnified distal and proximal images, respectively. (I-K) 3D immunofluorescence of 18mo AMP (I), AIJ (J), and ISM-UTJ (K) regions showing E-CAD and SOX17-expressing epithelial cells lined the diverticula that connected into the oviduct lumen (yellow arrows in I-K).

4.3.2. A large cytoplasmic vacuole with an apically displaced, crescent-shaped deformed nucleus was uniquely noted in INF/AMP MCCs of the aged oviduct.

To investigate any age-related changes at the cellular level, we examined transverse sections of oviducts isolated from 4-month-old (4mo) and 18mo females from four distinct regions: INF/AMP, AIJ, ISM and UTJ (Figure 4.2A-D, K-P). In the 4mo INF/AMP epithelium, the nucleus of epithelial cells was round or oval shaped and positioned basally (Figure 4.2A, B). Many epithelial cells in the 18mo INF/AMP epithelium carried a large cytoplasmic vacuole, with apically displaced nucleus that was often crescent-shaped due to the vacuole (Figure 4.2C). Nuclear FLTP-H2B-Venus expression indicated that all vacuolated cells were MCCs (Figure 4.2D). We measured the distance between the base of the nucleus and the stroma (Figure 4.2E) to quantify the severity of nuclear displacement and found that the apical displacement of MCC nuclei in 18mo mice was significantly larger than in 4mo mice (Figure 4.2F). The nucleus of secretory cells (SCs) was also apically displaced and protruded from the epithelial monolayer in 18mo oviducts, although their nuclear shape remained round or oval (Figure 4.2C, D). Similar to MCCs, the apical displacement of SC nuclei at 18mo was significantly larger than at 4mo (Figure 4.2G). It is reported that SC protrusion from the epithelial monolayer is observed during the female hormonal cycle [17]. In agreement with this, we found that protrusion of SC nuclei, marked by PAX8, was prevalent during diestrus stage (Figure 4.2H, J), as compared to estrus stage (Figure 4.2I, J) in young females, suggesting that SC protrusion was not exclusive to aging.

Interestingly, the MCC vacuolation and apically displaced crescent-shaped nuclei were observed in the INF/AMP epithelium (Figure 4.2A-D), but not in the other regions of the oviduct. The nuclear shape in the AIJ, ISM and UTJ epithelium was generally round or oval, with no sign of cytoplasmic vacuolation (Figure 4.2K-P). There was no apparent difference in the distribution pattern (Figure 4.2A-D, K-P) and proportion (Figure 4.2Q) of MCCs between

4mo and 18mo oviducts. We concluded that MCC vacuolation and apical displacement of the nucleus were aging phenotypes unique to the INF/AMP epithelium.

We previously established that there is a sharp boundary between each distinct region of the oviduct, visualized by changes in transcription factor expression, MCC proportion/distribution and mucosal fold morphology [1]. At the bevelled AMP-AIJ boundary, located between oviduct coiling/turning points 2 and 3, the AMP epithelium occupied the anti-mesosalpinx side recognized by a higher proportion of MCCs, while the AIJ epithelium began on the mesosalpinx side (Figure 4.2R, S). We found that only AMP MCCs, indicated by lack of PAX8 expression, had a large cytoplasmic vacuole with an apically displaced, crescent-shaped nucleus, while the AIJ MCCs did not show any apparent morphological abnormality, despite identical proximity to the ovary (Figure 4.2T-V). This suggests that the aging-associated MCC vacuolation in the INF/AMP epithelium is linked with its unique cell property rather than physical proximity to the ovary.

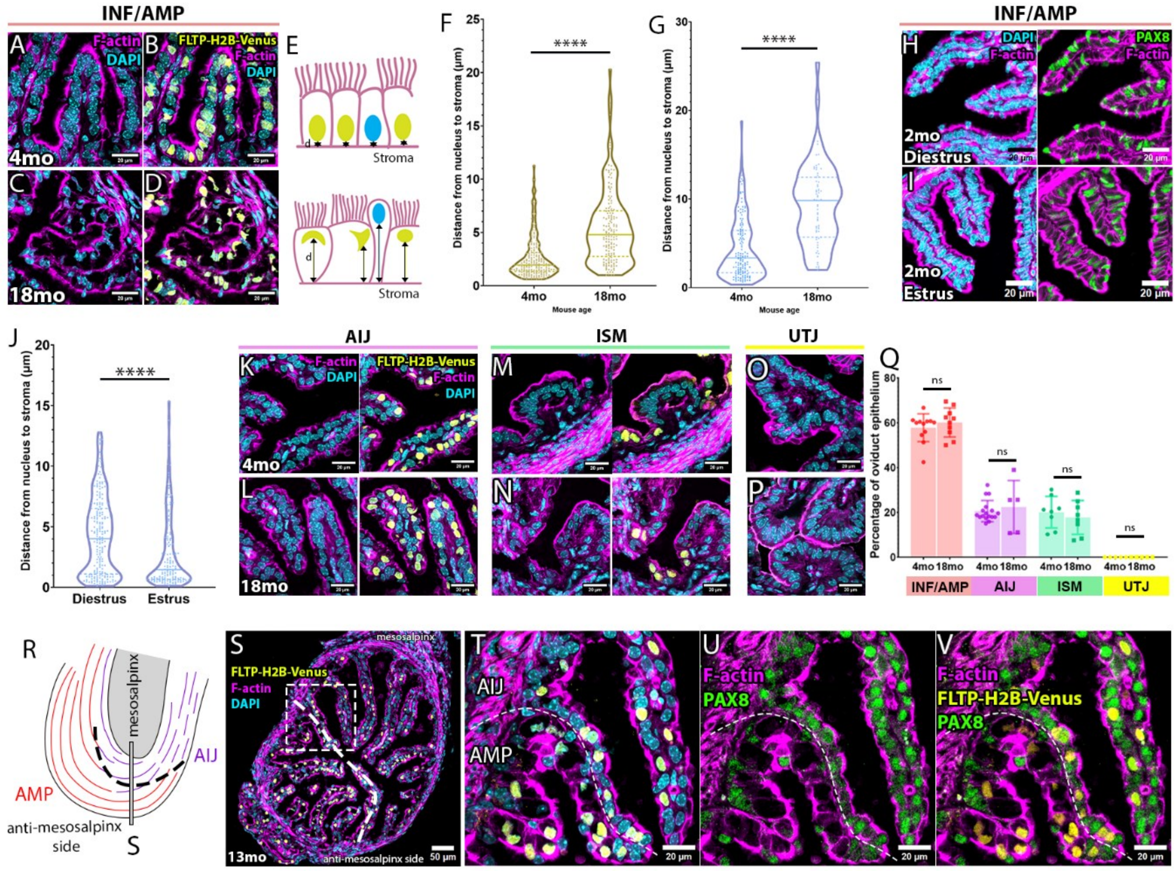

Figure 4. 2: Aging-associated apical displacement of nucleus and nuclear anomaly were restricted to INF/AMP MCCs.

(A-D) Morphology of epithelial cells lining the INF/AMP mucosal folds in oviducts dissected from 4mo (A, B) and 18mo (C, D) mice. SC nuclei and misshapen MCC nuclei, identified by FLTP-H2B-Venus-ve and +ve nuclei respectively, in the 18mo INF/AMP region were apically displaced (D), relative to 4mo INF/AMP (B). (E) Illustration showing measurement of nuclear apical displacement in 4mo (top) and 18mo (bottom) INF/AMP epithelium. (F) Measurements of the distance between MCC nucleus to stroma in the INF/AMP region of 4mo (mean ± SD, 2.606 ± 1.958 µm; N=3) and 18mo (5.482 ± 3.541 µm; N=3) oviducts. (G) Measurements of the distance between SC nuclei to stroma in the INF/AMP region of 4mo (4.415 ± 3.45 µm; N=3) and 18mo (9.324 ± 4.559 µm; N=3) oviducts. Each point represents a measurement/cell.

The continuous line represents the median, while the dotted lines show the quartiles. **** = $p < 0.0001$. (H, I) Morphology of epithelial cells lining the INF/AMP mucosal folds of young 2mo mice in diestrus (top) and estrus (bottom) stages. PAX8+ve SCs protrude from the epithelial monolayer at diestrus stage (H). At estrus stage, PAX8+ve SCs were embedded in the epithelial monolayer (I). (J) Measurements of the distance of SC nuclei to stroma in the INF/AMP region of oviducts isolated at diestrus stage (4.28 ± 3.219 µm; N=3) and estrus stage (2.791 ± 3.007 µm; N=3). (K-P) Morphology of epithelial cells lining the AIJ (K, L), ISM (M, N) and UTJ (O, P) mucosal folds in oviducts dissected from 4mo (K, M, O) and 18mo (L, N, P) mice. No reproducible cellular changes were noted in the epithelium. (Q) No significant change in the proportion of MCCs in the INF/AMP, AIJ, ISM and UTJ of 4mo and 18mo oviducts, ns = $p > 0.05$. Error bars indicate standard deviation. (R) Illustration of the bevelled, sharp boundary of mucosal fold morphology, cell subtype, and change in proportion of MCCs between turns 2 and 3. Black dotted line marks the boundary, and gray rectangle represents location of image in S. (S) Transverse section of the sharp boundary between turns 2 and 3, as illustrated in (R). Drop in MCC proportion on the mesosalpinx side (top), characteristic of the AMP-AIJ boundary. White dotted line marks the boundary. White, dotted square indicates location of T-V. (T-V) Apical displacement of nucleus was restricted to the AMP (bottom), but not evident in the AIJ (top, T). Change in PAX8 expression pattern in the AMP and AIJ epithelium (U), with MCCs being PAX8-ve in the AMP but PAX8+ve in the AIJ (U, V), confirming distinct INF/AMP-specific aging phenotype even at the boundary.

4.3.3. Progressive increase in size, frequency of MCC vacuolation and apical nuclear displacement in the INF/AMP epithelium after 6 months

To determine the timeline of this age-related phenotype in the distal INF/AMP epithelium, we examined 7mo and 13mo oviducts. Both 7mo and 13mo INF/AMP epithelium had varying proportions of apically displaced MCC nuclei, with most SC nuclei protruding from the epithelial monolayer (Figure 4.3A, B). The position of the nucleus in INF/AMP MCCs was progressively, apically displaced from 4mo to 18mo (Figure 4.3C). Apical displacement of SC nuclei at 13mo was significantly larger than 4mo and 7mo, but not significantly different from 18mo (Figure 4.3D), due to SC body protrusion from the epithelial monolayer at 13mo and 18mo (Figure 4.3B, 4.2D). We found individual female variation in 7mo oviducts: 1) some individuals exhibited exaggerated apical displacement of MCC nuclei and large, empty cytoplasmic spaces in many cells (Figure 4.3E; N=2/3), similar to that noted in 13mo or 18mo mice, and 2) an individual presented with low-to-moderate apical displacement with small cytoplasmic spaces (Figure 4.3F; N=1/3).

The vacuole was located at the basal side of MCCs, clearly distinct from secretory vesicles typically located at the apical side. It appeared to cause apical displacement and crescent-shaped deformation of the nucleus. Haematoxylin and eosin (H&E) staining showed empty cytoplasmic spaces, ruling out the possibility of diluted cytoplasm, protein inclusions, or nucleic acid accumulation (Figure 4.3E, F). In agreement with this, a classic TEM study of the AMP epithelium in 7- to 24-month-old mice show MCCs with large vacuoles containing heterogeneously dense materials, with no obvious changes in other organelles including cilia [17]. We found that the large cytoplasmic vacuole was lined with sodium/potassium-transporting ATPase subunit alpha-1 (ATP1A1; Fig. 4.3G) and did not show lipid or glycogen accumulation (Supplementary Figure S4.1A-C), suggesting aqueous/fluid accumulation in

INF/AMP MCCs. Cytoplasmic, punctate ATP1A1 localization surrounded the small vacuoles in MCCs with low-to-moderate apical displacement (Figure 4.3H). Cytoplasmic ATPA1 was not observed in the proximal regions (Supplementary Figure S4.1D-F). Occasional punctate ATP1A1 was noted in the INF/AMP of 3mo mice (Supplementary Figure S4.1G).

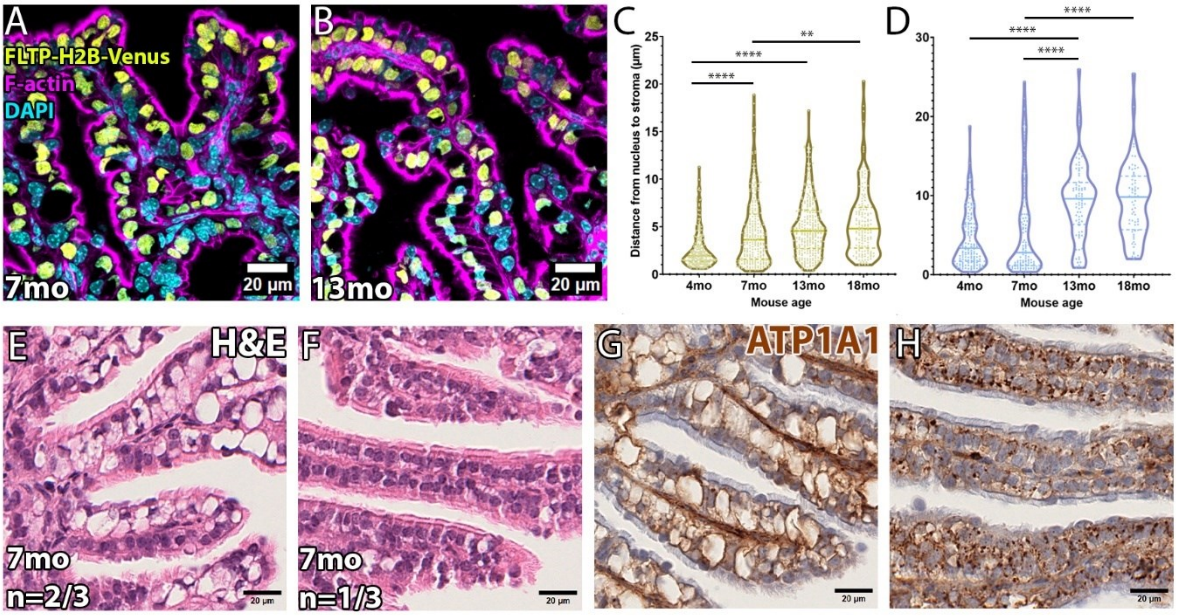

Figure 4. 3: Progressive apical displacement of nucleus and vacuolation with aqueous accumulation.

(A, B) Morphology of epithelial cells lining the INF/AMP mucosal folds in oviducts dissected from 7mo (A) and 13mo (B) mice. SC nuclei and misshapen MCC nuclei, identified by FLTP-H2B-Venus-ve and +ve nucleus respectively, were apically displaced. (C) Measurements of the distance from MCC nucleus to stroma in the INF/AMP region of 4mo, 7mo (4.476±3.543 µm; N=3), 13mo (5.014±3.085 µm; N=3), and 18mo oviducts showed progressive apical displacement. (D) Measurements of the distance from SC nucleus to stroma in the INF/AMP region of 4mo, 7mo (5.628±6.045 µm; N=3), 13mo (9.285±4.790 µm; N=3), and 18mo oviducts. Each point represents a measurement/cell. The continuous line represents the median, while the dotted lines show the quartiles. **** = $p < 0.0001$, ** = $p < 0.001$. (E, F) H&E staining of the 7mo INF/AMP region. Two phenotypes were noted: 1) exaggerated/large, empty cytoplasmic vacuoles and apically displaced nuclei (E) and 2) small/indiscernible empty spaces/vacuoles and nuclei located in the centre of the cells (F). (G, H) ATP1A1 expression in 7mo INF/AMP region. Large cytoplasmic vacuoles were lined with ATP1A1 (G), while MCCs with small/indiscernible vacuoles contained apically located ATP1A1+ve punctae (H).

4.3.4. INF/AMP MCC vacuolation was independent of ovulation and estrous cycling

The INF/AMP region is located directly adjacent to the ovary, a reproductive organ that undergoes ovulation every 4-5 days in mice [18]. We considered two possibilities: 1) Ovulation-associated events like cell damage due to the proximity to the ovary. The distal oviduct is exposed to events like exposure to oxidative stress, inflammation-like response, and production of reactive oxygen species (ROS), associated with ovulation, that induce repetitive stress in the adjacent INF/AMP epithelium [19]. 2) The other possibility is estrous cycle-associated events like epithelial cell turnover. It is known that the INF/AMP epithelium shows fluctuation in the proportion of SCs and MCCs in response to hormonal regulation [20]. Decline in estrous cyclicity occurs by ~9-months in inbred mice [21], characterized by a progressive lengthening of estrous cycles followed by cyclic cessation and anestrus by 11 to 16-months of age. Thus, age-associated lack of the hormonal cycling may contribute to MCC vacuolation.

To address these possibilities, we performed bilateral ovariectomy (OVX) in 2mo mice and evaluated the short and long-term impact to oviduct epithelial cells. For short-term analysis, we isolated the reproductive tracts 1-month post OVX. In these oviducts, discernible cytoplasmic vacuoles were not observed (Figure 4.4A), suggesting that MCC vacuolation was not a response to lack of estrous cycling. It is of worth to note that the INF/AMP SC nuclei were displaced apically due to SC protrusion from the epithelial monolayer (Figure 4.4A, E), similar to the diestrus stage in non-OVX females.

For the long-term analyses, we isolated reproductive tracts 5- and 11-months post OVX. At 5-months post OVX, when the age of these mice was 7mo, we observed MCC vacuolation in the INF/AMP epithelium (Figure 4.4B), showing that the timeline of MCC vacuolation was unaffected by OVX. In agreement with this, vacuoles were not noted in the INF/AMP of mice

3-months post OVX, when the age of the mice was 5mo (Supplementary Figure S4.2A). Thus, OVX did not facilitate or prevent MCC vacuolation. Interestingly, the apical displacement of the nucleus in MCCs at 5-months post OVX was not significantly different from 1-month post OVX (Figure 4.4D), despite noticeable vacuole formation. Instead, the cellular height of the MCC epithelium in mice 5-months post OVX (8.557±1.84 µm) was lower than 1-month post OVX (9.427±2.244 µm). The shape of MCCs was cuboidal with a round nucleus in OVX females while it is packed and columnar with an oval-shaped nucleus in non-OVX females. Taken together, bilateral OVX did not prevent or facilitate MCC vacuolation, but the height of the epithelial cells was decreased. This was reflected in a significant decrease in apical displacement of INF/AMP SC nuclei at 5-months post OVX, despite obvious protrusion from the epithelial monolayer (Figure 4.4B, E). A large cytoplasmic vacuole was noted in individual INF/AMP MCCs at 11-months post OVX, with an apically displaced nucleus (Figure 4.4C, D). INF/AMP SC nuclei at 11-months post OVX were also apically displaced relative to 5-months post OVX (Figure 4.4E), due to progressive enlargement of cytoplasmic vacuoles resulting in increased epithelial cell height at 11-months post OVX. Finally, despite cell shape change and loss of estrous cycling/ovulation, there was no significant difference in the proportion of MCCs in the INF/AMP region isolated from mice that were 2-4mo, or 1- and 11-months post bilateral OVX (Figure 4.4F), suggesting low epithelial cell turnover, consistent with previous studies [20, 22]. No discernible cytoplasmic vacuoles were noted in the AIJ, ISM, and UTJ at 11-months post OVX (Supplementary Figure S4.2B-D).

Since bilateral OVX completely terminates the ovarian hormonal cycle, we performed unilateral ovariectomy surgery in 2mo mice to delineate ovulation and hormonal cycle-associated homeostatic events in the epithelium. We isolated reproductive tracts 5-months post unilateral OVX (Figure 4.4G) and found MCC vacuolation on both sides, with no apparent difference between OVX and control sides (Figure 4.4H, I). Maintenance of estrous cycling without ovulation did not prevent MCC vacuolation. However, apical displacement of MCC nuclei on the OVX side was smaller than the control/intact side, which could be a result of cyclic cell shape changes to accommodate OCCs following ovulation. Additionally, there was no significant difference in MCC nucleus apical displacement between the OVX side and mice 5-months post bilateral OVX (Figure 4.4J) or in displacement of SC nuclei (Figure 4.4K). Thus, we conclude that the MCC vacuolation is not caused by repetitive ovulation or estrous cycle-associated events.

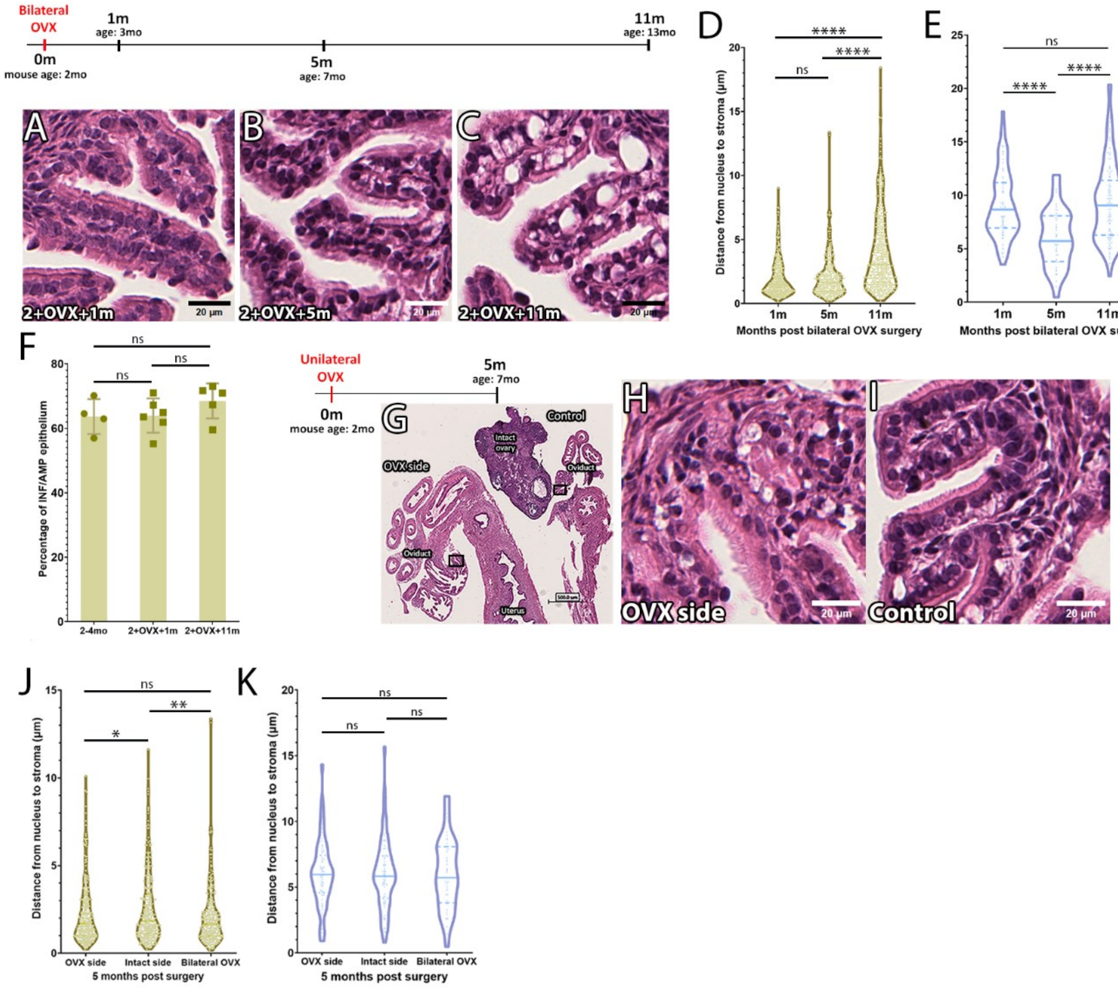

Figure 4. 4: Timeline of MCC-specific cytoplasmic vacuolation is unaffected regardless of loss of ovulation and estrous cycling.

(A-C) H&E staining of the INF/AMP region in oviducts dissected from mice 1 month (A), 5 months (B), and 11 months (C) post bilateral OVX. Vacuoles were observed in INF/AMP regions of mice 5- and 11-months post bilateral OVX. (D) Measurements of the distance from MCC nucleus to stroma in the INF/AMP region of mice 1m (1.937±1.402 µm; N=3), 5m (2.077±1.656 µm; N=3), and 11m (3.977±2.977 µm; N=4) post bilateral OVX. (E) Measurements of the distance from SC nucleus to stroma in the INF/AMP region of mice 1m (9.124±3.146 µm), 5m (5.994±2.682 µm), and 11m (9.334±3.694 µm) post bilateral OVX. Changes in apical displacement of SC nucleus corresponded with changes in the height of MCC epithelium. (F) No change in proportion of MCCs in the INF/AMP of oviducts from non-OVX 2-4mo mice, and OVX mice dissected at 1m and 11m post surgery, ns = $p > 0.05$. Error bars indicate standard deviation. (G-I) H&E staining of the INF/AMP region in oviducts dissected from mice 5 months post unilateral OVX. Cytoplasmic vacuoles were noted in the ovariectomized/OVX side (H) and side with the ovary intact/control side (I). (J) Measurements of the distance from MCC nucleus to stroma in the INF/AMP region of mice 5m post unilateral OVX, comparing distances on the OVX side (2.220±1.705 µm; N=3) and control side (2.550±1.982 µm; N=3) to the INF/AMP region of mice 5m following bilateral OVX. The intact side had the largest apical nuclear displacement. (K) Measurements of the distance of SC nuclei to stroma in the INF/AMP region of mice 5 months post unilateral (OVX side = 6.013±2.493 µm, intact side = 5.955±2.642 µm) and bilateral OVX. Each point represents a measurement/cell. The continuous line represents the median, while the dotted lines show the quartiles. **** = $p < 0.0001$, ** = $p < 0.001$, * = $p < 0.01$, ns = $p > 0.05$.

4.3.5. Enrichment of genesets associated with ER, metabolic, mitochondrial stress and/or ATP metabolism in aged INF/AMP cells, suggesting a metabolically stressed microenvironment.

To investigate the changes in the aged INF/AMP microenvironment accompanying MCC vacuolation, we performed single-cell RNASeq of 16,948 cells pooled from the INF/AMP region of three 18mo mice (Aged_INFAMP) and compared this to 10,281 cells isolated from the INF/AMP of a single estrus stage 3mo mouse (Estrus_INFAMP). Cells from the INF/AMP region of the mouse oviduct clustered into 15 clusters that were then grouped into 10 cell types/populations based on a combination of their top 5 highly expressed genes and known cell subtype markers (Figure 4.5A, Supplementary Figure S4.3, S4.4A-M). These cell populations include: 1 - secretory cells/SCs (cluster 1, 2, 11 expressing Epcam, Wt1, Pax8, Ovgp1, Sox17; Supplementary Figure S4.3, S4.4A-D), 2 - stromal cells (cluster 3, 7, 10 expressing Dcn, Igfbp6, Pdgfra; Supplementary Figure S4.3, S4.4F), 3 - multi-ciliated cells/MCCs (cluster 4 expressing Epcam, Wt1, Foxj1; Supplementary Figure S4.4A, B, E), 4 - smooth muscle cells (cluster 5, 14 expressing Acta2, Actg2, Dmd; Supplementary Figure S4.3), 5 - endothelial cells (cluster 6 expressing Pecam1, Sox17; Supplementary Figure S4.4D, G), 6 - antigen presenting cells/APCs (cluster 8 expressing Cd52, H2-Aa; Supplementary Figure S4.3, S4.4H), 7 - vascular smooth muscle cells/VSMCs (cluster 9 expressing Acta2, Rgs5; Supplementary Figure S4.3), 8 - T-cells (cluster 12 expressing Cd52, Cd3e; Supplementary Figure S4.4H, I), 9 - mesothelial cells (cluster 13 expressing Wt1, Msln, Dcn, Igfbp6; Supplementary Figure S4.3, S4.4B, H), and 10 - red blood cells/RBCs (cluster 15 expressing Hbb-bs, Supplementary Figure S4.3). Surprisingly, despite the apparent morphological differences, there was no difference in cell states/populations. All populations in Estrus_INFAMP and Aged_INFAMP overlapped with each other (Figure 4.5B). In all clusters, cells from Aged_INFAMP had more upregulated genes than downregulated genes, relative to Estrus_INFAMP (Figure 4.5C).

Using Gene Set Enrichment Analysis (GSEA), we found that aged 18mo INF/AMP MCCs (cluster 4) showed downregulation of genes associated with cilia movement and organization, and upregulation of genes associated with hydrogen peroxide metabolism, unfolded protein response (UPR), and negative regulation of cell death (Figure 4.5D). This reflects an adaptive/compensatory response to cellular stress, in particular, endoplasmic reticulum (ER) stress in MCCs. Further, aged 18mo INF/AMP SCs (clusters 1, 2, 11) showed downregulation of genes associated with transmembrane receptor protein tyrosine kinase signaling, actin filament-based process, and cell migration/movement. Similar to the MCCs, they showed upregulation of genes associated with stress responses such as UPR, ATP metabolic process, and mitochondrial organization/transport (Figure 4.5E; Supplementary Figure S4.5A-C). Since many of the upregulated genesets are associated with ER stress, we stained for p-EIF2α, a key translational regulator regulating stress responses [23], and found nuclear staining in most SCs and MCCs of 4mo and 13mo mice (Supplementary Figure S4.6A, B). Additionally, we also found cytoplasmic, punctate staining in both INF/AMP SCs and MCCs of 13mo mice (Supplementary Figure S4.6B), which could suggest stress granules.

Stromal cells were divided into three clusters and showed downregulation of genes associated with ECM production in cluster 3 (Supplementary Figure S4.5D) and 7 (Supplementary Figure S4.5E), ribosome biogenesis and RNA processing in cluster 10 (Supplementary Figure S4.5F). Cluster 3 stromal cells showed upregulation of genesets associated with various biosynthetic and metabolic processes (fatty acid, organic acid, monocarboxylic acid), negative regulation of cell death, and immune system activity regulation (lymphocyte and T-cell activation) (Supplementary Figure S4.5D), reflecting adaptive mechanisms in response to cellular stress and/or a gradual decline in metabolic efficiency. On the other hand, cluster 7 stromal cells did not show significant upregulation of genesets, as compared to 3mo cells (Supplementary Figure S4.5E). Cluster 10 stromal cells showed upregulation of genes associated with acute inflammatory response, cell adhesion, and cytokine production (Supplementary Figure S4.5F), reflecting a response to inflammation/resolution of inflammation, facilitation of tissue repair, and/or cellular senescence.

Cluster 5 smooth muscle cells showed downregulation of genes associated with muscle organisation, blood circulation, RNA metabolic processes, and ribosome biogenesis, and upregulation in tissue growth, cell adhesion, and negative regulation of cell death (Supplementary Figure S4.5G). There was no enrichment of genesets in cluster 14 smooth muscle cells (Supplementary Figure S4.5I). Taken together, most populations were typically responding to cellular metabolic stresses, with a shift/decrease in biogenesis activities, and facilitation of tissue repair to maintain structural integrity. VSMCs showed downregulation of genes associated with tissue growth, while upregulation in genesets associated with vascular tone alteration, regulation of IGFR signaling, removal of ROS/RNS species, ATP metabolism, and monocarboxylic, carbohydrate metabolism (Supplementary Figure S4.5H).

Among immune cells, T-cells and APCs (B-cells, macrophages, dendritic cells) showed upregulation of genesets associated with UPR (Supplementary Figure S4.5J, K), suggestive of response to cellular stress. Endothelial cells showed downregulation in tissue and blood vessel growth, while upregulation in with antigen presentation, superoxide radical/hydrogen peroxide removal, and various metabolic processes (Supplementary Figure S4.5L). Finally, the mesothelial cells that line the INF/AMP serosa showed downregulation in nerve function and ECM organization, while upregulation in UPR, mitochondrial transport/organization, ATP metabolism, and regulation of cell death (Supplementary Figure S4.5M), suggesting ER stress, energy demand compensation, and response to cellular stress.

Taken together, the single-cell transcriptomes of all isolated cells from 18mo INF/AMP indicated a general reduction of biogenesis and growth-related genes, and upregulated stress response genes and ATP energy demands compensation, without a clear indication of inflammation.

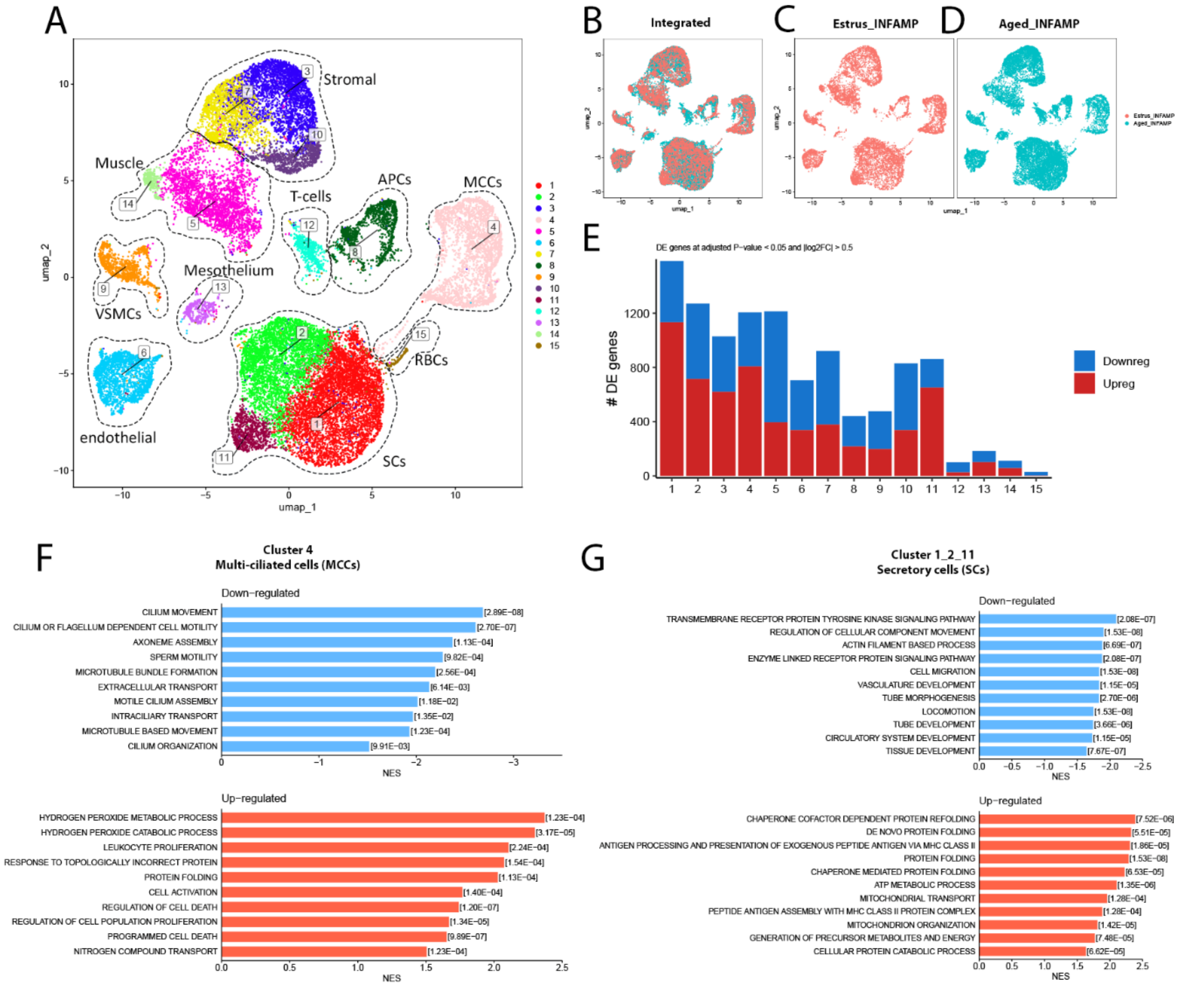

Figure 4. 5: Genesets associated with ROS metabolism, ER stress, and cell death regulation were upregulated in 18mo INF/AMP MCCs, while ER stress, ATP metabolism, mitochondrial transport genesets were upregulated in 18mo INF/AMP SCs.

(A) Integrated UMAP plot colour-coded by cluster membership, cell populations are labelled and enclosed within dotted lines, identified based on top 5 genes and known markers shown in (Supplementary Figure S4.3, 4.4) (A). (B) UMAP clustering of cells isolated from a 3mo estrus stage mouse (orange) and 18mo mice (blue) showed overlap between the two (left). (C)

Number of differentially expressed genes in each cluster, adjusted for p-value < 0.05 and $|\log2FC| > 0.5$, between INF/AMP cell populations isolated from 3mo estrus stage mouse and 18mo mice. (D) Genesets downregulated (top) and upregulated (bottom) in INF/AMP MCCs of 18mo mice, as compared to a 3mo estrus stage mouse. (E) Genesets downregulated (top) and upregulated (bottom) in INF/AMP SCs of 18mo mice, as compared to a 3mo estrus stage mouse.

4.3.6. Hypoxia or hydroxyurea treatment induced MCC vacuolation in vitro organotypic slice cultures.

It has been shown that cellular vacuolation in *in vitro* cultures occurs in response to ER stress, ATP depletion/shortage, cellular senescence, metabolic imbalance, bacterial toxins/viral components, exposure to drugs/toxic chemicals/pollutants, and hypoxia [24-26]. To determine the potential cause of MCC vacuolation, we developed an *in vitro* organotypic slice culture system (150µm thick slices). Since many of the upregulated genesets in 18mo MCCs and SCs were associated with ER stress (Figure 4.5D, E), we treated INF/AMP slice cultures with 5µM tunicamycin (TUN) for 24 hours to induce ER stress. However, TUN treatments did not result in any noticeable cellular changes (Supplementary Figure S4.6C, D), suggesting that MCC vacuolation was not a consequence of ER stress.

ATP depletion using a combination of Antimycin A and 2-deoxyglucose (2-DG) treatment results in internalization of Na, K-ATPase in MDCK cells [27]. The combined treatment of these two inhibitors visibly affected INF/AMP MCCs after 24hrs. Many MCCs protruded from the epithelial monolayer, along with condensed nucleus and occasional cleaved caspase 3 expression (Figure 4.6A-F), suggesting apoptotic MCCs. While Antimycin A treatment alone also resulted in similar MCC protrusion in INF/AMP MCCs (Figure 4.6G, J) and termination of cilia beating (data not shown), 2-DG alone did not (Supplementary Figure S4.6E-G), suggesting that INF/AMP MCCs were highly dependent on cellular respiration. Antimycin A-induced MCC protrusion was unique to INF/AMP slices but not observed in AIJ and ISM slices (Figure 4.6G-L), suggesting region-specific cellular respiration dependency. This is consistent with a recent study that reported distinct cell state/type responses to mitochondrial dysfunction in the lung, dependent on cellular context [28].

No significant enrichment in genesets associated with cellular senescence was noted in the single-cell transcriptomic analysis (Supplementary Figure S4.6H). In agreement with this, we did not find significant changes in the expression of cellular senescence-associated pseudo-DNA damage response genes including cell cycle arrest-associated P16 and P21, or DNA damage marker phospho-H2AX [29] in 18mo and 2mo mice (Supplementary Figure S4.6I-N). Although we found the absence of Lamin-B1, often associated with cellular senescence, in the 18mo oviduct (Supplementary Figure S4.6O), we discovered that Lamin-B1 showed a cyclic expression pattern during the estrous cycle in young females, with high intensity nuclear membrane localization in the estrus stage (Supplementary Figure S4.6P) and low intensity in diestrus stage (Supplementary Figure S4.6Q). Unexpectedly, phospho-H2Ax nuclear punctae were predominantly observed in INF/AMP MCCs throughout adulthood and in aging (Supplementary Figure S4.6M, N).

Induction of metabolic stress/nutrient deprivation with 2μM 6-AN (pentose phosphate pathway inhibitor; Supplementary Figure S4.6R), 1μM YZ9 (PFKFB3/glycolysis inhibitor; Supplementary Figure S4.6S), 0.8μM ST045849 (hexosamine biosynthesis pathway inhibitor; Supplementary Figure S4.6T), 1μM Shikonin (PKM2/glycolysis inhibitor; Supplementary Figure S4.6U), and 10μg/ml CHX (cycloheximide, protein synthesis inhibitor; Supplementary Figure S4.6V) for 24 hours in *in vitro* organotypic slice cultures did not result in significant, discernible cellular changes.

Although there was no significant enrichment of genesets associated with hypoxia in 18mo INF/AMP (Supplementary Figure S4.6W), *in vitro* INF/AMP tissue slices cultured for 4 days in 3% O_2 (chronic, mild hypoxia) reproducibly induced cytoplasmic vacuolation and deformed nucleus in MCCs (Figure 4.6P, S), but similar 4-day-long culture in 21% O_2 (normoxia) did not (Figure 4.6M, S). Chronic hypoxia results in reduced ATP demand and rate of mitochondrial oxygen consumption due to ROS elevation [30]. Thus, the cytoplasmic vacuolation induced by hypoxia could be a MCC response to ATP shortage and not ATP depletion. Interestingly, hypoxia-induced MCC vacuolation was not restricted to the INF/AMP epithelium but also observed in AIJ and ISM epithelia (Figure 4.6N, O, Q, R, S). No vacuolated SCs were noted in slice cultures of any of the regions (Figure 4.6M-R, Supplementary Figure S4.6X, Y). While the cause for unique MCC vacuolation in the INF/AMP epithelium *in vivo* remains a question, *in vitro* experiments suggest that MCCs are more sensitive to hypoxia than SCs.

Hydroxyurea (HU) treatment in *in vitro* organotypic slice cultures at low doses, known to induce ROS in cycling cells [31], did not result in discernible cellular changes (Figure 4.6T, U, W). Interestingly, 24-hour-long treatment with high dose HU, known to cause dNTP depletion and replication stress in cycling cells [32], induced a large cytoplasmic vacuole and deformed nucleus in MCCs (Figure 4.6V, W).

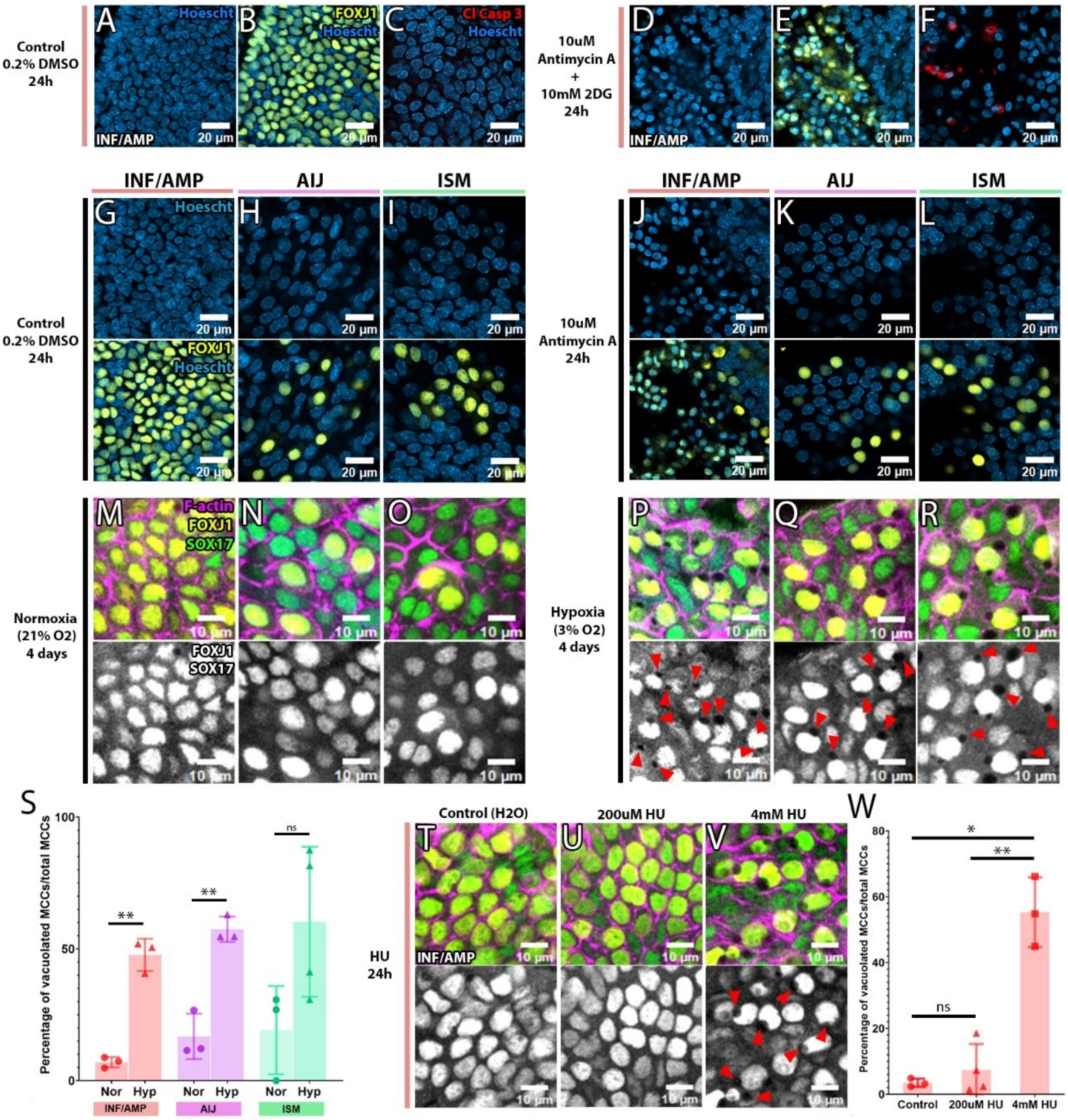

Figure 4. 6: Hypoxia or HU treatment induced MCC vacuolation.

(A-F) Inhibition of cellular respiration and glycolysis in organotypic slice cultures of the INF/AMP region. (A-C) Cultured slice from INF/AMP region with round nuclei (A), of which most cells were FOXJ1+ve MCCs (B) and Cleaved Caspase 3-ve, suggesting no apoptotic cells (C). (D-F) Treatment with Antimycin A and 2-DG for 24 hours resulted in MCCs with condensed nucleus (D, E), of which some cells were positive for Cleaved Caspase 3, suggesting apoptotic cells (F). (G-L) Inhibition of cellular respiration in organotypic slice cultures of the

INF/AMP (G, J), AIJ (H, K), and ISM (I, L). 24-hour-long Antimycin A treatment resulted in MCC protrusion from the epithelial monolayer and condensed nucleus (J) but did not affect AIJ and ISM MCCs (K, L). Scale bars = 20µm. (M-R) Organotypic slice culture for 4 days in normoxia (M-O) or hypoxia (P-R). When cultured in hypoxia, FOXJ1+ve MCCs of the INF/AMP (P), AIJ (Q) and ISM (R) present with empty vacuoles and deformed nucleus, while very few vacuoles formed in normoxia (M-O). FOXJ1 and SOX17, marking oviduct MCCs and SCs, were changed to white for easier visualization of vacuoles (bottom). (S) Percentage of vacuolated MCCs in the INF/AMP, AIJ, and ISM in normoxia (7.005±1.995%, 16.971±8.603%, and 19.205±16.739% respectively) versus hypoxia (47.728±6.129%, 58.82±5.938%, and 70.121±25.148% respectively). Increased instances of vacuolation were noted in hypoxia, as compared to normoxia. Error bars indicate standard deviation. ** = $p < 0.001$. (T-V) Hydroxyurea (HU) treatment for 24 hours in INF/AMP organotypic slice cultures. 200µM/low dose HU treatment did not result in discernible cellular changes (U), while 4mM/high dose HU treatment resulted in cytoplasmic vacuolation and nucleus deformation (V). FOXJ1 and SOX17, marking oviduct MCCs and SCs, were changed to white for easier visualization of vacuoles (bottom). Scale bars = 10µm. (W) Percentage of vacuolated MCCs in the INF/AMP when treated with water (2.786±0.573%), low dose HU (7.397±7.865%), and high dose HU (55.32±10.622%) for 24 hours. Increased instances of vacuolation were noted in high dose HU treatment, as compared to low dose or water control. Error bars indicate standard deviation. ** = $p < 0.001$, ** = $p < 0.001$, ns = $p > 0.05$.

4.3.7. MCC vacuolation restricted to the INF/AMP epithelium in vivo was linked to aging-associated changes in blood flow via the ovarian artery

Although our *in vitro* experiments indicated that all oviduct MCCs were sensitive to hypoxic stress and form cytoplasmic vacuoles, age-associated MCC vacuolation was uniquely restricted to the INF/AMP MCCs *in vivo*. This suggests that, in addition to the distinct cellular property of the INF/AMP epithelium [1, 13], the local environment within the INF/AMP could be different from the rest of the oviduct. Since metabolic stress-associated genesets were upregulated, we investigated blood circulation that supplies the reproductive tract. Three arteries feed the female reproductive organs: ovarian, uterine and vaginal arteries. The ovarian artery is derived from the abdominal aorta, while uterine and vaginal arteries are derived from the internal iliac artery [33]. These patterns are evolutionarily conserved between mice and humans despite anatomical differences in the female reproductive tract.

To track blood circulation, we performed cardiac perfusion of a CellMask, a fixable cell membrane staining fluorescent dye. This allowed us to visualize the blood vessels around the female reproductive tract, particularly the ovarian and uterine arteries (Figure 4.7A, B, F, G). We noticed that a branch of the ovarian artery fed into the ovary and parts of the oviduct (Figure 4.7A, B, C-E, H-J), while the uterine artery fed into the proximal oviduct and the uterus (Figure 4.7A, B, F, G). Interestingly, this branch of the ovarian artery ran along the mesosalpinx, branching into two vessels, with one directly feeding into the INF/AMP and the other supplying parts of the proximal oviduct (Figure 4.7D, E, I, J). Since the INF/AMP was supplied by only this branch of the ovarian artery, we speculated that circulation to the ovary was linked to that of the INF/AMP. Further, using the Flk1-gfp mouse line, which labels endothelial cells at embryonic stages [34, 35], we found an intricate network of vessels throughout the upper female reproductive tract, likely marking arterioles and/or capillaries (Figure 4.7K-M). The density of FLK-GFP expressing vessels was sparse in the AMP, as compared to the ISM (Figure 4.7N, O), suggesting distal-proximal differences in microvasculature. Interestingly, while CellMask entered the oviduct in young mice (Figure 4.7C), indicating dilated vessels/active blood flow, CellMask was not noted in the ovaries or oviducts of aged mice (Figure 4.7P, Q). Thus, blood flow into the ovary declined in tandem with ovarian aging, as evidenced by small ovaries and few to no oocytes in aged mice (Figure 4.7R-U). Ovarian aging and oocyte depletion progressively occurs in 3-12 mo mice, with significant decrease in number of oocytes at 6mo, and more pronounced reduction at 9mo and 12mo [36]. This timeline of oocyte depletion and ovarian aging occurs concurrently with INF/AMP MCC vacuolation, likely due to changes in circulation via the ovarian artery.

Since aging-associated decline in female fertility is caused by ovarian aging/oocyte depletion, we wondered if MCC vacuolation contributed to this decline in fertility by hindering OCC movement into the oviduct. Regardless of cytoplasmic vacuoles in MCCs, superovulation of 13mo mice resulted in the successful entry of OCCs into the oviduct (Figure 4.7V), indicating that vacuolation did not affect proper INF/AMP functions mediated by MCC beating [2]. Indeed, INF/AMP MCCs in aged 13mo mice were still beating (data not shown), suggesting continued ATP consumption of MCCs in aged oviducts.

Pregnancy modulates blood circulation around the female reproductive tract to support fetal growth. It is shown that the uterine artery contributes 68%, and the uterine branch of the ovarian artery contributes 32% to the placenta/fetuses [37], indicating that the ovarian artery also supports the continuation of pregnancy. We wondered whether gravidity, defined as number of pregnancies, would impact INF/AMP MCC vacuolation. Interestingly, INF/AMP MCCs in 13mo mice that have given birth to 7-8 litters in their lifetime (last litter at age 8-9mo/4-5 months prior to euthanasia) presented with decreased frequency of vacuolation and apical displacement of nucleus, relative to 13mo mice that have given birth to 3-4 litters in their lifetime (last litter at age 5-6mo/7-8 months prior to euthanasia) (Figure 4.7W-Y). We also found that 13mo mice with 7-8 litters had larger and less atrophic ovaries, as compared to mice with 3-4 litters (Figure 4.7Z, a). As expected, MCC vacuolation was restricted to the INF/AMP epithelium and not noted in the other regions of the oviduct (Supplementary Figure S4.8). Taken together, we propose that changes in blood circulation via the ovarian artery contribute to ovarian and distal oviduct aging. Reduced blood circulation results in a constant, mildly stressed environment within the INF/AMP region leading to MCC vacuolation.

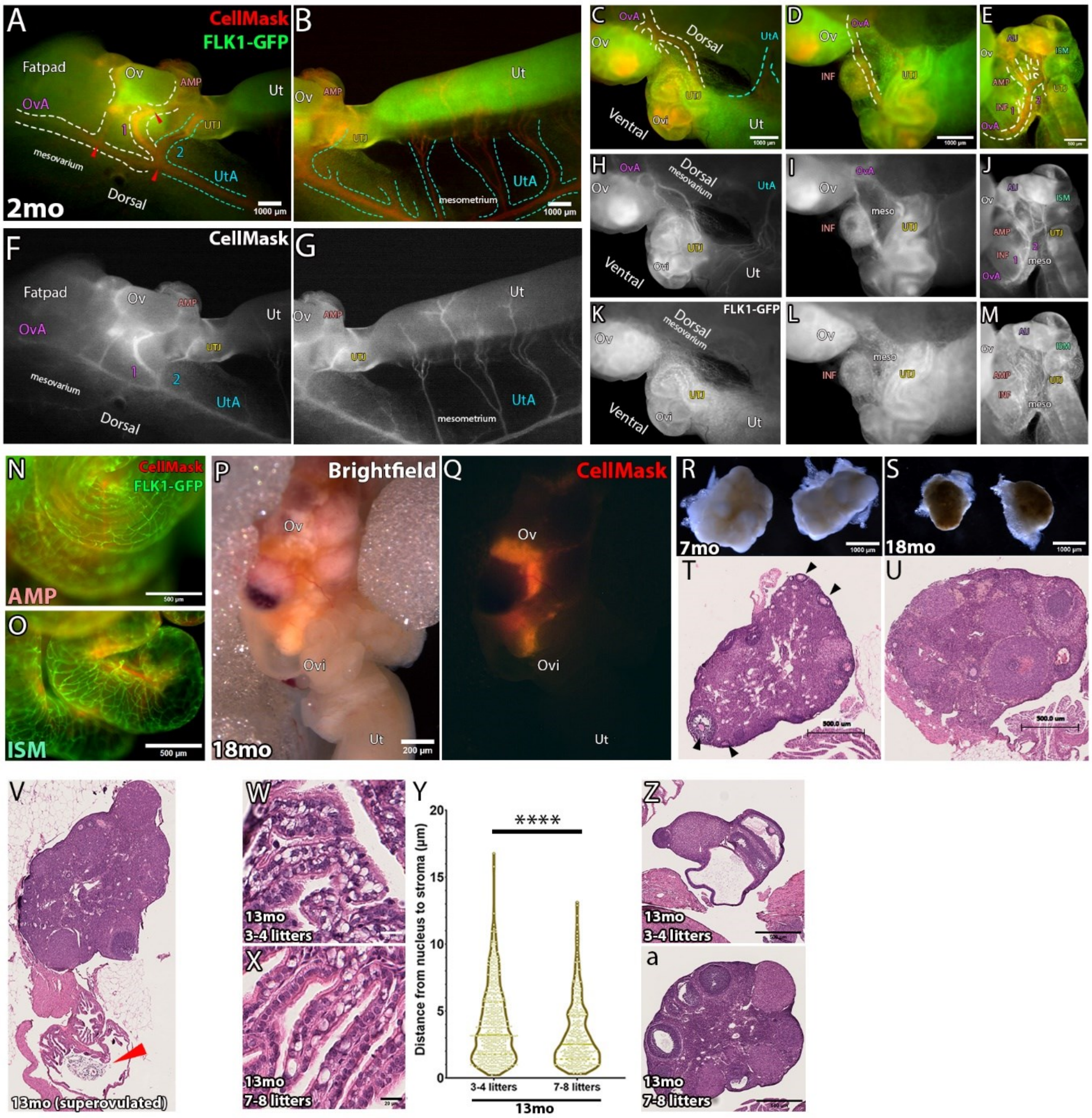

Figure 4. 7: Decline in circulation via the ovarian artery in aged females.

(A-J) Ovarian artery (OvA) and uterine artery (UtA) were labelled by cardiac perfusion of CellMask in a 2mo *Flk1-gfp* mouse. The ovarian artery ran along the connective tissue that connected the ovary (Ov), oviduct (Ovi) and uterus (Ut), with branches feeding into the ovary. From the anastomosis of the ovarian and uterine arteries, two branches diverged: 1) one fed into the ovary and branched again to supply the distal oviduct, and 2) the other fed into the proximal oviduct. The ovarian and uterine arteries were traced by white and cyan dotted lines, respectively. Branching is labelled by red arrows. (A, F). Following the anastomosis point, the uterine artery ran along the broad ligament on the mesometrial side, with numerous branches connecting into the uterus (B, G). The ovarian artery as seen from a different angle, with branches that connected into the ovary and the oviduct (C, H). The oviduct was partially stretched out to visualise a branch of the ovarian artery that ran along the mesosalpinx (D, I). This artery further branched out: 1) one branch directly fed into the INF/AMP, while 2) the other branch split into numerous vessels that supplied the proximal oviduct (E, J). (K-M) FLK1-GFP expressing vessels formed an intricate network throughout the upper reproductive tract, likely labeling arterioles and/or capillaries. (N, O) Microvasculature differences between distal and proximal oviduct. Network of FLK1-GFP expressing vessels was less dense in the AMP, relative to the ISM. (P, Q) Decreased blood flow to ovary and oviduct in aged mice. No CellMask labelling was noted in the upper female reproductive tract in aged 18mo mice. (R-U) Age-associated ovarian atrophy, decrease in ovary size, and oocyte numbers. Ovaries from 18mo mice were smaller and had a smooth surface (S) and no oocytes were noted in 18mo ovaries (U), as compared to 7mo ovaries (R, T). (V) MCC function was unaffected by vacuolation. OCCs were noted in the AMP region of 13mo superovulated mice. (W-Y) Reduced severity in apical displacement of nucleus in INF/AMP MCCs of 13mo mice with higher gravidity. Fewer vacuolated MCCs were noted in 13mo mice that have had 7-8 litters (X; 3.2096±2.411 μm), relative to those that have had 3-4 litters (W; 3.9743±2.7131 μm). Measurements of the distance from MCC nuclei to stroma in the INF/AMP region of dams with 3-4 litters or 7-8 litters (Y). Each point represents a measurement/cell. The continuous line represents the median, while the dotted lines show the quartiles. **** = $p < 0.0001$. (Z, a) 13mo mice that have had 7-8 litters in their lifetime had larger and less atrophic ovaries (a), as compared to those with 3-4 litters (Z).

4.4. Discussion

In this study, we show that the INF/AMP MCCs uniquely present with aging-associated cytoplasmic vacuolation and nuclear anomaly. We initially suspected that repetitive exposure to inflammatory factors or ROS released during ovulation [19] could be part of the cause. However, ovariectomy did not affect the timeline of MCC vacuolation in the INF/AMP epithelium. Additionally, the MCC vacuolation phenotype was restricted to the INF/AMP epithelium and not observed in the AIJ epithelium despite the same proximity to the ovary in a single transverse section. We concluded that MCC vacuolation in the INF/AMP epithelium was not associated with proximity to the ovary but was due to a distinct regional cellular subtype, suggesting its intrinsic vulnerability.

MCCs in the INF/AMP epithelium are constantly beating regardless of the female hormonal cycles and ovulation. Although changes in cilia beat frequencies (CBF) are reported during the different hormonal stages, it does not impact OCC transport along the AMP [4]. We observed that MCCs in the aged INF/AMP continued to beat and transport OCCs into the AMP despite MCC vacuolation. In *in vitro* organotypic slice cultures, inhibition of cellular respiration terminated cilia beating (data not shown) and resulted in INF/AMP MCC protrusion/death within 24 hours of treatment, with no noticeable changes in SCs or AIJ/ISM MCCs. This is consistent with a recent study showing that lung MCCs and their progenitors respond differently to mitochondrial dysfunction [28]. Taken together, this suggests that INF/AMP MCCs rely heavily on oxidative phosphorylation to fulfill high ATP usage required for constant cilia beating.

The most ATP-consuming biochemical events in adult cells are 1) Na+, K+ ATPase activity responsible for the establishment and maintenance of ion homeostasis, membrane potential, active transport of substrates, and 2) protein turnover [30, 38]. However, constant MCC beating in the INF/AMP epithelium continued even after the cessation of ovarian functions and MCC vacuolation, suggesting that these cells prioritize cilia function/motility. Acute ATP depletion induced by combined inhibition of glycolysis and cellular respiration in MDCK cells results in the internalization of Na+, K+ ATPase and E-cadherin [27]. Thus, the cytoplasmic vacuoles lined with Na+, K+ ATPase α1 subunit (ATP1A1) observed in INF/AMP MCCs of aged mice could be indicative of cellular adaptation to ATP shortage.

In contrast to *in vivo*, MCC vacuolation was induced in hypoxia (3% O2) or high dose HU treatment in *in vitro* slice cultures, but not by ER stress inducers or inhibition of protein synthesis, glycolysis, hexosamine biosynthesis or pentose phosphate pathway. Acute hypoxia promotes Na+, K+ ATPase internalization by generating mitochondrial ROS [39], while chronic hypoxia results in ROS elevation and diminished ATP demand [30]. In line with this, INF/AMP MCCs in 18mo mice showed downregulation of genesets associated with cilia function/motility, reflecting decreased ATP demand, and upregulation of genesets associated with ROS metabolism/catabolism, suggesting that the MCCs are adapting to environmental stress.

HU treatment, known to inhibit DNA synthesis, resulted in MCC vacuolation. HU predominantly affects the S-phase of the cell cycle, inducing dNTP depletion and replication fork stalling in cycling cells [32] by inhibiting ribonucleotide reductase (RNR). Hypoxia also induces dNTP depletion and replication stress in cycling cells [40], as oxygen is an essential co-factor for RNRs [41]. Based on our finding of phospho-H2AX punctae in INF/AMP MCCs throughout adulthood and aging, it is interesting to speculate that vacuolation may be a response to replicative stress, despite MCCs being terminally differentiated, non-cycling cells. Interestingly, prolonged HU treatment results in formation of heterogeneous numbers of centrosomes in cycling Chinese Hamster Ovary (CHO) cells, suggesting that HU may countermand the suppression of centriole/centrosome formation [42]. Thus, in non-dividing

MCCs with numerous centrioles, another possibility is that prolonged, high-dose HU treatment deregulates centriole numbers.

Although MCCs from all three regions of the oviduct were sensitive to hypoxia and presented vacuolation phenotypes *in vitro*, the MCC vacuolation phenotype *in vivo* was restricted to the INF/AMP epithelium. This suggests not only intrinsic vulnerability but also unique environmental differences in the INF/AMP epithelium, relative to the rest of the oviduct.

Three arteries feed into the female reproductive tract: ovarian, uterine and cervical arteries [33]. We found that the ovarian artery feeds into the ovary and INF/AMP region, while the uterine artery supports the proximal oviduct. Interestingly, in some Mayer-Rokitansky-Küster-Hauser (MRKH) syndrome patients, the distal end of Fallopian tube is intact despite the lack of the uterus [43], suggesting that its circulation is independent of the uterus. Branches of the ovarian artery connect into the distal region, while the uterine artery feeds into the proximal Fallopian tube [44]. Thus, blood circulation patterns in mice and humans are conserved despite apparent anatomical differences between mouse and human female reproductive tracts.

Our data showed blood circulation to the INF/AMP region relied on the ovarian artery, which was tightly linked to ovarian function. In aging, we found reduced blood circulation to the ovary and the INF/AMP. We propose that this creates a chronic, mild low oxygen and low nutrient condition in the INF/AMP region, reflected by MCC vacuolation.

Finally, the distal fimbria of the human Fallopian tube is recognized the site of origin of High Grade Serous Ovarian Carcinomas (HGSCs) [10]. It is interesting to speculate that low blood circulation to the distal Fallopian tube via the ovarian artery in postmenopausal individuals could lead to a constant, mild environmental stress that facilitates the initiation and progression of HGSCs. In one human study, while variations exist between individuals and hormonal conditions, changes in the ovarian/uterine artery calibers are observed in FTs of cycling and postmenopausal women, suggesting that FTs from cycling humans receive blood supply mainly from the ovarian artery and FTs from postmenopausal humans predominantly receive blood supply from the uterine artery [45]. In addition, while region-specificity is unclear, stretches of vacuolated epithelial cells are reported in human FT samples obtained from older patients of average age 61 years [46]. Further, we also showed that parity was directly proportional to decreased severity of MCC nucleus displacement and vacuolation, suggesting that pregnancy provided a protective effect. Likewise, the P53 signature, considered a latent HGSC precursor, is significantly associated with lower parity [47], and thus with increased number of ovulations. While cytoplasmic vacuolation occurred independent of estrous cycling and/or ovulation, the severity of vacuolation decreased with higher gravidity/parity. Pregnancy involves increased blood flow and oxygenation of the reproductive tract [37], including the distal oviduct and ovary, also resulting in larger size and decreased atrophy of ovaries in mice with higher gravidity.

Taken together, we propose that the INF/AMP epithelium has unique intrinsic properties and circulatory environment, as compared to the rest of the oviduct. Changes in blood circulation were associated with cessation of ovarian function and resulted in environmental stress that was reflected by INF/AMP-specific MCC vacuolation.

4.5. Methods and Materials

4.5.1. Animals

Our study exclusively examined female mice because the organ is only relevant in females. All animal work was performed in accordance with institutional guidelines and was approved by the Faculty of Medicine Animal Care Committee (AUP #7843); it was undertaken at the Goodman Cancer Research Institute animal facility. Aging phenotypes were confirmed in *Fltp-H2B-Venus* [48] mice that were a kind gift from Dr. Heiko Lickert and Tdtomato flox/flox mice (Ai14) acquired from JAX (#007914). Wild-type B6N mice acquired from McGill's Integrated Core of Animal Modeling (MICAM) were used for ovariectomy surgeries (N=3-4 for each time-point), and results were confirmed in *Fltp-H2B-Venus* mice (N=2-3 for each time-point). 13mo retired B6N dams with 3-4 (N=3) or 7-8 litters (N=3) were acquired from MICAM, where trio breeding is the standard. Where required, estrous stages were analyzed using vaginal smears stained with crystal violet [49].

4.5.2. 3D confocal imaging

Oviducts were collected and straightened by removing the mesosalpinx. The straightened oviduct was fixed with DMSO (Dimethyl sulfoxide, Sigma Aldrich D8418): methanol (BioShop Canada Inc., MET302.1) in the ratio 1:4 and placed at −20°C overnight. The antibody staining protocol was as described in [50]. Blocking was done overnight in solution containing 1% Triton X-100 (Sigma-Aldrich, T8787), 2% powdered milk, and 1X phosphate-buffered saline (PBS, BioShop Canada Inc., PBS405), henceforth referred to as PBSMT. Primary and secondary antibody staining was performed in PBSMT for 5 and 2 days, respectively, at 4° on a shaker. After six 30-minute-long PBSMT washes, the oviduct pieces were transferred successively to methanol:PBT (1:1, PBT: 1× PBS and 1% Triton X-100), 100% methanol, 3% H2O2 (BioShop Canada Inc., HYP001.1), and 100% methanol prior to benzyl alcohol/benzyl benzoate (BABB) clearing. BABB-cleared samples were placed on a #1.5 coverslip (Fisher Scientific, 12-545F) with 10–15 µl BABB prior to imaging using the 10X objective (0.30 numerical aperture/NA) on LSM 800 or 710 (Zeiss). Section interval for 3D confocal imaging was 4.32 µm. Usually, 40–110 optical sections were taken.

4.5.3. Bilateral and unilateral ovariectomy surgeries

Surgery preparation and female reproductive tract exposure was as described previously [51]. Mice were anesthetised with isoflurane (McGill's Comparative Medicine and Animal Resources Centre/CMARC pharmacy) and injected with subcutaneous 20mg/kg Carprofen (CMARC pharmacy) prior to fur removal and surgery. A dorsal midline skin incision (~1 cm) was created, followed by an incision in the body wall located directly above the ovarian fat pad. This ovarian fat pad was pulled out using a pair of curved forceps (Fisher Scientific, NC0696845), exposing the upper female reproductive tract (ovary, oviduct, uterus). The tract was placed on a sterile gauze soaked in saline and a bulldog clamp (Fisher Scientific, 50-822-230) was secured on the fat pad to keep the tract exposed. Under a stereomicroscope (SteREO Discovery.V8, Zeiss), the ovarian bursa was cut open to expose and cut out the ovary using a pair of sterile microdissection scissors (Fisher Scientific, 089531B). Following ovary removal, body wall and skin incisions were sutured close using absorbable vicryl sutures (Fisher Scientific, 50-118-0847). Mice were administered Carprofen for 3 days and monitored for 10 days.

4.5.4. Isolation of INF/AMP cells for single cell RNA sequencing

Oviducts from a single 3mo mouse in estrus (Estrus_INFAMP) or three 18mo mice (Aged_INFAMP) were straightened out in 1X PBS (Bio Basic, Cat# PD8117). The INF/AMP region was separated from the rest of the tube by slicing in between turns 1 and 2. INF/AMP regions were moved into media containing 1X PBS, 100 IU/ml of Penicillin & 100ug/ml of Streptomycin (Gibco, 15140122), and 10% fetal bovine serum (FBS, Wisent Bioproducts, 090-150). These pieces of tissue were transferred onto empty plates with a drop of media containing 5mg/ml collagenase B (Sigma-Aldrich, COLLB-RO) and 5U/100ul DNase I (Thermo Scientific, EN0521) and chopped into smaller pieces with a No. 21 blade (Paragon, P307). This solution with small tissue pieces was transferred to a 1.5ml tube containing 100µl of the above-mentioned dissociation solution and incubated for 35-40 minutes at 37°C. This was then spun down at 1,500rpm for 5 minutes, resuspended in 500µl 1X PBS, and spun down again to resuspend in 50µl of warmed 0.25% Trypsin-EDTA (Gibco, Cat# 25200056) followed by a 7-minute incubation at 37°C. Trypsinization was halted with media, and mechanical dissociation was performed by passing through a 27 ½ gauge insulin needle (BD, #324704). The resulting single cell suspension was passed through a 40µm cell strainer (Corning, 352340), centrifuged at 1,500rpm for 7 minutes and resuspended in 200µl 1X PBS.

4.5.5. Single Cell RNA sequencing (scRNASeq)

Quality control and scRNASeq was performed by the McGill Genome Centre. For initial quality control, an aliquot was taken from the cell suspension and incubated in a working concentration of 2mM calcein-AM and 4mM Ethidium-Homodimer1 (Thermofisher L3224). After 10 minutes of incubation at room temperature, sample viability, concentration, segregation, size and absence of large debris were verified by loading stained cell suspension onto hemocytometer (Incyto DHC-N01-5) and imaged on bright field, GFP (for Calcein-AM) and RFP (for Ethidium homodimer-1) channels using a EVOS FL Auto Fluorescent microscope (ThermoFisher). Samples with a viability of 70% or more proceeded to scRNASeq. Single cell gene expression data was generated according to Chromium Single Cell User Guide (v3.1 Chemistry, 10X genomics). Briefly, cells were suspended into Reverse Transcription

(RT) Master Mix (10X genomics) then pipetted into Well-1 of a Chip ‘‘G’’ (10X genomics), followed by Gel Beads (10X genomics) and Partition oil (10X genomics). The chip assembly was run on a Chromium Controller (10X genomics) which generated Gel Bead-In-EMulsions (GEMs). Following RT protocol on a thermocycler (Biorad T100), emulsion beads were broken, and quality (size distribution) and concentration of cDNA was assessed using LabChip (Perkin Elmer 760517, CLS760672). Barcoded cDNAs were pooled for amplification, and the final PCR product (or sequence ready library) was purified, and quality controlled using LabChip. Finally, the libraries were converted to MGI and sequenced on 1 lane of MGI G400, DNBSEQ-G400 sequencer (MGI Tech Co. Ltd).

4.5.6. scRNASeq analyses

Droplet libraries were processed using the Cell Ranger count pipeline (v7.0.1) [52]. Sequencing reads were aligned to the mm10 mouse reference genome, and transcript counts were quantified for each annotated gene within every cell. Count matrices (genes × cells) were loaded into the R package Seurat (v5.0.1) [53] for quality control and downstream analyses. Low-quality cells were filtered out using the following criteria: (1) the number of detected genes is <= 200; (2) percentage of mitochondrial RNA >= 10% per cell. Following SCTransform normalization, individual samples were integrated using the Harmony procedure. UMAP dimension reduction was generated based on the first 15 principal components. A nearest-neighbor graph using the first 15 principal components was calculated using FindNeighbors function, followed by clustering using FindClusters function with resolution = 0.35. Cluster-specific marker genes were identified using the function FindMarkers with cutoffs: log2 fold change > 0.5 and adjusted P-value < 0.05 (up-regulated genes only). Per-cluster differential expression testing between two groups of cells was conducted using the FindMarkers function. The Wilcoxon rank-sum test was utilized for the differential analysis, and p-values were corrected for multiple testing using the Benjamini-Hochberg method. Gene set enrichment analysis based on pre-ranked gene list by t-statistic was performed using the R package fgsea (http://bioconductor.org/packages/fgsea/).

4.5.7. Live imaging cilia beating

INF regions of the oviduct were cut off and sliced radially in warm 1X PBS. These pieces were gently transferred to a #1.5 coverslip (VWR, 48393-251) with a 120µm spacer (Invitrogen, S24737) stuck on the surface, and any remaining PBS was replaced with a ~10µl of warmed media containing Advanced DMEM/F12 (Gibco, 12634010), 2mM GlutaMax (Gibco, #35050061), 5% FBS, and 50U/ml penicillin/streptomycin. A second #1.5 coverslip was placed on top to sandwich the tissue pieces, and they were imaged within 30 minutes using a 20X objective (0.75 N.A) on a widefield microscope system (Nikon), built around a Nikon TI2-E stand, equipped with Nikon's Perfect Focus System, a LED light source (SpectraX, Lumencor) and sCMOS cameras (Orca Fusion-BT, Hamamatsu) enclosed by a custom-built environmental chamber (Digital Pixel), and controlled using Nikon NIS Elements AR software. 2.5-second-long, >400 fps, brightfield, 512 x 512 ROI videos of tissue edges covered with MCCs were imaged at 37°C.

4.5.8. Superovulation

13mo mice were administered 100µl of CARD HyperOva (Cosmo Bio Ltd., KYD-010-EX) intraperitoneally at 5pm. 48 hours later, 7.5 IU of human Chorionic Gonadotropin (hCG; Sigma, CG-10) was administered intraperitoneally. Mice were euthanized 15-17 hours after hCG injection, and tracts were isolated for paraffin processing.

4.5.9. Organotypic slice culture

Reproductive tracts were dissected out of 2-3-month-old mice and dropped into a petri dish containing ice-cold 1X PBS to reduce contractions. Ovaries were removed, and oviducts were straightened out by removing the mesosalpinx. ~1ml of warmed 4% low melting agarose (LMA, IBI Scientific, IB70051) was pipetted into a cryomold (Fisherbrand, 22363553). The straightened oviduct was embedded in the LMA and placed on ice to set. A portion of the uterus was kept intact to stabilize the tract in the LMA while sectioning. The solidified LMA block was superglued (Krazy Glue) onto the metal specimen holder such that the cut side of the uterus faced the specimen holder, and the distal tip of the uncoiled oviduct faced the ceiling. After the glue dried, the specimen holder was placed in the buffer tray containing ice cold 1X PBS, surrounded by ice in the ice bath tray. The block was sectioned into 150µm thick, transverse slices at a speed and amplitude of 0.8mm/s and 1.60mm respectively, using a vibratome (Leica). Slices were picked up using a brush and placed in a well of a 24-well-plate (Fisher Scientific, FB012929) containing 250µl of ice-cold media. Tissue slices embedded in agarose were transferred to a 4- (Fisher Scientific, Cat# FB012926) or 25cm^2 dish (Fisher Scientific, 08-757-500) and 500µl/8ml of fresh, ice-cold media was added to each well/dish. Media contained Advanced DMEM/F12, 2mM GlutaMax, 5% FBS, and 50U/ml penicillin/streptomycin.

25cm^2 dishes were used for experiments comparing normoxia to 3% hypoxia, while 4-well or 24-well plates were used for all other treatments. Organotypic slice cultures in 25cm^2 dishes were placed in normoxia or hypoxia on the day of sectioning. Hypoxia (3.5% O_2, 5% CO_2, 91.5% N_2) was maintained in a separate, humidified CO_2 incubator with O_2 control (Heracell 150i, ThermoFisher). Organotypic slice cultures in 4-well plates were placed in a humidified CO_2 incubator for 24 hours prior to inhibitor treatments. Inhibitors/treatments used were 200µM/4mM hydroxyurea (HU, Sigma Aldrich, H8627-5G), 10µg/ml cycloheximide (CHX, Cayman Chemical Company, 14126), 2µM 6-Aminonicotinamide (6-AN, Sigma, A68203-1G), 1µM YZ-9 (Cayman Chemical Company, 15352), 5µM tunicamycin (TUN, Sigma Aldrich, T7765-10MG), 1µM shikonin (Cayman Chemical Company, 14751), 0.8µM ST045849 (Sigma Aldrich, SML2702-5MG), 10µM Antimycin-A (Sigma Aldrich, A8674) and/or 10mM 2-deoxyglucose (2-DG, Sigma Aldrich, D6134).

4.5.10. Immunofluorescence and immunohistochemistry

Uncoiled or coiled oviducts/reproductive tracts were fixed with 4% paraformaldehyde (PFA, Polysciences) for 30 minutes, followed by three washes with 1X PBS. For cryosectioning, fixed samples were calibrated in 15% and 30% sucrose either at 4 degrees overnight prior to OCT (Fisher HealthCare, #23-730-571) embedding and sectioning at 5-7- or 10-micron thickness. For immunofluorescence (IF), sections were brought to room temperature and washed with 1X PBS, 0.1% Triton X-100 (Sigma-Aldrich, T8787), and 0.5% Triton X-100. Slides were incubated in permeabilization and blocking solution (0.1% Triton X-100 and 1% FBS in 1X PBS) for 2 hours at room temperature. Primary antibody staining was performed overnight at 4°C in permeabilization and blocking solution. Primary antibodies were washed off with multiple washes of 1X PBS and 0.1% Tween (Sigma Aldrich, P9416), followed by secondary antibody staining in 1X PBS overnight at 4°C. After the secondary antibodies were washed off, 1-2 drops of homemade mounting media were pipetted onto the sections and #1.5 coverslips (Fisher Scientific, 12-545F) were placed over the stained sections. Coverslips were sealed to the slides using nail polish. IF sections were imaged with 20x (N.A 0.8) or 63x (N.A 1.4) objectives, on LSM710 or LSM800 confocal microscopes (Zeiss). Homemade mounting media was made of 1-part 10X PBS, 9 parts glycerol (BioShop, GLY001), and slowly stirred in 0.1 parts of 20% w/v propyl gallate (Sigma Aldrich, P3130; dissolved in DMSO). Paraffin processing, Haematoxylin & Eosin (H&E), immunohistochemistry (IHC), and digital slide scanning (NanoZoomer S210, Hamamatsu) were performed by the Goodman Cancer Research Institute Histology Innovation Platform. Embedded blocks were sectioned on a microtome at 4–6-micron thickness. For IF on paraffin sections, deparaffinization involved heating at 50°C, two incubations of 5 minutes each in Histo Clear (National Diagnostics, HS-202) and 3-minute-long incubations in successive ethanol solutions (100%, 90%, 70%, 50%, 0% in water). Antigen retrieval was performed with homemade 1X EDTA buffer for 7 minutes in a pressure cooker. Primary and secondary antibody staining was performed as stated above.

150µm thick organotypic slice cultures were transferred to 4-well plates and fixed in 4% PFA for 30 minutes at room temperature, on a shaker. PFA was replaced by 1X PBS thrice, each wash with shaking for 10 minutes at room temperature. 1X PBS was replaced by permeabilization and blocking solution and incubated overnight at 4°C on a shaker. Primary antibody staining was performed in permeabilization and blocking solution overnight at 4°C on a shaker, followed by multiple 1X PBS and 0.1% Tween washes, secondary antibody staining in 1X PBS on day 3, and multiple washes. Slices were transferred to a #1.5 coverslip with a 120µm spacer stuck on the surface. Any solution remaining on the coverslip was replaced by a drop of homemade mounting media, followed by a second #1.5 coverslip on top, such that the slices were sandwiched between two coverslips. Stained slices were imaged with a 20x objective (0.8 N. A) on LSM710 or LSM800 confocal microscopes.

4.5.11. Antibodies

Primary antibodies (1/250 dilution, unless specified): anti-SOX17 (R&D Systems, AF1924), anti-PAX8 (Proteintech, 10336-1-AP), anti-FOXJ1 (Abcam, ab235445), anti-mcherry (Abcam, ab213511/Invitrogen, #M11217), anti-GFP (Abcam, ab13970), anti-ATP1A1 (a2F, DSHB), anti-LaminB1 (Cell Signaling, 13435S), anti-γH2AX (Cell Signalling, 9718T), anti-P16 (Cell Signalling, 92803T), anti-P21 (Cell Signalling, 2947T), anti-phospho-EIF2A (Abcam, Cat#ab32157).

Secondary antibodies (1/450 dilution): Alexa Fluor (AF) anti-rabbit 555 (Invitrogen, A31572), AF anti-rabbit 649 (Invitrogen, A21245), AF anti-rabbit 488 (Invitrogen, A21206), AF anti-mouse 649 (Invitrogen, A32787), AF anti-mouse 488 (Invitrogen, A21202), AF anti-goat 568 (Invitrogen, A11057), AF anti-rat 488 (Invitrogen, A21208), anti-chicken 488 (Sigma, SAB4600031), DAPI (4′ ,6-diamidino-2-phenylindole, Thermo Fisher, 62248), Hoescht 33342 (Thermo Fisher, 62249), AF 488 phalloidin (Lifetech, A12379), and AF 635 phalloidin (Lifetech, A34054).

4.5.12. Image analysis and statistics

Stained sections were visualized using FIJI, Zen (Zeiss) or ImageScope x64 (Aperio). Apical displacement of nuclei was measured manually on FIJI by drawing a line from the base of nucleus to the basal lamina/stroma as parallel to the lateral domain as possible, using either 63x IF images taken on a confocal microscope or 40x H&E-stained digital slides that were converted to TIFF format using ndpitools and ndpi2tiff plugins. Cellular/epithelial monolayer height was measured manually on FIJI by drawing a line from base to apical side of MCCs. Measurements were performed from base to base for each mucosal fold, such that cells at the base, side and tip of the mucosal fold were included. Cell counts were performed on 20x confocal images using the Cell Counter plugin. Although FLTP-H2B-Venus and FOXJ1 were used interchangeably as MCC markers, cell counts were compared only between samples stained with the same marker. Since vacuoles in organotypic slice cultures were sometimes on a different z-stack, the number of MCCs was first counted on a single z-stack, and then vacuolated MCCs were identified by inspecting the next 2-3 stacks. GraphPad Prism was used to perform unpaired, two-tailed t-test and create graphs/plots.

4.5.13. Cardiac perfusion for blood vessel visualization

Mice were anesthetized with isoflurane, and cardiac chamber was opened to expose the heart. A catheter was inserted into the left ventricle, the right ventricle was cut open, and 30ml 0.85% saline was injected to flush the arteries. After flushing, 4ml of 0.25% CellMask (Invitrogen, C10045), diluted in 0.85% saline, was injected into the left ventricle. The female reproductive tract was dissected and imaged under a stereomicroscope (SteREO Lumar. V12, Zeiss).

4.6. Acknowledgements

The authors would like to thank Drs. Arnold Hayer and Alain Nepveu for sharing equipment to image cilia beating and perform hypoxia experiments, respectively. We would also like to thank Dr. Yu Chang Wang, Mr. Haig Hugo Vrej Djambazian and Dr. Jiannis Ragoussis (McGill Genome Centre) for help with the scRNASeq. As well, we thank the Rosalind and Morris Goodman Cancer Research Institute Histology Facility, the McGill Advanced Bioimaging Facility (ABIF), and the McGill Integrated Core of Animal Modeling (MICAM) for technical support.

4.7. References

[1] Harwalkar, K., Ford, M.J., Teng, K., Yamanaka, N., Yang, B., Burtscher, I., Lickert, H., and Yamanaka, Y. (2021). Anatomical and cellular heterogeneity in the mouse oviduct—its potential roles in reproduction and preimplantation development†. Biology of Reproduction 104, 1249-1261. 10.1093/biolre/ioab043.

[2] Harwalkar, K., and Yamanaka, Y. (2021). Female fertility gets cilia(r) and cilia(r): ciliary defects in the oviduct compromises female fertility†. Biol Reprod 105, 1086-1088. 10.1093/biolre/ioab159.

[3] Yuan, S., Wang, Z., Peng, H., Ward, S.M., Hennig, G.W., Zheng, H., and Yan, W. (2021). Oviductal motile cilia are essential for oocyte pickup but dispensable for sperm and embryo transport. Proc Natl Acad Sci U S A 118. 10.1073/pnas.2102940118.

[4] Shi, D., Komatsu, K., Uemura, T., and Fujimori, T. (2011). Analysis of ciliary beat frequency and ovum transport ability in the mouse oviduct. Genes Cells 16, 282-290. 10.1111/j.1365-2443.2011.01484.x.

[5] Ishikawa, Y., Usui, T., Yamashita, M., Kanemori, Y., and Baba, T. (2016). Surfing and Swimming of Ejaculated Sperm in the Mouse Oviduct. Biol Reprod 94, 89. 10.1095/biolreprod.115.135418.

[6] Nelson, J.F., Felicio, L.S., Randall, P.K., Sims, C., and Finch, C.E. (1982). A longitudinal study of estrous cyclicity in aging C57BL/6J mice: I. Cycle frequency, length and vaginal cytology. Biol Reprod 27, 327-339. 10.1095/biolreprod27.2.327.

[7] Wu, Y., Li, M., Zhang, J., and Wang, S. (2023). Unveiling uterine aging: Much more to learn. Ageing Research Reviews 86, 101879. https://doi.org/10.1016/j.arr.2023.101879.

[8] Nelson, S.M., Telfer, E.E., and Anderson, R.A. (2013). The ageing ovary and uterus: new biological insights. Hum Reprod Update 19, 67-83. 10.1093/humupd/dms043.

[9] Patel, R., Moffatt, J.D., Mourmoura, E., Demaison, L., Seed, P.T., Poston, L., and Tribe, R.M. (2017). Effect of reproductive ageing on pregnant mouse uterus and cervix. J Physiol 595, 2065-2084. 10.1113/jp273350.

[10] Piek, J.M., van Diest, P.J., Zweemer, R.P., Jansen, J.W., Poort-Keesom, R.J., Menko, F.H., Gille, J.J., Jongsma, A.P., Pals, G., Kenemans, P., and Verheijen, R.H. (2001). Dysplastic changes in prophylactically removed Fallopian tubes of women predisposed to developing ovarian cancer. J Pathol 195, 451-456. 10.1002/path.1000.

[11] Medeiros, F., Muto, M.G., Lee, Y., Elvin, J.A., Callahan, M.J., Feltmate, C., Garber, J.E., Cramer, D.W., and Crum, C.P. (2006). The tubal fimbria is a preferred site for early

adenocarcinoma in women with familial ovarian cancer syndrome. Am J Surg Pathol 30, 230-236. 10.1097/01.pas.0000180854.28831.77.

[12] Karst, A.M., and Drapkin, R. (2010). Ovarian cancer pathogenesis: a model in evolution. J Oncol 2010, 932371. 10.1155/2010/932371.

[13] Ford, M.J., Harwalkar, K., Pacis, A.S., Maunsell, H., Wang, Y.C., Badescu, D., Teng, K., Yamanaka, N., Bouchard, M., Ragoussis, J., and Yamanaka, Y. (2021). Oviduct epithelial cells constitute two developmentally distinct lineages that are spatially separated along the distal-proximal axis. Cell Rep 36, 109677. 10.1016/j.celrep.2021.109677.

[14] Puisieux, A., Pommier, R.M., Morel, A.P., and Lavial, F. (2018). Cellular Pliancy and the Multistep Process of Tumorigenesis. Cancer Cell 33, 164-172. 10.1016/j.ccell.2018.01.007.

[15] Quirk, J.T., Natarajan, N., and Mettlin, C.J. (2005). Age-specific ovarian cancer incidence rate patterns in the United States. Gynecol Oncol 99, 248-250. 10.1016/j.ygyno.2005.06.052.

[16] Winkler, I., Tolkachov, A., Lammers, F., Lacour, P., Daugelaite, K., Schneider, N., Koch, M.L., Panten, J., Grünschläger, F., Poth, T., et al. (2024). The cycling and aging mouse female reproductive tract at single-cell resolution. Cell 187, 981-998.e925. 10.1016/j.cell.2024.01.021.

[17] Komatsu, M., and Fujita, H. (1978). Electron-microscopic studies on the development and aging of the oviduct epithelium of mice. Anat Embryol (Berl) 152, 243-259. 10.1007/bf00350523.

[18] Bertolin, K., and Murphy, B.D. (2014). 7 - Reproductive Tract Changes During the Mouse Estrous Cycle. In The Guide to Investigation of Mouse Pregnancy, B.A. Croy, A.T. Yamada, F.J. DeMayo, and S.L. Adamson, eds. (Academic Press), pp. 85-94. https://doi.org/10.1016/B978-0-12-394445-0.00007-2.

[19] Murdoch, W.J., and Martinchick, J.F. (2004). Oxidative damage to DNA of ovarian surface epithelial cells affected by ovulation: carcinogenic implication and chemoprevention. Exp Biol Med (Maywood) 229, 546-552. 10.1177/153537020422900613.

[20] Ford, M.J., Harwalkar, K., Kazemdarvish, H., Yamanaka, N., and Yamanaka, Y. (2023). CD133/Prom1 marks proximal mouse oviduct epithelial progenitors and adult epithelial cells with a low generative capacity. Biol Open 12. 10.1242/bio.059963.

[21] Felicio, L.S., Nelson, J.F., and Finch, C.E. (1984). Longitudinal studies of estrous cyclicity in aging C57BL/6J mice: II. Cessation of cyclicity and the duration of persistent vaginal cornification. Biol Reprod 31, 446-453. 10.1095/biolreprod31.3.446.

[22] Roberson, E.C., Tran, N.K., Konjikusic, M.J., Fitch, R.D., Gray, R.S., and Wallingford, J.B. (2020). A comparative study of the turnover of multiciliated cells in the mouse trachea, oviduct, and brain. Dev Dyn 249, 898-905. 10.1002/dvdy.165.

[23] Teske, B.F., Wek, S.A., Bunpo, P., Cundiff, J.K., McClintick, J.N., Anthony, T.G., and Wek, R.C. (2011). The eIF2 kinase PERK and the integrated stress response facilitate activation of ATF6 during endoplasmic reticulum stress. Mol Biol Cell 22, 4390-4405. 10.1091/mbc.E11-06-0510.

[24] Henics, T., and Wheatley, D.N. (1999). Cytoplasmic vacuolation, adaptation and cell death: a view on new perspectives and features. Biol Cell 91, 485-498. 10.1016/s0248-4900(00)88205-2.

[25] Denoyelle, C., Abou-Rjaily, G., Bezrookove, V., Verhaegen, M., Johnson, T.M., Fullen, D.R., Pointer, J.N., Gruber, S.B., Su, L.D., Nikiforov, M.A., et al. (2006). Anti-oncogenic role of the endoplasmic reticulum differentially activated by mutations in the MAPK pathway. Nat Cell Biol 8, 1053-1063. 10.1038/ncb1471.

[26] Shubin, A.V., Demidyuk, I.V., Komissarov, A.A., Rafieva, L.M., and Kostrov, S.V. (2016). Cytoplasmic vacuolization in cell death and survival. Oncotarget 7, 55863-55889. 10.18632/oncotarget.10150.

[27] Mandel, L.J., Doctor, R.B., and Bacallao, R. (1994). ATP depletion: a novel method to study junctional properties in epithelial tissues. II. Internalization of Na+,K(+)-ATPase and E-cadherin. J Cell Sci 107 (Pt 12), 3315-3324. 10.1242/jcs.107.12.3315.

[28] Xu, L., Tan, C., Barr, J., Talaba, N., Verheyden, J., Chin, J.S., Gaboyan, S., Advani, I., Elgamal, R.M., Gaulton, K.J., et al. (2024). Context-dependent functions of mitochondria protein quality control in lung. bioRxiv, 2022.2012.2008.519642. 10.1101/2022.12.08.519642.

[29] Pospelova, T.V., Demidenko, Z.N., Bukreeva, E.I., Pospelov, V.A., Gudkov, A.V., and Blagosklonny, M.V. (2009). Pseudo-DNA damage response in senescent cells. Cell Cycle 8, 4112-4118. 10.4161/cc.8.24.10215.

[30] Wheaton, W.W., and Chandel, N.S. (2011). Hypoxia. 2. Hypoxia regulates cellular metabolism. Am J Physiol Cell Physiol 300, C385-393. 10.1152/ajpcell.00485.2010.

[31] Somyajit, K., Gupta, R., Sedlackova, H., Neelsen, K.J., Ochs, F., Rask, M.-B., Choudhary, C., and Lukas, J. (2017). Redox-sensitive alteration of replisome architecture safeguards genome integrity. Science 358, 797-802. doi:10.1126/science.aao3172.

[32] Musiałek, M.W., and Rybaczek, D. (2021). Hydroxyurea—The Good, the Bad and the Ugly. Genes 12. 10.3390/genes12071096.

[33] Chaudhry R, C.K. (2023). Anatomy, Abdomen and Pelvis: Uterine Arteries. In (In: StatPearls [Internet]. Treasure Island (FL): StatPearls Publishing).

[34] Shalaby, F., Rossant, J., Yamaguchi, T.P., Gertsenstein, M., Wu, X.-F., Breitman, M.L., and Schuh, A.C. (1995). Failure of blood-island formation and vasculogenesis in Flk-1-deficient mice. Nature 376, 62-66. 10.1038/376062a0.

[35] Ema, M., Takahashi, S., and Rossant, J. (2006). Deletion of the selection cassette, but not cis-acting elements, in targeted Flk1-lacZ allele reveals Flk1 expression in multipotent mesodermal progenitors. Blood 107, 111-117. 10.1182/blood-2005-05-1970.

[36] Ansere, V.A., Ali-Mondal, S., Sathiaseelan, R., Garcia, D.N., Isola, J.V.V., Henseb, J.D., Saccon, T.D., Ocañas, S.R., Tooley, K.B., Stout, M.B., et al. (2021). Cellular hallmarks of aging emerge in the ovary prior to primordial follicle depletion. Mech Ageing Dev 194, 111425. 10.1016/j.mad.2020.111425.

[37] Raz, T., Avni, R., Addadi, Y., Cohen, Y., Jaffa, A.J., Hemmings, B., Garbow, J.R., and Neeman, M. (2012). The Hemodynamic Basis for Positional- and Inter-Fetal Dependent Effects in Dual Arterial Supply of Mouse Pregnancies. PLOS ONE 7, e52273. 10.1371/journal.pone.0052273.

[38] Kelly, J.M., and McBride, B.W. (1990). The sodium pump and other mechanisms of thermogenesis in selected tissues. Proc Nutr Soc 49, 185-202. 10.1079/pns19900023.

[39] Gusarova, G.A., Trejo, H.E., Dada, L.A., Briva, A., Welch, L.C., Hamanaka, R.B., Mutlu, G.M., Chandel, N.S., Prakriya, M., and Sznajder, J.I. (2011). Hypoxia leads to Na,K-ATPase downregulation via Ca(2+) release-activated Ca(2+) channels and AMPK activation. Mol Cell Biol 31, 3546-3556. 10.1128/mcb.05114-11.

[40] Foskolou, I.P., Jorgensen, C., Leszczynska, K.B., Olcina, M.M., Tarhonskaya, H., Haisma, B., D'Angiolella, V., Myers, W.K., Domene, C., Flashman, E., and Hammond, E.M. (2017). Ribonucleotide Reductase Requires Subunit Switching in Hypoxia to Maintain DNA Replication. Mol Cell 66, 206-220.e209. 10.1016/j.molcel.2017.03.005.

[41] Huang, M., Parker, M.J., and Stubbe, J. (2014). Choosing the right metal: case studies of class I ribonucleotide reductases. J Biol Chem 289, 28104-28111. 10.1074/jbc.R114.596684.

[42] Kuriyama, R., Terada, Y., Lee, K.S., and Wang, C.L.C. (2007). Centrosome replication in hydroxyurea-arrested CHO cells expressing GFP-tagged centrin2. Journal of Cell Science 120, 2444-2453. 10.1242/jcs.008938.

[43] Garrett, L.A., Vargas, S.O., Drapkin, R., and Laufer, M.R. (2008). Does the fimbria have an embryologic origin distinct from that of the rest of the fallopian tube? Fertil Steril 90, 2008.e2005-2008. 10.1016/j.fertnstert.2008.01.071.

[44] Verco, C.J. (1994). Fallopian Tube Anatomy, Microanatomy, Microcirculation and Counter-current Exchange. held in London, 1994//. J.G. Grudzinskas, M.G. Chapman, T. Chard, and O. Djahanbakhch, eds. (Springer London), pp. 3-15.

[45] Brökelmann, J. (1989). [Functional morphology of the fallopian tube]. Arch Gynecol Obstet 245, 391-395. 10.1007/bf02417339.

[46] Hunt, J. L., & Lynn, A. A. (2002). Histologic features of surgically removed fallopian tubes. Arch Pathol Lab Med, 126(8), 951-955. https://doi.org/10.5858/2002-126-0951-hfosrt.

[47] Saleemuddin, A., Folkins, A.K., Garrett, L., Garber, J., Muto, M.G., Crum, C.P., and Tworoger, S. (2008). Risk factors for a serous cancer precursor ("p53 signature") in women with inherited BRCA mutations. Gynecol Oncol 111, 226-232. 10.1016/j.ygyno.2008.07.018.

[48] Gegg, M., Böttcher, A., Burtscher, I., Hasenoeder, S., Van Campenhout, C., Aichler, M., Walch, A., Grant, S.G., and Lickert, H. (2014). Flattop regulates basal body docking and positioning in mono- and multiciliated cells. Elife 3. 10.7554/eLife.03842.

[49] McLean, A.C., Valenzuela, N., Fai, S., and Bennett, S.A. (2012). Performing vaginal lavage, crystal violet staining, and vaginal cytological evaluation for mouse estrous cycle staging identification. J Vis Exp, e4389. 10.3791/4389.

[50] Arora, R., Fries, A., Oelerich, K., Marchuk, K., Sabeur, K., Giudice, L.C., and Laird, D.J. (2016). Insights from imaging the implanting embryo and the uterine environment in three dimensions. Development 143, 4749-4754. 10.1242/dev.144386.

[51] Harwalkar, K., Yamanaka, N., and Yamanaka, Y. (2023). Somatic Genome-Engineered Mouse Models Using *In Vivo* Microinjection and Electroporation. J Vis Exp. 10.3791/65131.

[52] Zheng GX, Terry JM, Belgrader P, Ryvkin P, Bent ZW, Wilson R, Ziraldo SB, Wheeler TD, McDermott GP, Zhu J, Gregory MT, Shuga J, Montesclaros L, Underwood JG, Masquelier DA, Nishimura SY, Schnall-Levin M, Wyatt PW, Hindson CM, Bharadwaj R, Wong A, Ness KD, Beppu LW, Deeg HJ, McFarland C, Loeb KR, Valente WJ, Ericson NG, Stevens EA, Radich JP, Mikkelsen TS, Hindson BJ, and Bielas JH. (2017). Massively parallel digital transcriptional profiling of single cells. Nat Commun. 2017 Jan 16;8:14049. doi: 10.1038/ncomms14049.

[53] Hao Y, Hao S, Andersen-Nissen E, Mauck WM 3rd, Zheng S, Butler A, Lee MJ, Wilk AJ, Darby C, Zager M, Hoffman P, Stoeckius M, Papalexi E, Mimitou EP, Jain J, Srivastava A, Stuart T, Fleming LM, Yeung B, Rogers AJ, McElrath JM, Blish CA, Gottardo R, Smibert P, and Satija R. (2021). Integrated analysis of multimodal single-cell data. Cell. 2021 Jun 24;184(13):3573-3587.e29. doi: 10.1016/j.cell.2021.04.048.

4.8. Supplementary figures

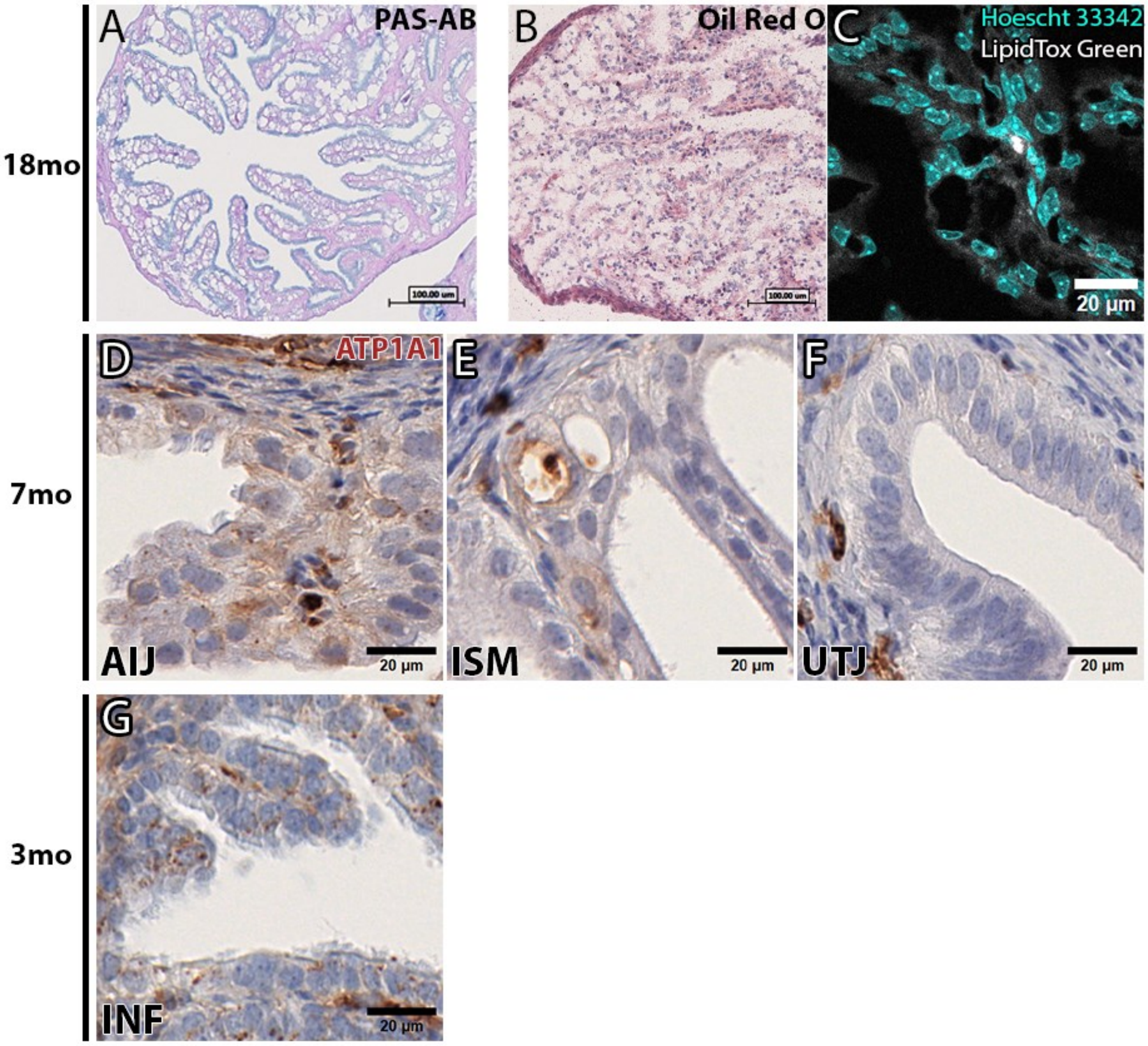

Supplementary Figure S4. 1*: Aging-associated cytoplasmic vacuoles do not contain glycogen or lipids, and no ATP1A1 localization was noted in the proximal oviduct.*

(A) Periodic acid-Schiff/PAS staining of the 18mo INF/AMP region. Cytoplasmic vacuoles were negative for PAS, indicating that vacuoles do not contain polysaccharides like glycogen or mucus-like substances. (B, C) Lipid staining of the 18mo INF/AMP region. Cytoplasmic vacuoles were negative for Oil Red O (B) and LipidTox Green (C), indicating that vacuoles do not contain lipid. (D-F) ATP1A1 IHC staining in the AIJ (D), ISM (E) and UTJ (F) regions isolated from 7mo mice, showing no specific localization to lateral surfaces or in the cytoplasm.

(G) ATP1A1 IHC staining in the INF/AMP region isolated from 3mo mice, showing occasional punctate staining.

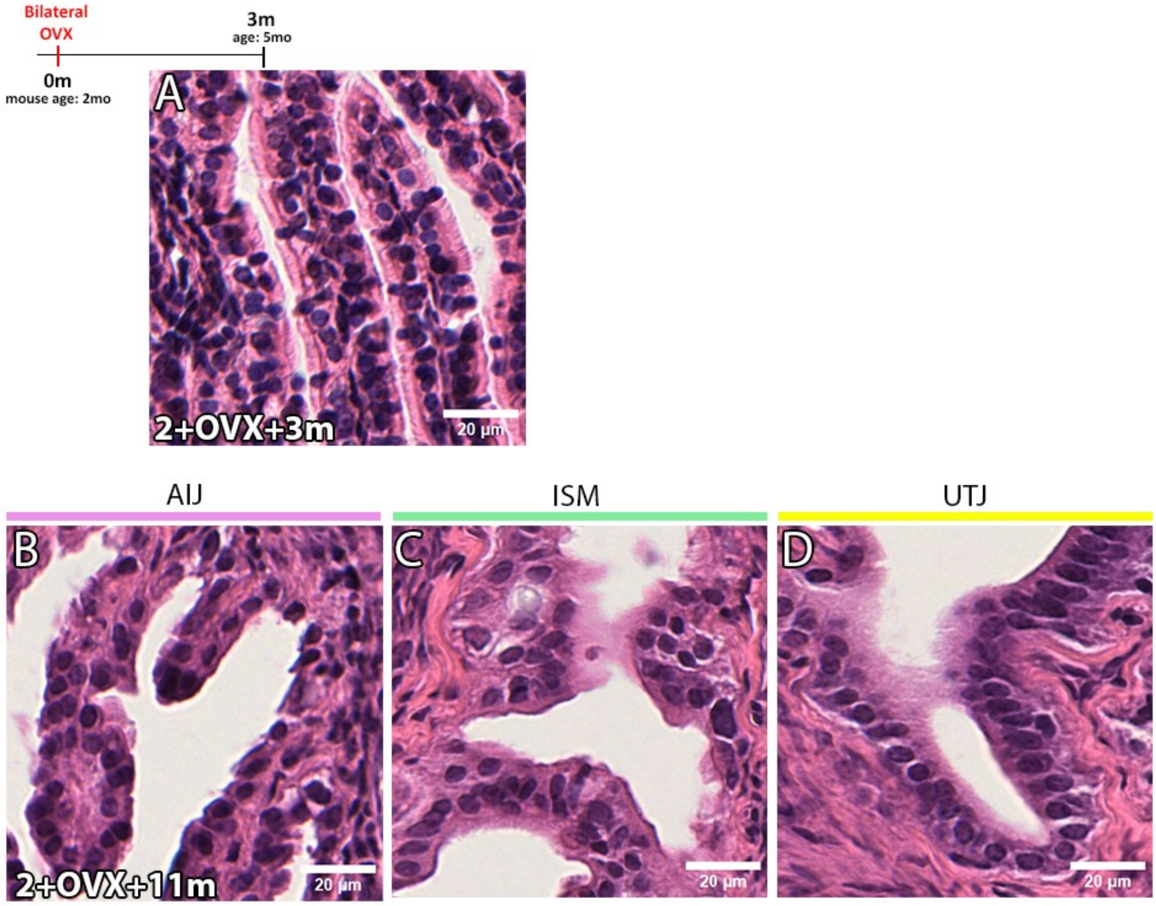

Supplementary Figure S4. 2: *No discernible vacuoles in the INF/AMP region of mice 3 months following OVX and in the AIJ, ISM, and UTJ regions of mice 11 months post OVX.*

(A) H&E staining of the INF/AMP region in oviducts from mice 3 months post bilateral OVX. No discernible cytoplasmic vacuoles were noted. (B-D) H&E staining of the AIJ (B), ISM (C) and UTJ (D) region in oviducts from mice 11 months post bilateral OVX. No discernible cytoplasmic vacuoles were noted.

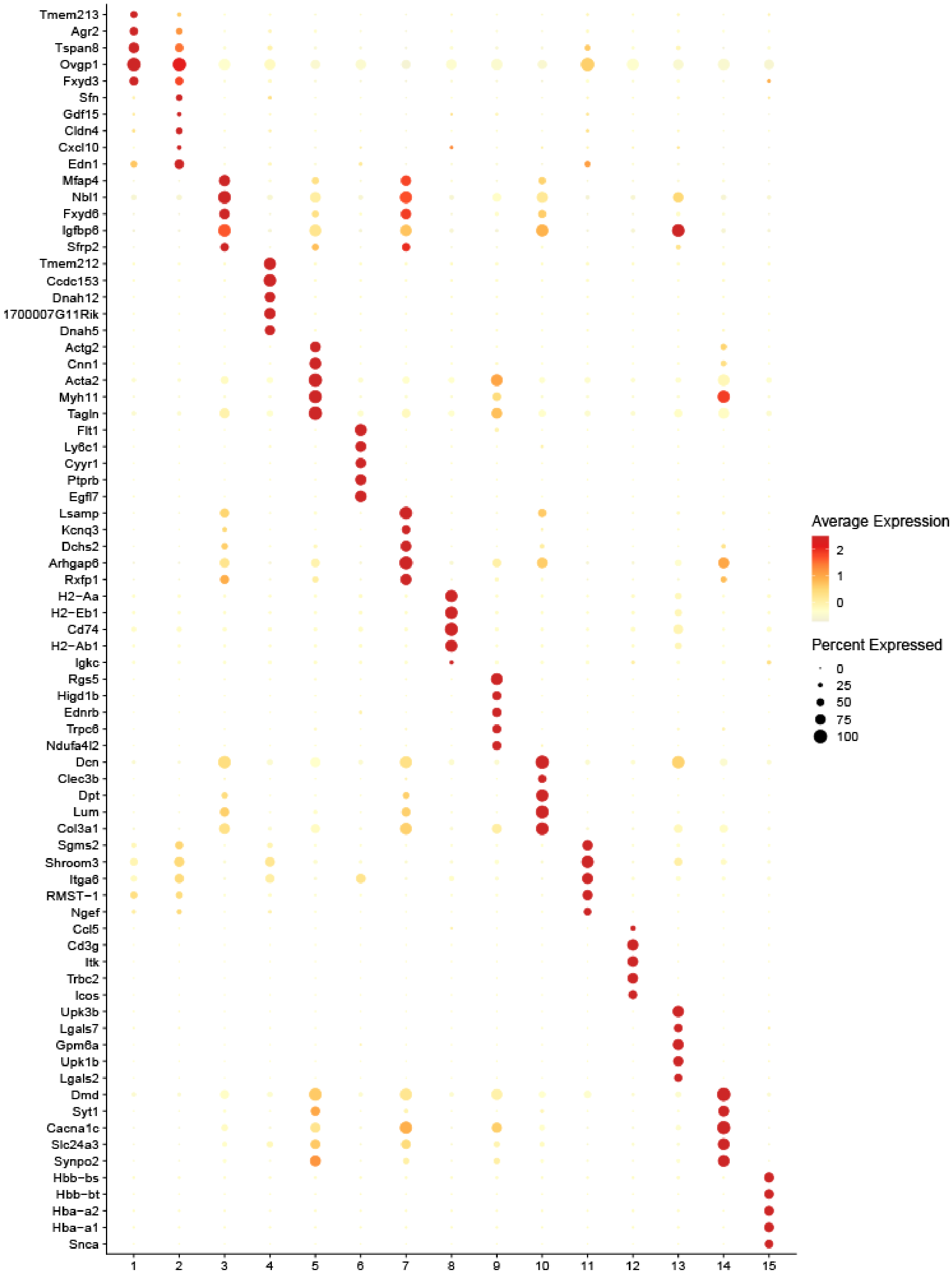

Supplementary Figure S4. 3: *Dotplot of top 5 markers in each cluster.*

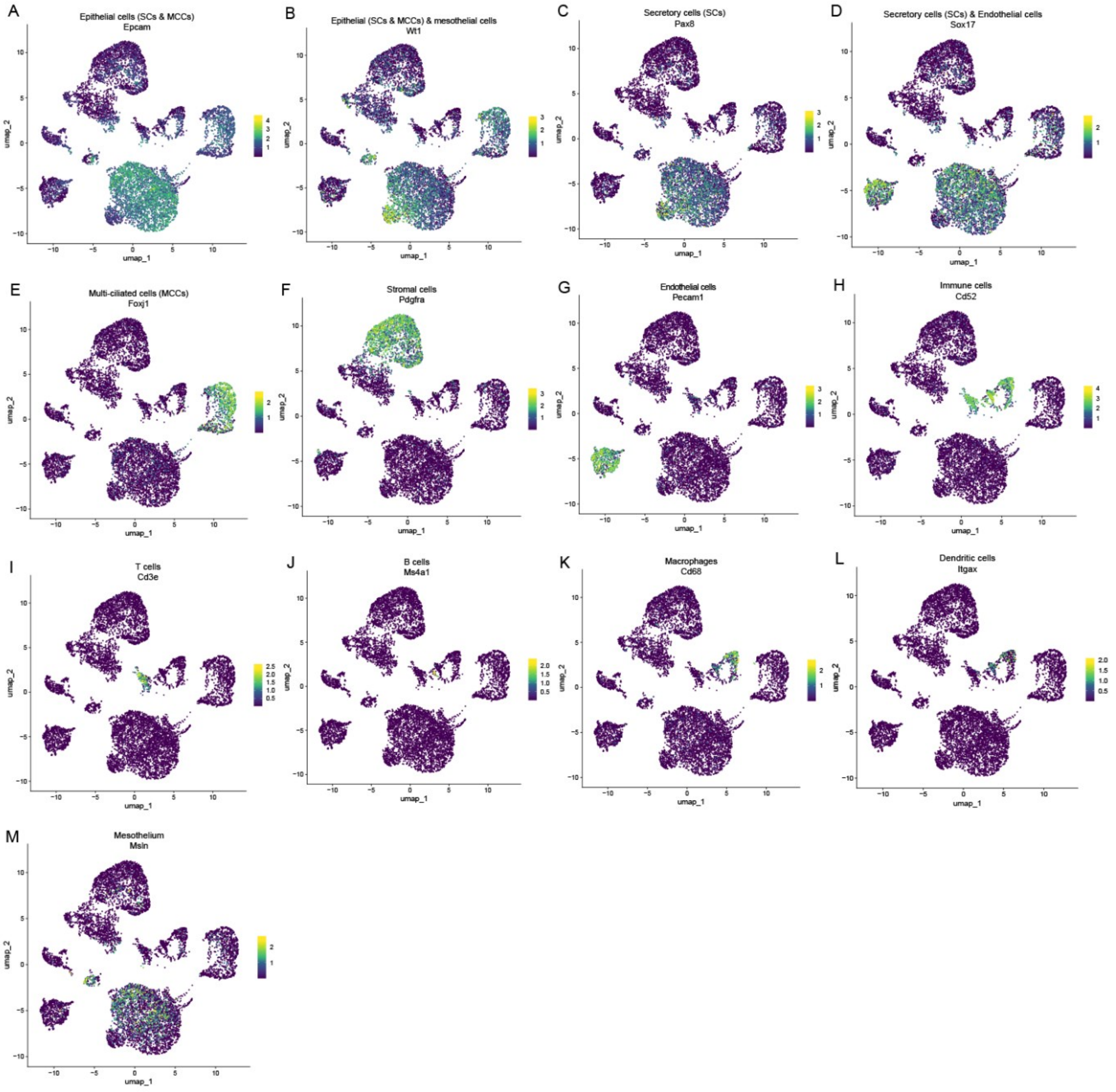

Supplementary Figure S4. 4: *Identification of isolated cell populations using gene expression pattern of known markers.*

(A-M) Gene expression of known markers that were not included in the dotplot, such as Epcam (A), Wt1 (B), Pax8 (C), Sox17 (D), Foxj1 (E), Pdgfra (F), Pecam1 (G), Cd52 (H), Cd3e (I), Cd20 (J), Cd68 (K), Cd11c (L), Msln (M).

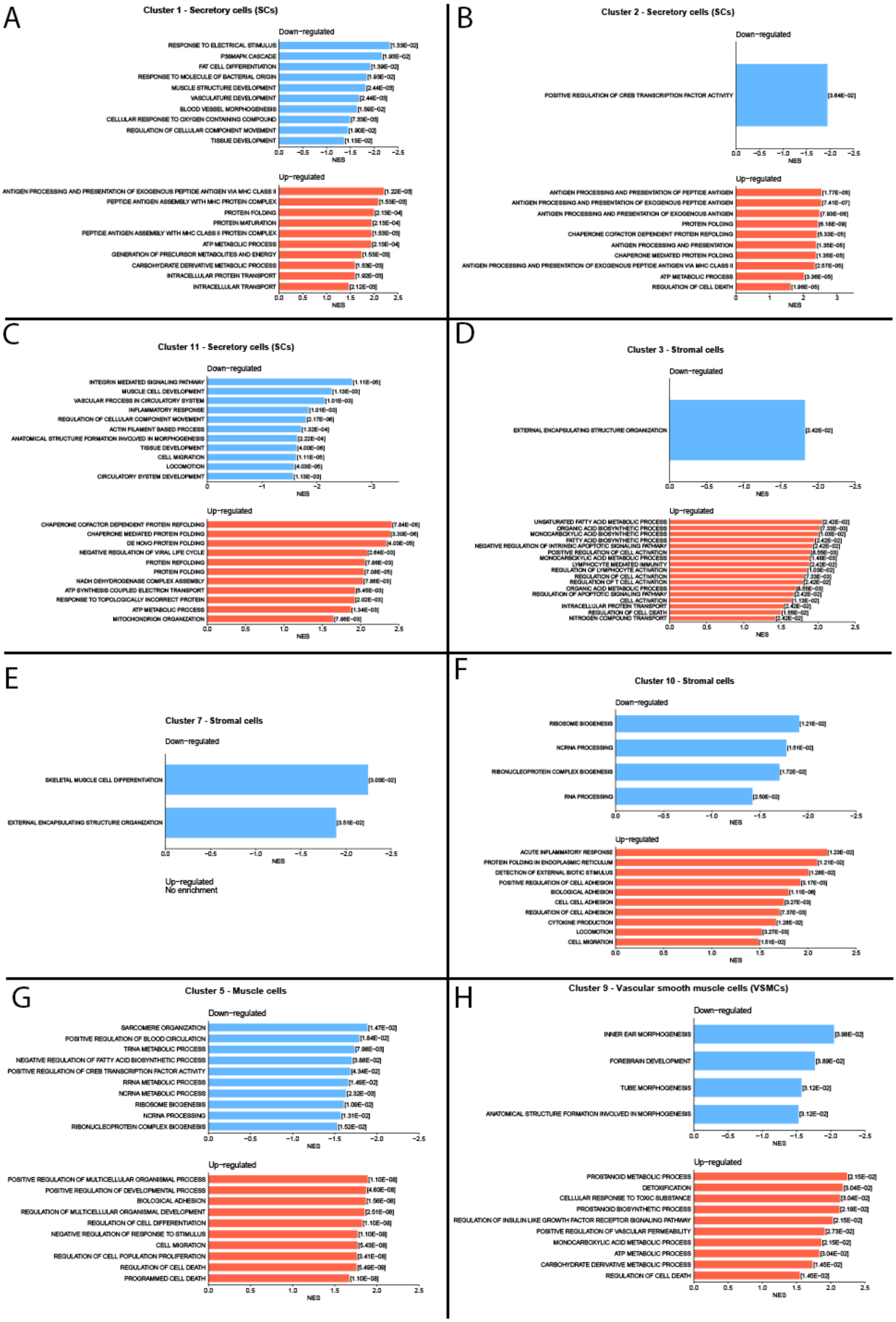
A
Cluster 1 - Secretory cells (SCs)
Down−regulated
RESPONSE TO ELECTRICAL STIMULUS [1.33E−02]
P38MAPK CASCADE [1.93E−02]
FAT CELL DIFFERENTIATION [1.39E−02]
RESPONSE TO MOLECULE OF BACTERIAL ORIGIN [1.93E−02]
MUSCLE STRUCTURE DEVELOPMENT [2.44E−03]
VASCULATURE DEVELOPMENT [2.44E−03]
BLOOD VESSEL MORPHOGENESIS [1.59E−02]
CELLULAR RESPONSE TO OXYGEN CONTAINING COMPOUND [7.33E−03]
REGULATION OF CELLULAR COMPONENT MOVEMENT [1.90E−02]
TISSUE DEVELOPMENT [1.13E−02]
0.0 −0.5 −1.0 −1.5 −2.0 −2.5
NES
Up−regulated
ANTIGEN PROCESSING AND PRESENTATION OF EXOGENOUS PEPTIDE ANTIGEN VIA MHC CLASS II [1.22E−03]
PEPTIDE ANTIGEN ASSEMBLY WITH MHC PROTEIN COMPLEX [1.53E−03]
PROTEIN FOLDING [2.13E−04]
PROTEIN MATURATION [2.13E−04]
PEPTIDE ANTIGEN ASSEMBLY WITH MHC CLASS II PROTEIN COMPLEX [1.53E−03]
ATP METABOLIC PROCESS [2.13E−04]
GENERATION OF PRECURSOR METABOLITES AND ENERGY [1.53E−03]
CARBOHYDRATE DERIVATIVE METABOLIC PROCESS [1.53E−03]
INTRACELLULAR PROTEIN TRANSPORT [1.92E−03]
INTRACELLULAR TRANSPORT [2.12E−03]
0.0 0.5 1.0 1.5 2.0 2.5
NES
B
Cluster 2 - Secretory cells (SCs)
Down−regulated
POSITIVE REGULATION OF CREB TRANSCRIPTION FACTOR ACTIVITY [3.64E−02]
0.0 −0.5 −1.0 −1.5 −2.0 −2.5
NES
Up−regulated
ANTIGEN PROCESSING AND PRESENTATION OF PEPTIDE ANTIGEN [1.77E−06]
ANTIGEN PROCESSING AND PRESENTATION OF EXOGENOUS PEPTIDE ANTIGEN [7.41E−07]
ANTIGEN PROCESSING AND PRESENTATION OF EXOGENOUS ANTIGEN [7.93E−06]
PROTEIN FOLDING [6.18E−09]
CHAPERONE COFACTOR DEPENDENT PROTEIN REFOLDING [5.33E−05]
ANTIGEN PROCESSING AND PRESENTATION [1.35E−05]
CHAPERONE MEDIATED PROTEIN FOLDING [1.35E−05]
ANTIGEN PROCESSING AND PRESENTATION OF EXOGENOUS PEPTIDE ANTIGEN VIA MHC CLASS II [2.57E−05]
ATP METABOLIC PROCESS [3.36E−05]
REGULATION OF CELL DEATH [1.98E−05]
0 1 2 3
NES
C
Cluster 11 - Secretory cells (SCs)
Down−regulated
INTEGRIN MEDIATED SIGNALING PATHWAY [1.11E−05]
MUSCLE CELL DEVELOPMENT [1.13E−03]
VASCULAR PROCESS IN CIRCULATORY SYSTEM [1.01E−03]
INFLAMMATORY RESPONSE [1.01E−03]
REGULATION OF CELLULAR COMPONENT MOVEMENT [2.17E−06]
ACTIN FILAMENT BASED PROCESS [1.32E−04]
ANATOMICAL STRUCTURE FORMATION INVOLVED IN MORPHOGENESIS [2.22E−04]
TISSUE DEVELOPMENT [4.00E−06]
CELL MIGRATION [1.11E−05]
LOCOMOTION [4.03E−06]
CIRCULATORY SYSTEM DEVELOPMENT [1.13E−03]
0 −1 −2 −3
NES
Up−regulated
CHAPERONE COFACTOR DEPENDENT PROTEIN REFOLDING [7.84E−05]
CHAPERONE MEDIATED PROTEIN FOLDING [3.30E−06]
DE NOVO PROTEIN FOLDING [4.03E−05]
NEGATIVE REGULATION OF VIRAL LIFE CYCLE [2.64E−03]
PROTEIN REFOLDING [7.86E−03]
PROTEIN FOLDING [7.08E−05]
NADH DEHYDROGENASE COMPLEX ASSEMBLY [7.86E−03]
ATP SYNTHESIS COUPLED ELECTRON TRANSPORT [5.45E−03]
RESPONSE TO TOPOLOGICALLY INCORRECT PROTEIN [2.02E−03]
ATP METABOLIC PROCESS [1.34E−03]
MITOCHONDRION ORGANIZATION [7.86E−03]
0.0 0.5 1.0 1.5 2.0 2.5
NES
D
Cluster 3 - Stromal cells
Down−regulated
EXTERNAL ENCAPSULATING STRUCTURE ORGANIZATION [2.42E−02]
0.0 −0.5 −1.0 −1.5 −2.0 −2.5
NES
Up−regulated
UNSATURATED FATTY ACID METABOLIC PROCESS [2.42E−02]
ORGANIC ACID BIOSYNTHETIC PROCESS [7.33E−03]
MONOCARBOXYLIC ACID BIOSYNTHETIC PROCESS [1.03E−02]
FATTY ACID BIOSYNTHETIC PROCESS [2.42E−02]
NEGATIVE REGULATION OF INTRINSIC APOPTOTIC SIGNALING PATHWAY [2.42E−02]
POSITIVE REGULATION OF CELL ACTIVATION [8.55E−03]
MONOCARBOXYLIC ACID METABOLIC PROCESS [1.48E−03]
LYMPHOCYTE MEDIATED IMMUNITY [2.42E−02]
REGULATION OF LYMPHOCYTE ACTIVATION [1.03E−02]
REGULATION OF CELL ACTIVATION [7.33E−03]
REGULATION OF T CELL ACTIVATION [2.42E−02]
ORGANIC ACID METABOLIC PROCESS [8.55E−03]
REGULATION OF APOPTOTIC SIGNALING PATHWAY [2.42E−02]
CELL ACTIVATION [1.13E−02]
INTRACELLULAR PROTEIN TRANSPORT [2.42E−02]
REGULATION OF CELL DEATH [1.55E−02]
NITROGEN COMPOUND TRANSPORT [2.42E−02]
0.0 0.5 1.0 1.5 2.0 2.5
NES
E
Cluster 7 - Stromal cells
Down−regulated
SKELETAL MUSCLE CELL DIFFERENTIATION [3.03E−02]
EXTERNAL ENCAPSULATING STRUCTURE ORGANIZATION [3.51E−02]
0.0 −0.5 −1.0 −1.5 −2.0 −2.5
NES
Up−regulated
No enrichment
F
Cluster 10 - Stromal cells
Down−regulated
RIBOSOME BIOGENESIS [1.21E−02]
NCRNA PROCESSING [1.51E−02]
RIBONUCLEOPROTEIN COMPLEX BIOGENESIS [1.72E−02]
RNA PROCESSING [2.50E−02]
0.0 −0.5 −1.0 −1.5 −2.0 −2.5
NES
Up−regulated
ACUTE INFLAMMATORY RESPONSE [1.23E−02]
PROTEIN FOLDING IN ENDOPLASMIC RETICULUM [1.21E−02]
DETECTION OF EXTERNAL BIOTIC STIMULUS [1.28E−02]
POSITIVE REGULATION OF CELL ADHESION [3.17E−03]
BIOLOGICAL ADHESION [1.11E−06]
CELL CELL ADHESION [3.27E−03]
REGULATION OF CELL ADHESION [7.37E−03]
CYTOKINE PRODUCTION [1.28E−02]
LOCOMOTION [3.27E−03]
CELL MIGRATION [1.51E−02]
0.0 0.5 1.0 1.5 2.0 2.5
NES
G
Cluster 5 - Muscle cells
Down−regulated
SARCOMERE ORGANIZATION [1.47E−02]
POSITIVE REGULATION OF BLOOD CIRCULATION [1.84E−02]
TRNA METABOLIC PROCESS [7.98E−03]
NEGATIVE REGULATION OF FATTY ACID BIOSYNTHETIC PROCESS [3.88E−02]
POSITIVE REGULATION OF CREB TRANSCRIPTION FACTOR ACTIVITY [4.34E−02]
RRNA METABOLIC PROCESS [1.49E−02]
NCRNA METABOLIC PROCESS [2.32E−03]
RIBOSOME BIOGENESIS [1.09E−02]
NCRNA PROCESSING [1.31E−02]
RIBONUCLEOPROTEIN COMPLEX BIOGENESIS [1.52E−02]
0.0 −0.5 −1.0 −1.5 −2.0 −2.5
NES
Up−regulated
POSITIVE REGULATION OF MULTICELLULAR ORGANISMAL PROCESS [1.10E−08]
POSITIVE REGULATION OF DEVELOPMENTAL PROCESS [4.60E−08]
BIOLOGICAL ADHESION [1.56E−08]
REGULATION OF MULTICELLULAR ORGANISMAL DEVELOPMENT [2.51E−08]
REGULATION OF CELL DIFFERENTIATION [1.10E−08]
NEGATIVE REGULATION OF RESPONSE TO STIMULUS [1.10E−08]
CELL MIGRATION [5.43E−08]
REGULATION OF CELL POPULATION PROLIFERATION [3.41E−08]
REGULATION OF CELL DEATH [5.49E−09]
PROGRAMMED CELL DEATH [1.10E−08]
0.0 0.5 1.0 1.5 2.0 2.5
NES
H
Cluster 9 - Vascular smooth muscle cells (VSMCs)
Down−regulated
INNER EAR MORPHOGENESIS [3.98E−02]
FOREBRAIN DEVELOPMENT [3.89E−02]
TUBE MORPHOGENESIS [3.12E−02]
ANATOMICAL STRUCTURE FORMATION INVOLVED IN MORPHOGENESIS [3.12E−02]
0.0 −0.5 −1.0 −1.5 −2.0 −2.5
NES
Up−regulated
PROSTANOID METABOLIC PROCESS [2.15E−02]
DETOXIFICATION [3.04E−02]
CELLULAR RESPONSE TO TOXIC SUBSTANCE [3.04E−02]
PROSTANOID BIOSYNTHETIC PROCESS [2.19E−02]
REGULATION OF INSULIN LIKE GROWTH FACTOR RECEPTOR SIGNALING PATHWAY [2.15E−02]
POSITIVE REGULATION OF VASCULAR PERMEABILITY [2.73E−02]
MONOCARBOXYLIC ACID METABOLIC PROCESS [2.15E−02]
ATP METABOLIC PROCESS [3.04E−02]
CARBOHYDRATE DERIVATIVE METABOLIC PROCESS [1.45E−02]
REGULATION OF CELL DEATH [1.45E−02]
0.0 0.5 1.0 1.5 2.0 2.5
NES

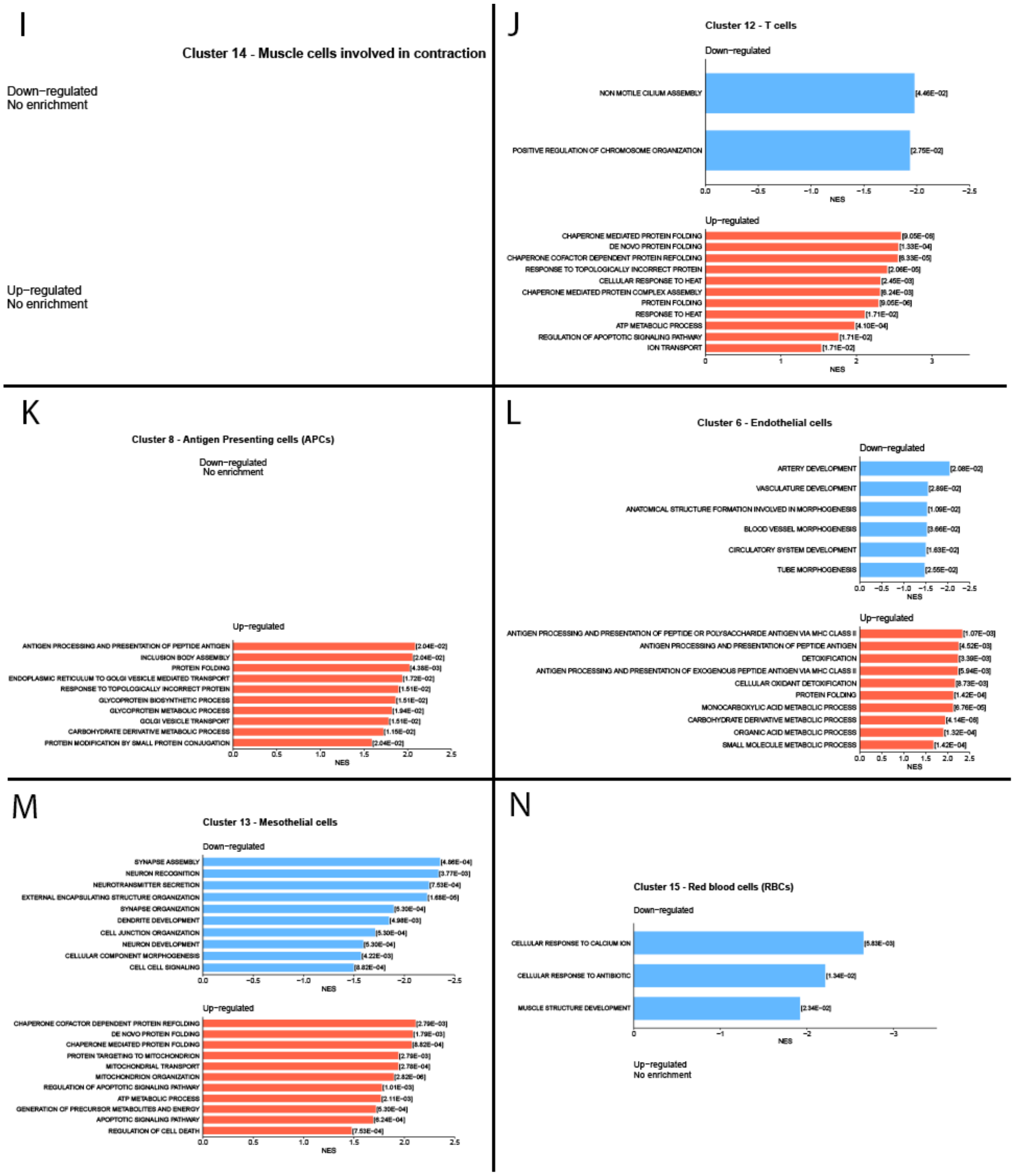

Supplementary Figure S4. 5: *GSEA of each cluster showing genesets down- or upregulated in 18mo INF/AMP cells, relative to 3mo INF/AMP cells.*

(A-C) GSEA showing down- and upregulated genesets in SC clusters 1 (A), 2 (B), and 11 (C). (D-F) GSEA showing down- and upregulated genesets in stromal cell clusters 3 (D), 7 (E), and 10 (F). (G-I) GSEA showing down- and upregulated genesets in muscle cell clusters 5 (G), 9

(H), and 14 (I). (J, K) GSEA showing down- and upregulated genesets in immune cell clusters, including cluster 12, identified as T-cells (J), and cluster 8, identified as antigen presenting cells/APCs (K). (L) GSEA showing down- and upregulated genesets in cluster 6, identified as endothelial cells. (M) GSEA showing down- and upregulated genesets in cluster 13, identified as mesothelial cells. (N) GSEA showing down- and upregulated genesets in cluster 15, identified as red blood cells/RBCs.

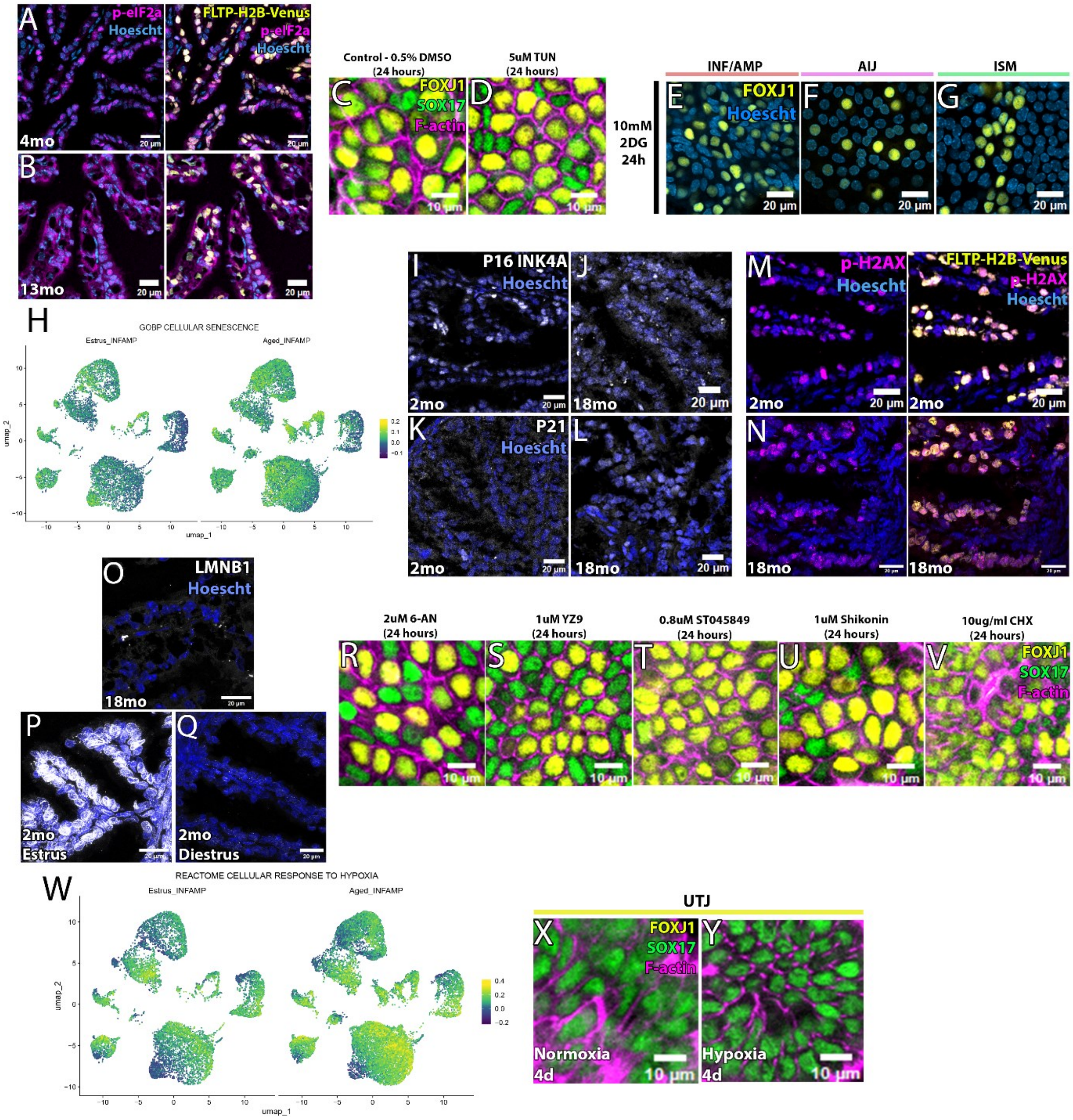

Supplementary Figure S4. 6: *MCC vacuolation is unaffected by ER stress induction, or inhibition of glycolysis, pentose phosphate, or hexosamine pathways.*

(A, B) Phosphorylated EIF2α staining in the INF/AMP region of young and aged mice. While nuclear staining was noted in SCs and MCCs of both young (A) and aged (B) samples, cytoplasmic punctate staining was noted in only 13mo mice (B). (C, D) ER stress was induced by treating with Tunicamycin/TUN for 24 hours in INF/AMP organotypic slice cultures. No obvious cellular differences were noted in treated cultures (D) and controls (C). (E-G) Inhibition of glycolysis in organotypic slice cultures. 24-hour-long 2-DG treatment did not induce any obvious cellular differences in the INF/AMP (E), AIJ (F), or ISM (G). (H-Q) Cellular senescence markers in the INF/AMP region of aged and young mice. Expression of cellular senescence-associated geneset between young (left) and aged (right) INF/AMP cells (H). Similar expression patterns of P16 (I, J), P21 (K, L), and phospho-H2AX (M, N) in young and aged mice. Lamin B1 expression in young and aged mice (O-Q). Lamin B1 was not detected in 18mo INF/AMP (O). Distinct LaminB1 expression levels in the INF/AMP region of 2mo mice in estrus (P) and diestrus stages (Q). (R-V) Induction of metabolic stress/nutrient deprivation in INF/AMP slice cultures. No cellular differences were noted upon inhibition of pentose phosphate pathway (R), hexosamine biosynthesis pathway (S), PFKFB3 (T), PKM2 (U), and protein synthesis (V). (W) UMAP showing expression of geneset associated with cellular response to hypoxia in young (left) and aged (right) INF/AMP cells. (X, Y) No discernible cellular changes in 4-day-long *in vitro* organotypic slices cultures of the UTJ region in both normoxia (X) and hypoxia (Y).

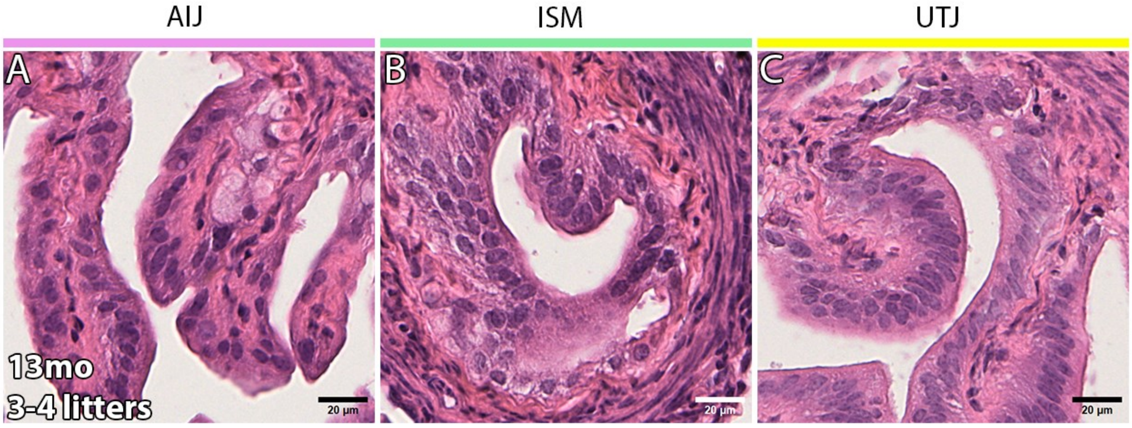

Supplementary Figure S4. 7*: No discernible vacuoles in the AIJ, ISM, and UTJ regions of 13mo mice with 3-4 litters.*

(A-C) Vacuoles were not reproducibly observed in the AIJ (A), ISM (B) and UTJ (C) regions of 13mo mice that had given birth to 3-4 litters.

5. General discussion

In this body of work, I identify and characterize anatomical, cellular and physiological differences along the mouse oviduct epithelium across adulthood and aging using a combination of transgenic mouse lines, 3-dimensional, 2-dimensional imaging, *in vitro* culture, and RNASeq, aiding reliable comparison between distinct oviduct regions in normal and/or disease states.

The mouse oviduct, a conduit for gametes and embryos, is a highly coiled tube that extends from the uterus. I demonstrated that the coiling is reproducible between oviducts/mice, with 11 turning points that were used as landmarks along the tube. I speculate that the process of oviduct coiling is similar to intestine looping. The intestine, a well-known looped organ, has a consistent looping pattern with occasional variation due to contractile movement. Its looping points are tightly linked with intestine regionalities and artery access points [120]. Prior to looping, the artery network reaches specific sites of the intestine via the mesentery, a membranous organ connecting the entire intestinal tube. Looping morphogenesis follows the pre-existing regionalities and artery network. Mechanical contributions of the mesentery are crucial for this morphogenesis [121, 122]. This is a developmentally controlled process with minimal variation. The oviduct-mesosalpinx structural relationship and the sequence of the developmental events appears similar to that of the intestine-mesentery. The coiled, adult oviduct was straightened out by removing the mesosalpinx, suggesting that the coils are tucked in due to constant tension in the mesosalpinx. At embryonic stages, the developing oviduct is initially looped around the developing ovary and slips to the bottom of the ovary by E18.5, followed by tucking during early postnatal stages [20, 123]. The morphogenetic process of the oviduct coiling is an interesting subject for future study. I predict that oviduct lengthening/growth while being constrained by the mesosalpinx likely results in tube buckling and coiling.

Unique mucosal fold morphologies correspond to each region: 1) the INFAMP and UTJ form continuous, longitudinal folds, 2) The AIJ forms broken, longitudinal folds, and 3) the ISM forms transverse/circumferential folds. Mucosal fold morphologies, specifically the longitudinal folds of the AMP, result from a combination of planar cell polarity (PCP) signaling/localization at the cellular level, mechanical properties of each layer including stiffness and rigidity, length and thickness of each layer, smooth muscle contraction, and mechanical buckling of the proliferating epithelial layer during development [6, 8, 124]. Loss of Celsr1 induced ectopic branching but did not prevent mucosal folding [7], suggesting that PCP signaling contributes to the fold pattern formation but may not affect folding initiation.

The mouse oviduct would be an interesting model to study initiation and maintenance of three distinct fold patterns in a single tube. Differentiation and constriction of the smooth muscle layers is important for vilification in the gut [125], and the oviduct may use a similar mechanism for folding initiation. Smooth muscle differentiation in the mouse oviduct occurs at postnatal day 1 (P1). However, mucosal folding is first noted in the AMP at P2-P3, while folds in the ISM are noted at P6-P7 [4, 86], which may reflect sequential differentiation of smooth muscle along the developing oviduct. Like in the chick midgut [125], differentiation of circumferentially oriented smooth muscle could result in constriction of the proliferating mesenchyme and epithelium, leading to inward buckling and continuous, longitudinal folds that protrude into the AMP or UTJ lumen. On the other hand, I speculate that differentiation of longitudinally oriented smooth muscle could act as a constraint, resulting in ISM epithelium buckling and transverse folds. Mucosal folds in the AIJ are longitudinal but discontinuous/broken, seemingly a transition between the AMP and ISM folds, reflecting a gradient of smooth muscle orientation or direction of contraction during postnatal development. This hypothesis can be tested by mapping out the timeline of smooth muscle differentiation in postnatal oviducts, and by removal of smooth muscle/muscle relaxant treatment in *in vitro* organotypic slice cultures from adult oviducts. However, it is important to note that studies on gut vilification mainly focus on chick gut, where differentiation of smooth muscle layers constrain the proliferative mesenchyme and endoderm [125], but recent studies in the mammalian gut shows that self-organized mesenchymal aggregate formation drives vilification [126], suggesting evolutionary differences in fold pattern initiation.

The proportions and distribution patterns of MCCs in each oviduct region are different, with the highest proportion in the INF/AMP (~60%), sparse distribution in the AIJ (~20%), clustered distribution at the trenches of the ISM (~20%), and no MCCs in the UTJ. The boundary between two regions is sharp, with the region farthest from the ovary/proximal region of each sharp boundary beginning on the mesosalpinx side, and the distal region extending proximally on the anti-mesosalpinx side. I speculate that these oviduct epithelial regions are specified prior to oviduct coiling, with blunt boundaries in a relatively straight tube. As the oviduct lengthens and coils, the mesosalpinx side is constrained by the mesosalpinx, while the anti-mesosalpinx side is unconstrained and lengthens – uneven growth (or stretch) of the epithelium on the inside/mesosalpinx side and outside/anti-mesolsapinx side stabilized on a fixed base - the uterus. Thus, the distal populations on the anti-mesosalpinx side, the outer side of the curved tube, unevenly stretches toward the uterus, resulting in bevelled boundaries (Figure 5.1). The distal-most AMP-AIJ transition was wider than the ISM-UTJ, further supporting this idea. There are a few mouse mutants where oviducts fail to coil such as *Amhr2-cre; Rosa*^{Notch1} [5] or *Wnt7a-/-* [unpublished data]. If this idea is correct, their regional boundaries should be blunt.

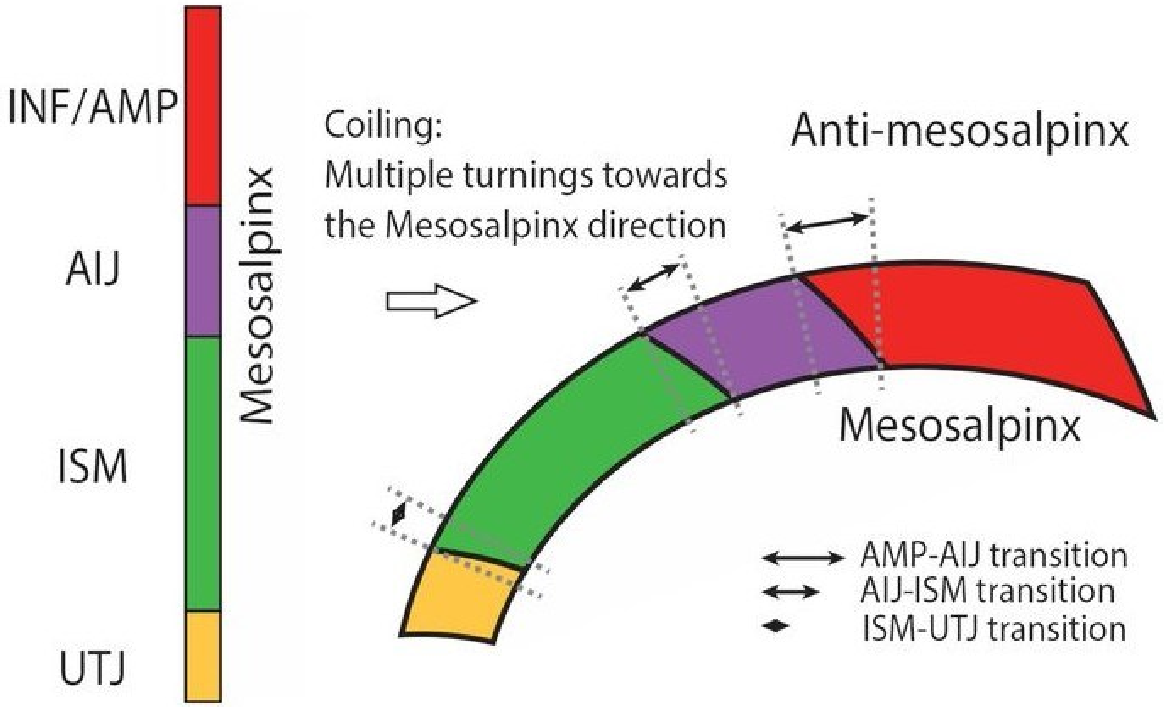

Figure 5. 1: A model for formation of boundary beveling.

(left) The blunt boundaries are specified before coiling. (right) Coiling, multiple turns toward the mesosalpinx side, causes the distance gap between the inner and outer side of the tube. The base of the oviduct is less affected by coiling but further away from the base, the gap becomes wider.

WT1 and PAX2 expression, restricted to the distal and proximal regions of the adult oviduct respectively, show a similar distal/proximal-specific expression from as early as E13.5. Interestingly, distal and proximal epithelial cells embedded in extracellular matrix and cultured in Wnt-high media grow into hollow spheres with monolayer epithelium that expresses WT1 and PAX2, respectively [17], suggesting the distal/proximal cellular identity is maintained without underlying stroma. Until my work in chapters 2 & 3, there was no molecular marker to separate the proximal epithelium aside from epithelial fold morphology and MCC distribution pattern. My results permit the study of the four morphologically distinct regions - I speculate that they will maintain their cellular identity, as defined by combinations of TFs, regardless of culture in the same condition, even in the absence of stromal cells. Epithelial organoids derived from the distal and proximal oviduct undergo ciliogenesis [17], and it is interesting to speculate that *in vivo* MCC proportions, particularly the lack of MCCs in the UTJ, are associated with regional identity and can be maintained in culture.

Enrichment of distinct biological processes in regionally restricted 3 MCC and 4 SC subtypes reflects their distinct functions during estrus stage. However, AIJ-specific acidic mucus secretion was noted in metestrus and diestrus stage, while INF/AMP MCC beat frequency differences are reported in estrus and diestrus stages [23], suggesting distinct function or biological processes depending on estrous stage. Since there was no clear separation of region-specific subtypes using PCA, it is interesting to speculate that fluid production and/or secretion associated genes/genesets were in abundance at estrus stage. Thus, SmartSeq sequencing of the 7 subtypes of epithelium in other estrous stages could amplify differences between regionally restricted subtypes, indicating additional distinct functions for each region.

Interestingly, the proximal oviduct epithelium showed differential enrichment of *Hif1a*, a transcriptional regulator of cellular response to hypoxia, with low expression in AIJ SCs, ISM epithelium, and high expression in the UTJ epithelium of estrus stage mice. While it is unknown whether Hif1a expression changes during estrous cycling, it is interesting to speculate that preimplantation embryo transport in the oviduct occurs in a hypoxic luminal environment. In line with this, low oxygen consumption is characteristic of 1 to 8-cell stage embryos [127] that were transported along the proximal regions.

A series of studies from our group including this body of work has uncovered cell subtype, physiological, developmental and homeostatic differences between the INF/AMP and the rest of the tube [17, 86, 128]. This is particularly interesting in the context of HGSCs, which originate in the distal tip of the FT. *Pax8-rtTA;tetO-Cre* mouse line crossed with Mosaic Analysis with Double Markers(*MADM)*-mutants resulted in large and small clones throughout the oviduct epithelium, with large clones predominantly located in the distal INF/AMP region [118], suggesting distinct susceptibility to oncogenic mutations. To directly test this distinct susceptibility, *in vivo* luminal injection and electroporation of CRISPR-Cas9 plasmids to mutate *Trp53*, *Brca1*, and *Pten* in the proximal oviduct epithelium, as performed previously in the distal oviduct epithelium by our group, could be performed. It is shown that the distal epithelium responds to mutations in *Trp53*, *Brca1*, and *Pten* by undergoing malignant transformation and progression [119], I predict that proximal epithelium will respond differently to the same mutation combination. Since distinct cell subtypes could be differently susceptible to specific mutation combinations [129], other mutation combinations commonly associated with HGSC could also be tested.

While SCs are considered the cell-of-origin of HGSCs, a recent study showed that pre-ciliated transitional cells within the INF/AMP form precursor lesions and HGSC in response to inactivation of *Trp53* and *Rb1 [88]*. This is in line with the concept of cellular pliancy, which posits that distinct differentiation states within a cellular lineage are uniquely susceptible to malignant transformation [129]. The minor double positive I3 population identified in Chapter 3 could correspond to this susceptible transitional cell type. Alongside this distinct cellular identity and/or cellular state, a permissive microenvironment, like that observed in the aged INF/AMP region, likely promotes pre-cancerous lesion formation and/or progression. *In vivo* injection and electroporation of CRISPR-Cas9 plasmids to mutate *Trp53*, *Brca1*, and *Pten* or other mutation combinations, followed by *in vitro* organotypic slice cultures in normoxia and hypoxia to test for changes in cell proliferation could determine whether a hypoxic environment constitutes a permissive environment for HGSC initiation.

6. Conclusions and future directions

The objective of my PhD was to investigate why the distal Fallopian tube (FT) was distinctly susceptible to malignant transformation. Since not much is known about the FT/oviduct, I began by describing mouse oviduct coiling and mucosal fold morphologies, thus demarcating the oviduct into 5 morphologically distinct regions: INF, AMP, AIJ, ISM and UTJ. Using a combination of 3D imaging and fluorescence reporter mouse lines, I showed that each region had a distinct MCC proportion and distribution pattern, unlike the simple gradient that is commonly described. Each region contained a unique pair of MCCs and SCs, expressing distinct combinations of a TFs.

Using *Fltp-h2b-Venus*; *Sox17-mCherry* double fluorescence reporter mice that marked all MCCs and SCs, I isolated MCCs and SCs from each region for low input, pooled SmartSeq and discovered cell subtype-specific differentially expressed genes, region-specific TFs, and potential functions, suggesting distinct cellular identities/states. Further studies involve investigating region-specific TF expression in organoids derived from each region to test whether regional identity is maintained in culture, without the influence of underlying, non-epithelial populations. Additionally, region-specific TF expression should be investigated in postnatal oviducts to determine when these populations are specified and whether regional identities are developmentally distinct, similar to distal-proximal identity.

Finally, I reported a distal INF/AMP MCC-specific cytoplasmic vacuolation phenotype in aged mice that was unaffected by lack of estrous cycling and/or ovulation, suggesting intrinsic and physiological differences. Similar MCC-specific vacuolation was induced in *in vitro* organotypic cultures maintained in hypoxia or treated with HU, however, unlike the *in vivo* INF/AMP specificity, vacuoles were noted in MCCs regardless of region. I showed that this phenotype reflected an altered, stressed INF/AMP microenvironment, caused by decline in circulation via the ovarian artery that supplied the ovary and INF/AMP. This is particularly interesting in the context of HGSCs that originate from the distal FT, and it would be interesting to test whether this altered luminal microenvironment contributes to pre-cancerous lesion formation and/or progression.

Taken together, I uncovered anatomical, cellular, physiological, and functional differences between the INF/AMP and the rest of the tube, which could contribute to its distinct susceptibility to malignant transformation.

7. Master reference list

Covering chapters 1 and 5:

[1] Rosner J, S.T., Sarao MS. (2024). Physiology, Female Reproduction. . In T.I.F.S. Publishing, ed.

[2] Cunha, G.R., Robboy, S.J., Kurita, T., Isaacson, D., Shen, J., Cao, M., and Baskin, L.S. (2018). Development of the human female reproductive tract. Differentiation 103, 46-65. 10.1016/j.diff.2018.09.001.

[3] Lyons, R.A., Saridogan, E., and Djahanbakhch, O. (2006). The reproductive significance of human Fallopian tube cilia. Human Reproduction Update 12, 363-372. 10.1093/humupd/dml012.

[4] Agduhr, E. (1927). STUDIES ON THE STRUCTURE AND DEVELOPMENT OF THE BURSA OVARICA AND THE TUBA UTERINA IN THE MOUSE. Acta Zoologica 8, 1-133. https://doi.org/10.1111/j.1463-6395.1927.tb00649.x.

[5] Ferguson, L., Kaftanovskaya, E.M., Manresa, C., Barbara, A.M., Poppiti, R.J., Tan, Y., and Agoulnik, A.I. (2016). Constitutive Notch Signaling Causes Abnormal Development of the Oviducts, Abnormal Angiogenesis, and Cyst Formation in Mouse Female Reproductive Tract. Biol Reprod 94, 67. 10.1095/biolreprod.115.134569.

[6] Koyama, H., and Fujimori, T. (2018). Biomechanics of epithelial fold pattern formation in the mouse female reproductive tract. Curr Opin Genet Dev 51, 59-66. 10.1016/j.gde.2018.06.010.

[7] Shi, D., Komatsu, K., Hirao, M., Toyooka, Y., Koyama, H., Tissir, F., Goffinet, A.M., Uemura, T., and Fujimori, T. (2014). Celsr1 is required for the generation of polarity at multiple levels of the mouse oviduct. Development 141, 4558-4568. 10.1242/dev.115659.

[8] Koyama, H., Shi, D., and Fujimori, T. (2019). Biophysics in oviduct: Planar cell polarity, cilia, epithelial fold and tube morphogenesis, egg dynamics. Biophys Physicobiol 16, 89-107. 10.2142/biophysico.16.0_89.

[9] Santana Gonzalez, L., Rota, I.A., Artibani, M., Morotti, M., Hu, Z., Wietek, N., Alsaadi, A., Albukhari, A., Sauka-Spengler, T., and Ahmed, A.A. (2021). Mechanistic Drivers of Müllerian Duct Development and Differentiation Into the Oviduct. Front Cell Dev Biol 9, 605301. 10.3389/fcell.2021.605301.

[10] Mullen, R.D., and Behringer, R.R. (2014). Molecular genetics of Müllerian duct formation, regression and differentiation. Sex Dev 8, 281-296. 10.1159/000364935.

[11] Miyamoto, N., Yoshida, M., Kuratani, S., Matsuo, I., and Aizawa, S. (1997). Defects of urogenital development in mice lacking Emx2. Development 124, 1653-1664. 10.1242/dev.124.9.1653.

[12] Kobayashi, A., Shawlot, W., Kania, A., and Behringer, R.R. (2004). Requirement of Lim1 for female reproductive tract development. Development 131, 539-549. 10.1242/dev.00951.

[13] Orvis, G.D., and Behringer, R.R. (2007). Cellular mechanisms of Müllerian duct formation in the mouse. Dev Biol 306, 493-504. 10.1016/j.ydbio.2007.03.027.

[14] Torres, M., Gómez-Pardo, E., Dressler, G.R., and Gruss, P. (1995). Pax-2 controls multiple steps of urogenital development. Development 121, 4057-4065. 10.1242/dev.121.12.4057.

[15] Carroll, T.J., Park, J.S., Hayashi, S., Majumdar, A., and McMahon, A.P. (2005). Wnt9b plays a central role in the regulation of mesenchymal to epithelial transitions underlying organogenesis of the mammalian urogenital system. Dev Cell 9, 283-292. 10.1016/j.devcel.2005.05.016.

[16] Major, A.T., Estermann, M.A., Roly, Z.Y., and Smith, C.A. (2022). An evo-devo perspective of the female reproductive tract. Biol Reprod 106, 9-23. 10.1093/biolre/ioab166.

[17] Ford, M.J., Harwalkar, K., Pacis, A.S., Maunsell, H., Wang, Y.C., Badescu, D., Teng, K., Yamanaka, N., Bouchard, M., Ragoussis, J., and Yamanaka, Y. (2021). Oviduct epithelial cells constitute two developmentally distinct lineages that are spatially separated along the distal-proximal axis. Cell Rep 36, 109677. 10.1016/j.celrep.2021.109677.

[18] Newman, L., Chopra, J., Dossett, C., Shepherd, E., Bercusson, A., Carroll, M., Walker, W., Lucas, J.S., and Cheong, Y. (2023). The impact of primary ciliary dyskinesia on female and male fertility: a narrative review. Hum Reprod Update 29, 347-367. 10.1093/humupd/dmad003.

[19] Briceag, I., Costache, A., Purcarea, V.L., Cergan, R., Dumitru, M., Briceag, I., Sajin, M., and Ispas, A.T. (2015). Fallopian tubes--literature review of anatomy and etiology in female infertility. J Med Life 8, 129-131.

[20] Stewart, C.A., and Behringer, R.R. (2012). Mouse Oviduct Development. In Mouse Development: From Oocyte to Stem Cells, J.Z. Kubiak, ed. (Springer Berlin Heidelberg), pp. 247-262. 10.1007/978-3-642-30406-4_14.

[21] Talbot, P., Geiske, C., and Knoll, M. (1999). Oocyte pickup by the mammalian oviduct. Mol Biol Cell 10, 5-8. 10.1091/mbc.10.1.5.

[22] Yuan, S., Wang, Z., Peng, H., Ward, S.M., Hennig, G.W., Zheng, H., and Yan, W. (2021). Oviductal motile cilia are essential for oocyte pickup but dispensable for sperm and embryo transport. Proc Natl Acad Sci U S A 118. 10.1073/pnas.2102940118.

[23] Shi, D., Komatsu, K., Uemura, T., and Fujimori, T. (2011). Analysis of ciliary beat frequency and ovum transport ability in the mouse oviduct. Genes Cells 16, 282-290. 10.1111/j.1365-2443.2011.01484.x.

[24] Murray, M.K. (1997). Morphological features of epithelial cells in the sheep isthmus oviduct during early pregnancy. Anat Rec 247, 368-378. 10.1002/(sici)1097-0185(199703)247:3<368::Aid-ar8>3.0.Co;2-q.

[25] Abe, H., Onodera, M., Sugawara, S., Satoh, T., and Hoshi, H. (1999). Ultrastructural features of goat oviductal secretory cells at follicular and luteal phases of the oestrous cycle. J Anat 195 (Pt 4), 515-521. 10.1046/j.1469-7580.1999.19540515.x.

[26] Abe, H. (1994). Regional variations in the ultrastructural features of secretory cells in the rat oviductal epithelium. Anat Rec 240, 77-85. 10.1002/ar.1092400108.

[27] Abe, H., and Oikawa, T. (1991). Regional differences in the ultrastructural features of secretory cells in the golden hamster (Mesocricetus auratus) oviductal epithelium. J Anat 175, 147-158.

[28] Komatsu, M., and Fujita, H. (1978). Electron-microscopic studies on the development and aging of the oviduct epithelium of mice. Anat Embryol (Berl) 152, 243-259. 10.1007/bf00350523.

[29] Wang, S., and Larina, I.V. (2021). *In vivo* dynamic 3D imaging of oocytes and embryos in the mouse oviduct. Cell Rep 36, 109382. 10.1016/j.celrep.2021.109382.

[30] Harris, E.A., Stephens, K.K., and Winuthayanon, W. (2020). Extracellular Vesicles and the Oviduct Function. Int J Mol Sci 21. 10.3390/ijms21218280.

[31] Rizos, D., Fair, T., Papadopoulos, S., Boland, M.P., and Lonergan, P. (2002). Developmental, qualitative, and ultrastructural differences between ovine and bovine embryos produced *in vivo* or *in vitro*. Mol Reprod Dev 62, 320-327. 10.1002/mrd.10138.

[32] Lloyd, R.E., Romar, R., Matás, C., Gutiérrez-Adán, A., Holt, W.V., and Coy, P. (2009). Effects of oviductal fluid on the development, quality, and gene expression of porcine blastocysts produced *in vitro*. Reproduction 137, 679-687. 10.1530/rep-08-0405.

[33] Muro, Y., Hasuwa, H., Isotani, A., Miyata, H., Yamagata, K., Ikawa, M., Yanagimachi, R., and Okabe, M. (2016). Behavior of Mouse Spermatozoa in the Female Reproductive Tract from Soon after Mating to the Beginning of Fertilization. Biol Reprod 94, 80. 10.1095/biolreprod.115.135368.

[34] La Spina, F.A., Puga Molina, L.C., Romarowski, A., Vitale, A.M., Falzone, T.L., Krapf, D., Hirohashi, N., and Buffone, M.G. (2016). Mouse sperm begin to undergo acrosomal exocytosis in the upper isthmus of the oviduct. Dev Biol 411, 172-182. 10.1016/j.ydbio.2016.02.006.

[35] Yamaguchi, R., Muro, Y., Isotani, A., Tokuhiro, K., Takumi, K., Adham, I., Ikawa, M., and Okabe, M. (2009). Disruption of ADAM3 impairs the migration of sperm into oviduct in mouse. Biol Reprod 81, 142-146. 10.1095/biolreprod.108.074021.

[36] Fujihara, Y., Miyata, H., and Ikawa, M. (2018). Factors controlling sperm migration through the oviduct revealed by gene-modified mouse models. Exp Anim 67, 91-104. 10.1538/expanim.17-0153.

[37] Frayne, J., and Hall, L. (1999). Mammalian sperm-egg recognition: does fertilin beta have a major role to play? Bioessays 21, 183-187. 10.1002/(sici)1521-1878(199903)21:3<183::Aid-bies1>3.0.Co;2-f.

[38] Yanagimachi, R. (2022). Mysteries and unsolved problems of mammalian fertilization and related topics. Biol Reprod 106, 644-675. 10.1093/biolre/ioac037.

[39] Qu, Y., Chen, Q., Guo, S., Ma, C., Lu, Y., Shi, J., Liu, S., Zhou, T., Noda, T., Qian, J., et al. (2021). Cooperation-based sperm clusters mediate sperm oviduct entry and fertilization. Protein Cell 12, 810-817. 10.1007/s13238-021-00825-y.

[40] Hino, T., and Yanagimachi, R. (2019). Active peristaltic movements and fluid production of the mouse oviduct: their roles in fluid and sperm transport and fertilization†. Biol Reprod 101, 40-49. 10.1093/biolre/ioz061.

[41] Ishikawa, Y., Usui, T., Yamashita, M., Kanemori, Y., and Baba, T. (2016). Surfing and Swimming of Ejaculated Sperm in the Mouse Oviduct. Biol Reprod 94, 89. 10.1095/biolreprod.115.135418.

[42] Kong, N., Xu, X., Zhang, Y., Wang, Y., Hao, X., Zhao, Y., Qiao, J., Xia, G., and Zhang, M. (2017). Natriuretic peptide type C induces sperm attraction for fertilization in mouse. Sci Rep 7, 39711. 10.1038/srep39711.

[43] Wang, Z., Wei, H., Wu, Z., Zhang, X., Sun, Y., Gao, L., Zhang, W., Su, Y.Q., and Zhang, M. (2022). The oocyte cumulus complex regulates mouse sperm migration in the oviduct. Commun Biol 5, 1327. 10.1038/s42003-022-04287-8.

[44] Suarez, S.S., and Pacey, A.A. (2006). Sperm transport in the female reproductive tract. Hum Reprod Update 12, 23-37. 10.1093/humupd/dmi047.

[45] Suarez, S.S. (1987). Sperm transport and motility in the mouse oviduct: observations in situ. Biol Reprod 36, 203-210. 10.1095/biolreprod36.1.203.

[46] Suarez, S.S., and Dai, X. (1992). Hyperactivation enhances mouse sperm capacity for penetrating viscoelastic media. Biol Reprod 46, 686-691. 10.1095/biolreprod46.4.686.

[47] Wang, S., and Larina, I.V. (2018). *In vivo* three-dimensional tracking of sperm behaviors in the mouse oviduct. Development 145. 10.1242/dev.157685.

[48] Jansen, R.P. (1995). Ultrastructure and histochemistry of acid mucus glycoproteins in the estrous mammal oviduct. Microsc Res Tech 32, 24-49. 10.1002/jemt.1070320104.

[49] Lefebvre, R., Chenoweth, P.J., Drost, M., LeClear, C.T., MacCubbin, M., Dutton, J.T., and Suarez, S.S. (1995). Characterization of the oviductal sperm reservoir in cattle. Biol Reprod 53, 1066-1074. 10.1095/biolreprod53.5.1066.

[50] Smith, T.T., and Yanagimachi, R. (1991). Attachment and release of spermatozoa from the caudal isthmus of the hamster oviduct. J Reprod Fertil 91, 567-573. 10.1530/jrf.0.0910567.

[51] Suarez, S., Redfern, K., Raynor, P., Martin, F., and Phillips, D.M. (1991). Attachment of boar sperm to mucosal explants of oviduct *in vitro*: possible role in formation of a sperm reservoir. Biol Reprod 44, 998-1004. 10.1095/biolreprod44.6.998.

[52] Hunter, R.H., and Nichol, R. (1983). Transport of spermatozoa in the sheep oviduct: preovulatory sequestering of cells in the caudal isthmus. J Exp Zool 228, 121-128. 10.1002/jez.1402280113.

[53] Thomas, P.G., Ball, B.A., and Brinsko, S.P. (1994). Interaction of equine spermatozoa with oviduct epithelial cell explants is affected by estrous cycle and anatomic origin of explant. Biol Reprod 51, 222-228. 10.1095/biolreprod51.2.222.

[54] Sasanami, T., Matsuzaki, M., Mizushima, S., and Hiyama, G. (2013). Sperm storage in the female reproductive tract in birds. J Reprod Dev 59, 334-338. 10.1262/jrd.2013-038.

[55] Suarez, S.S. (2001). Carbohydrate-mediated formation of the oviductal sperm reservoir in mammals. Cells Tissues Organs 168, 105-112. 10.1159/000016811.

[56] Halbert, S.A., Becker, D.R., and Szal, S.E. (1989). Ovum transport in the rat oviductal ampulla in the absence of muscle contractility. Biol Reprod 40, 1131-1136. 10.1095/biolreprod40.6.1131.

[57] Bianchi, E., Sun, Y., Almansa-Ordonez, A., Woods, M., Goulding, D., Martinez-Martin, N., and Wright, G.J. (2021). Control of oviductal fluid flow by the G-protein coupled receptor Adgrd1 is essential for murine embryo transit. Nat Commun 12, 1251. 10.1038/s41467-021-21512-w.

[58] Wang, H., Guo, Y., Wang, D., Kingsley, P.J., Marnett, L.J., Das, S.K., DuBois, R.N., and Dey, S.K. (2004). Aberrant cannabinoid signaling impairs oviductal transport of embryos. Nat Med 10, 1074-1080. 10.1038/nm1104.

[59] McGlade, E.A., Herrera, G.G., Stephens, K.K., Olsen, S.L.W., Winuthayanon, S., Guner, J., Hewitt, S.C., Korach, K.S., DeMayo, F.J., Lydon, J.P., et al. (2021). Cell-type

specific analysis of physiological action of estrogen in mouse oviducts. Faseb j 35, e21563. 10.1096/fj.202002747R.

[60] Lopera-Vasquez, R., Hamdi, M., Maillo, V., Gutierrez-Adan, A., Bermejo-Alvarez, P., Ramírez, M., Yáñez-Mó, M., and Rizos, D. (2017). Effect of bovine oviductal extracellular vesicles on embryo development and quality *in vitro*. Reproduction 153, 461-470. 10.1530/rep-16-0384.

[61] Huang, J.C., Goldsby, J.S., Arbab, F., Melhem, Z., Aleksic, N., and Wu, K.K. (2004). Oviduct prostacyclin functions as a paracrine factor to augment the development of embryos. Hum Reprod 19, 2907-2912. 10.1093/humrep/deh520.

[62] Huang, J.C., Wun, W.S., Goldsby, J.S., Matijevic-Aleksic, N., and Wu, K.K. (2004). Cyclooxygenase-2-derived endogenous prostacyclin enhances mouse embryo hatching. Hum Reprod 19, 2900-2906. 10.1093/humrep/deh524.

[63] Huang, J.C., Wun, W.S., Goldsby, J.S., Wun, I.C., Falconi, S.M., and Wu, K.K. (2003). Prostacyclin enhances embryo hatching but not sperm motility. Hum Reprod 18, 2582-2589. 10.1093/humrep/deg490.

[64] Huang, J.C., Goldsby, J.S., and Wun, W.S. (2004). Prostacyclin enhances the implantation and live birth potentials of mouse embryos. Hum Reprod 19, 1856-1860. 10.1093/humrep/deh352.

[65] Qu, P., Zhao, Y., Wang, R., Zhang, Y., Li, L., Fan, J., and Liu, E. (2019). Extracellular vesicles derived from donor oviduct fluid improved birth rates after embryo transfer in mice. Reprod Fertil Dev 31, 324-332. 10.1071/rd18203.

[66] Wake, Y., Endo, M., Tsunoda, S., Tawara, H., Abe, H., Nakagawa, Y., and Kaneko, T. (2023). Successful induction of pseudopregnancy using sonic vibration in mice. Sci Rep 13, 3604. 10.1038/s41598-023-30774-x.

[67] Chabbert-Buffet, N., and Bouchard, P. (2002). The normal human menstrual cycle. Rev Endocr Metab Disord 3, 173-183. 10.1023/a:1020027124001.

[68] Vollman, R.F. (1977). The menstrual cycle. Major Probl Obstet Gynecol 7, 1-193.

[69] Treloar, A.E., Boynton, R.E., Behn, B.G., and Brown, B.W. (1967). Variation of the human menstrual cycle through reproductive life. Int J Fertil 12, 77-126.

[70] Reed BG, C.B. (2018). The Normal Menstrual Cycle and the Control of Ovulation. . In A.B. Feingold KR, Blackman MR, et al., editors. Endotext [Internet]. South Dartmouth (MA): MDText.com, Inc., ed.

[71] Bertolin, K., and Murphy, B.D. (2014). 7 - Reproductive Tract Changes During the Mouse Estrous Cycle. In The Guide to Investigation of Mouse Pregnancy, B.A. Croy, A.T. Yamada, F.J. DeMayo, and S.L. Adamson, eds. (Academic Press), pp. 85-94. https://doi.org/10.1016/B978-0-12-394445-0.00007-2.

[72] Miller, B.H., and Takahashi, J.S. (2014). Central Circadian Control of Female Reproductive Function. Frontiers in Endocrinology 4. 10.3389/fendo.2013.00195.

[73] Ma, W.G., Song, H., Das, S.K., Paria, B.C., and Dey, S.K. (2003). Estrogen is a critical determinant that specifies the duration of the window of uterine receptivity for implantation. Proc Natl Acad Sci U S A 100, 2963-2968. 10.1073/pnas.0530162100.

[74] Winkler, I., Tolkachov, A., Lammers, F., Lacour, P., Daugelaite, K., Schneider, N., Koch, M.L., Panten, J., Grünschläger, F., Poth, T., et al. (2024). The cycling and aging mouse female reproductive tract at single-cell resolution. Cell 187, 981-998.e925. 10.1016/j.cell.2024.01.021.

[75] Nishimura, A., Sakuma, K., Shimamoto, C., Ito, S., Nakano, T., Daikoku, E., Ohmichi, M., Ushiroyama, T., Ueki, M., Kuwabara, H., et al. (2010). Ciliary beat frequency controlled by oestradiol and progesterone during ovarian cycle in guinea-pig Fallopian tube. Exp Physiol 95, 819-828. 10.1113/expphysiol.2010.052555.

[76] Bylander, A., Nutu, M., Wellander, R., Goksör, M., Billig, H., and Larsson, D.G. (2010). Rapid effects of progesterone on ciliary beat frequency in the mouse fallopian tube. Reprod Biol Endocrinol 8, 48. 10.1186/1477-7827-8-48.

[77] Winuthayanon, W., Bernhardt, M.L., Padilla-Banks, E., Myers, P.H., Edin, M.L., Lih, F.B., Hewitt, S.C., Korach, K.S., and Williams, C.J. (2015). Oviductal estrogen receptor α signaling prevents protease-mediated embryo death. Elife 4, e10453. 10.7554/eLife.10453.

[78] Li, S., O'Neill, S.R., Zhang, Y., Holtzman, M.J., Takemaru, K.I., Korach, K.S., and Winuthayanon, W. (2017). Estrogen receptor α is required for oviductal transport of embryos. Faseb j 31, 1595-1607. 10.1096/fj.201601128R.

[79] McGlade, E.A., Stephens, K.K., Winuthayanon, S., Anamthathmakula, P., Holtzman, M.J., and Winuthayanon, W. (2023). Classical Estrogen Signaling in Ciliated Epithelial Cells of the Oviduct Is Nonessential for Fertility in Female Mice. Endocrinology 165. 10.1210/endocr/bqad163.

[80] Herrera, G.G.B., Lierz, S.L., Harris, E.A., Donoghue, L.J., Hewitt, S.C., Rodriguez, K.F., Jefferson, W.N., Lydon, J.P., DeMayo, F.J., Williams, C.J., et al. (2020). Oviductal Retention of Embryos in Female Mice Lacking Estrogen Receptor α in the Isthmus and the Uterus. Endocrinology 161. 10.1210/endocr/bqz033.

[81] Vinijsanun, A., and Martin, L. (1990). Effects of progesterone antagonists RU486 and ZK98734 on embryo transport, development and implantation in laboratory mice. Reprod Fertil Dev 2, 713-727. 10.1071/rd9900713.

[82] Akison, L.K., Boden, M.J., Kennaway, D.J., Russell, D.L., and Robker, R.L. (2014). Progesterone receptor-dependent regulation of genes in the oviducts of female mice. Physiol Genomics 46, 583-592. 10.1152/physiolgenomics.00044.2014.

[83] Tibbetts, T.A., Mendoza-Meneses, M., O'Malley, B.W., and Conneely, O.M. (1998). Mutual and intercompartmental regulation of estrogen receptor and progesterone receptor expression in the mouse uterus. Biol Reprod 59, 1143-1152. 10.1095/biolreprod59.5.1143.

[84] Ghosh, A., Syed, S.M., and Tanwar, P.S. (2017). *In vivo* genetic cell lineage tracing reveals that oviductal secretory cells self-renew and give rise to ciliated cells. Development 144, 3031-3041. 10.1242/dev.149989.

[85] Ghosh, A., Syed, S.M., Kumar, M., Carpenter, T.J., Teixeira, J.M., Houairia, N., Negi, S., and Tanwar, P.S. (2020). *In Vivo* Cell Fate Tracing Provides No Evidence for Mesenchymal to Epithelial Transition in Adult Fallopian Tube and Uterus. Cell Rep 31, 107631. 10.1016/j.celrep.2020.107631.

[86] Ford, M.J., Harwalkar, K., Kazemdarvish, H., Yamanaka, N., and Yamanaka, Y. (2023). CD133/Prom1 marks proximal mouse oviduct epithelial progenitors and adult epithelial cells with a low generative capacity. Biol Open 12. 10.1242/bio.059963.

[87] Roberson, E.C., Tran, N.K., Konjikusic, M.J., Fitch, R.D., Gray, R.S., and Wallingford, J.B. (2020). A comparative study of the turnover of multiciliated cells in the mouse trachea, oviduct, and brain. Dev Dyn 249, 898-905. 10.1002/dvdy.165.

[88] Flesken-Nikitin, A., Ralston, C.Q., Fu, D.-J., De Micheli, A.J., Phuong, D.J., Harlan, B.A., Ashe, C.S., Armstrong, A.P., McKellar, D.W., Ghuwalewala, S., et al. (2024). Pre-ciliated tubal epithelial cells are prone to initiation of high-grade serous ovarian carcinoma. Nature Communications 15, 8641. 10.1038/s41467-024-52984-1.

[89] Xie, Y., Park, E.S., Xiang, D., and Li, Z. (2018). Long-term organoid culture reveals enrichment of organoid-forming epithelial cells in the fimbrial portion of mouse fallopian tube. Stem Cell Res 32, 51-60. 10.1016/j.scr.2018.08.021.

[90] Ford, M.J., Harwalkar, K., and Yamanaka, Y. (2022). Protocol to generate mouse oviduct epithelial organoids for viral transduction and whole-mount 3D imaging. STAR Protoc 3, 101164. 10.1016/j.xpro.2022.101164.

[91] Female age-related fertility decline. Committee Opinion No. 589. (2014). Fertil Steril 101, 633-634. 10.1016/j.fertnstert.2013.12.032.

[92] Broekmans, F.J., Soules, M.R., and Fauser, B.C. (2009). Ovarian aging: mechanisms and clinical consequences. Endocr Rev 30, 465-493. 10.1210/er.2009-0006.

[93] O'Connor, K.A., Holman, D.J., and Wood, J.W. (2001). Menstrual cycle variability and the perimenopause. Am J Hum Biol 13, 465-478. 10.1002/ajhb.1078.

[94] Allshouse, A., Pavlovic, J., and Santoro, N. (2018). Menstrual Cycle Hormone Changes Associated with Reproductive Aging and How They May Relate to Symptoms. Obstet Gynecol Clin North Am 45, 613-628. 10.1016/j.ogc.2018.07.004.

[95] Nelson, J.F., Felicio, L.S., Randall, P.K., Sims, C., and Finch, C.E. (1982). A longitudinal study of estrous cyclicity in aging C57BL/6J mice: I. Cycle frequency, length and vaginal cytology. Biol Reprod 27, 327-339. 10.1095/biolreprod27.2.327.

[96] Nelson, J.F., Felicio, L.S., Osterburg, H.H., and Finch, C.E. (1981). Altered profiles of estradiol and progesterone associated with prolonged estrous cycles and persistent vaginal cornification in aging C57BL/6J mice. Biol Reprod 24, 784-794. 10.1095/biolreprod24.4.784.

[97] Flurkey, K., Gee, D.M., Sinha, Y.N., Wisner, J.R., Jr., and Finch, C.E. (1982). Age effects on luteinizing hormone, progesterone and prolactin in proestrous and acyclic C57BL/6j mice. Biol Reprod 26, 835-846. 10.1095/biolreprod26.5.835.

[98] Nelson, J.F., Felicio, L.S., Osterburg, H.H., and Finch, C.E. (1992). Differential contributions of ovarian and extraovarian factors to age-related reductions in plasma

estradiol and progesterone during the estrous cycle of C57BL/6J mice. Endocrinology 130, 805-810. 10.1210/endo.130.2.1733727.

[99] Aschheim, P. (1961). [Repeated pseudogestation in senile rats]. C R Hebd Seances Acad Sci 253, 1988-1990.

[100] Felicio, L.S., Nelson, J.F., and Finch, C.E. (1984). Longitudinal studies of estrous cyclicity in aging C57BL/6J mice: II. Cessation of cyclicity and the duration of persistent vaginal cornification. Biol Reprod 31, 446-453. 10.1095/biolreprod31.3.446.

[101] Patel, R., Moffatt, J.D., Mourmoura, E., Demaison, L., Seed, P.T., Poston, L., and Tribe, R.M. (2017). Effect of reproductive ageing on pregnant mouse uterus and cervix. J Physiol 595, 2065-2084. 10.1113/jp273350.

[102] Wu, N.Y., Huang, H.S., Chao, T.H., Chou, H.M., Fang, C., Qin, C.Z., Lin, C.Y., Chu, T.Y., and Zhou, H.H. (2017). Progesterone Prevents High-Grade Serous Ovarian Cancer by Inducing Necroptosis of p53-Defective Fallopian Tube Epithelial Cells. Cell Rep 18, 2557-2565. 10.1016/j.celrep.2017.02.049.

[103] Bowtell, D.D., Böhm, S., Ahmed, A.A., Aspuria, P.J., Bast, R.C., Jr., Beral, V., Berek, J.S., Birrer, M.J., Blagden, S., Bookman, M.A., et al. (2015). Rethinking ovarian cancer II: reducing mortality from high-grade serous ovarian cancer. Nat Rev Cancer 15, 668-679. 10.1038/nrc4019.

[104] Reid, B.M., Permuth, J.B., and Sellers, T.A. (2017). Epidemiology of ovarian cancer: a review. Cancer Biol Med 14, 9-32. 10.20892/j.issn.2095-3941.2016.0084.

[105] Piek, J.M., van Diest, P.J., Zweemer, R.P., Jansen, J.W., Poort-Keesom, R.J., Menko, F.H., Gille, J.J., Jongsma, A.P., Pals, G., Kenemans, P., and Verheijen, R.H. (2001). Dysplastic changes in prophylactically removed Fallopian tubes of women predisposed to developing ovarian cancer. J Pathol 195, 451-456. 10.1002/path.1000.

[106] Medeiros, F., Muto, M.G., Lee, Y., Elvin, J.A., Callahan, M.J., Feltmate, C., Garber, J.E., Cramer, D.W., and Crum, C.P. (2006). The tubal fimbria is a preferred site for early adenocarcinoma in women with familial ovarian cancer syndrome. Am J Surg Pathol 30, 230-236. 10.1097/01.pas.0000180854.28831.77.

[107] Kindelberger, D.W., Lee, Y., Miron, A., Hirsch, M.S., Feltmate, C., Medeiros, F., Callahan, M.J., Garner, E.O., Gordon, R.W., Birch, C., et al. (2007). Intraepithelial carcinoma of the fimbria and pelvic serous carcinoma: Evidence for a causal relationship. Am J Surg Pathol 31, 161-169. 10.1097/01.pas.0000213335.40358.47.

[108] Fathalla, M.F. (1971). Incessant ovulation--a factor in ovarian neoplasia? Lancet 2, 163. 10.1016/s0140-6736(71)92335-x.

[109] Murdoch, W.J., and Martinchick, J.F. (2004). Oxidative damage to DNA of ovarian surface epithelial cells affected by ovulation: carcinogenic implication and chemoprevention. Exp Biol Med (Maywood) 229, 546-552. 10.1177/153537020422900613.

[110] Karst, A.M., and Drapkin, R. (2010). Ovarian cancer pathogenesis: a model in evolution. J Oncol 2010, 932371. 10.1155/2010/932371.

[111] Crum, C.P., Drapkin, R., Miron, A., Ince, T.A., Muto, M., Kindelberger, D.W., and Lee, Y. (2007). The distal fallopian tube: a new model for pelvic serous carcinogenesis. Curr Opin Obstet Gynecol 19, 3-9. 10.1097/GCO.0b013e328011a21f.

[112] Saleemuddin, A., Folkins, A.K., Garrett, L., Garber, J., Muto, M.G., Crum, C.P., and Tworoger, S. (2008). Risk factors for a serous cancer precursor ("p53 signature") in women with inherited BRCA mutations. Gynecol Oncol 111, 226-232. 10.1016/j.ygyno.2008.07.018.

[113] Iodice, S., Barile, M., Rotmensz, N., Feroce, I., Bonanni, B., Radice, P., Bernard, L., Maisonneuve, P., and Gandini, S. (2010). Oral contraceptive use and breast or ovarian

cancer risk in BRCA1/2 carriers: a meta-analysis. Eur J Cancer 46, 2275-2284. 10.1016/j.ejca.2010.04.018.

[114] Havrilesky, L.J., Moorman, P.G., Lowery, W.J., Gierisch, J.M., Coeytaux, R.R., Urrutia, R.P., Dinan, M., McBroom, A.J., Hasselblad, V., Sanders, G.D., and Myers, E.R. (2013). Oral contraceptive pills as primary prevention for ovarian cancer: a systematic review and meta-analysis. Obstet Gynecol 122, 139-147. 10.1097/AOG.0b013e318291c235.

[115] Vitale, S.G., Capriglione, S., Zito, G., Lopez, S., Gulino, F.A., Di Guardo, F., Vitagliano, A., Noventa, M., La Rosa, V.L., Sapia, F., et al. (2019). Management of endometrial, ovarian and cervical cancer in the elderly: current approach to a challenging condition. Archives of Gynecology and Obstetrics 299, 299-315. 10.1007/s00404-018-5006-z.

[116] Perets, R., Wyant, G.A., Muto, K.W., Bijron, J.G., Poole, B.B., Chin, K.T., Chen, J.Y., Ohman, A.W., Stepule, C.D., Kwak, S., et al. (2013). Transformation of the fallopian tube secretory epithelium leads to high-grade serous ovarian cancer in Brca;Tp53;Pten models. Cancer Cell 24, 751-765. 10.1016/j.ccr.2013.10.013.

[117] Zhai, Y., Wu, R., Kuick, R., Sessine, M.S., Schulman, S., Green, M., Fearon, E.R., and Cho, K.R. (2017). High-grade serous carcinomas arise in the mouse oviduct via defects linked to the human disease. J Pathol 243, 16-25. 10.1002/path.4927.

[118] Zeng, J., Alvarez-Yela, A.C., Casarez, E., Jiang, Y., Wang, L., Kelly, B.E., Jenkins, T., Ke, E., Atkins, K.A., Janes, K.A., et al. (2023). Dichotomous ovarian cancer-initiating potential of Pax8+ cells revealed by a mouse genetic mosaic model. iScience 26, 106742. 10.1016/j.isci.2023.106742.

[119] Teng, K., Ford, M.J., Harwalkar, K., Li, Y., Pacis, A.S., Farnell, D., Yamanaka, N., Wang, Y.C., Badescu, D., Ton Nu, T.N., et al. (2021). Modeling High-Grade Serous

Ovarian Carcinoma Using a Combination of *In Vivo* Fallopian Tube Electroporation and CRISPR-Cas9-Mediated Genome Editing. Cancer Res 81, 5147-5160. 10.1158/0008-5472.Can-20-1518.

[120] Soffers, J.H., Hikspoors, J.P., Mekonen, H.K., Koehler, S.E., and Lamers, W.H. (2015). The growth pattern of the human intestine and its mesentery. BMC Dev Biol 15, 31. 10.1186/s12861-015-0081-x.

[121] Huycke, T.R., Miller, B.M., Gill, H.K., Nerurkar, N.L., Sprinzak, D., Mahadevan, L., and Tabin, C.J. (2019). Genetic and Mechanical Regulation of Intestinal Smooth Muscle Development. Cell 179, 90-105.e121. 10.1016/j.cell.2019.08.041.

[122] Nerurkar, N.L., Mahadevan, L., and Tabin, C.J. (2017). BMP signaling controls buckling forces to modulate looping morphogenesis of the gut. Proc Natl Acad Sci U S A 114, 2277-2282. 10.1073/pnas.1700307114.

[123] McKey, J., Anbarci, D.N., Bunce, C., Ontiveros, A.E., Behringer, R.R., and Capel, B. (2022). Integration of mouse ovary morphogenesis with developmental dynamics of the oviduct, ovarian ligaments, and rete ovarii. Elife 11. 10.7554/eLife.81088.

[124] Koyama, H., Shi, D., Suzuki, M., Ueno, N., Uemura, T., and Fujimori, T. (2016). Mechanical Regulation of Three-Dimensional Epithelial Fold Pattern Formation in the Mouse Oviduct. Biophys J 111, 650-665. 10.1016/j.bpj.2016.06.032.

[125] Shyer, A.E., Tallinen, T., Nerurkar, N.L., Wei, Z., Gil, E.S., Kaplan, D.L., Tabin, C.J., and Mahadevan, L. (2013). Villification: how the gut gets its villi. Science 342, 212-218. 10.1126/science.1238842.

[126] Huycke, T.R., Häkkinen, T.J., Miyazaki, H., Srivastava, V., Barruet, E., McGinnis, C.S., Kalantari, A., Cornwall-Scoones, J., Vaka, D., Zhu, Q., et al. (2024). Patterning and folding of intestinal villi by active mesenchymal dewetting. Cell 187, 3072-3089.e3020. 10.1016/j.cell.2024.04.039.

[127] Houghton, F.D., Thompson, J.G., Kennedy, C.J., and Leese, H.J. (1996). Oxygen consumption and energy metabolism of the early mouse embryo. Molecular Reproduction and Development 44, 476-485. https://doi.org/10.1002/(SICI)1098-2795(199608)44:4<476::AID-MRD7>3.0.CO;2-I.

[128] Harwalkar, K., Ford, M.J., Teng, K., Yamanaka, N., Yang, B., Burtscher, I., Lickert, H., and Yamanaka, Y. (2021). Anatomical and cellular heterogeneity in the mouse oviduct—its potential roles in reproduction and preimplantation development†. Biology of Reproduction 104, 1249-1261. 10.1093/biolre/ioab043.

[129] Puisieux, A., Pommier, R.M., Morel, A.P., and Lavial, F. (2018). Cellular Pliancy and the Multistep Process of Tumorigenesis. Cancer Cell 33, 164-172. 10.1016/j.ccell.2018.01.007.